BEILSTEIN JOURNAL OF NANOTECHNOLOGY

Biomimetics and bioinspired surfaces: from nature to theory and applications

Edited by Rhainer Guillermo Ferreira, Thies Büscher, Manuela Rebora, Poramate Manoonpong, Zhendong Dai and Stanislav Gorb

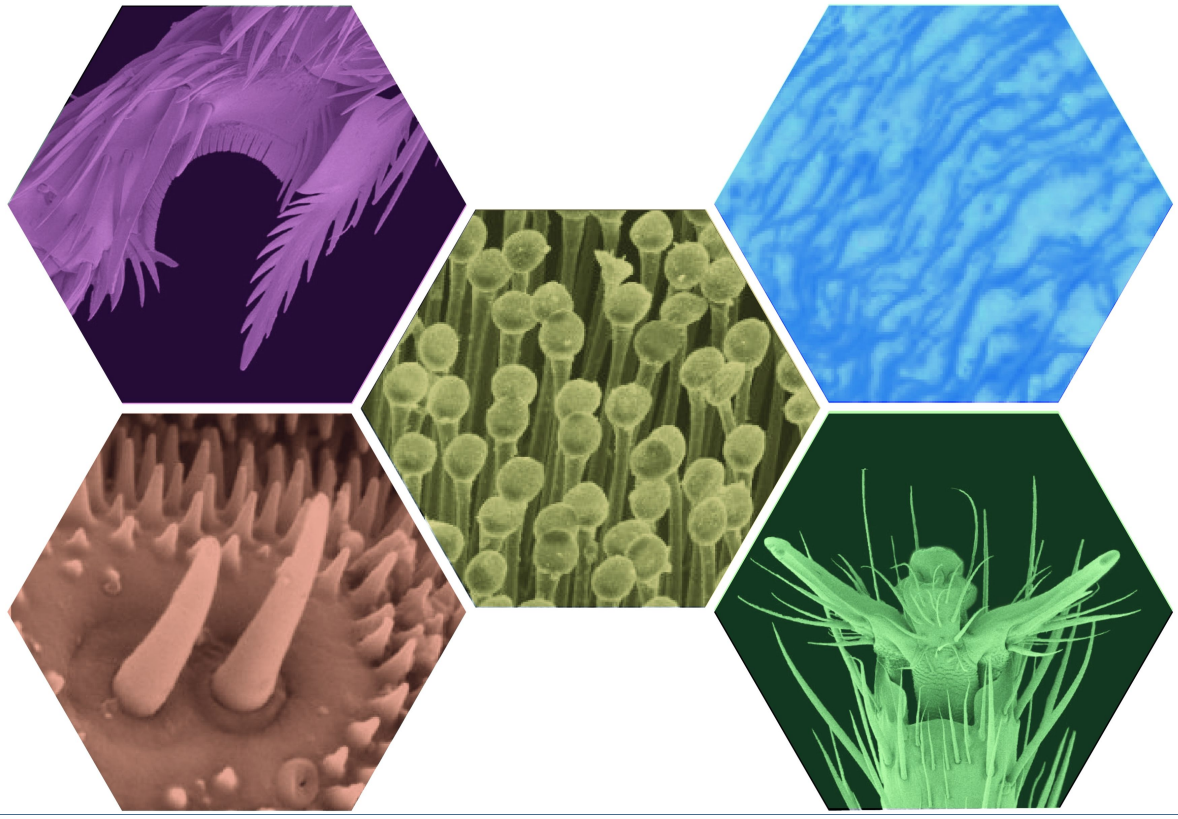

Generated on 11 August 2026, 17:02

The copyright to this document as a whole, which is published in the *Beilstein Journal of Nanotechnology*, is held by the Beilstein-Institut zur Förderung der Chemischen Wissenschaften. The copyright to the individual articles in this document is held by the respective authors, subject to a Creative Commons Attribution license.

Imprint

Beilstein Journal of Nanotechnology
www.bjnano.org
ISSN 2190-4286
Email: journals-support@beilstein-institut.de

The *Beilstein Journal of Nanotechnology* is published by the Beilstein-Institut zur Förderung der Chemischen Wissenschaften.

Beilstein-Institut zur Förderung der Chemischen Wissenschaften
Trakehner Straße 7–9
60487 Frankfurt am Main
Germany
www.beilstein-institut.de

The upper left and lower right part of the cover image was adapted from Beilstein J. Nanotechnol. 2024, 15, 1333–1352 (© 2024 V. M. Lopez et al.). This content is not subject to CC BY 4.0. The middle part was adapted from Beilstein J. Nanotechnol. 2024, 15, 385–395 (© 2024 E. V. Gorb et al.), the lower left part was adapted from Beilstein J. Nanotechnol. 2024, 15, 867–883 (© 2024 M. Grote et al.), the upper right part was adapted from Beilstein J. Nanotechnol. 2024, 15, 612–630 (© 2024 J. Thomas et al.), published by Beilstein-Institut, distributed under the terms of the Creative Commons Attribution 4.0 International License, https://creativecommons.org/licenses/by/4.0).

BEILSTEIN JOURNAL OF NANOTECHNOLOGY

Biomimetics and bioinspired surfaces: from nature to theory and applications

Rhainer Guillermo Ferreira*[1], Thies H. Büscher[2], Manuela Rebora[3], Poramate Manoonpong[4], Zhendong Dai[5] and Stanislav N. Gorb[2]

Editorial

Open Access

Address:
[1]Lestes Lab, Federal University of Triângulo Mineiro, Uberaba, Minas Gerais, Brazil, [2]Department of Functional Morphology and Biomechanics, Kiel University, Am Botanischen Garten 1–9, 24098 Kiel, Germany, [3]Dipartimento di Chimica, Biologia e Biotecnologie, University of Perugia, Via Elce di Sotto 8, 06121 Perugia, Italy, [4]Embodied AI & Neurorobotics Lab, The Maersk Mc-Kinney Moller Institute, The University of Southern Denmark,Campusvej 55, 5230 Odense, Denmark and [5]State Key Laboratory of Mechanics and Control for Aerospace Structures, College of Mechanical and Electrical Engineering, Nanjing University of Aeronautics and Astronautics, Nanjing, China

Email:
Rhainer Guillermo Ferreira* - rhainer.ferreira@uftm.edu.br

* Corresponding author

Keywords:
adhesives; bioengineering; biomimetics; drag reduction; functional morphology; insects; medical coatings; microstructures; nanostructures; wettability

Beilstein J. Nanotechnol. **2025,** *16,* 418–421.
https://doi.org/10.3762/bjnano.16.32

Received: 16 January 2025
Accepted: 30 January 2025
Published: 26 March 2025

This article is part of the thematic issue " Biomimetics and bioinspired surfaces: from nature to theory and applications".

Editor-in-Chief: G. Wilde

© 2025 Ferreira et al.; licensee Beilstein-Institut.
License and terms: see end of document.

The surfaces of living organisms are continuously interacting with their surroundings. As a result, they encounter a variety of challenges arising from both external and internal stimuli. Consequently, these surfaces must be multifunctional and adapt to numerous environmental pressures. Such pressures involve intricate interactions between surface structures and the environment across different scales, including nano-, micro-, and macroscales.

Biomimetics aims at making use of understanding how these adaptations and the particular material properties of these surfaces influence their performance and at drawing inspiration for modern technology from the vast array of solutions found in nature [1]. By examining the multiscale structures and mechanisms in biological systems, innovative and technologically advanced solutions can be developed for practical applications. Bioinspired nanotechnology plays a crucial role by harnessing nanoscale properties and processes to create highly effective surfaces and interfaces at various scales.

In May 2023, the Beilstein Nanotechnology Symposium “Functional Micro- and Nanostructured Surfaces: from Biology to Biomimetics” gathered diverse researchers from various disciplines in Limburg, Germany, to showcase important advances in biomimetics and discuss ideas providing an interdisciplinary platform to discuss novel developments and trends in the field of biological and bioinspired surfaces. This thematic issue in the *Beilstein Journal of Nanotechnology* emerged from this fruitful exchange of ideas.

The symposium featured a range of topics across biomimetic and bioinspired approaches, as well as the characterization of biological surfaces with properties of technological interest. A significant deal of research focused on understanding the biological systems and their potential as inspiration for innovation in producing biomimetic and bioinspired surfaces.

Key topics included bioinspired micro- and nanostructured surfaces, and their tribological properties like friction, wear resistance, and adhesion. Discussions also addressed surfaces with self-cleaning and wettability functionalities, as well as photonic surfaces, highlighting the broad sense and intent of the symposium for bridging biology and biomimetics in advanced materials sciences. The panel was composed of experts from all around the world resulting in the compilation of studies that form this thematic issue.

The thematic issue "Biomimetics and Bioinspired Surfaces: From Nature to Theory and Applications" is composed of nine articles that not only show the possibilities of analyzing natural phenomena in detail, but also empirical applications of bioinspired technology and new insights into the future of this field of research. Striking advance has been made regarding the study of surfaces on biological models, especially insects. For instance, insect attachment devices and adhesive secretions were thoroughly studied regarding the impact of contamination [2] and ageing [3]. Gorb and Gorb [2] experimentally investigated how different plant waxes affect the attachment performance of leaf beetles and how the adhesive system of these beetles are vulnerable to the shape and dimensions of wax contaminations. A study on larger insects (stick insects) with a considerable long-life expectancy by Grote et al. [3] focused on the structure and performance changes of the adhesive system during aging. The attachment performance of these insects decreases with increasing age, and was shown to be related to changes of the attachment pads regarding their elasticity, substrate compliance, and overall pad geometry. The attachment system of a second stick insect species was structurally investigated by Thomas et al. [4]. This article employed a range of imaging techniques to elucidate the ultrastructure and material composition of the two attachment pad types of this species.

Other possible sources of bioinspiration have been extensively examined by a review on functional surfaces in Hymenoptera, which include bees, wasps, and ants [5]. This diverse group of insects offers a rich array of surfaces that are adapted to realize different tasks, providing insights into the structure–function relationships of these surfaces useful for translational approaches. Further general insights into biological principles and their subsequent transfer into biomimetic engineering are provided in a multiscale biological analysis by Amador et al. [6], ranging from viruses to mammals while addressing the functional fibrillar interfaces in biological hair.

Presenting one applied example for biomimetic approaches, Ali et al. [7] used the hydrophobicity of the integument of spring tail (Collembola) as a template for the bioinspired development of nanofilament coatings that reduce scaling on steel surfaces. Using silicone nanofilaments, they achieved 75.5% reduction of calcium carbonate deposition on treated steel samples.

While many articles concentrated on using natural designs to inspire technological innovation (biology-push), others took an application-driven (technology-pull) approach. For instance, Bartoli et al. [8] reviewed the potential applications of nanostructured carbon coatings – such as nanodiamonds, carbon nanotubes, and graphene-based materials – to improve interaction on the interface between medical implants and living cells. Several biological materials exhibit microstructures that reduce drag; for instance, bees and wasps have structures on the wings that facilitate flying [5]. Zhu et al. [9] applied this concept in using microtextures to rotating blades of aircraft engines. Their results show that the microtextures may improve energy efficiency by 3.7% of a single blade by reducing the drag, which improves the overall performance of the engine. Finally, Sameoto [10] presents a stimulating perspective article on bioinspired adhesives, which advocates for a paradigm shift in biomimetics research. Instead of merely drawing inspiration from nature to discover new materials, the work proposes focusing on re-engineering applications to enhance manufacturing processes and improve the performance of biomimetic adhesives, thereby pushing the boundaries of this dynamic field further.

Overall, this thematic issue serves as an original resource of novel approaches and data regarding bioinspired surfaces, bridging biology and materials science. The high-quality contributions showcase innovative designs and practical applications of biomimetic surfaces. We express our gratitude to all the authors, who contributed their research to this collection, and to the reviewers, who helped us to critically discuss and improve the manuscripts. It is our hope that these studies inspire scientists, engineers, and innovators to further explore the possibilities of biomimetic designs, forging new paths in material science and technology.

Dedication

Biomimetics, the key connective element of this thematic issue, was fundamentally influenced by Prof. Dr. Werner Nachtigall (Figure 1). He is considered one of the pioneers of this field and contributed with outstanding achievements in theory and praxis to biomimetics. Numerous books, studies on biological tem-

plates, and bioinspired applications have been published with his participation. Sadly, the biomimetic community lost this major personality on the 5th of September, 2024, who passed away at the age of 90 years old. We dedicate this thematic issue on biomimetic surfaces to commemorate his achievements and motivation.

Figure 1: Werner Nachtigall during one of his visits in Kiel, 2012 (photograph by Stanislav N. Gorb). This content is not subject to CC BY 4.0.

Werner Nachtigall's unparalleled commitment to establishing the concept of biomimetics and promoting bioinspired problem solving left clear marks. In 1990, he established the study curriculum *Technical Biology and Biomimetics* within the Biology program at Saarland University where he worked as full professor since 1969 and remained there until his retirement in 2002. He founded the *Society for Technical Biology and Biomimetics* of which he served as the first chairman until 2003 to support the field nationally and internationally, as well as the *Biomimetics Network of Excellence e.V.* (BIOKON).

Werner Nachtigall enriched the scientific community through various activities. He acted as a trusted lecturer for the German National Academic Foundation, as a long-time reviewer for the German Research Foundation, as a member of the Mainz Academy of Sciences and Literature, and as a member of the Sudeten German Academy of Sciences and Arts in Munich. We received the news of the passing of Werner Nachtigall with great sadness during the compilation of this thematic issue. With more than 300 publications, he remains visible in the field and the memories of biomimeticists, as highlighted in detail in an obituary by Reihnard Blickhahn [11]. Most noteworthy, he will be remembered for his comprehensive books on the conceptualization and establishment of biomimetics as a scientific discipline, such as *Biomechanik* (biomechanics) [12], *Bionik – Grundlagen und Beispiele für Ingenieure und Naturwissenschaftler* (Biomimetics – basics and examples for engineers and scientists) [13] or *Bionik als Wissenschaft* (Biomimetics as a scientific discipline) [14] which remain influential for the scientific community. His book on biological attachment mechanisms and their use in bioengineering has been influential for scientists working on biomimetic surfaces since the 1970 [15] and paved the way for one of the core topics of this thematic issue.

Rhainer Guillermo Ferreira, Thies H. Büscher, Manuela Rebora, Poramate Manoonpong, Zhendong Dai and Stanislav N. Gorb

Uberaba, Kiel, Perugia, Odense, and Nanjing, January 2025

Author Contributions

Rhainer Guillermo Ferreira: conceptualization; writing – original draft; writing – review & editing. Thies H. Büscher: conceptualization; writing – original draft; writing – review & editing. Manuela Rebora: conceptualization; writing – review & editing. Poramate Manoonpong: conceptualization; writing – review & editing. Zhendong Dai: conceptualization; writing – review & editing. Stanislav N. Gorb: conceptualization; writing – review & editing.

ORCID® iDs

Rhainer Guillermo Ferreira - https://orcid.org/0000-0001-7774-5252
Thies H. Büscher - https://orcid.org/0000-0003-0639-4699
Manuela Rebora - https://orcid.org/0000-0002-4271-6336
Stanislav N. Gorb - https://orcid.org/0000-0001-9712-7953

Data Availability Statement

Data sharing is not applicable as no new data was generated or analyzed in this study.

References

1. Vincent, J. F. V.; Bogatyreva, O. A.; Bogatyrev, N. R.; Bowyer, A.; Pahl, A.-K. *J. R. Soc., Interface* **2006,** *3,* 471–482. doi:10.1098/rsif.2006.0127

2. Gorb, E. V.; Gorb, S. N. *Beilstein J. Nanotechnol.* **2024,** *15,* 385–395. doi:10.3762/bjnano.15.35
3. Grote, M.; Gorb, S. N.; Büscher, T. H. *Beilstein J. Nanotechnol.* **2024,** *15,* 867–883. doi:10.3762/bjnano.15.72
4. Thomas, J.; Gorb, S. N.; Büscher, T. H. *Beilstein J. Nanotechnol.* **2024,** *15,* 612–630. doi:10.3762/bjnano.15.52
5. Lopez, V. M.; Polidori, C.; Ferreira, R. G. *Beilstein J. Nanotechnol.* **2024,** *15,* 1333–1352. doi:10.3762/bjnano.15.107
6. Amador, G. J.; van Oorschot, B. K.; Liao, C.; Wu, J.; Wei, D. *Beilstein J. Nanotechnol.* **2024,** *15,* 664–677. doi:10.3762/bjnano.15.55
7. Ali, S. D.; Rasmussen, M. H.; Catalano, J.; Frederiksen, C. H.; Weidner, T. *Beilstein J. Nanotechnol.* **2025,** *16,* 25–34. doi:10.3762/bjnano.16.3
8. Bartoli, M.; Cardano, F.; Piatti, E.; Lettieri, S.; Fin, A.; Tagliaferro, A. *Beilstein J. Nanotechnol.* **2024,** *15,* 1041–1053. doi:10.3762/bjnano.15.85
9. Zhu, Q.; Zhang, C.; Yu, F.; Xu, Y. *Beilstein J. Nanotechnol.* **2024,** *15,* 833–853. doi:10.3762/bjnano.15.70
10. Sameoto, D. *Beilstein J. Nanotechnol.* **2024,** *15,* 965–976. doi:10.3762/bjnano.15.79
11. Blickhan, R. *J. Comp. Physiol., A* **2024**. doi:10.1007/s00359-024-01726-1
12. Nachtigall, W. *Biomechanik;* Friedr. Vieweg & Sohn Verlagsgesellschaft: Wiesbaden, Germany, 2001. doi:10.1007/978-3-663-01611-3
13. Nachtigall, W. *Bionik-Grundlagen und Beispiele für Ingenieure und Naturwissenschaftler;* Springer: Berlin, Heidelberg, 1998. doi:10.1007/978-3-642-18996-8
14. Nachtigall, W. *Bionik Als Wissenschaft: Erkennen-Abstrahieren-Umsetzen;* Springer: Berlin, Heidelberg, 2010. doi:10.1007/978-3-642-10320-9
15. Nachtigall, W. *Biological Mechanisms of Attachment: The Comparative Morphology and Bioengineering of Organs for Linkage, Suction, and Adhesion;* Springer Science & Business Media: Berlin, Heidelberg, 2013.

License and Terms

This is an open access article licensed under the terms of the Beilstein-Institut Open Access License Agreement (https://www.beilstein-journals.org/bjnano/terms), which is identical to the Creative Commons Attribution 4.0 International License (https://creativecommons.org/licenses/by/4.0). The reuse of material under this license requires that the author(s), source and license are credited. Third-party material in this article could be subject to other licenses (typically indicated in the credit line), and in this case, users are required to obtain permission from the license holder to reuse the material.

The definitive version of this article is the electronic one which can be found at:
https://doi.org/10.3762/bjnano.16.32

BEILSTEIN JOURNAL OF NANOTECHNOLOGY

Insect attachment on waxy plant surfaces: the effect of pad contamination by different waxes

Elena V. Gorb*,‡ and Stanislav N. Gorb‡

Full Research Paper

Open Access

Address:
Department of Functional Morphology and Biomechanics, Zoological Institute, Kiel University, Am Botanischen Garten 9, 24118 Kiel, Germany

Email:
Elena V. Gorb* - egorb@zoologie-kiel.de

* Corresponding author ‡ Equal contributors

Keywords:
adhesion; *Chrysolina fastuosa*; Chrysomelidae; Coleoptera; epicuticular wax projections; tenent setae; traction force

Beilstein J. Nanotechnol. **2024,** *15,* 385–395.
https://doi.org/10.3762/bjnano.15.35

Received: 18 January 2024
Accepted: 22 March 2024
Published: 11 April 2024

This article is part of the thematic issue " Biomimetics and bioinspired surfaces: from nature to theory and applications".

Associate Editor: K. Koch

© 2024 Gorb and Gorb; licensee Beilstein-Institut.
License and terms: see end of document.

Abstract

This study focuses on experimental testing of the contamination hypothesis and examines how the contamination of insect adhesive pads with three-dimensional epicuticular waxes of different plant species contributes to the reduction of insect attachment. We measured traction forces of tethered *Chrysolina fastuosa* male beetles having hairy adhesive pads on nine wax-bearing plant surfaces differing in both shape and dimensions of the wax structures and examined insect adhesive organs after they have contacted waxy substrates. For comparison, we performed the experiments with the same beetle individuals on a clean glass sample just before (gl1) and immediately after (gl2) the test on a plant surface. The tested insects showed a strong reduction of the maximum traction force on all waxy plant surfaces compared to the reference experiment on glass (gl1). After beetles have walked on waxy plant substrates, their adhesive pads were contaminated with wax material, however, to different extents depending on the plant species. The insects demonstrated significantly lower values of both the maximum traction force and the first peak of the traction force and needed significantly longer time to reach the maximum force value in the gl2 test than in the gl1 test. These effects were especially pronounced in cases of the plant surfaces covered with wax projections having higher aspect ratios. The data obtained clearly indicated the impact of waxy plant surfaces on the insect ability to subsequently attach to the clean smooth surface. This effect is caused by the contamination of adhesive pads and experimentally supports the contamination hypothesis.

Introduction

It has been shown in numerous experimental studies that insects possessing hairy adhesive pads (i.e., specialized tarsal attachment devices) are able to establish a highly reliable contact and adhere successfully to a great variety of substrates having both smooth and microrough topographies [1-3]. However, in cases of waxy plant surfaces, where the plant cuticle is covered by

micro/nanoscopic three-dimensional (3D) epicuticular wax projections, insects usually fail to attach to [4-6]. The reducing effect of such plant surfaces on insect adhesion has been shown for many plant and insect species using various experimental approaches, from direct behavioral observations and simple inversion [7] or incline [8] tests up to precise measurements of attachment forces with different experimental techniques, such as pulling [9] and centrifugal [10] setups. It has been demonstrated that not only the presence of wax projections on the plant cuticle surface, but also their size, distribution, and density (number per unit area) influence insect attachment [11,12].

As an explanation for reduced insect adhesion on waxy plant surfaces, several contributing mechanisms have been previously suggested, such as (1) specific micro/nanoroughness created by wax projections (roughness hypothesis), (2) contamination of insect adhesive pads by plant wax during the contact (contamination hypothesis), (3) absorption of the insect pad secretion by the wax coverage (fluid absorption hypothesis), (4) hydroplaning induced by dissolution of the wax in the pad fluid (wax dissolution hypothesis), and (5) detached wax particles forming a separation layer between insect pads and the plant surface and serving as a kind of lubricant (separation layer hypothesis) [7,13].

To date, several experimental studies have been performed to test the first three hypotheses. As for the roughness hypothesis, it was revealed in centrifugal and pulling tests with some insect species bearing hairy attachment pads and mostly artificial substrates having different surface roughness. Insects showed several times higher attachment forces on both smooth and rather coarse microrough surfaces (>3 μm asperity size) compared to force values on 0.3 and 1 μm rough surfaces, where the range of asperity dimensions corresponded to that of typical plant wax projections [1,14-19]. This great reduction in the adhesion force was explained by the strong decrease of the real contact area between the micro/nanorough surface profile and the tips of tenent setae covering insect adhesive pads, which are responsible for establishing an intimate contact with the surface [14].

The fluid absorption hypothesis assumes that because of the high capillarity of the 3D wax coverage, the adhesive fluid may be absorbed from the insect pad surface. The ability to absorb oil, which is one, in beetles possibly even the main, component of the pad secretion [20-22], has been demonstrated experimentally for the wax coverage in the carnivorous plant *Nepenthes alata* Blanco (Nepenthaceae) [23]. Force measurements of the beetle *Coccinella septempunctata* (L.) (Coleoptera, Coccinellidae) on microporous substrates able to absorb both polar (water) and non-polar (oil) fluids clearly showed a strong reduction of the attachment force on these substrates compared to reference smooth solid substrates [24]. The latter result has been explained by absorption of the fluid from insect adhesive pads by porous media and/or the effect of surface roughness. Because of the more elaborate experimental design (three additional force measurements on the solid sample after the test on the porous substrate), a later study with the beetle *Harmonia axyridis* (Pallas) (Coleoptera, Coccinellidae) proved the primary effect of absorption of the insect pad secretion by the porous substrate on the insect attachment force [25].

According to the contamination hypothesis, wax projections can completely or partially detach from the plant surface and adhere to the insect pads covered with the fluid secretion. Such contamination may diminish the attachment ability of the pad. Several previous studies performed with some coleopteran and dipteran species (both having hairy adhesive pads) have reported on grooming behavior of test insects after walking on waxy surfaces of *Eucalyptus niten*s (H. Deane & Maiden) Maiden (Myrtaceae) [26] and *N. alata* [27]. Both earlier and rather recent studies gave direct indications that 3D waxes of the plant species from the genera *Brassica* (Brassicaceae) [8,28,29] and *Nepenthes* [30-33] contaminated insect adhesive pads. Also our previous investigation of twelve waxy plant surfaces verified the contaminating ability of plant waxes, which differed among test plant species depending on the micromorphology, primarily dimensions and shape, of the wax projections [34].

The effect of geometrical parameters of wax projections on their fracture behavior, which in turn determines their contamination ability, was examined using a theoretical mechanical approach [35]. It was demonstrated that during contact formation between insect pads and a plant surface, the wax projections having very high slenderness ratio (i.e., aspect ratio) may easily brake because of buckling, whereas other projections only in some cases fracture by bending.

To date, a very few experimental studies carried out with insects and waxy plant surfaces could confirm only indirectly the contamination hypothesis. Thus, inversion tests performed with the beetle *Chrysolina fastuosa* Scop. (Coleoptera, Chrysomelidae) having hairy adhesive pads on various (among them twelve waxy) plant substrates have shown that *Acer negund*o L. (Aceraceae) stems reduced the further attachment ability of beetles for a certain amount of time, whereas other waxy plant surfaces either did not affect or impaired insect attachment only for a very short period of time [7]. The follow-up study on the contamination of insect pads by plant waxes explained the above effect in a more quantitative way [34].

The aim of this study was to experimentally examine how the contamination of insect adhesive pads by the plant wax contributes to the reduction of insect attachment on waxy plant surfaces and to the subsequent long-term reduction of their attachment ability. We measured the traction forces of *C. fastuosa* male beetles on nine waxy plant surfaces and a reference smooth glass substrate. The experimental design included two force measurements on glass (before and just after experiment on the plant surface) to test whether there is an effect of the plant surface on the ability of insects to subsequently attach to the smooth surface. If there was such an effect, the contamination of pads by the plant wax had a primary effect on the force reduction. Contaminability of insect pads by waxes of different plant species was visualized in an additional experiment.

Results and Discussion

Waxy plant surfaces

The plant surfaces studied are densely covered by different types of epicuticular wax projections depending on the plant species (Figure 1). Both ribbon-shaped polygonal rodlets in *A. negundo* (Figure 1a) and apical filamentous branches of tubules in *B. oleracea* (Figure 1d), although differing greatly in size (length ca. 20 µm in *A. negundo* according to [7,34] and 2 µm in *B. oleracea* according to [19,36]), show very high aspect ratios (ca. 100 [34] and ca. 33 [19,36], respectively). These wax structures have relatively small contact area with the underlying cuticle (*A. negundo*) or with wax tubules (*B. oleracea*). Cylindrical wax tubules in both *A. vulgaris* (Figure 1c) and *C. majus* (Figure 1e) are almost the smallest (<1 µm long [7,34]) structures with the lowest aspect ratios (3–5 [34]) among

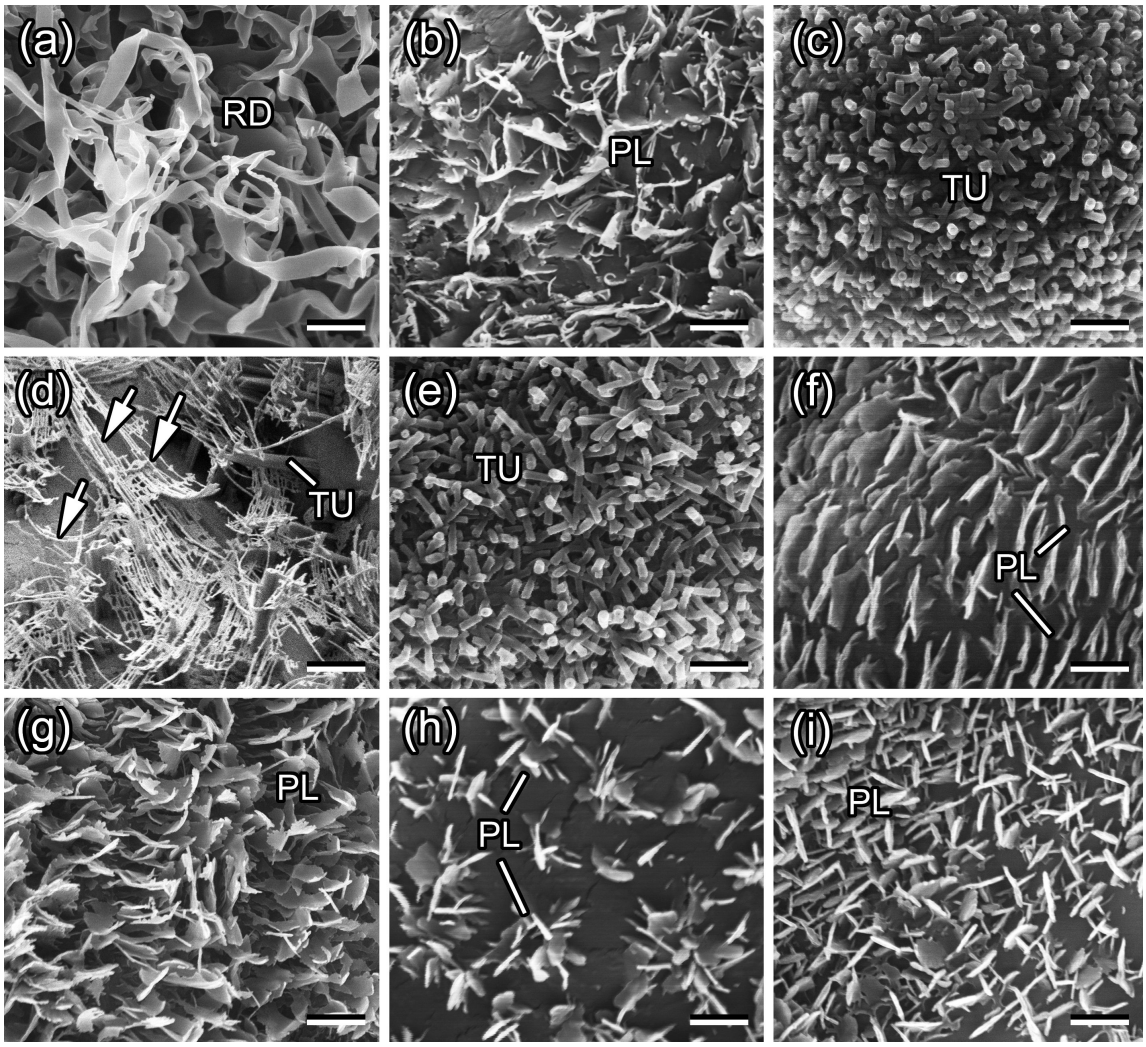

Figure 1: Scanning electron microscopy (SEM) micrographs of waxy plant surfaces in the young stem of *Acer negundo* (a) and adaxial (upper) leaf sides of *Aloe vera* (b), *Aquilegia vulgaris* (c), *Brassica oleracea* (d), *Chelidonium majus* (e), *Chenopodium album* (f), *Iris germanica* (g), *Lactuca serriola* (h), and *Trifolium montanum* (i). PL, wax platelets; RD, wax rodlets; TU, wax tubules. Arrows in (d) denote filament-like branches on top of the tubules. Scale bars: 2 µm (a, b, d, g, h) and 1 µm (c, e, f, i).

the plant species studied. As these projections are oriented at various angles in relation to the underlying cuticle, the contact area with the latter also varies. Flat, plate-like membranous (*A. vera*) or irregular (*C. album*, *I. germanica*, *L. serriola*, and *T. montanum*) wax platelets (Figure 1b,f–i), exhibiting intermediate values for both dimension and aspect ratio (0.6–1.7 µm and 9–22, respectively [7,34]), are arranged more or less perpendicularly to the surface. Because of such an arrangement, these platelets could achieve rather firm contact with the underlying cuticle using their whole thin side. Additionally, there are differences in distribution of the wax features. While in *L. serriola*, groups of platelets form clearly distinguishable clusters called rosettes (Figure 1h), the wax projections in other plant species are dispersed rather uniformly and almost completely cover the surfaces.

Data on the wax morphology are in line with our previous studies [7,34] for all plant species except *B. oleracea*, whose projections have been classified as terete rodlets. In later publications [19,36], where cryo-SEM was applied for the examination of plant surfaces, these projections were considered as round or angular tubules with dendrite-like branches on their tops. In the present study, we follow the latter opinion and treat *B. oleracea* wax projections as tubules bearing apical filamentous branches. Data on the dimension and aspect ratio given here for this plant species are related only to the branches, which are usually exposed to the environment, but not to the whole tubules.

Attachment organs of the *Chrysolina fastuosa* male beetle

General morphology

The tarsus of *C. fastuosa* possesses two distally located claws and adhesive pads situated on the ventral side of three (out of five) proximal tarsomeres (later referred to as basal, middle, and distal) (Figure 2a,b). In common with most beetles from the family Chrysomelidae [37], this species has hairy tarsal adhesive pads (according to [1,38]). Tenent setae of these pads have different shapes of the tip: (1) a flat discoidal terminal element in mushroom-like setae situated in the central part of the basal and distal tarsomeres (only in males, present in all legs); (2) a flat and widened end plate called spatula in setae located around the field of the mushroom-like setae and in the distal part of the middle pad; and (3) a pointed sharp tip in all setae of the middle pad and in the periphery of the basal and distal pads (Figure 2b).

Recent detailed experimental studies on different beetle species, such as *Leptinotarsa decemlineata* Say, *Gastrophysa viridula* De Geer, *Chrysolina americana* L. (all Chrysomelidae), *C. septempunctata*, and *H. axyridis* (both Coccinellidae) showing a distinct sexual dimorphism in structure and attachment performance of adhesive pads [15,17,24,25,39-42], as well as on mushroom-shaped contact elements of artificial attachment systems [43,44], revealed a strong adaptation of the discoidal tips to long-term adhesion on smooth substrates, especially needed for firm attachment of males to smooth female elytra during mating. Setae with spatula-shaped or pointed tips are better adapted to short-term temporary adhesion and locomotion on various microrough surfaces.

Contamination of insect pads by plant wax material

As well as in our previous study [34], we considered here only the discoidal setal tips allowing for (1) easier visualization of the contamination and (2) more precise evaluation of the degree of contamination. After insects have walked on various waxy plant substrates, adhesive pads demonstrated contamination of the setal tips by wax material in all cases (Figure 3 and

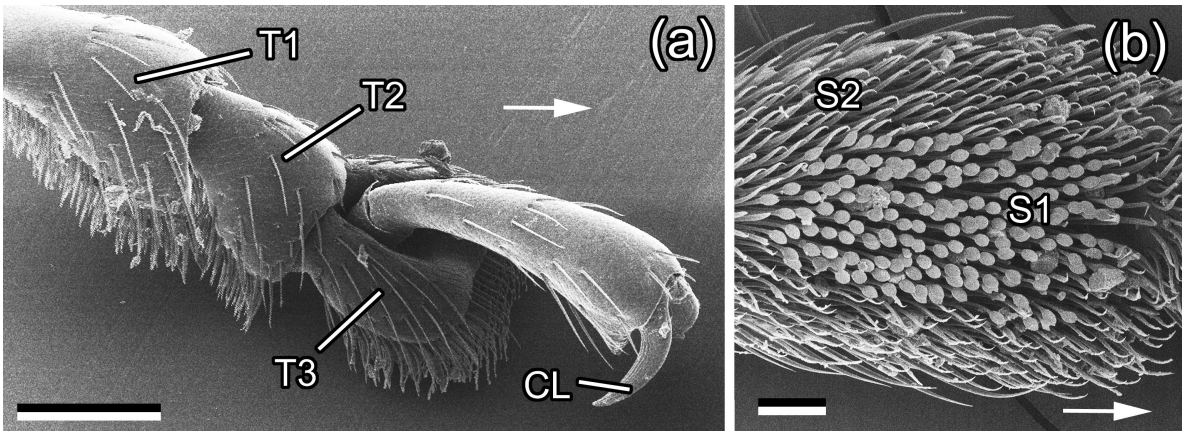

Figure 2: SEM micrographs of attachment organs of a *Chrysolina fastuosa* male beetle. (a) Tarsus with pretarsus, dorso-lateral view. (b) The first (basal) proximal tarsomere (T1), ventral view. CL, claw; S1, setae with discoidal tips; S2, setae with pointed tips; T1-T3, three proximal tarsomeres. Arrows point to the distal direction. Scale bars: 200 µm (a) and 50 µm (b).

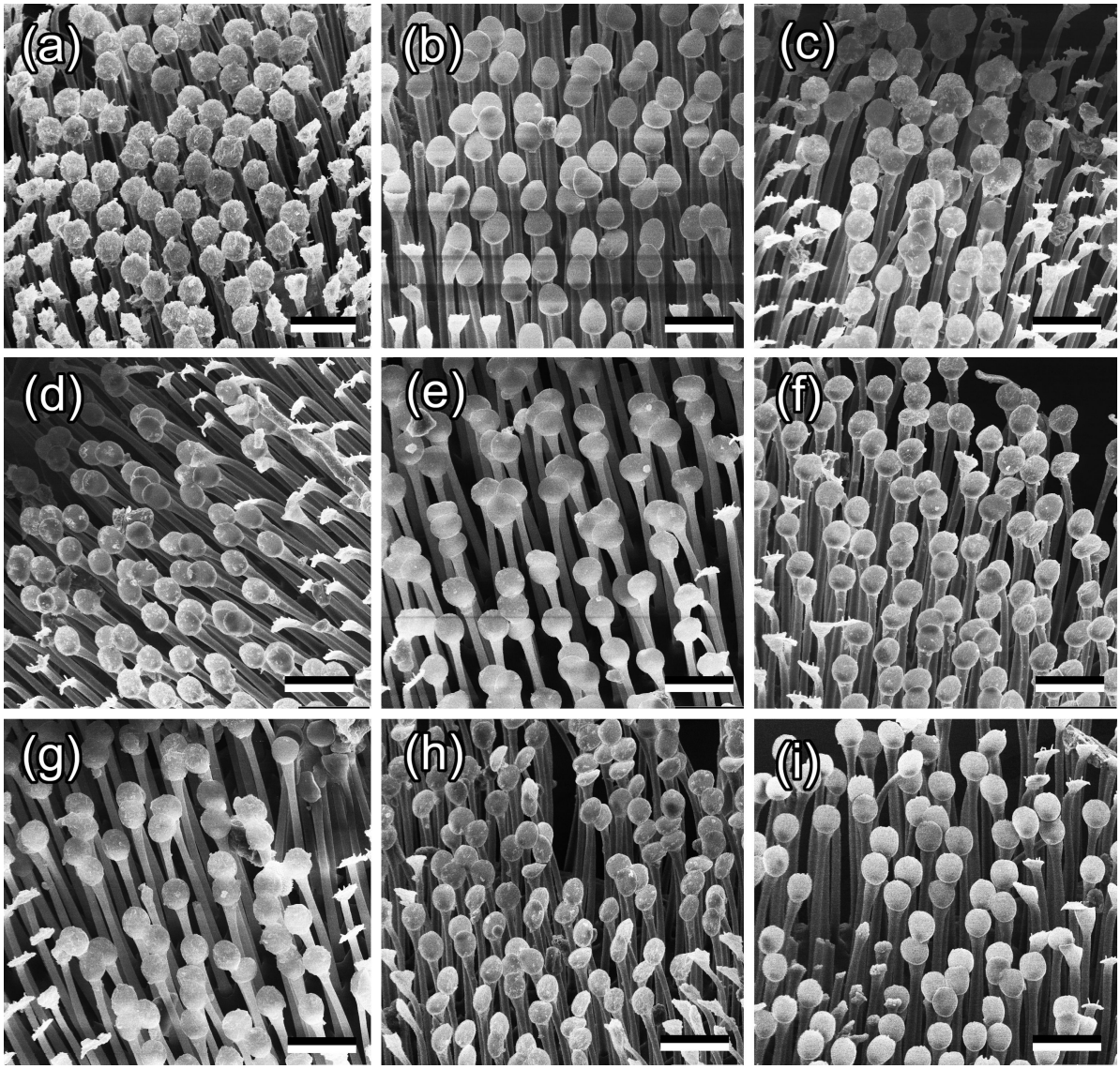

Figure 3: SEM micrographs of the ventral view of the first (basal) proximal tarsomere in *Chrysolina fastuosa* male beetles after they have walked on various plant waxy substrates: *Acer negundo* (a), *Aloe vera* (b), *Aquilegia vulgaris* (c), *Brassica oleracea* (d), *Chelidonium majus* (e), *Chenopodium album* (f), *Iris germanica* (g), *Lactuca serriola* (h), and *Trifolium montanum* (i). Scale bars: 20 µm.

Figure 4). Depending on the plant species, contamination differed in the texture of adhered wax (more or less homogeneous or structured to different extents) and in degree of contamination. Both parameters describing the contamination degree, such as the portion of setal tip surface covered with contaminating wax and the portion of setae contaminated by wax, differed significantly among the plant species used and positively correlated with each other [34]. The degree of pad contamination was higher in the tests with plants having larger dimensions and higher aspect ratios of the wax projections; however, the correlation between these two factors was non-significant in both cases ($P = 0.068$ for dimension and $P = 0.059$ for aspect ratio) [34].

Beetle attachment

Figure 5 shows typical force–time curves obtained from one beetle individual in a set of tests on reference glass gl1 (Figure 5a), waxy plant surface (Figure 5b), and in the second experiment on glass gl2 (Figure 5c). Using such curves, the maximal traction force F_{max}, the value of the first peak of the traction force F_{peak1}, and the time T_{Fmax} needed to reach the maximum traction force value were measured (Figure 5a).

Values of F_{max}, F_{peak1}, and T_{Fmax} were compared among different surfaces inside the experimental set (gl1 vs plant for F_{max} and gl1 vs gl2 for F_{max}, F_{peak1}, T_{Fmax}) for data on all test

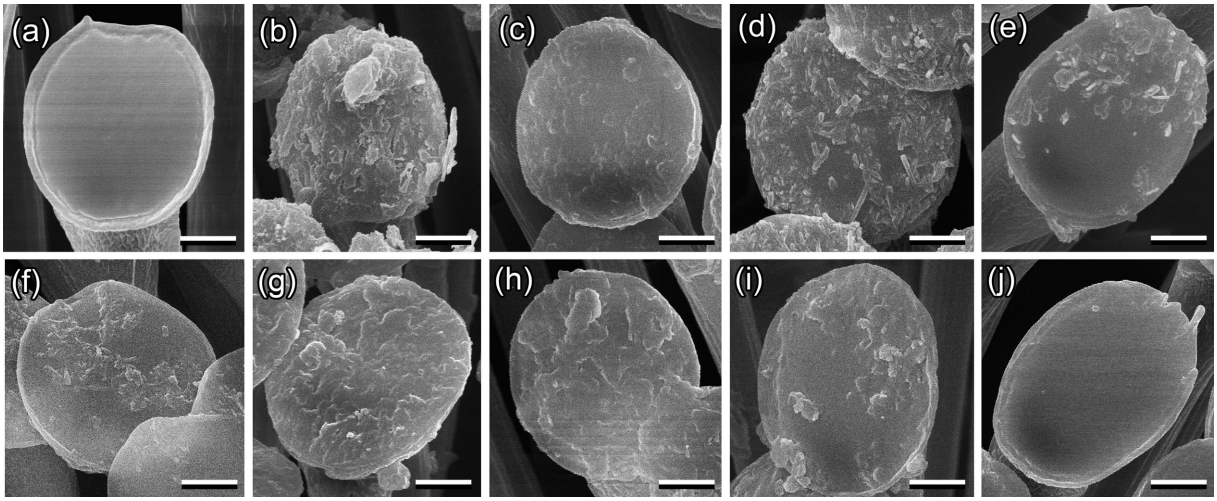

Figure 4: SEM micrographs of the ventral view of discoidal tips in exemplary mushroom-shaped setae of the first (basal) proximal tarsomere of *Chrysolina fastuosa* male beetles in clean (a) and contaminated conditions after the beetles have walked on various plant waxy surfaces: *Acer negundo* (b), *Aloe vera* (c), *Aquilegia vulgaris* (d), *Brassica oleracea* (e), *Chelidonium majus* (f), *Chenopodium album* (g), *Iris germanica* (h), *Lactuca serriola* (i), and *Trifolium montanum* (j). Note differences in the degree of contamination and in the texture of adhered wax depending on the plant species. Scale bars: 2 µm.

insects pooled together (i.e., in experiments with all waxy plant surfaces) and for data obtained from five insect individuals on each plant surface (species) separately. Original results on the forces and time in the case of pooled data are presented in Figure 6, whereas for the second case (separate plant species), graphs in Figure 7 show the force and time values normalized to the corresponding ones obtained in the first experiment on glass gl1.

Considering force data obtained from all insect individuals and all waxy plant surfaces tested (pooled data), we found a highly significant reduction (ca. 24-fold in average) of the maximum traction force F_{max} on the waxy plant surfaces compared to those obtained in the corresponding first (control) force measurements on the glass substrate gl1 (paired *t*-test: $t = 26.286$, $p < 0.001$) (Figure 6a). The maximum traction forces F_{max} from the second experiment on glass gl2 (performed immediately after tests on a waxy plant surface) were significantly lower than those from the first experiment on glass gl1 in all beetles (paired *t*-test: $t = 5.451$, $p < 0.001$) (Figure 6a). Also the comparison of the first peaks of the traction force F_{peak1} measured from the force–time curves obtained in the first and second experiment on glass (gl1 vs gl2) showed significantly lower values in the second experiment gl2 (paired *t*-test: $t = 5.962$, $p = 0.033$) (Figure 6b). To reach the maximum traction force values, all insects needed significantly more time during the second experiment on glass gl2 compared with the first experiment on glass gl1 (paired *t*-test: $t = 2.203$, $p = 0.033$) (Figure 6c).

Considering force data obtained in experiments with different plant species, we found that in all plants studied, the waxy surface significantly reduced the maximum traction force F_{max} compared to that produced in the first experiment on glass gl1 (Table 1). The force reduction varied greatly between plant species ranging from ca. 12-fold in *C. album* to over 30-fold in *C. majus* (Figure 7a). The comparison of the maximum traction force values F_{max} between the first gl1 and second gl2 experiments on glass showed significant differences only in the experiments with *A. negundo, B. oleracea*, and *T. montanum* (Figure 7b and Table 1), where force values were lower in the second experiment on glass g2. The first peak of the traction force F_{peak1} was significantly lower in the second gl2 experiment than in the first gl1 experiment on glass in the cases of *A. negundo, B. oleracea*, and *L. serriola* (Figure 7c and Table 1), whereas the difference was not significant in experiments with other plant surfaces. Regarding the time needed to reach the maximum traction force T_{Fmax} in the first gl1 and second gl2 experiments on glass, only in the case of *I. germanica*, it was significantly shorter during the second experiment on glass gl2 (Figure 7d and Table 1); for all other plants, this time was not significantly longer.

Thus, the comparison of the maximum traction forces F_{max} obtained here from *C. fastuosa* males on nine waxy plant surfaces with those measured in the first experiment on the reference glass gl1 demonstrated the anti-adhesive properties of the wax coverage in the studied plant species. This effect was clearly seen when we compared data (maximum traction force values

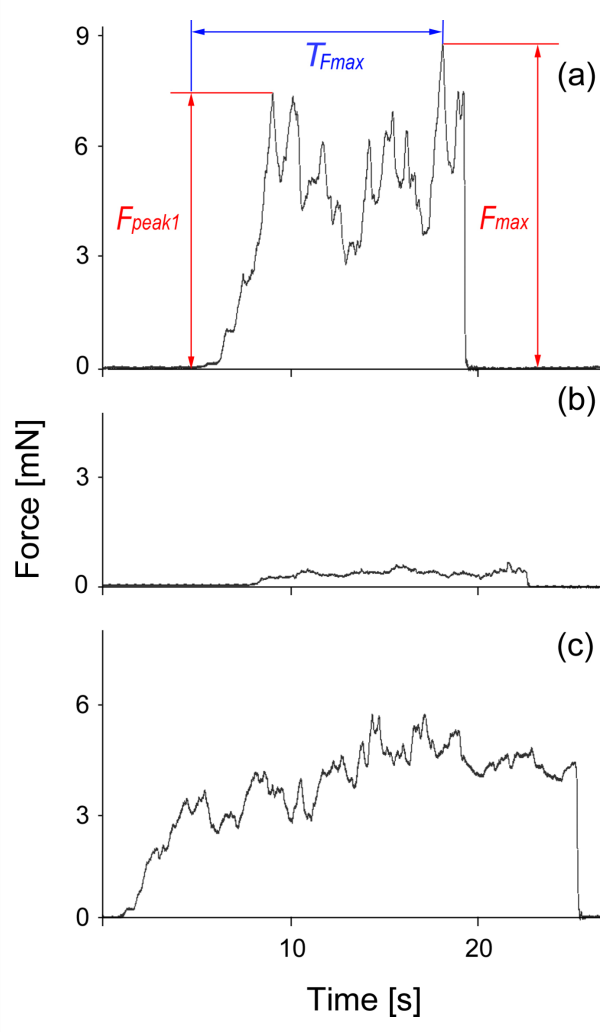

Figure 5: Exemplary force–time curves obtained from one beetle individual in a set of tests on the following surfaces: reference glass gl1 (a), plant (b), and glass gl2 (performed immediately after the test on plant) (c). Here, results for beetle no. 3 tested on an *Acer negundo* waxy stem are presented. F_{max}, maximal traction force; F_{peak1}, value of the first peak of the traction force; T_{Fmax}, time needed to reach the F_{max} value.

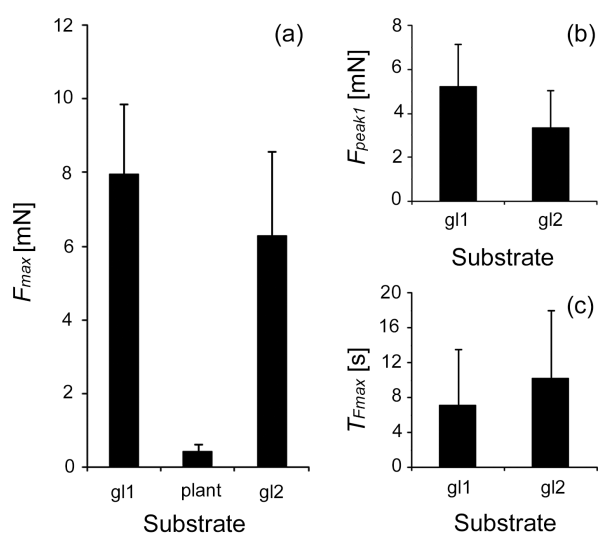

Figure 6: Maximum traction force F_{max} (a), first peak of the traction force F_{peak1} (b), and time T_{Fmax} needed to reach the maximum traction force (c) obtained on waxy plant surfaces and in the first and second experiments on glass. Data on all insects (i.e., from experiments with all plant surfaces) are pooled together. gl1, the first experiment on glass; gl2, the second experiment on glass; plant, waxy plant surfaces.

F_{max}) on all test insects and all plant species pooled together (ca. 24-fold reduction in average) as well as data obtained from five insects tested on each plant surface separately (from 12-fold to over 30-fold reduction). Our results are in line with previously reported findings in many plant and insect species [4-6].

The contaminating ability of plant waxes has been previously shown for many plants [8,28-34]. Our study clearly revealed the effect of pad contamination by plant wax material as an important mechanism of insect attachment reduction on waxy plant surfaces. First, contamination of insect pads by wax was verified for all plant species studied here. Second, we obtained significantly lower values of both the maximum traction force F_{max} and the first peak of the traction force F_{peak1}, and significantly longer times T_{Fmax} that the insects needed to reach the maximum traction force value, in the second experiment on glass gl2 compared to the reference (i.e., the first experiment on glass gl1) in all insect individuals and all waxy plant surfaces tested (pooled data). These results show the reduced ability of insects to subsequently attach to a smooth surface after having a previous contact with a waxy plant surface. In combination with our SEM data on contaminated beetle feet, the above outcomes of the force tests indicated that the contamination of pads by the plant wax is responsible for the attachment force reduction on waxy plant surfaces and has a short-term effect on the subsequent attachment to a smooth surface.

The comparison of experimental data among the plant species demonstrated certain differences between the species. Waxy surfaces of *A. negundo* and *B. oleracea* caused a decrease in both force values (maximum traction force F_{max} and the first peak of the traction force F_{peak1}). In these plants, wax projections have highly elongated shapes and exhibit the highest aspect ratios among the plant species studied [19,34,36]. As these wax projections have rather small contact area with the underlying plant surface, they may wholly detach from it and, consequently, easily cause heavy pad contamination. Moreover, according to [35], such wax structures may also readily brake during contact formation with insect pads and contaminate them. Interestingly, it has been previously reported that the *A. negundo* stem surface diminished the further attachment

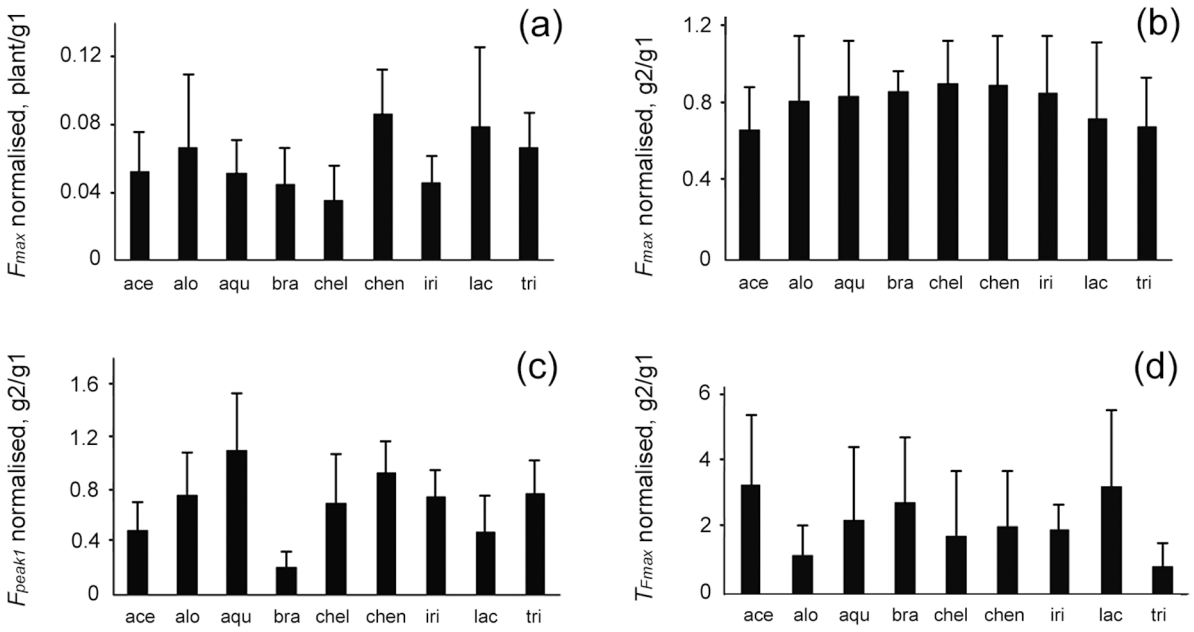

Figure 7: Maximum traction force F_{max} (a, b), first peak of the traction force F_{peak1} (c), and time T_{Fmax} needed to reach the maximum traction force (d) on the waxy plant surface (a) and in the second experiment on glass (b–d) obtained in sets of tests with different plant species. Here, normalized data (divided by the corresponding value obtained in the first experiment on glass) are presented. ace, *Acer negundo*; alo, *Aloe vera*; agu, *Aquilegia vulgaris*; bra, *Brassica oleracea*; chel, *Chelidonium majus*; chen, *Chenopodium album*; gl1, the first experiment on glass; gl2, the second experiment on glass; iri, *Iris germanica*; lac, *Lactuca serriola*; plant, waxy plant surface; tri, *Trifolium montanum*.

Table 1: Results of the paired *t*-test for comparisons between the first experiment on glass (gl1) and waxy plant surface (plant) and between the first (gl1) and second (gl2) experiments on glass for experimental sets with different plant species.[a]

Plant species	Maximum traction force F_{max} gl1 vs plant	Maximum traction force F_{max} gl1 vs gl2	First peak force F_{peak1} gl1 vs gl2	Time to reach maximum traction force T_{Fmax} gl1 vs gl2
Acer negundo	t = 10.821 p = 0.001*	t = 3.040 p = 0.038*	t = 5.305 p = 0.037*	t = 1.790 p = 0.123
Aloe vera	t = 15.193 p = 0.001*	t = 1.28 p = 0.270	t = 1.555 p = 0.195	t = 0.293 p = 0.784
Aquilegia vulgaris	t = 7.131 p = 0.002*	t = 1.087 p = 0.338	t = 0.048 p = 0.964	t = 1.106 p = 0.331
Brassica oleracea	t = 7.560 p = 0.002*	t = 2.790 p = 0.049*	t = 5.305 p = 0.006*	t = 1.951 p = 0.123
Chelidonium majus	t = 7.907 p = 0.001*	t = 1.215 p = 0.291	t = 1.975 p = 0.119	t = 0.385 p = 0.720
Chenopodium album	t = 10.206 p = 0.001*	t = 1.139 p = 0.318	t = 0.987 p = 0.380	t = 0.648 p = 0.553
Iris germanica	t = 10.746 p = 0.001*	t = 1.512 p = 0.205	t = 2.437 p = 0.071	t = 3.096 p = 0.036*
Lactuca serriola	t = 4.918 p = 0.008*	t = 2.041 p = 0.111	t = 3.490 p = 0.025*	t = 2.279 p = 0.085
Trifolium montanum	t = 10.088 p = 0.001*	t = 2.824 p = 0.048*	t = 1.818 p = 0.143	t = 1.539 p = 0.199

[a]p, probability value; t, test statistics; *, significant difference.

ability of *C. fastuosa* beetles, but the recovery time was relatively short [7]. Also, three other waxy plant surfaces studied here evoked a significant difference between the results of the first gl1 and the second gl2 experiments on glass, however, concerning only one of the attachment parameters measured: *T. montanum* regarding the maximum traction force F_{max},

L. serriola regarding the first peak of the traction force F_{peak1}, and *I. germanica* regarding the time needed to reach the maximum traction force T_{Fmax}. Since these plant surfaces are covered by middle-sized wax platelets with intermediate values of aspect ratio [34], they may yield a certain pad contamination, which in turn, may worsen the subsequent attachment ability of beetles for a short time. The waxy plant surfaces bearing small wax projections with low aspect ratio (especially compact, submicroscopic tubules in *A. vulgaris* and *C. majus*) caused inconsiderable pad contamination and, in turn, did not significantly affect further beetle attachment.

Conclusion

Traction experiments with tethered male individuals of the *Chrysolina fastuosa* beetles equipped with hairy adhesive pads clearly demonstrated a great reduction of attachment (maximum traction) force on all tested nine plant surfaces covered with three dimensional epicuticular waxes. The examination of adhesive pads after they had contacted the waxy plant substrates showed that (1) setal tips were contaminated by wax material and (2) the contamination degree differed between plant species depending on the micromorphology (primarily shape and size/aspect ratio) of the wax projections. The comparison of the maximum traction force value, the first peak of the traction force, and the time needed to reach the maximum force value in experiments on glass performed just before and immediately after the tests on the waxy plant surfaces revealed both significantly lower force values and significantly longer times in the case of the second experiment on glass compared to the first one in all tested insect individuals. When comparing the effect of different plant surfaces, this was more strongly pronounced in *A. negundo* and *B. oleracea* having wax projections with very high aspect ratios. These results evidently demonstrate that the impact of wax-covered plant surfaces on attachment to these surfaces and on subsequent attachment to a smooth surface is strongly influenced by the contamination of insect adhesive pads with the plant wax material.

Experimental

Plants

Nine plants species from different plant families were used in the experiments: *A. negundo*, *Aloe vera* (L.) Webb. & Berth. (Asphodelaceae), *Aquilegia vulgaris* L. (Ranunculacear), *Brassica oleracea* L. (Brassicaceae), *Chelidonium majus* L. (Papaveraceae), *Chenopodium album* L. (Chenopodiaceae), *Iris germanica* L. (Iridaceae), *Lactuca serriola* Torner (Asteraceae), and *Trifolium montanum* L. (*Fabaceae*). Young stems (*A. negundo)* or leaves (all other species) of these plants bearing 3D epicuticular wax coverage were collected near Jagotyn (Kyiv District, Ukraine; 50° 15′ 25″ N, 31° 46′ 54″ E) and used fresh in the force tests.

Insect

The leaf beetle *C. fastuosa* served as a model insect species in this study because it has been used in previous relevant experimental studies on insect attachment to various plant surface types [7] and contaminability of different plant waxes [34]. Additionally, it occurred in great numbers at the study site. The insects were used in the force experiments immediately after capture. In this study, only male beetles (body mass: 26 ± 6 mg, mean ± S.D., n = 10) were tested.

Scanning electron microscopy

To visualize the waxy plant surfaces and attachment devices in the *C. fastuosa* male beetle in both clean and contaminated conditions, scanning electron microscopy was employed. For plant surfaces, small (ca. 1 cm^2) pieces of plant organs were used. In the case of insect attachment organs, beetles were placed on a clean glass plate and their legs were cut off using a sharp razor blade. To get contaminated insect feet, a beetle was first allowed to walk on a fresh waxy plant surface for 1 min and then immediately transferred to the glass plate with the feet up, avoiding any contact, for cutting off the legs. Air-dried samples (parts of plant organs and clean or contaminated insect legs) were mounted on holders, sputter-coated with gold–palladium (thickness 8 nm for plants and 10 nm for insects), and examined in a Hitachi S-800 scanning electron microscope (Hitachi High-Technologies Corporation, Tokyo, Japan) at an acceleration voltage of 2–20 kV (plants) or 20 kV (insects). In the characterization of the waxy plant surfaces, we used the classification of plant epicuticular waxes according to [45].

Force measurements

Force experiments were carried out using a load cell force sensor FORT-10 (10 g capacity; World Precision Instruments Inc., Sarasota, FL, USA) connected to a force transducer MP 100 (Biopac Systems Ltd., Santa Barbara, CA, USA) [24,46]. First, in order to make a test beetle incapable of flying, its elytra were glued together with a small drop of molten beeswax. At the same time, a 10–15 cm long human hair was stuck to the wax drop. After the wax had hardened and the insect recovered from the treatment, a free end of the hair was attached to the force sensor. Then, the tethered beetle walked on a horizontally placed test substrate pulling the hair for ca. 30 s, while the friction (traction) force thus produced by the moving insect was registered. Since the insects walked parallel to the measurement axis of the sensor, the recorded force corresponded to the total traction force. Force–time curves obtained were used to estimate the maximal traction force F_{max}, the value of the first peak of the traction force F_{peak1}, and the time T_{Fmax} needed to reach the maximum traction force value (Figure 5a).

With each insect individual, three successive force tests were carried out on the following substrates: (1) a smooth hydrophilic glass used as a reference substrate (gl1), (2) a waxy plant surface (plant), and (3) once more a glass surface for comparison (gl2). Taking into consideration that these waxy plant surfaces are capable of contaminating insect attachment organs with wax particles [34], we performed the second experiment on glass immediately after the test on the plant, in order to completely exclude a possible effect of feet cleaning or grooming by insects. This aided in the examination of the influence of dirty adhesive pads on the subsequent attachment ability of the beetles. On each set of substrates, five individual male beetles were tested. In all, 135 force experiments were conducted. Force tests were carried out at 22–25 °C temperature and 60%–75% relative humidity.

The statistical analyses of the values of the maximum traction force F_{max}, the first peak of the traction force F_{peak1}, and the time T_{Fmax} needed to reach the maximum traction force for the comparisons between gl1 and plant and between gl1 and gl2 were performed using the paired *t*-test (SigmaStat 3.5, Systat Software Inc., Point Richmond, CA, USA). The comparisons were conducted for both (1) data on all test insects pooled together, that is, experiments with all waxy plant surfaces (d.f. = 44) and (2) data obtained from five test insects on each plant surface separately (d.f. = 4).

ORCID® iDs

Elena V. Gorb - https://orcid.org/0000-0002-9051-6259
Stanislav N. Gorb - https://orcid.org/0000-0001-9712-7953

Data Availability Statement

The data that supports the findings of this study is available from the corresponding author upon reasonable request.

References

1. Gorb, S. N. *Attachment Devices of Insect Cuticle;* Kluwer Academic Publishers: New York, NY, USA, 2001.
2. Gorb, S. N. *Am. Entomol.* **2005,** *51,* 31–35. doi:10.1093/ae/51.1.31
3. Federle, W. *J. Exp. Biol.* **2006,** *209,* 2611–2621. doi:10.1242/jeb.02323
4. Eigenbrode, S. D. Plant Surface Waxes and Insect Behaviour. In *Plant Cuticles – an Integrated Functional Approach;* Kerstiens, G., Ed.; BIOS Scientific Publishers: Oxford, UK, 1996; pp 201–222.
5. Müller, C. Plant-insect Interactions on Cuticular Surfaces. In *Biology of the Plant Cuticle;* Riederer, M.; Müller, C., Eds.; Blackwell: Oxford, UK, 2006; pp 398–422. doi:10.1002/9780470988718.ch13
6. Gorb, E. V.; Gorb, S. N. *J. Exp. Bot.* **2017,** *68,* 5323–5337. doi:10.1093/jxb/erx271
7. Gorb, E. V.; Gorb, S. N. *Entomol. Exp. Appl.* **2002,** *105,* 13–28. doi:10.1046/j.1570-7458.2002.01028.x
8. Stork, N. E. *Entomol. Exp. Appl.* **1980,** *28,* 100–107. doi:10.1111/j.1570-7458.1980.tb02992.x
9. Stork, N. E. *J. Exp. Biol.* **1980,** *88,* 91–107. doi:10.1242/jeb.88.1.91
10. Federle, W.; Rohrseitz, K.; Hölldobler, B. *J. Exp. Biol.* **2000,** *203,* 505–512. doi:10.1242/jeb.203.3.505
11. Gorb, E.; Voigt, D.; Eigenbrode, S. D.; Gorb, S. *Arthropod-Plant Interact.* **2008,** *2,* 247–259. doi:10.1007/s11829-008-9049-0
12. Gorb, E.; Böhm, S.; Jacky, N.; Maier, L.-P.; Dening, K.; Pechook, S.; Pokroy, B.; Gorb, S. *Beilstein J. Nanotechnol.* **2014,** *5,* 1031–1041. doi:10.3762/bjnano.5.116
13. Gorb, E. V.; Purtov, J.; Gorb, S. N. *Sci. Rep.* **2014,** *4,* 5154. doi:10.1038/srep05154
14. Peressadko, A.; Gorb, S. Surface Profile and Friction Force Generated by Insects. In *Proceedings of the 1st International Conference Bionik,* Boblan, I.; Bannasch, R., Eds.; Hannover, Germany, 2004; pp 257–263.
15. Voigt, D.; Schuppert, J. M.; Dattinger, S.; Gorb, S. N. *J. Insect Physiol.* **2008,** *54,* 765–776. doi:10.1016/j.jinsphys.2008.02.006
16. Gorb, E.; Gorb, S. *Entomol. Exp. Appl.* **2009,** *130,* 222–228. doi:10.1111/j.1570-7458.2008.00806.x
17. Bullock, J. M. R.; Federle, W. *J. Exp. Biol.* **2009,** *212,* 1876–1888. doi:10.1242/jeb.030551
18. England, M. W.; Sato, T.; Yagihashi, M.; Hozumi, A.; Gorb, S. N.; Gorb, E. V. *Beilstein J. Nanotechnol.* **2016,** *7,* 1471–1479. doi:10.3762/bjnano.7.139
19. Salerno, G.; Rebora, M.; Piersanti, S.; Büscher, T. H.; Gorb, E. V.; Gorb, S. N. *Physiol. Entomol.* **2022,** *47,* 20–37. doi:10.1111/phen.12368
20. Kosaki, A.; Yamaoka, R. *Jpn. J. Appl. Entomol. Zool.* **1996,** *40,* 47–53.
21. Attygalle, A. B.; Aneshansley, D. J.; Meinwald, J.; Eisner, T. *Zoology (Munich, Ger.)* **2000,** *103,* 1–6.
22. Geiselhardt, S. F.; Geiselhardt, S.; Peschke, K. *Chemoecology* **2009,** *19,* 185–193. doi:10.1007/s00049-009-0021-y
23. Gorb, E. V.; Hofmann, P.; Filippov, A. E.; Gorb, S. N. *Sci. Rep.* **2017,** *7,* 45483. doi:10.1038/srep45483
24. Gorb, E. V.; Hosoda, N.; Miksch, C.; Gorb, S. N. *J. R. Soc., Interface* **2010,** *7,* 1571–1579. doi:10.1098/rsif.2010.0081
25. Gorb, E. V.; Lemke, W.; Gorb, S. N. *J. R. Soc., Interface* **2019,** *16,* 20180696. doi:10.1098/rsif.2018.0696
26. Edwards, P. B. *Aust. J. Ecol.* **1982,** *7,* 347–352. doi:10.1111/j.1442-9993.1982.tb01309.x
27. Gaume, L.; Gorb, S.; Rowe, N. *New Phytol.* **2002,** *156,* 479–489. doi:10.1046/j.1469-8137.2002.00530.x
28. Stork, N. E. The Form of Plant Waxes: a Means Preventing Insect Attachment?. In *Insects and the Plant Surface;* Juniper, B. E.; Southwood, T. R. E., Eds.; Edward Arnold: London, UK, 1986; pp 346–347.
29. Eigenbrode, S. D.; Castagnola, T.; Roux, M.-B.; Steljes, L. *Entomol. Exp. Appl.* **1996,** *81,* 335–343. doi:10.1046/j.1570-7458.1996.00104.x
30. Juniper, B. E.; Burras, J. K. *New Sci.* **1962,** *269,* 75–77.
31. Juniper, B. E.; Robins, R. J.; Joel, D. M. *The Carnivorous Plants;* Academic Press: London, UK, 1989.
32. Gaume, L.; Perret, P.; Gorb, E.; Gorb, S.; Labat, J.-J.; Rowe, N. *Arthropod Struct. Dev.* **2004,** *33,* 103–111. doi:10.1016/j.asd.2003.11.005
33. Gorb, E.; Haas, K.; Henrich, A.; Enders, S.; Barbakadze, N.; Gorb, S. *J. Exp. Biol.* **2005,** *208,* 4651–4662. doi:10.1242/jeb.01939

34. Gorb, E. V.; Gorb, S. N. Do Plant Waxes Make Insect Attachment Structures Dirty? Experimental Evidence for the Contamination Hypothesis. In *Ecology and Biomechanics: a Mechanical Approach to the Ecology of Animals and Plants;* Herrel, A.; Speck, T.; Rowe, N. P., Eds.; CRC Press: Boca Raton, FL, USA, 2006; pp 147–162.
35. Borodich, F. M.; Gorb, E. V.; Gorb, S. N. *Appl. Phys. A: Mater. Sci. Process.* **2010,** *100,* 63–71. doi:10.1007/s00339-010-5794-x
36. Salerno, G.; Rebora, M.; Gorb, E.; Gorb, S. *Sci. Rep.* **2018,** *8,* 10975. doi:10.1038/s41598-018-29175-2
37. Stork, N. E. *Zool. J. Linn. Soc.* **1980,** *68,* 173–306. doi:10.1111/j.1096-3642.1980.tb01121.x
38. Beutel, R. G.; Gorb, S. N. *J. Zool. Syst. Evol. Res.* **2001,** *39,* 177–207. doi:10.1046/j.1439-0469.2001.00155.x
39. Heepe, L.; Wolff, J. O.; Gorb, S. N. *Beilstein J. Nanotechnol.* **2016,** *7,* 1322–1329. doi:10.3762/bjnano.7.123
40. Heepe, L.; Petersen, D. S.; Tölle, L.; Wolff, J. O.; Gorb, S. N. *Appl. Phys. A: Mater. Sci. Process.* **2017,** *123,* 34. doi:10.1007/s00339-016-0684-5
41. Voigt, D.; Tsipenyuk, A.; Varenberg, M. *R. Soc. Open Sci.* **2017,** *4,* 171108. doi:10.1098/rsos.171108
42. Matsumura, Y.; Gorb, E. V.; Gorb, S. N. *J. R. Soc., Interface* **2023,** *20,* 20230324. doi:10.1098/rsif.2023.0324
43. Gorb, S. N.; Varenberg, M. *J. Adhes. Sci. Technol.* **2007,** *21,* 1175–1183. doi:10.1163/156856107782328317
44. Heepe, L.; Gorb, S. N. *Annu. Rev. Mater. Res.* **2014,** *44,* 173–203. doi:10.1146/annurev-matsci-062910-100458
45. Barthlott, W.; Neinhuis, C.; Cutler, D.; Ditsch, F.; Meusel, I.; Theisen, I.; Wilhelmi, H. *Bot. J. Linn. Soc.* **1998,** *126,* 237–260. doi:10.1111/j.1095-8339.1998.tb02529.x
46. Gorb, S. N.; Popov, V. L. *Philos. Trans. R. Soc., A* **2002,** *360,* 211–225. doi:10.1098/rsta.2001.0926

License and Terms

This is an open access article licensed under the terms of the Beilstein-Institut Open Access License Agreement (https://www.beilstein-journals.org/bjnano/terms), which is identical to the Creative Commons Attribution 4.0 International License (https://creativecommons.org/licenses/by/4.0). The reuse of material under this license requires that the author(s), source and license are credited. Third-party material in this article could be subject to other licenses (typically indicated in the credit line), and in this case, users are required to obtain permission from the license holder to reuse the material.

The definitive version of this article is the electronic one which can be found at:
https://doi.org/10.3762/bjnano.15.35

BEILSTEIN JOURNAL OF NANOTECHNOLOGY

Comparative analysis of the ultrastructure and adhesive secretion pathways of different smooth attachment pads of the stick insect *Medauroidea extradentata* (Phasmatodea)

Julian Thomas*, Stanislav N. Gorb and Thies H. Büscher

Full Research Paper

Open Access

Address:
Functional Morphology and Biomechanics, Institute of Zoology, Kiel University, Am Botanischen Garten 9, 24118 Kiel, Germany

Email:
Julian Thomas* - jthomas@zoolgie.uni-kiel.de

* Corresponding author

Keywords:
adhesion; arolium; biomechanics; euplantulae; friction; functional morphology; tarsal secretion

Beilstein J. Nanotechnol. **2024,** *15,* 612–630.
https://doi.org/10.3762/bjnano.15.52

Received: 29 February 2024
Accepted: 08 May 2024
Published: 29 May 2024

This article is part of the thematic issue " Biomimetics and bioinspired surfaces: from nature to theory and applications".

Associate Editor: J. Lahann

© 2024 Thomas et al.; licensee Beilstein-Institut.
License and terms: see end of document.

Abstract

The mechanism by which insects achieve attachment and locomotion across diverse substrates has long intrigued scientists, prompting extensive research on the functional morphology of attachment pads. In stick insects, attachment and locomotion are facilitated by two distinct types of smooth cuticular attachment pads: the primary adhesion force-generating arolium and the friction force-generating euplantulae. They are both supported by an adhesive secretion delivered into the interspace between the attachment pads and the substrate. In this study, we analysed and compared internal morphology, material composition and ultrastructure, as well as the transportation pathways in both adhesive organs in the stick insect *Medauroidea extradentata* using scanning electron microscopy, micro-computed tomography, light microscopy, and confocal laser scanning microscopy. Our observations revealed structural differences between both attachment pads, reflecting their distinct functionality. Furthermore, our results delineate a potential pathway for adhesive secretions, originating from exocrine epidermal cells and traversing various layers before reaching the surface. Within the attachment pad, the fluid may influence the viscoelastic properties of the pad and control the attachment/detachment process. Understanding the material composition of attachment pads and the distribution process of the adhesive secretion can potentially aid in the development of more effective artificial attachment systems.

Introduction

Throughout their evolutionary timeline, insects evolved various surfaces interacting with the environment. These include friction-based adhesive organs, which are essential for locomotion by generating frictional and adhesive forces [1-4]. Two morphologically different friction-based adhesive principles convergently emerged in insects multiple times: hairy and smooth

adhesive organs [5-7]. Both principles are used for multiple functions from locomotion [8,9] to attachment during copulation [10] and predator resistance [11].

To fulfil their functions, smooth attachment pads need to enhance the actual contact area between the pad and the substrate for the realisation of efficient attachment due to adhesion and friction forces [3,9,12-14]. Smooth attachment pads have independently evolved in most large insect groups, possessing multiple specialized types of pads on the same leg that are adapted to attachment through the division of labour by preferably generating more adhesion or friction [5]. Adhesive secretion in the contact zone between the attachment pad and substrate supports the functionality of the pads [15].

The adhesive secretion can fill the gaps in the substrate roughness and thereby increase the contact area [14,16-19]. It can aid in the enhancement of viscous and capillary forces further increasing the attachment strength [9,14,20-24]. The adhesive secretion can be essential for the self-cleaning mechanism by binding smaller contamination particles together into larger complexes for easier removal [25,26]. It can also improve attachment to surfaces with different surface chemistry by mediating between the two surfaces in contact [27,28]. The lipid-containing pad secretion protects the insect from additional water loss through the thin-walled attachment pads [29] and assists in chemical communication [30].

The tarsal secretion can facilitate these functions due to its chemical composition and the resulting physical properties. Chemical analyses of the tarsal fluid revealed that its composition differs between different insect groups but mostly contains water-soluble and lipid-soluble substances [31-35] creating lipid droplets in an aqueous fluid [27,36] or hydrophilic nanodroplets embedded in an oily continuous phase [23,37]. Additionally, the tarsal secretion could be a mixture of multiple substances that are present in varying mixture ratios, which would also influence its properties and thus its functions [38]. Secretion with more long-chain carbons and higher branching bonds is more viscous and would potentially exert stronger viscous forces [39,40].

The functional differentiation of the smooth attachment pads likely arises from differences in the ultrastructure and material composition of the pad types and is potentially supported by possible differences in the produced tarsal secretion. Despite extensive research on the attachment capabilities and the ultrastructure of the different attachment pads in various insect groups (for example, Coleoptera [5], Hemiptera [41], Diptera [42,43], Orthoptera [5,20,44], and Blattodea [45]), knowledge on the differences in the internal ultrastructure and fluid transportation between different types of smooth attachment pads located on the same tarsus is scarce, especially in Phasmatodea. Recent investigations of the ultrastructure and material properties of the smooth tarsal attachment pads of phasmids complement our information on the morphology of the droplets [38], biomechanics of their attachment performance [28,46-51], and the complementarity of the two pad types [47,52,53].

In this study, we compare the ultrastructure and material composition of the two smooth tarsal (euplantulae) and pretarsal (arolium) attachment pads of the stick insect *Medauroidea extradentata* (Brunner von Wattenwyl, 1907), focusing on their functional differences as well as on the tarsal secretion production pathways. It was previously shown that the euplantulae are used to generate stationary attachment forces and propulsion (frictional pad) and the arolium to generate adhesion forces (adhesion pad) [52,54]. *M. extradentata* was selected here due to its relatively large adhesive organs that bear no further surface microstructures [47,55,56] and because the droplet morphology of its tarsal secretion has been recently analysed [28,38,47,55,56].

Combining different imaging techniques, including scanning electron microscopy (SEM), confocal laser scanning microscopy (CLSM), histological staining of longitudinal and cross sections (toluidine blue and Cason), and micro-computed tomography (μCT), our investigation of the arolium and euplantulae of the stick insect *M. extradentata* addresses the following questions: (1) Are there structural and material differences between the tarsal frictional pads (euplantulae) and the pretarsal adhesion pads (arolia)? (2) Where is the adhesive secretion produced and stored? (3) How many different types of exocrine cells producing pad secretions do exist? (4) How is the adhesive secretion transported from the production site to the pad surface? The results could enhance our overall comprehension of the functionality of the two smooth attachment organs, euplantulae and arolium, also shedding light on the fluid production and transportation processes in different smooth pads of Phasmida.

Materials and Methods

Animal

We used the phasmid species *Medauroidea extradentata* (Brunner von Wattenwyl, 1907) (Figure 1A), because of the availability of livestock and the presence of the functional morphology data on its tarsal attachment system [28,46-49].

Individuals were obtained from the laboratory cultures of the Department of Functional Morphology and Biomechanics (Kiel University, Germany). The insects were fed with blackberry leaves *ad libitium* and kept in a regular day and night cycle.

Only adult female individuals were selected. The animals were kept with blackberry leaves in clean hard plastic boxes to reduce contamination of the attachment pads.

Light microscopy

Two tarsi of adult female *M. extradentata* were dissected into five tarsomeres. The proximal four tarsomeres bear one euplantula each, whereas the fifth tarsomere additionally carries the pretarsus including the arolium (see Figure 1B, Figure 1C). The five tarsomeres were fixed in 2.5% glutaraldehyde in (pH 7.4) phosphate-buffered saline (PBS) for 24 h, washed two times in PBS for 30 min each, fixed in 1% aqueous OsO_4 for 1 h, and washed two times in double-distilled water, for 30 min each. After fixation, the samples were dehydrated using an ascending ethanol series from 30% to 100% (each step for 20 min). All steps were performed on a shaker and at 4 °C. For the last step, the samples were embedded in Epon 812 (Glycidether 100; Carl Roth GmbH, Karlsruhe, Germany) and polymerized at 60 °C for 48 h.

The embedded samples were cut into semi-thin sections of 0.2–1.0 µm using a Leica EM UC7 ultramicrotome (Leica Microsystems GmbH, Wetzlar, Germany) (at 21.5 °C room temperature), mounted on polylysine-covered glass slides (Gerhard Menzel GmbH, Braunschweig, Germany) and stained with toluidine blue or Cason's triple stain (Romeis 2010). Toluidine blue is a basic metachromatic dye, which selectively stains basophilic tissue components and has a high affinity to acidic tissue (nucleic acids are stained blue and polysaccharides purple). Previous experiments have also shown that the dye stains soft parts of the cuticle dark blue, and sclerotized parts of the cuticle light blue. In addition, the blue colour intensity corresponds to the relative electron density of the tissue in TEM [57-59].

Cason's triple stain allows for the differentiation of differently sclerotized regions from brown over orange to yellow (with a decreasing degree of sclerotization) to resilin-bearing regions stained from violet to pink [60,61].

For staining with toluidine blue, the glass slides were incubated with 0.1% toluidine blue solution for 2 min and rinsed using a stream of distilled water. Cason's triple stain (consisted of 1 g of phosphotungstic acid, 2 g of orange G, 1 g of aniline blue, and 3 g of acid fuchsine, dissolved in 200 mL of distilled water [60,61]. Cason stain was applied onto the glass slides for 5 min at 60 °C and rinsed with 70%–100% EtOH and tap water.

The stained samples were observed using a light microscope (Zeiss Axioplan, Carl Zeiss Microscopy GmbH, Jena, Germany) with 40× and 100× lenses. The images were processed using Adobe Photoshop (version CS6; Adobe Systems Inc., San Jose, CA, USA).

Scanning electron microscopy

Tarsi of *M. extradentata* were cut from adult females and fixed in 2.5% glutaraldehyde in PBS for 24 h. Then, they were washed two times with PBS for 30 min and two times with double-distilled water for 30 min each. Afterwards, the samples were dehydrated in an ascending ethanol series. Each step was performed on ice (4 °C) and on a shaker. Afterwards, the samples were critical point dried (Leica EM CPD300, Leica, Wetzlar, Germany). Then, the dry pretarsal arolium and tarsal euplantulae were dissected at the centre using two fine tweezers to achieve a clean breaking edge. The samples were mounted on aluminium stubs and sputter-coated with a 10 nm layer of gold–palladium (Leica BalTec SCD 500, Leica, Wetzlar, Germany). The images were obtained using a scanning electron microscope (TM 3000, Hitachi High-Technologies Corp, Tokyo, Japan) at 3 kV acceleration voltage. The recorded images were stitched, merged, and processed using the software Photoshop CS6 (Adobe Systems Inc., San Jose, CA, USA).

Confocal laser scanning microscopy

Whole tarsi and cross sections of the pretarsal (arolium) and tarsal (euplantulae) attachment pads of adult female stick insects *M. extradentata* were analysed using CLSM. Fresh tarsi of *M. extradentata* were cut off, directly placed in 100% Triton X-100 (Sigma-Aldrich Chemie GmbH, Steinheim, Germany) for 30 min, and then transferred to glycerine. To analyse the entire tarsus, it was directly transferred onto a glass slide and mounted with a coverslip (thickness = 0.170 ± 0.005 mm, refractive index = 1.52550 ± 0.00015, Carl Zeiss Microscopy GmbH, Jena, Germany). For the cross sections of arolium and euplantulae, the attachment pads were cut with a carbon blade and individually transferred onto a glass slide and mounted with a coverslip (specifications as above).

For analysis, a confocal laser scanning microscope (Zeiss LSM 700, Carl Zeiss Microscopy GmbH, Jena, Germany) and four stable solid-state lasers (wavelengths 405, 488, 555, and 639 nm in combination with the respective bandpass and longpass emission filters BP420–480, LP490, LP560, LP640 nm) were used.

The whole tarsi were visualised with a 5× lens (Zeiss Plan-Apochromat, air immersion, numerical aperture = 0.16, Carl Zeiss Microscopy GmbH, Jena, Germany) and the cross sections of the attachment pads with a 20× lens (Zeiss Plan-Apochromat, air immersion, numerical aperture = 0.17, Carl Zeiss Microscopy GmbH, Jena, Germany). Maximum intensity projections were created using the ZEN 2008 software

(https://www.zeiss.de/mikroskopie) and subsequently, the contrast and brightness were adjusted in Adobe Photoshop (version CS6; Adobe Systems Inc., San Jose, CA, USA). Three colours: red, green, and blue were assigned according to the emitted autofluorescence wavelength representing to some extent the degree of sclerotization. Red represents the highest sclerotization degree, green – the medium one, and blue – the lowest one (see Figure 1B).

Micro-computed tomography

A whole tarsus of an adult female *M. extradentata* was cut off at the base of the tibia, directly fixed in 2.5% glutaraldehyde in PBS, and washed in PBS. For the preparation of the µCT scan, the tarsus was dehydrated with an ascending EtOH sequence at 4 °C on a shaker, and subsequently critical point dried using Leica EM CPD300 (Leica, Wetzlar, Germany). The tarsus was scanned using a Skyscan®1172 µCT (Bruker micro-CT; CT-scanner settings: X-ray source: 40 kV, 250 µA, 360 rotation, 0.2 rotation step, 10 frames averaging, and 10 random movements), reconstructed in Nrecon®1.0.7.4 (Bruker micro-CT, Billerica, MA, USA), segmented with Amira®6.2 (Thermo Fisher Scientific, Waltham, MA, USA), and visualized with the open-source 3D creation software Blender 2.82a (Blender Foundation, Amsterdam, Netherlands) and Affinity Designer (Serif, Nottingham, UK).

Results

Tarsal structure

The structure of the tarsus of *M. extradentata* was observed using CLSM and SEM (Figure 1B,C). It comprises five tarsomeres (ta 1–5) and the pretarsus. Tarsomeres one to four (ta 1–4) each bear a pair of euplantulae (eu 1–4) at their distal ends. The pretarsus features the arolium (ar) situated between a pair of claws (cl). The euplantulae, the cuticle between them,

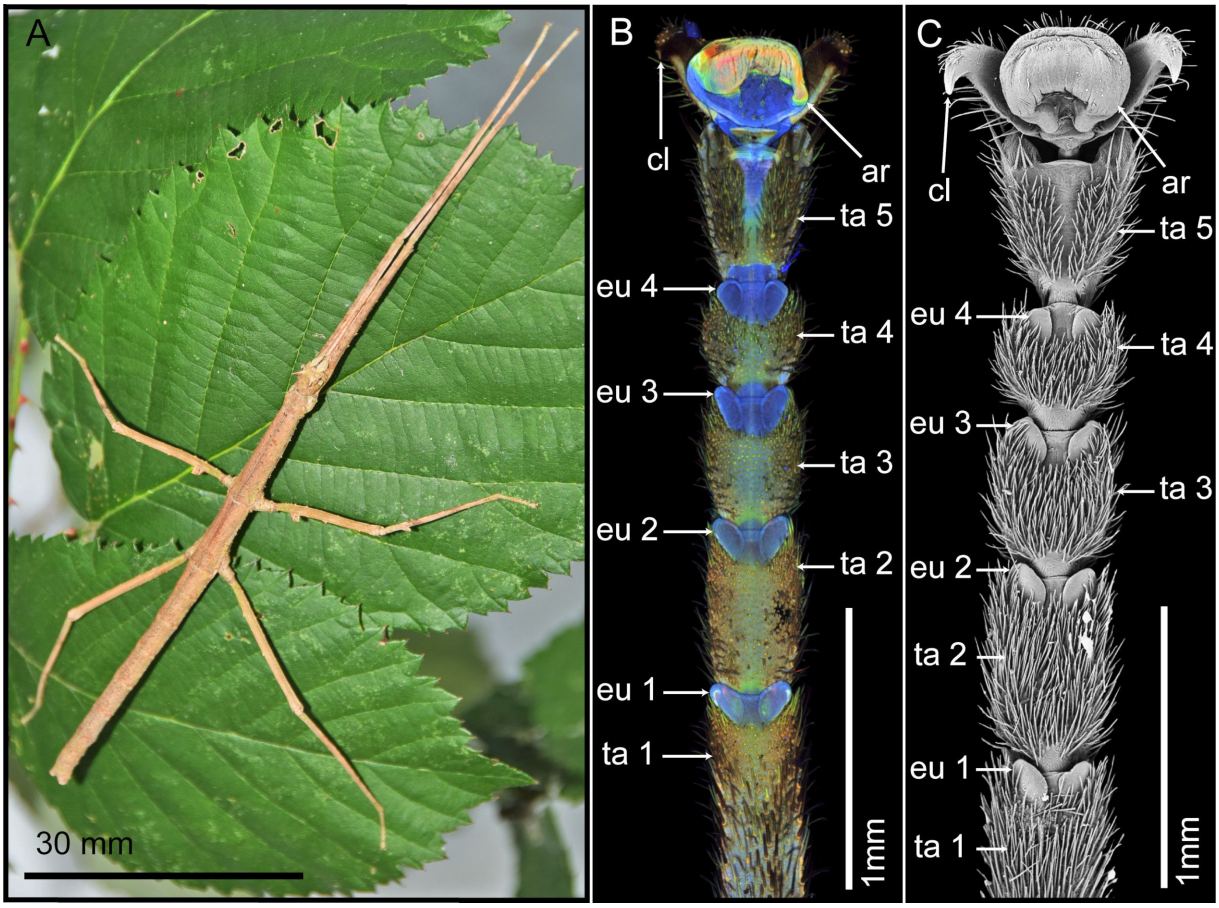

Figure 1: *Medauroidea extradentata* and its tarsal structures. Example images of the animals used in the experiments and their tarsi. (A) Female. (B) CLSM maximum intensity projection of the tarsus. (C) SEM image of the tarsus. ar = arolium; cl = claw; eu 1–5 = euplantulae 1–5; ta 1–5 = tarsomeres 1–5. Figure 1C was adapted with permission of The Company of Biologists Ltd., from [28] ("Influence of surface free energy of the substrate and flooded water on the attachment performance of stick insects (Phasmatodea) with different adhesive surface microstructures" by J. Thomas et al., *J. Exp. Biol.*, vol. 226, issue 2, jeb244295, © 2023); permission conveyed through Copyright Clearance Center, Inc. This content is not subject to CC BY 4.0.

and the arolium bear a rather smooth surface structure. The remaining surface of the tarsomeres, where no attachment pads are situated, is covered with setae (Figure 1C). The CLSM images revealed that both types of attachment pads and the cuticle between the euplantulae and between the tarsomeres show a low degree of sclerotization (blue coloration). In contrast, the cuticle of the remaining tarsomeres has a higher degree of sclerotization (green/yellow coloration). Notably, the distal ventral region of the arolium displays a relatively higher degree of sclerotization (green/yellow coloration). Additionally, red coloration is visible inside the arolium; however, this does not correspond to the cuticle, but presumably to the glandular tissue of the arolium (Figure 1B).

Arolium structure

The pretarsus of *M. extradentata* is 500 µm wide and 400 µm long. The ventral face of the arolium consists of a thickened layer of fibrous cuticle composing the actual smooth attachment pad (ap) [1]. Toluidine blue staining resulted in a blue hue of the attachment pad, indicating the presence of a meshed network of flexible cuticle fibres within the attachment pad (Figure 2B). This coarse meshed-fibre structure was also observed in SEM (Figure 2C). In addition, using CLSM, the attachment pad structure exhibited a low degree of sclerotization indicating a presumably soft cuticle (Figure 2D). Internally, the main part of the arolium consists of a large epithelium, recognizable by the light hue of the toluidine blue staining. The epithelium mainly consists of exocrine cells (ex) which display a large surface area towards the hemolymph due to irregular protrusions (Figure 2B). These evaginations are also visible in the µCT cross sections as radio-dense layers (Figure 2A). The exocrine cells exhibited a mixed red/blue signal in CLSM (Figure 2D) and appeared densely packed in the SEM sections (Figure 2C). The exocrine cells are likely surrounded by the hemolymph (he), which appeared yellowish when stained with toluidine blue (Figure 2A).

On the back of the arolium, epidermal cells (ep) are present, separated from the exocrine cells by the hemolymph (Figure 2B). These epidermal cells were stained in a relatively darker hue by toluidine blue (Figure 2B) and displayed a reddish fluorescence signal in CLSM (Figure 2D). However, they were not visible in the µCT cross sections (Figure 2A).

The arolium exhibits a sclerotized cuticle (cu) on its dorsal side. The sclerotized cuticle is composed of two layers, the inner

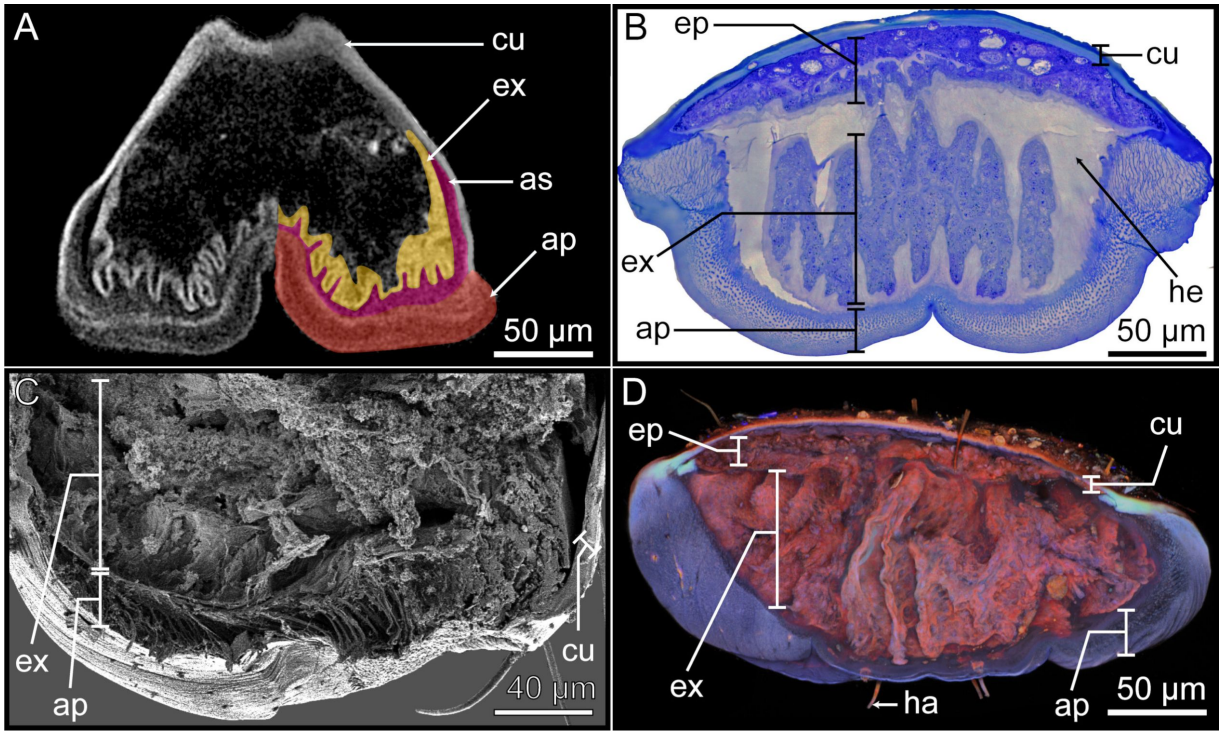

Figure 2: Sections of the arolium visualized with different imaging techniques. The internal ultrastructure of the arolium was visualized using four different methods, which show the different layers and highlight their morphological and structural characteristics. The following methods were used: (A) µCT. (B) Cross section stained with toluidine blue, light microscopy. (C) SEM. (D) CLSM. For images (C) and (D) the arolium had to be dissected. All images are similarly positioned: the ventral side of the arolium is located at the bottom of the picture. Ap = attachment pad; as = adhesive secretion reservoir; cu = cuticle; ep = epidermal cells; ex = exocrine cells; ha = hair/seta; he = hemolymph.

layer showing light blue staining by toluidine blue (Figure 2B) and a light red fluorescence signal in CLSM (Figure 2D), while the outer layer is stained dark blue by toluidine blue (Figure 2B) and shows a dark red fluorescence signal in CLSM (Figure 2D). Both layers show radiodensity in µCT (Figure 2A).

Arolium ultrastructure

The internally located ≈10 µm wide endocuticle layer 1 (e1) is characterized by its loose, parallel arrangement of sheets, which are discernible through their red staining with Cason (Figure 3A) and blue staining with toluidine blue (Figure 3B). This parallel arrangement is also evident in SEM (Figure 3D) and in longitudinal microtome sections in the light microscope (Figure 3B). In CLSM, the endocuticle layer 1 exhibits a relatively low degree of sclerotization (Figure 3C).

On top of the endocuticle layer 1 there is a ≈30 µm thick primary rod layer (pr) consisting of wide rods extending towards the surface of the arolium and branching into finer rods forming another ≈10 µm thick branching rod layer (br) (Figure 3). The primary rod layer and the branching rod layer are notably stained red by Cason stain (Figure 3A) and blue by toluidine blue stain (Figure 3B), confirming their cuticular origin. The CLSM images further revealed that both layers emit a blue signal, indicative of the presence of resin (rubber-like protein) with relatively soft properties (Figure 3C). The morphological details of these layers are also apparent in longitudinal microtome sections (Figure 3B) and SEM sections (Figure 3D). The primary rod layer is comprised of relatively thick cuticle fibres that branch into finer ones within the branching rod layer, terminating in the superficial layer (sf) (Figure 3D).

The superficial layer is the outermost layer in the arolium and is in direct contact with the environment. When examined with a light microscope, this layer appeared remarkably smooth. Notably, Cason staining resulted in a deep red hue, while toluidine blue staining resulted in a dark blue coloration (Figure 3A, Figure 3B), indicating that the superficial layer consists of a more densely packed cuticle if compared to the rods of the primary rod layer and branching rod layer. Additionally, the cuticle of the superficial layer displays a low degree of sclerotization as indicated by CLSM results (Figure 3C).

Arolium exocrine cells

The exocrine cells (ex) of the epidermal cell layer are separated from the hemolymph reservoir (he) by a basal layer (bl) which is stained light blue by toluidine blue. (Figure 3B, Figure 3E). The identification of exocrine cell bodies is facilitated by their blue coloration when stained with toluidine blue (Figure 3B, Figure 3E), alongside the presence of a thick basal lamina and numerous discernible cellular structures. When observed in CLSM, the exocrine cells exhibit a red autofluorescence signal (Figure 3C). Notably, the exocrine cells possess large nuclei (nu) with multiple nucleoli, which are prominently stained in shades of blue by toluidine blue (Figure 3B, Figure 3E). Light microscopy revealed the presence of numerous vesicles (ve), which can be distinguished as either black when stained with toluidine blue and Cason or show an orange colour without staining (Figure 3A,B,E). When observed using SEM, these vesicles appear smooth and appear to be detached from the surrounding cellular structures (Figure 3F). Furthermore, round and unstained areas were observed (Figure 3A,B,E). When examined in SEM, these structures appear as hollow, empty spaces (Figure 3F). These structures are named hollow spaces (hs). Based on all these characteristics, the exocrine cells of the epidermal cell layer are likely classified as exocrine cells type I [62].

The basal and apical sides of the exocrine cells exhibit surface expansions towards the basal layer (basal) and the adhesive secretion reservoir (as) (apical) (Figure 3B). The adhesive secretion reservoir is stained light blue with toluidine blue and is situated between the exocrine cells and the epicuticle layer 1 (Figure 2A; Figure 3B).

Tarsomere structure

Only tarsomeres that possess an attachment pad (euplantulae) were examined and are described below. These tarsomeres measure ≈330 µm in length and ≈210 µm in width (depending on the tarsomere).

The septa (se) separate the interior of the tarsomere into four sections. Two thin septa laterally segregate it into two areas on the ventral side (vn), while a comparably thicker septa separates the tarsomere into central and dorsal areas. The central area (ca) accommodates the tendon (te), and the dorsal area (da) the tracheal structures (tr) and nerve bundles (nb). Notably, each of these areas possesses an individual hemolymph channel for circulatory and possible structural purposes through hydrostatic pressure (Figure 4). The septa are dyed blue by toluidine blue and show a parallel cuticle layering in SEM (Figure 4B, Figure 4C).

The cuticle on the ventral part of the dorsal area shows distinctive morphological and structural characteristics compared to the rest of the cuticle, as it lacks the typical toluidine blue staining and autofluorescence of the sclerotized cuticle. In contrast, the region is stained light blue with toluidine blue and exhibits a low degree of sclerotization in CLSM. Moreover, it presents a unique morphology, appearing fanned out, suggesting a more flexible structure (Figure 4B, Figure 4D). Based on these characteristics, this cuticle region is named flex-

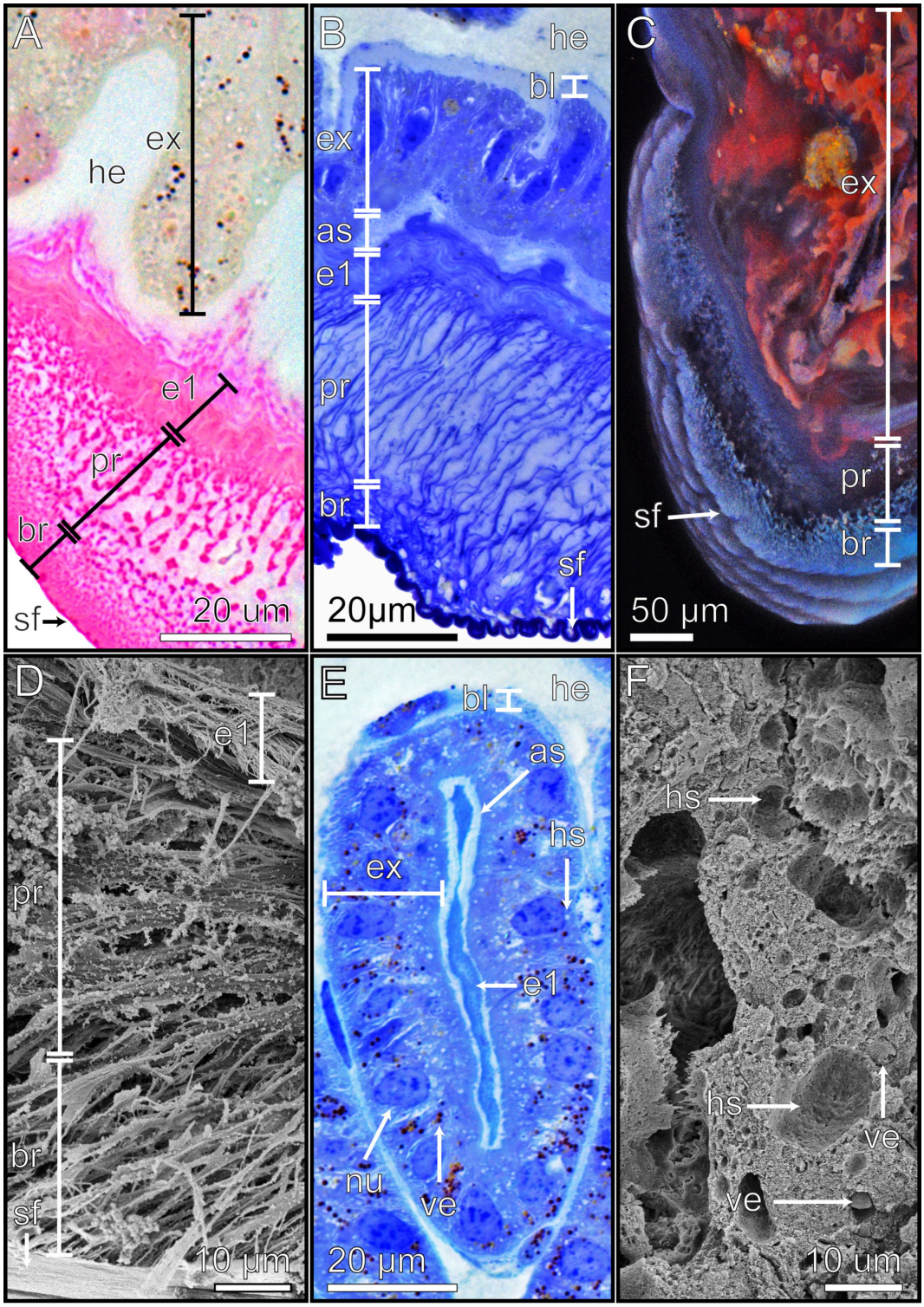

Figure 3: Arolium material structure visualised using different techniques. Detailed images of the adhesive pad of the arolium. The different methods highlight the morphological and structural characteristics of the respective layers and structures. (A) Light microscopy image of the cross section stained with the Cason triple stain. (B) Light microscopy image of the longitudinal section stained with toluidine blue. (C) CLSM image of the cross section. (D) SEM image of the cross section. (E) Light microscopy of the longitudinal section of the exocrine cells stained with toluidine blue. (F) SEM image of the cross section of the exocrine cells. The ventral side of the arolium is oriented towards the bottom of the pictures. As = adhesive secretion reservoir; bl = basal layer; br = branching rod layer; e1 = endocuticle layer 1; ex = exocrine cells; he = hemolymph; hs = hollow spaces; nu = nucleus; pr = primary rod layer; sf = superficial layer; ve = vesicles.

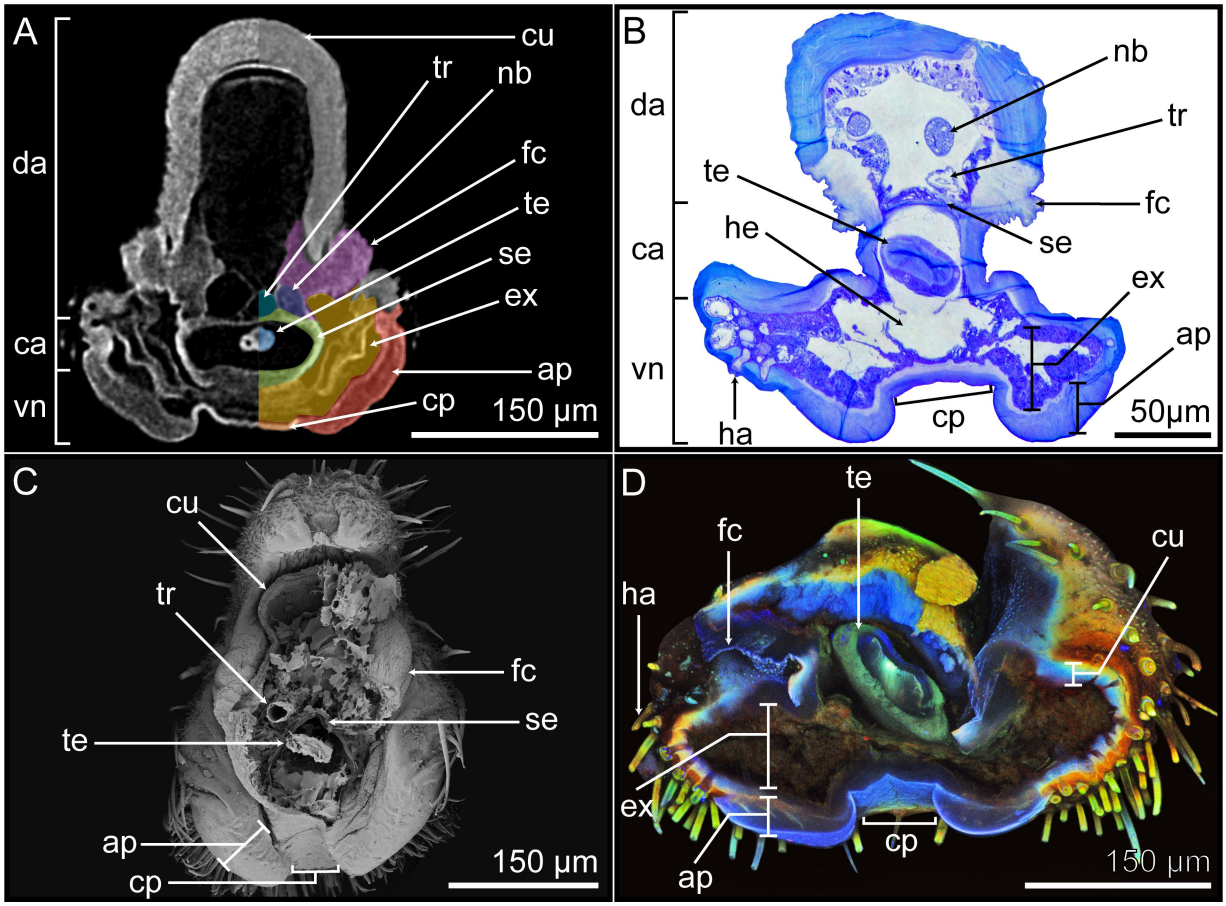

Figure 4: Morphology of the tarsomere. The internal ultrastructure of the tarsomere was visualized using four different methods, which show the different layers and highlight their morphological and structural characteristics. The following methods were used: (A) µCT image of the cross section. (B) Light microscopy cross section stained with toluidine blue. (C) SEM overview of the entire tarsomere. (D) CLSM cross section of the tarsomeres. The ventral sides of the euplantulae are oriented towards the bottom of the images. The examined sections originate from individual tarsomeres along the tarsus, whereby the length and width proportions can differ. ap = attachment pad; ca = central area; cp = connective pad; cu = sclerotized cuticle; da = dorsal area; ex = exocrine cells; fc = flexible cuticle; ha = hair/seta; he = hemolymph; nb = nerve bundle; se = septum; te = tendon; tr = trachea; vn = ventral area.

ible cuticle (fc). The µCT imaging of the ventral side of the euplantulae revealed a dense hull (lighter grey) and a more X-ray transparent body (darker grey) (Figure 4A). Toluidine blue staining detected a darker blue stained hull and a lighter blue body (Figure 4B). The SEM images unveiled a rather smooth surface topography (Figure 4C). Furthermore, CLSM detected a weak degree of sclerotization (blue autofluorescence signal) of the whole structure (Figure 4D). All these features indicate that this ventral structure is the euplantula attachment pad (ap) that makes direct contact with the substrate. The attachment pad is ≈60 µm wide and laterally merges with the sclerotized cuticle of the tarsomere. This is recognizable by the different coloration of the lateral exoskeleton which shows the staining by toluidine blue and CLSM autofluorescence wavelength signals typical for the sclerotized cuticle (Figure 4B, Figure 4D). The attachment pads of the tarsomeres internally extend into the corresponding tarsomere.

The structure connecting the two attachment pads shows morphological similarities with the attachment pad. In the µCT, the outer hull of this structure exhibits high radiodensity and the inner body shows lesser density (Figure 4A). Similarly, light microscopy with toluidine blue staining showed the outer hull in dark blue and the inner body in a lighter shade of blue (Figure 4B). The SEM images revealed a smooth surface (Figure 4C), while CLSM analysis demonstrated a low degree of sclerotization, suggesting the presence of soft cuticle (Figure 4D). Due to these morphological similarities and the fact that this structure connects the attachment pads, it is referred to as a connective pad (cp).

On the internal side of both the attachment pad and connective pad, an epidermal cell layer is situated. This layer encompasses the entire surface of the ventral interior of the tarsomeres, restricting the hemolymph reservoir inside. The layer is separat-

ed from the remaining tarsomere tissue by septa. The epidermal cells appear radiolucent in the µCT cross sections (Figure 4A) and are stained blue with toluidine blue (Figure 4B). Also, they show a weak green autofluorescence signal in CLSM (Figure 4D). These findings indicate that the epidermal cell layer consists of exocrine cells (ex). Furthermore, the lateral sides of the tarsomeres exhibited discernible nerve bundles and hair/seta attachment sites (ha), extending into the epidermal layer (Figure 4B).

Euplantula ultrastructure

The inner layer of the attachment pad (ap) is ≈1.5 µm wide, stained light red and blue by Cason and toluidine blue, respectively (Figure 5A, Figure 5B), exhibiting a low degree of sclerotization in CLSM (Figure 5C) and composed of parallel layers of cuticle sheets (Figure 5D). This composition identifies the layer as the endocuticle layer 1 (e1).

From the endocuticle layer 1 emerges a ≈12 µm thick layer of dense wide rods, which subsequently ventrally branches towards the surface into finer, denser rods, and finally terminate into a ≈4 µm thick superficial layer (sf) (Figure 5A,B,D). The layer composed of thick rods is the primary rod layer (pr) and the layer with the finer rods is the branching rod layer (br) (Figure 5D). Cason and toluidine blue staining resulted in a lighter red and blue coloration, respectively, for the cuticle of the primary rod layer compared to that of the branching rod layer, likely reflecting the denser fibrous structure of the latter (Figure 5A, Figure 5B). The CLSM analysis revealed a low degree of sclerotization in both layers, suggesting soft cuticle, with discernible regions of reddish autofluorescence signals, possibly attributed to residual adhesive secretions within the cuticle layers, or to underlying epidermal cells (Figure 5C).

The finer fibers of the branching rod layer ultimately terminate in the superficial layer (Figure 5A,B,D). The thin superficial layer is the outermost layer of the euplantulae, establishing direct contact with the substrate (Figure 5D). Examination in the light microscope and SEM revealed a smooth surface of the pad (e.g., Figure 4C). Staining with Cason and toluidine blue resulted in a dark red or dark blue hue, respectively, indicative of a tightly packed cuticle (Figure 5A, Figure 5B). Additionally, CLSM unveiled a low degree of sclerotization in the superficial layer (Figure 5C).

Euplantulae exocrine cells

The hemolymph reservoir (he) is ventrally surrounded by a layer of epidermal cells. The basal region of this layer establishes direct contact with the hemolymph with evaginations increasing the contact surface area (Figure 5B). When stained with toluidine blue or Cason, the epidermal cell layer displays deep blue and light red colorations, respectively (Figure 5A,B,E). In CLSM, the layer exhibited a strong green signal with weak red signal portions (Figure 5C). The cells within the epidermal layer house a prominent nucleus with multiple nucleoli, stained in a deeper blue and red by the two staining methods, respectively (Figure 5A,B,E). Due to these characteristics, the cells within the epidermal layer are identified as exocrine cells (ex). Additionally, light microscopy images revealed vesicles (ve) inside the cells. These either exhibited substantial staining intensity due to the applied staining methods or displayed an orange coloration without staining (Figure 5A,B,E). Upon examination through SEM, they appeared spherical and presented either a smooth or slightly rough surface (Figure 5F). Within the exocrine cell layer, unstained larger hollow spaces (hs) were observed (Figure 5A,B,E). Examination via SEM revealed these hollow spaces to appear within the exocrine cell layer, after chemical fixation and critical point drying (Figure 5F). These morphological characteristics identify these cells within the euplantulae as exocrine cells type I [62]. The exocrine cells are enveloped and separated on the ventral side by a thin cuticle layer. This layer is notably more intensely stained in blue (toluidine blue) and red (Cason) compared to the exocrine cells, and is identified as the endocuticle layer 2 (Figure 5A, Figure 5B). The endocuticle layer 2 ventrally borders a ≈2 µm wide layer which runs along the entire length of the attachment pad and the connective pad, laterally terminating into the sclerotized cuticle of the tarsomeres. This layer is very lightly stained by toluidine blue and Cason (Figure 5A, Figure 5B) and named adhesive secretion reservoir (as).

Connective pad

The connective pad medially connects the two euplantulae (Figure 4A, Figure 4B; Figure 6A, Figure 6B). The ultrastructure of the connective pad comprises two layers of parallel cuticle sheets with a ventral terminating superficial layer (sf). The adhesive secretion reservoir and exocrine cells of the euplantulae internally extend and connect the tissues of the two euplantulae (Figure 5). The two parallel cuticular layers are distinguishable in terms of coloration through Cason and toluidine blue staining. The layer situated dorsally adjacent to the adhesive secretion reservoir, exhibited a light red hue stained with Cason and a light blue hue with toluidine blue, identifying it as the endocuticle layer 1 (e1). The outer layer presented a more intense coloration identifying it as the outer parallel layer (op) (Figure 6A, Figure 6B). The CLSM analysis indicates a blue indistinguishable autofluorescence signal in both layers, indicating their low degree of sclerotization (Figure 6C). The SEM images revealed structural similarities between the two layers, with the outer parallel layer displaying a slightly denser layering (Figure 6D). The morphology of the superficial layer in

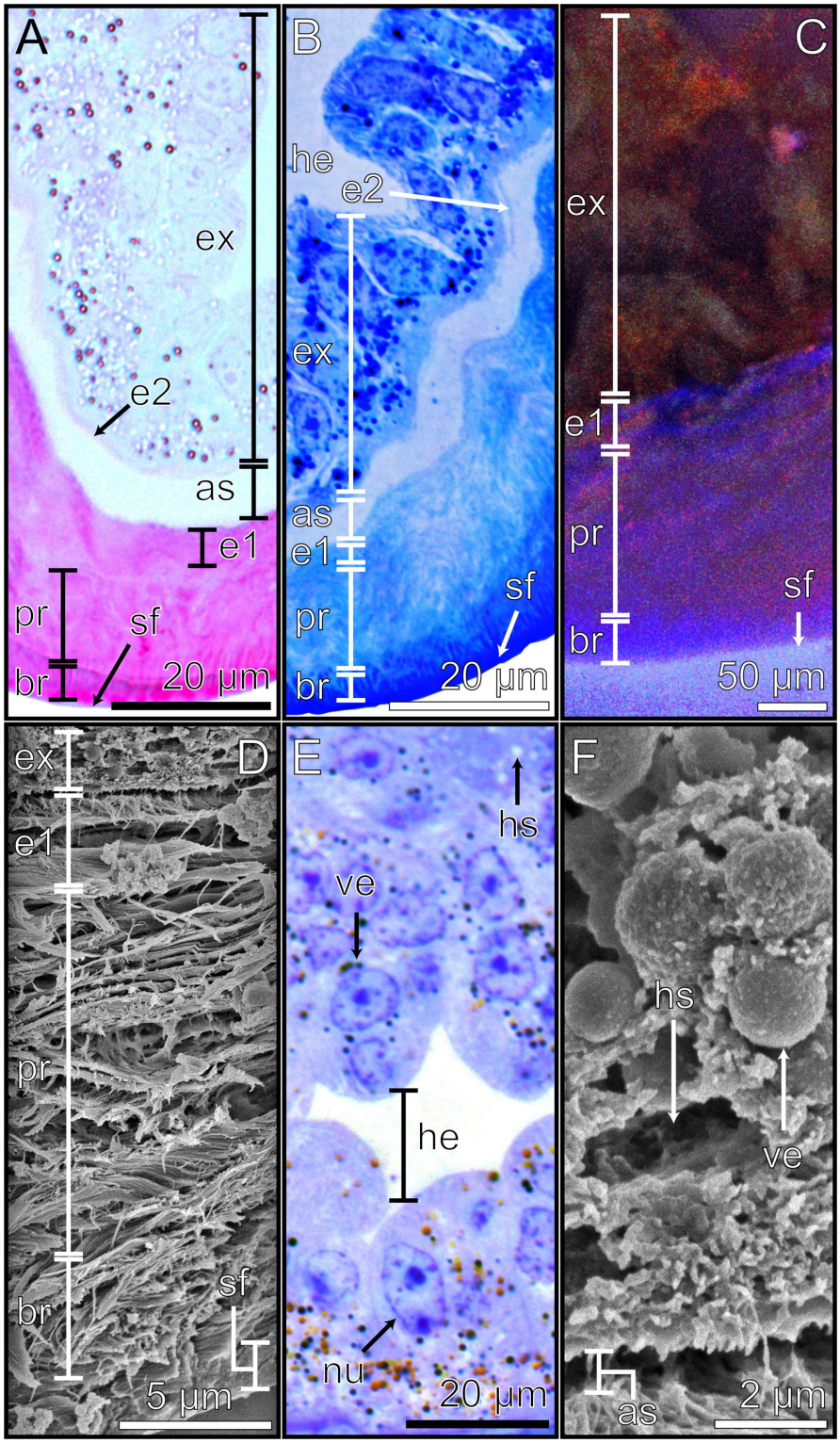

Figure 5: The euplantula sections. Detailed images of the attachment pad of the euplantula. The different methods highlight the morphological and structural characteristics of the respective layers and structures. (A) Cross section stained with Cason's stain, light microscopy. (B) Longitudinal section stained with toluidine blue, light microscopy. (C) Cross section in CLSM. (D) Cross section in SEM. (E) Longitudinal section of the exocrine cells stained with toluidine blue, light microscopy. (F) Cross section of the exocrine cells in SEM. The ventral side of the euplantulae is oriented towards the bottom of the images. as = adhesive secretion reservoir; br = branching rod layer; e1 = endocuticle layer 1; e2 = endocuticle layer 2; ex = exocrine cells; he = hemolymph; hs = hollow spaces; nu = nucleus; pr = primary rod layer; sf = superficial layer; ve = vesicles.

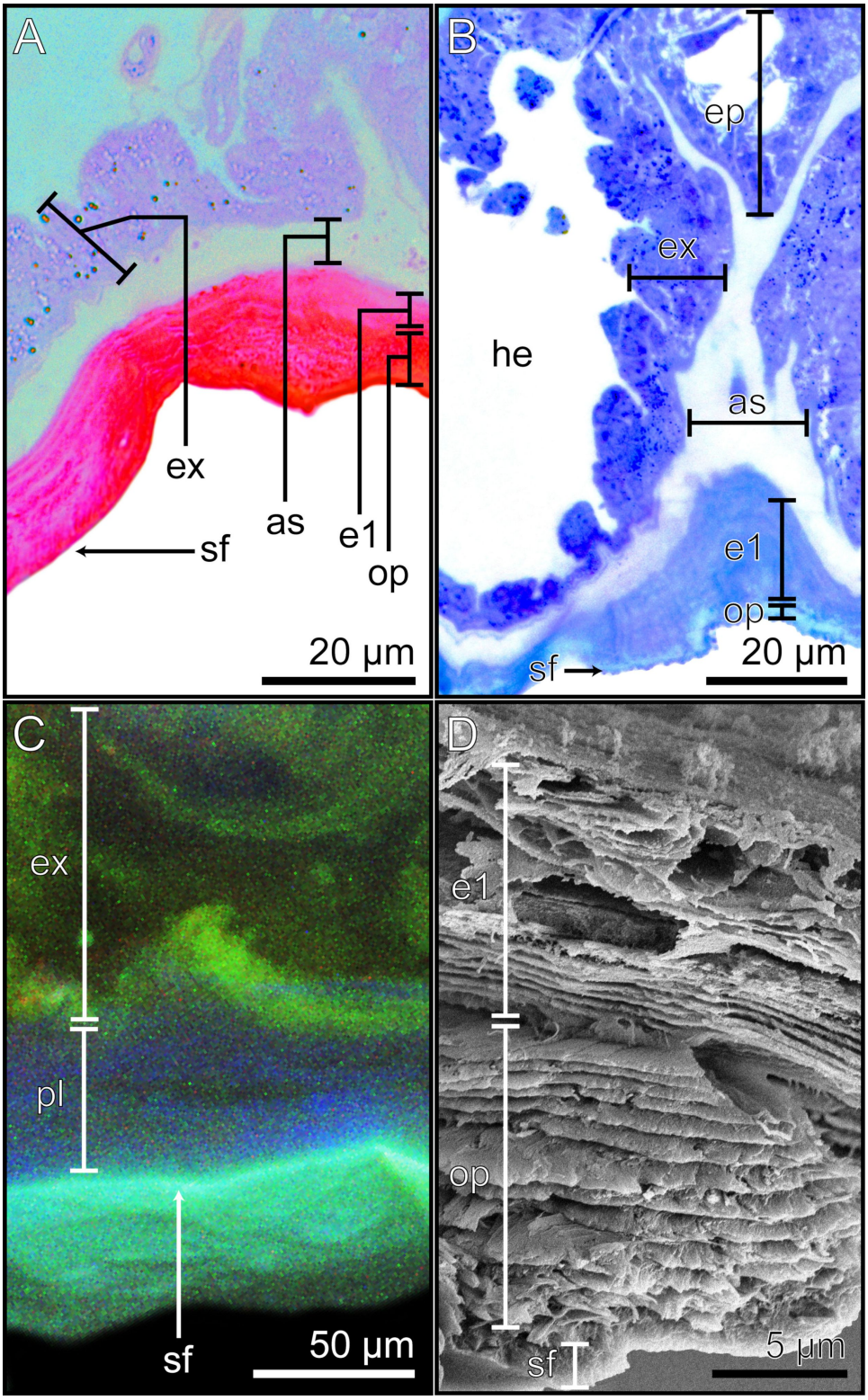

Figure 6: The connective pad between neighbouring euplantulae. Detailed images of the connective pad. The different methods highlight the morphological and structural characteristics of the respective layers and structures. (A) Cross section of the connective pad stained with Cason's stain, light microscopy. (B) Longitudinal section of the connective pad was stained with toluidine blue, light microscopy. (C) Cross section in the CLSM. (D) Cross section in the SEM. The ventral sides of the connective pads are oriented towards the bottom of the images. as = adhesive secretion reservoir; e1 = endocuticle layer 1; ex = exocrine cells; op = outer parallel layer; pl = parallel layer; sf = superficial layer.

the connective pad corresponds to the characteristics of the superficial layer in the attachment pads, exhibiting a more intense staining with Cason and toluidine blue (Figure 6A, Figure 6B), a low degree of sclerotization (Figure 6C), and a dense cuticle organization, evident via SEM, than that of the outer parallel layer and endocuticle layer 1 (Figure 6D). Both the exocrine cells and the adhesive secretion reservoir of the connective pad exhibit the same morphological characteristics as those of the attachment pads (Figure 5; Figure 6).

Additional morphological observations

The superficial layer of the connective pad bears distinctive spherical shapes, which are situated on the dorsal ridges of the connective pad in proximity to the central region of the tarsomere (Figure 7A, Figure 7B). These putatively anti-adhesive structures (aa) were also discovered on the dorsal edge of the arolium (Figure 3B). The SEM and light microscopy (toluidine blue staining) images revealed pore openings (po) in the superficial layer of the euplantulae (Figure 7C, Figure 7E). In addition, small spherical bodies were observed throughout the primary rod layer and branching rod layer, as well as directly beneath the superficial layer of the euplantulae and were identified as adhesive fluid residues (as) (Figure 7C, Figure 7D).

Discussion

Similarities between the two attachment pad types

The anatomy and material composition of the two tarsal attachment organs, euplantulae and arolium, were compared using different imaging techniques. The study revealed some similarities between them, corresponding to their roles in the attachment process [1]. In the interior of both organs, there is a hemolymph reservoir serving dual purposes as a hydrostatic support system and a supply of nutrients to the cells [63]. Following the hemolymph reservoir, exocrine cells are present in the epidermal layer of both organs. As transformed epidermal cells, the exocrine cells are responsible for the secretion of all cuticular layers apical to them, as well as the production of the adhesive secretion. These layers encompass the endocuticle layers 1 and 2, the adhesive secretion reservoir, the primary and branching rod layers, as well as the superficial layer [41,64]. These exocrine cells exhibit surface extensions into the hemolymph and adhesive secretion reservoir optimizing the substance absorption and discharge [31,65-67]. Adjacent to the exocrine cells is the adhesive secretion reservoir serving for the accumulation of the produced adhesive secretion. Both pad types share a similar organisation of the procuticle. The endocuticle layer 2 has a parallel cuticle layering, the primary rod layer is composed of wide cuticle rods ventrally branching into finer rods within the branching rod layer, terminating in the superficial layer (Figure 3; Figure 5).

Previous investigations of the smooth attachment pads (arolium and euplantulae) of *Gromphadorhina portentosa* (Schaum, 1853) by Schmitt and Betz [45] revealed a similar layering of both attachment pads. Similar structures of the procuticle, especially the primary rod-, branching rod-, and superficial layer were also reported by Gorb et al. [20], Gorb and Scherge [21], and Goodwyn et al. [44] in the smooth euplantulae of *Tettigonia viridissima* (L., 1758) and *Locusta migratoria* (L., 1758). Differences in the layering and the details of microstructure likely evolved due to variations in their ecological lifestyle.

Several insects possess hairy attachment organs, which morphologically differ from the smooth ones examined herein. The differences between them manifest primarily in the morphology of the procuticle region. Hairy attachment organs are characterized by cuticle outgrowths (e.g., setae or acanthae [5,68-71]), whereas smooth attachment organs consist of hierarchically split cuticle rods terminating in the superficial layer creating a rather smooth surface [20,70,71]. Both types of attachment organs utilise their distinct morphologies to efficiently replicate the substrate profile to a similar extent, thereby amplifying the actual contact area and, consequently, enhancing attachment [1,2,72,73].

Differences between smooth and hairy attachment pads

The primary difference between hairy and smooth attachment organs manifests in the cuticular morphology. Hairy attachment organs consist of cuticle outgrows (e.g., setae or acanthae [5,68-70]), the cuticle of smooth attachment organs consists of filaments that hierarchically split terminating in the superficial layer, creating a rather smooth surface at the level of light microscopy [20,70,71].

Both types of attachment pads efficiently replicate the surface profile of the substrate owing to their distinct structures, thereby augmenting the actual contact area and, consequently, enhancing attachment. Smooth attachment pads accomplish this through hierarchical organization and the viscoelastic properties of the cuticle [1,2,72,73].

Differences between the two attachment pad types

Despite the similar overall morphology, the two attachment organs show some distinct structural differences, which can be attributed to different functions that both types fulfil. Previous research on the attachment pads of the phasmid *Carausius*

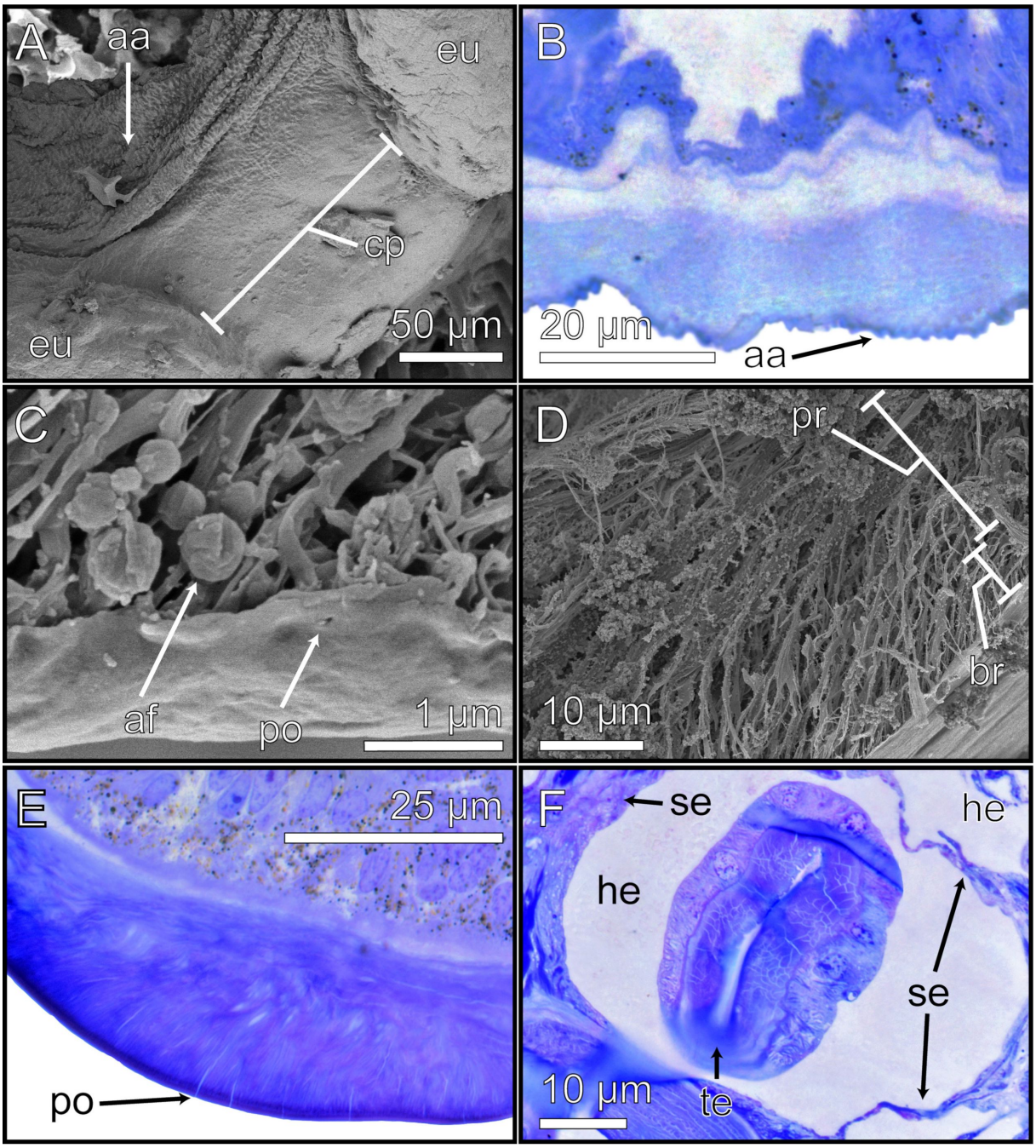

Figure 7: Detailed images of additional morphological observations. The different methods highlight the morphological and structural characteristics of the respective layers and structures. (A) The top view on the euplantulae of one tarsomere shows the connective pad, SEM. (B) Longitudinal section of the connective pad was stained with toluidine blue, light microscopy. (C, D) Cross sections of the arolium, SEM. (C) Superficial layer, SEM. (D) Primary rod layer and branching rod layer, SEM. (E) Longitudinal section of the euplantula stained with toluidine blue, light microscopy. (F) Cross section of the euplantula stained with toluidine blue, light microscopy. aa = anti-adhesive structures; af = adhesive fluid; br = branching rod layer; cp = connective pad; he = hemolymph; po = pore opening; pr = primary rod layer; se = septum; te = tendon.

morosus (Brunner von Wattenwyl, 1907) and the cockroach *Nauphoeta cinerea* (Olivier, 1789) proposed that the arolium primarily serves to generate adhesion, while the euplantulae predominantly function for the generation of friction, characterizing the arolium as an adhesive pad and the euplantulae as friction pads [52-54]. Adaptation to the specific requirements is realized in euplantulae and arolia by the different morphological organizations.

Primary rod layer and branching rod layer

In the arolium, the fibres in the primary rod layer and branching rod layer are notably thicker and more widely spaced compared to those in the euplantulae (Figure 3 (arolium); Figure 5 (euplantulae)). In general, the hierarchical organization of the fibres enables local deformation to adjust to the surface profile of the substrate (e.g., [20,45,70]). This results in anisotropic material properties (i.e., the pads are soft during compression); however, those withstand high tensile stress [74,75]. The more spaced fibres of the arolium consequently would bend more efficiently under pressure and easily adapt to surface irregularities increasing adhesion [44]. The euplantulae feature relatively thinner and with more densely distributed fibres enhances protection against environmental conditions such as wear [76] and evaporation [44]. This enhanced resilience comes at the expense of reduced adaptability to surface irregularities. As a frictional pad, the euplantula requires increased wear resistance, prioritizing it over optimal conformability to surfaces to withstand applied shear forces without undergoing degradation.

Similar morphological features have been previously described by Clemente and Federle [54] for the arolium and euplantulae of the cockroach *N. cinera*, by Bennemann et al. [71] for the arolium of the stick insect *C. morosus*, and by Schmitt and Betz [45] for the arolium and euplantulae of the cockroach *G. portentosa*.

The hollow spaces between fibres within the primary rod layer and the branching rod layer can also be important for adjusting the material properties of the attachment pads. Adhesive secretion kept within the spaces could impact the viscoelasticity of the pad, as well as its shape due to the internal pad pressure caused by the fluid. Spherical structures between the fibres, identified via SEM, could be indications for liquid residues (Figure 7C) (similar residues have been also identified by Gorb et al. in the euplantulae of *T. viridissima* [20]). In addition, the red CLSM autofluorescence signal within the euplantulae might have been caused by the adhesive fluid or by the exocrine cells (Figure 5C), assuming it contains organic molecules with a conjugated system of electrons caused by C=C double bonds [39,40]. The adhesive secretion within the primary rod layer and branching rod layer could work as a soft backing enhancing the conformability to the substrate and friction generation in contact with rough substrates [77].

Endocuticle layer 1

Another morphological difference between the arolium and euplantulae is observed in the endocuticle layer 1. In the arolium, the endocuticle layer 1 is thicker (arolium: ≈10 µm; euplantula: ≈5 µm) (Figure 3; Figure 5D) and more intensely stained with toluidine blue and Cason compared to that of the endocuticle layer 1 of the euplantulae (Figure 3; Figure 5). This difference potentially arises from the larger volume of the arolium, necessitating a stronger endocuticle layer 1 as a support for the primary and branching rod layers. Additionally, the parallel layer structure of the endocuticle layer 1 could give additional resistance against shear forces [78].

Exocrine cells

The exocrine cells of both attachment pads show multiple morphological similarities. Both exocrine cells display comparable staining patterns with toluidine blue and Cason. They possess a sizable nucleus containing numerous nucleoli, a substantial abundance of vesicles and hollow spaces, the absence of a discernible structural mechanism for product release (e.g., a duct), and the presence of a dedicated storage area for their respective products (e.g., the adhesive secretion reservoir).

Collectively, these distinctive features categorize the exocrine cells as exocrine cells type I [62]. Despite their morphological similarities, there are a few differences between the exocrine cells of the arolium and the euplantulae. The initial distinction is the presence of a wide basal layer in the arolium situated between the exocrine cells and the hemolymph (Figure 3; Figure 5). Although the euplantulae likely possess a very thin basal layer, similar to that found in *G. portentosa* [45], confirmation requires TEM analysis. The presence of the wide basal layer potentially augments the mechanical stability of the exocrine cells and ultimately of the arolium [79].

Another difference lies in the autofluorescence of both exocrine layers in CLSM. The exocrine cells of the arolium exhibit a stronger red autofluorescence signal, while those of the euplantulae display green autofluorescence (Figure 3 (arolium); Figure 5 (euplantulae)). Both attachment pads were separately scanned but under the same conditions and settings. Therefore, the difference in the autofluorescence signal could be the result of the two scans (i.e., surrounding material influencing the projected intensity) or be an indication of a difference in composition between the two cell aggregations.

Morphological investigations of the adhesive fluid of *M. extradentata* using cryo-SEM revealed different structures that the fluid can adopt, as well as slight differences between those of arolium and euplantulae [38]. It was postulated that these structures arise due to different mixing ratios of the fluid, and that the fluid can therefore fulfil different functions.

Our results remain ambiguous. The morphological similarities between the exocrine cells of both types of pads suggest that

both produce the same adhesive fluid, which is potentially differentiated by various mixing ratios or production rates. It is also possible that the difference in the autofluorescence indicates that the arolium and euplantulae produce different substances.

Schmitt and Betz [45] discovered no major morphological differences between the exocrine cells of the arolium and euplantulae of *G. portentosa* as well. This could be an indication that the adhesive fluid and its production may be similar between the two species.

Furthermore, the exocrine cell layer of the arolium is more strongly folded in comparison to that of the euplantulae (Figure 2 (arolium); Figure 4 (euplantulae)). The enlarged surface could offer more exocrine cell area increasing the discharge area of the secretion, as well as allowing the pad to deform more easily, making it more resistant to mechanical stresses.

Endocuticle layer 2

The endocuticle layer 2 is strongly pronounced around the exocrine cells of the euplantulae, as evidenced by the darker staining with toluidine blue and Cason (Figure 5A, Figure 5B). In the arolium, however, the endocuticle layer 2 is not recognizable.

The wider endocuticle layer 2 in the euplantulae could be a structural feature that increases the resistance to shear forces as well as the stability of the attachment organ. A layer with similar properties, the inner cuticular band, has been previously observed in the arolium and euplantulae of *G. portentosa* by Schmitt and Betz [45].

Adhesive secretion reservoir

The endocuticle layer 1 and endocuticle layer 2 are separated by a confined space measuring ≈10 µm in width, the adhesive secretion reservoir, which is slightly stained with toluidine blue and Cason in both the arolium and euplantulae (Figure 3; Figure 5). Based on the light staining with toluidine blue and Cason, the adhesive secretion reservoir probably consists of very loosely packed cuticle fibres which allow the adhesive secretion to be stored. Due to the potentially loose structure of the adhesive secretion reservoir, it is susceptible to rupture, whereby the actual size of the reservoir is difficult to determine. In addition to serving as a repository for the secretion, this reservoir could play an additional role in providing a pliant support structure when filled with adhesive secretion, thereby contributing to the stabilization of the respective attachment pad [77]. A morphologically similar adhesive secretion reservoir layer was also observed in the arolium and euplantulae of *G. portentosa*, as well as in the arolium of *T. viridissima* [45,80].

Internal subdivision of the euplantulae

The division of the euplantulae into four areas (Figure 4; Figure 7F) results in four independent volumes filled with hemolymph capable of generating internal hydraulic pressure. This pressure could potentially influence the shape of the euplantulae and therefore control the attachment process. Similar principles were discovered in the toe pads of tree frogs where the blood pressure maintains its shape [81], and in the arolia of ants where hemolymph pressure inflates them [82]. Dening et al. [83] showed in an artificial system that internal air-filled bladders can control attachment strength.

Anti-adhesive structures

The superficial layer of the connective pad is patterned in a hemispherical shape at the predominantly peripheral position towards the centre. This position suggests that such structures act as an adhesion- and friction-reducing system (anti-adhesive structures, Figure 7B) [86]. The hemispherical pattern reduces the contact area between the cuticle and the substrate, thus decreasing contact forces. Similar surface structures were observed in the wax coverage of plants where they decreased the attachment performance of insects [84]. A reduction of the contact area and the resulting reduced adhesion was shown by Wu et al. [85] for artificial structures. Reducing attachment could be helpful in the areas where such structures are found as they prevent the adhesion of folds in membranous cuticles in the regions of the connective pad. They might also reduce the risk of trapping contaminants in the inter-tarsomeric membranous region. The removal of particulate contaminants is very important as they are known to cause abrasive wear in the open insect joints [86]. Anti-adhesive surface structures in the periphery of the active working areas of the attachment pads could establish zones facilitating detachment. Such detachment movements are described for flies with hairy attachment pads [87], but would function similarly in smooth ones.

Connective pad

Our investigations have revealed a continuity of several underlying layers from beneath the euplantulae extending through the connective pad region. These layers encompass the hemolymph, exocrine cells, endocuticle layer 2, adhesive secretion reservoir, endocuticle layer 1, and superficial layer (Figure 6). Notably, the connective pad lacks both the primary rod layer and branching rod layer but exhibits an additional stratum of outer parallel cuticle. In CLSM, the exocrine cells exhibit green autofluorescence, whereas the procuticle emits blue autofluorescence, which is consistent with observations in the euplantulae.

Footprints of the connective pad revealed residues of the secretory fluid (pers. obs.). Given the identification as a soft cuticle, the structural attributes of the procuticle, and the presence of adhesive secretion, it is possible that the connective pad could participate in the attachment process.

Similar connective pad structures are present in insect species that also possess split euplantulae [88]. However, many euplantulae-bearing insect species do not have split euplantulae and therefore do not possess a connecting tissue [5,45,89-91], including several phasmid species [88,92].

Transportation pathway of the pad secretion

The schematic representation delineates the potential site of adhesive secretion production and its transportation from the hemolymph reservoir to the surface of the euplantula and arolium (Figure 8). The exocrine cells, situated in the epidermal tissue, obtain the educts for the adhesive secretion from the hemolymph. Both attachment pads exhibit exocrine cells with surface expansions into the hemolymph increasing the area for reactant uptake.

The adhesive fluid is secreted through pores in the endocuticle layer 2 [45] and accumulates in the adhesive secretion reservoir (indicated by the split arrow). Subsequently, the secretion traverses the endocuticle layer 1 via pores [45] and enters the primary rod layer. Within the primary rod layer and branching rod layer layers, the secretion fills the cavities between the rods (indicated by the split arrows), extending throughout the layers up to the superficial layer. The transportation of the adhesive

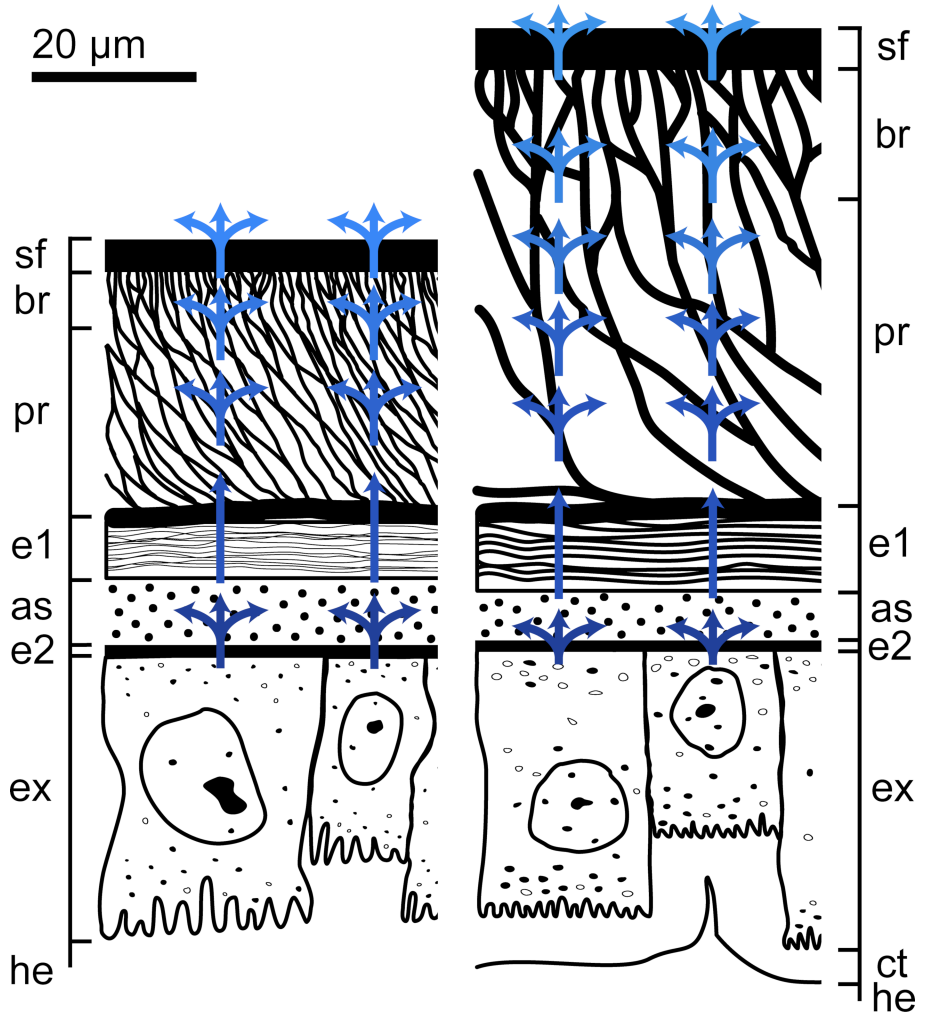

Figure 8: Scheme of the arolium (left) and euplantula (right) of *M. extradentata*. Schematic representation of the transportation of the adhesive secretion from its point of origin towards the substrate. A description of the production and transportation pathway of the adhesive secretion is provided in the text. as = adhesive secretion reservoir; bl = basal layer; br = branching rod layer; e1 = endocuticle layer 1; e2 = endocuticle layer 2; ex = exocrine cells; he = hemolymph; pr = primary rod layer; sf = superficial layer. Blue arrows indicate the pathway of the adhesive secretion in the respective pad type. Brightening of the arrows indicates a reduction in the amount of adhesive fluid.

secretion to the surface is facilitated through pores in the superficial layer [64] (Figure 7C,E).

The cuticle layering and morphology of the arolium and euplantulae facilitate the absorption, storage, and distribution of the produced adhesive secretion within the attachment pads, enabling its transport to the surface. As mentioned above, the presence of the fluid secretion in these layers modulates the stability of the corresponding layers, potentially serving as a soft backing enhancing attachment on the substrate by maximizing the contact area [77].

Dirks and Federle [15] observed that the adhesive secretion volume in the phasmid *C. morosus* was completely depleted after approximately 7–10 consecutive press-downs (steps), with a subsequent restoration to its original volume taking approximately 15 min, indicative of a steady-state supply. The existence of multiple reservoirs (the adhesive secretion reservoir as well as the hollow spaces in both the primary rod layer and branching rod layer) suggests a continuous supply of adhesive secretion toward the surface, minimizing the likelihood of complete depletion of the attachment pad. Additionally, the denser cuticle rod structure of the branching rod layer may potentially restrict the flow of adhesive secretion, thereby reducing the risk of excessive fluid production.

Schmitt and Betz [45] also postulated a comparable transport pathway for adhesive secretions in the smooth attachment pads of *G. portentosa*. There, the adhesive secretion produced by exocrine cells type I is transported through a two-layered inner cuticle band via pores (comparable to the endocuticle layer 2) and accumulates in the secretion reservoir. It then passes through a layered cuticle via pores (comparable to the endocuticle layer 1) into a sponge-like cuticle where it fills the hollow cavities (comparable to the primary rod layer and branching rod layer). The final route to the surface is via pores in the ventral cuticle band and the epicuticle (comparable to the superficial layer in this study).

Conclusion

The examination of the ultrastructure and material composition of the tarsal attachment apparatus of the stick insect *Medauroidea extradentata* yielded insights into the detailed structure of the two attachment pad types (arolium and euplantulae). Our findings revealed differences in the structure and material composition between them, indicative of their different roles during attachment. We proposed a potential pathway for the adhesive secretion from the exocrine cells to the surface and provided evidence suggesting the involvement of exocrine cells type I, which exhibit some variability between the arolium and euplantulae. For a more comprehensive understanding of the functional principles of both pad types, a detailed examination of their ultrastructure and testing of their material properties is required. Transmission electron microscopy and atomic force microscopy are ideal approaches for this purpose.

Acknowledgements

We thank Esther Appel and Dr. Alexander Kovalev (Department of Functional Morphology and Biomechanics, Kiel University, Germany) for their technical assistance. Dr. Carsten Müller (Zoological Institute and Museum, Department of General and Systematic Zoology, Greifswald University, Germany) is thanked for his scientific advice.

Funding

This work was supported by the German Research Foundation (DFG) (grant GO 995/34-1).

Competing Interests

The authors declare no competing or financial interests.

Author Contributions

Julian Thomas: conceptualization; data curation; formal analysis; investigation; methodology; validation; visualization; writing – original draft. Stanislav N. Gorb: conceptualization; funding acquisition; methodology; project administration; resources; writing – review & editing. Thies H. Büscher: conceptualization; data curation; methodology; project administration; supervision; validation; writing – review & editing.

ORCID® iDs

Julian Thomas - https://orcid.org/0000-0002-7923-7013
Stanislav N. Gorb - https://orcid.org/0000-0001-9712-7953
Thies H. Büscher - https://orcid.org/0000-0003-0639-4699

Data Availability Statement

All data that supports the findings of this study is available in the published article.

References

1. Gorb, S. N. *Attachment Devices of Insect Cuticle;* Springer: Dordrecht, Netherlands, 2001. doi:10.1007/0-306-47515-4
2. Scherge, M.; Gorb, S. N. *Biological Micro- and Nanotribology. Nature's Solutions;* Springer: Berlin, Germany, 2001. doi:10.1007/978-3-662-04431-5
3. Gorb, S. N. Smooth attachment devices in insects: Functional morphology and biomechanics. *Advances in Insect Physiology;* Elsevier: Amsterdam, Netherlands, 2007; pp 81–115. doi:10.1016/s0065-2806(07)34002-2
4. Schroeder, T. B. H.; Houghtaling, J.; Wilts, B. D.; Mayer, M. *Adv. Mater. (Weinheim, Ger.)* **2018,** *30,* e1705322. doi:10.1002/adma.201705322
5. Beutel, R. G.; Gorb, S. N. *J. Zool. Syst. Evol. Res.* **2001,** *39,* 177–207. doi:10.1046/j.1439-0469.2001.00155.x

6. Gorb, S. N. Biological fibrillar adhesives: Functional principles and biomimetic applications. In *Handbook of adhesion technology;* Da Silva, L. F. M.; Öchsner, A.; Adams, R. D., Eds.; Springer: Berlin, Heidelberg, 2011; pp 1409–1436. doi:10.1007/978-3-642-01169-6_54
7. Büscher, T. H.; Gorb, S. N. Convergent evolution of animal adhesive pads. *Convergent Evolution;* Springer Nature: Cham, Switzerland, 2023; pp 257–287. doi:10.1007/978-3-031-11441-0_10
8. Creton, C.; Gorb, S. *MRS Bull.* **2007,** *32,* 466–472. doi:10.1557/mrs2007.79
9. Ditsche, P.; Summers, A. P. *Beilstein J. Nanotechnol.* **2014,** *5,* 2424–2439. doi:10.3762/bjnano.5.252
10. Voigt, D.; Schuppert, J. M.; Dattinger, S.; Gorb, S. N. *J. Insect Physiol.* **2008,** *54,* 765–776. doi:10.1016/j.jinsphys.2008.02.006
11. Eisner, T.; Aneshansley, D. J. *Proc. Natl. Acad. Sci. U. S. A.* **2000,** *97,* 6568–6573. doi:10.1073/pnas.97.12.6568
12. Johnson, K. L. *Tribol. Int.* **1998,** *31,* 413–418. doi:10.1016/s0301-679x(98)00060-7
13. Dirks, J.-H.; Federle, W. *Soft Matter* **2011,** *7,* 11047. doi:10.1039/c1sm06269g
14. Dirks, J.-H. Adhesion in Insects. In *Encyclopedia of Nanotechnology;* Bhushan, B., Ed.; Springer: Dordrecht, Netherlands, 2015; pp 1–10. doi:10.1007/978-94-007-6178-0_101007-1
15. Dirks, J.-H.; Federle, W. *J. R. Soc., Interface* **2011,** *8,* 952–960. doi:10.1098/rsif.2010.0575
16. Barnes, W. J.; Smith, J.; Oines, C.; Mundl, R. *Tire Technol. Int.* **2002,** *2002,* 56–60.
17. Drechsler, P.; Federle, W. *J. Comp. Physiol., A* **2006,** *192,* 1213–1222. doi:10.1007/s00359-006-0150-5
18. Bullock, J. M. R.; Drechsler, P.; Federle, W. *J. Exp. Biol.* **2008,** *211,* 3333–3343. doi:10.1242/jeb.020941
19. Gorb, E. V.; Hosoda, N.; Miksch, C.; Gorb, S. N. *J. R. Soc., Interface* **2010,** *7,* 1571–1579. doi:10.1098/rsif.2010.0081
20. Gorb, S.; Jiao, Y.; Scherge, M. *J. Comp. Physiol., A* **2000,** *186,* 821–831. doi:10.1007/s003590000135
21. Gorb, S.; Scherge, M. *Proc. R. Soc. London, Ser. B* **2000,** *267,* 1239–1244. doi:10.1098/rspb.2000.1133
22. Stefan, J. *Ann. Phys. (Berlin, Ger.)* **1875,** *230,* 316–318. doi:10.1002/andp.18752300213
23. Federle, W.; Riehle, M.; Curtis, A. S. G.; Full, R. J. *Integr. Comp. Biol.* **2002,** *42,* 1100–1106. doi:10.1093/icb/42.6.1100
24. Dirks, J.-H. *Beilstein J. Nanotechnol.* **2014,** *5,* 1160–1166. doi:10.3762/bjnano.5.127
25. Clemente, C. J.; Bullock, J. M. R.; Beale, A.; Federle, W. *J. Exp. Biol.* **2010,** *213,* 635–642. doi:10.1242/jeb.038232
26. Clemente, C. J.; Federle, W. *Bioinspiration Biomimetics* **2012,** *7,* 046001. doi:10.1088/1748-3182/7/4/046001
27. Vötsch, W.; Nicholson, G.; Müller, R.; Stierhof, Y.-D.; Gorb, S.; Schwarz, U. *Insect Biochem. Mol. Biol.* **2002,** *32,* 1605–1613. doi:10.1016/s0965-1748(02)00098-x
28. Thomas, J.; Gorb, S. N.; Büscher, T. H. *J. Exp. Biol.* **2023,** *226,* jeb244295. doi:10.1242/jeb.244295
29. Lockey, K. H. *Comp. Biochem. Physiol., Part B: Comp. Biochem.* **1988,** *89,* 595–645. doi:10.1016/0305-0491(88)90305-7
30. Eltz, T. *J. Chem. Ecol.* **2006,** *32,* 907–915. doi:10.1007/s10886-006-9055-6
31. Bauchhenß, E. *Zoomorphology* **1979,** *93,* 99–123. doi:10.1007/bf00994125
32. Schmitt, U. *Experientia* **1990,** *46,* 1080–1082. doi:10.1007/bf01940680
33. Kosaki, A.; Yamaoka, R. *Jpn. J. Appl. Entomol. Zool.* **1996,** *40,* 47–53. doi:10.1303/jjaez.40.47
34. Geiselhardt, S. F.; Geiselhardt, S.; Peschke, K. *Chemoecology* **2011,** *21,* 181–186. doi:10.1007/s00049-011-0077-3
35. Betz, O.; Albert, K.; Boley, M.; Frenzel, M.; Gerhardt, H.; Grunwald, I.; Hartwig, A.; Kleemeier, M.; Maurer, A.; Neuenfeldt, M.; Rischka, K.; Sampalla, B.; Schmitt, C.; Speidel, M.; Steiner, M.; Verheyden, N.; Vogt, M. *Mitt. dtsch. Ges. allg. angew. Ent.* **2018,** *21,* 159–164.
36. Kölsch, G. *Can. J. Zool.* **2000,** *78,* 465–475. doi:10.1139/z99-213
37. Dirks, J.-H.; Clemente, C. J.; Federle, W. *J. R. Soc., Interface* **2010,** *7,* 587–593. doi:10.1098/rsif.2009.0308
38. Thomas, J.; Gorb, S. N.; Büscher, T. H. *Biomimetics* **2023,** *8,* 439. doi:10.3390/biomimetics8050439
39. Geiselhardt, S. F.; Federle, W.; Prüm, B.; Geiselhardt, S.; Lamm, S.; Peschke, K. *J. Insect Physiol.* **2010,** *56,* 398–404. doi:10.1016/j.jinsphys.2009.11.016
40. Speidel, M. W.; Kleemeier, M.; Hartwig, A.; Rischka, K.; Ellermann, A.; Daniels, R.; Betz, O. *Beilstein J. Nanotechnol.* **2017,** *8,* 45–63. doi:10.3762/bjnano.8.6
41. Rebora, M.; Salerno, G.; Piersanti, S.; Gorb, E. V.; Gorb, S. N. *Zoomorphology* **2021,** *140,* 85–102. doi:10.1007/s00435-020-00515-z
42. Gorb, S. N. *Proc. R. Soc. London, Ser. B* **1998,** *265,* 747–752. doi:10.1098/rspb.1998.0356
43. Gorb, S. N.; Beutel, R. G.; Gorb, E. V.; Jiao, Y.; Kastner, V.; Niederegger, S.; Popov, V. L.; Scherge, M.; Schwarz, U.; Vötsch, W. *Integr. Comp. Biol.* **2002,** *42,* 1127–1139. doi:10.1093/icb/42.6.1127
44. Perez Goodwyn, P.; Peressadko, A.; Schwarz, H.; Kastner, V.; Gorb, S. *J. Comp. Physiol., A* **2006,** *192,* 1233–1243. doi:10.1007/s00359-006-0156-z
45. Schmitt, C.; Betz, O. *Cell Tissue Res.* **2017,** *370,* 243–265. doi:10.1007/s00441-017-2661-5
46. Bußhardt, P.; Wolf, H.; Gorb, S. N. *Zoology (Munich, Ger.)* **2012,** *115,* 135–141. doi:10.1016/j.zool.2011.11.002
47. Büscher, T. H.; Gorb, S. N. *J. Exp. Biol.* **2019,** *222,* jeb209833. doi:10.1242/jeb.209833
48. Büscher, T. H.; Becker, M.; Gorb, S. N. *J. Exp. Biol.* **2020,** *223,* jeb226514. doi:10.1242/jeb.226514
49. Burack, J.; Gorb, S. N.; Büscher, T. H. *Insects* **2022,** *13,* 952. doi:10.3390/insects13100952
50. Winand, J.; Gorb, S. N.; Büscher, T. H. *J. Comp. Physiol., A* **2023,** *209,* 313–323. doi:10.1007/s00359-022-01570-1
51. Boisseau, R. P.; Büscher, T. H.; Klawitter, L. J.; Gorb, S. N.; Emlen, D. J.; Tobalske, B. W. *BMC Ecol. Evol.* **2022,** *22,* 39. doi:10.1186/s12862-022-01993-z
52. Labonte, D.; Federle, W. *PLoS One* **2013,** *8,* e81943. doi:10.1371/journal.pone.0081943
53. Labonte, D.; Williams, J. A.; Federle, W. *J. R. Soc., Interface* **2014,** *11,* 20140034. doi:10.1098/rsif.2014.0034
54. Clemente, C. J.; Federle, W. *Proc. R. Soc. B* **2008,** *275,* 1329–1336. doi:10.1098/rspb.2007.1660
55. Büscher, T. H.; Buckley, T. R.; Grohmann, C.; Gorb, S. N.; Bradler, S. *Front. Ecol. Evol.* **2018,** *6,* 69. doi:10.3389/fevo.2018.00069
56. Büscher, T. H.; Kryuchkov, M.; Katanaev, V. L.; Gorb, S. N. *J. R. Soc., Interface* **2018,** *15,* 20180281. doi:10.1098/rsif.2018.0281
57. Sridharan, G.; Shankar, A. A. *J. Oral Maxillofac. Pathol.* **2012,** *16,* 251–255. doi:10.4103/0973-029x.99081
58. Vidal, B. d. C.; Mello, M. L. S. *Acta Histochem.* **2019,** *121,* 101–112. doi:10.1016/j.acthis.2018.11.005
59. Wang, L.-Y.; Jafarpour, M.; Lin, C.-P.; Appel, E.; Gorb, S. N.; Rajabi, H. *Soft Matter* **2019,** *15,* 8272–8278. doi:10.1039/c9sm01687b
60. Cason, J. E. *Stain Technol.* **1950,** *25,* 225–226. doi:10.3109/10520295009110996

61. Mulisch, M.; Welsch, U., Eds. *Romeis Mikroskopische Technik,* 18th ed.; Spektrum Verlag: Heidelberg, Germany, 2010. doi:10.1007/978-3-8274-2254-5
62. Noirot, C.; Quennedey, A. *Annu. Rev. Entomol.* **1974,** *19,* 61–80. doi:10.1146/annurev.en.19.010174.000425
63. Mullins, D. E. Chemistry and physiology of the hemolymph. In *Comprehensive Insect Physiology, Biochemistry and Pharmacology;* Kerkut, G. A.; Gilbert, L. I., Eds.; Pergamon Press: New York, NY, USA, 1985; pp 355–400.
64. Betz, O. Adhesive exocrine glands in insects: morphology, ultrastructure, and adhesive secretion. In *Biological Adhesive Systems;* von Byern, J.; Grunwald, I., Eds.; Springer: Vienna, Austria; pp 111–152. doi:10.1007/978-3-7091-0286-2_8
65. Betz, O.; Mumm, R. *Arthropod Struct. Dev.* **2001,** *30,* 77–97. doi:10.1016/s1467-8039(01)00029-9
66. Betz, O. *J. Morphol.* **2003,** *255,* 24–43. doi:10.1002/jmor.10044
67. Eberhard, M. J. B.; Pass, G.; Picker, M. D.; Beutel, R.; Predel, R.; Gorb, S. N. *J. Morphol.* **2009,** *270,* 1247–1261. doi:10.1002/jmor.10754
68. Stork, N. E. *J. Nat. Hist.* **1983,** *17,* 829–835. doi:10.1080/00222938300770641
69. Federle, W. *J. Exp. Biol.* **2006,** *209,* 2611–2621. doi:10.1242/jeb.02323
70. Büscher, T. H.; Gorb, S. N. *Beilstein J. Nanotechnol.* **2021,** *12,* 725–743. doi:10.3762/bjnano.12.57
71. Bennemann, M.; Scholz, I.; Baumgartner, W. Functional morphology of the adhesive organs of stick insects (*Carausius morosus*). In *Bioinspiration, Biomimetics, and Bioreplication;* Martín-Palma, R. J.; Lakhtakia, A., Eds.; SPIE: San Diego, CA, USA, 2011; 79751A. doi:10.1117/12.888841
72. Kendall, K. *Molecular Adhesion and its Applications. The Sticky Universe;* Kluwer Academic Publishers: New York, NY, USA, 2001.
73. Popov, V. L. *Kontaktmechanik und Reibung. Von der Nanotribologie bis zur Erdbebendynamik,* 3rd ed.; Springer Vieweg: Berlin, Heidelberg, 2015. doi:10.1007/978-3-662-45975-1
74. Neville, A. C. *Biology of Fibrous Composites. Development Beyond the Cell Membrane;* Cambridge University Press: New York, NY, USA, 1993. doi:10.1017/cbo9780511601101
75. Scholz, I.; Baumgartner, W.; Federle, W. *J. Comp. Physiol., A* **2008,** *194,* 373–384. doi:10.1007/s00359-008-0314-6
76. Slifer, E. H. *Ann. Entomol. Soc. Am.* **1950,** *43,* 173–188. doi:10.1093/aesa/43.2.173
77. Glaser, N. C.; Langowski, J. K. A. *R. Soc. Open Sci.* **2023,** *10,* 221263. doi:10.1098/rsos.221263
78. Vincent, J. F. V.; Wegst, U. G. K. *Arthropod Struct. Dev.* **2004,** *33,* 187–199. doi:10.1016/j.asd.2004.05.006
79. Khalilgharibi, N.; Mao, Y. *Open Biol.* **2021,** *11,* 200360. doi:10.1098/rsob.200360
80. Henning, B. *Zoomorphology* **1974,** *79,* 323–342. doi:10.1007/bf00277513
81. Barnes, W. J. P.; Goodwyn, P. J. P.; Nokhbatolfoghahai, M.; Gorb, S. N. *J. Comp. Physiol., A* **2011,** *197,* 969–978. doi:10.1007/s00359-011-0658-1
82. Federle, W.; Brainerd, E. L.; McMahon, T. A.; Hölldobler, B. *Proc. Natl. Acad. Sci. U. S. A.* **2001,** *98,* 6215–6220. doi:10.1073/pnas.111139298
83. Dening, K.; Heepe, L.; Afferrante, L.; Carbone, G.; Gorb, S. N. *Appl. Phys. A: Mater. Sci. Process.* **2014,** *116,* 567–573. doi:10.1007/s00339-014-8504-2
84. Gorb, E. V.; Gorb, S. N. *J. Exp. Bot.* **2017,** *68,* 5323–5337. doi:10.1093/jxb/erx271
85. Wu, J.; Ji, K.; Liu, S.; Huo, T.; Wang, X.; Tu, C.; Zhao, J.; Deng, K.; Dai, Z.; Gorb, S. N. *Tribol. Int.* **2024,** *191,* 109178. doi:10.1016/j.triboint.2023.109178
86. Nadein, K.; Gorb, S. N. *Adv. Mater. Interfaces* **2024,** *11,* 2300743. doi:10.1002/admi.202300743
87. Niederegger, S.; Gorb, S. *J. Insect Physiol.* **2003,** *49,* 611–620. doi:10.1016/s0022-1910(03)00048-9
88. Büscher, T. H.; Grohmann, C.; Bradler, S.; Gorb, S. N. *Zoologica* **2019,** *164,* 1–94.
89. Grohmann, C.; Henze, M. J.; Nørgaard, T.; Gorb, S. N. *Proc. R. Soc. B* **2015,** *282,* 20142976. doi:10.1098/rspb.2014.2976
90. Beutel, R. G.; Gorb, S. N. *Arthropod Syst. Phylog.* **2006,** *64,* 3–25. doi:10.3897/asp.64.e31640
91. Beutel, R. G.; Gorb, S. N. *Syst. Entomol.* **2008,** *33,* 501–510. doi:10.1111/j.1365-3113.2008.00428.x
92. Büscher, T. H.; Gorb, S. N. *ZooKeys* **2017,** *645,* 1–11. doi:10.3897/zookeys.645.10783

License and Terms

This is an open access article licensed under the terms of the Beilstein-Institut Open Access License Agreement (https://www.beilstein-journals.org/bjnano/terms), which is identical to the Creative Commons Attribution 4.0 International License (https://creativecommons.org/licenses/by/4.0). The reuse of material under this license requires that the author(s), source and license are credited. Third-party material in this article could be subject to other licenses (typically indicated in the credit line), and in this case, users are required to obtain permission from the license holder to reuse the material.

The definitive version of this article is the electronic one which can be found at:
https://doi.org/10.3762/bjnano.15.52

BEILSTEIN JOURNAL OF NANOTECHNOLOGY

Functional fibrillar interfaces: Biological hair as inspiration across scales

Guillermo J. Amador*[1], Brett Klaassen van Oorschot[1], Caiying Liao[2], Jianing Wu[2] and Da Wei[3]

Review

Open Access

Address:
[1]Experimental Zoology Group, Department of Animal Sciences, Wageningen University & Research, De Elst 1, 6708 WD Wageningen, Netherlands, [2]School of Aeronautics and Astronautics, Shenzhen Campus of Sun Yat-sen University, Shenzhen, 518107, China and [3]Beijing National Laboratory for Condensed Matter Physics and Laboratory of Soft Matter Physics, Institute of Physics, Chinese Academy of Sciences, Beijing 100190, China

Email:
Guillermo J. Amador* - guillermo.amador@wur.nl

* Corresponding author

Keywords:
adhesion; fibers; fluid–structure interactions; mastigonemes; mechanosensing; setae; wettability

Beilstein J. Nanotechnol. **2024,** *15,* 664–677.
https://doi.org/10.3762/bjnano.15.55

Received: 31 January 2024
Accepted: 17 May 2024
Published: 06 June 2024

This article is part of the thematic issue "Biomimetics and bioinspired surfaces: from nature to theory and applications".

Guest Editor: M. Rebora

© 2024 Amador et al.; licensee Beilstein-Institut.
License and terms: see end of document.

Abstract

Hair, or hair-like fibrillar structures, are ubiquitous in biology, from fur on the bodies of mammals, over trichomes of plants, to the mastigonemes on the flagella of single-celled organisms. While these long and slender protuberances are passive, they are multifunctional and help to mediate interactions with the environment. They provide thermal insulation, sensory information, reversible adhesion, and surface modulation (e.g., superhydrophobicity). This review will present various functions that biological hairs have been discovered to carry out, with the hairs spanning across six orders of magnitude in size, from the millimeter-thick fur of mammals down to the nanometer-thick fibrillar ultrastructures on bateriophages. The hairs are categorized according to their functions, including protection (e.g., thermal regulation and defense), locomotion, feeding, and sensing. By understanding the versatile functions of biological hairs, bio-inspired solutions may be developed across length scales.

Introduction

Given the bottom-up approach that biology uses to create materials, fibrous structures formed by molecular chains are found everywhere. For example, internally in the form of collagen [1] and microtubules and microfilaments [2], and externally in the form of silk [3] and hair [4,5]. Among these prevalent, quasi-one-dimensional structures, here we loosely define biological "hairs" as high-aspect-ratio structures that are external and passive. This definition is loose yet intuitive. First, a structure must be on the exterior of an organism to be considered as "hair". This excludes the internal one-dimensional structures

such as microfilaments, veins, or bones. Second, in the definition presented here, "hairs" need to be passive, that is, the high-aspect-ratio structures must not be internally active. Obviously, this excludes organisms' slender body parts, such as elephant trunks, the legs of mammals and insects, and the cilia and flagella of eukaryotic microorganisms. As a side note, flagella of eukaryotic cells (e.g., algae, protists, and sperms) and prokaryotic cells (bacteria) should not be confused. Eukaryotic flagella are essentially the same organelles as cilia, consisting of a well-organized microtubular backbone and orchestrated internal protein motors, whereas bacterial flagella are simply passive, stiff filaments. The passive nature of the hairs does not lessen their importance. They play a crucial role in mediating an organism's interactions with the environment, serving various functions depending on their deformations, which are driven purely by their surroundings. Altogether, following the definition above, the structures covered in this review include the hair and fur of mammals, the feathers of birds, the trichomes of plants, the setae of arthropods, and the ultrastructures of single-celled organisms.

Figure 1A shows how the total hair mass m_h scales with body mass m_b. For m_h, a material density of 1 g·cm^{-3} was assumed. A relationship slightly exceeding isometry is observed, where $m_h \sim m_b^{1.10}$ with 95% confidence interval (CI) of (1.07, 1.15) for the exponent. For purely isometric scaling, if body mass decreases or increases by a factor of 100, then total hair mass decreases or increases by that same factor, respectively. Isometric scaling supports the fact that, with respect to certain characteristics, organisms are scaled copies of each other [6]. For example, as expected from isometry, the total surface area of a salamander was found to scale with $\sim m_b^{2/3}$ [7], and the same scaling was found for the total area of adhesive pads of animals within the same phylogenetic class, order, family, genus, and species [8].

However, hair mass deviates slightly from isometry, and it appears that larger organisms are more "hairy". First, the exponent for power-law fits increases with size, as evidenced by comparing the fits for cells and phages, insects, mammals, and birds (see caption of Figure 1A). Second, from the inset of

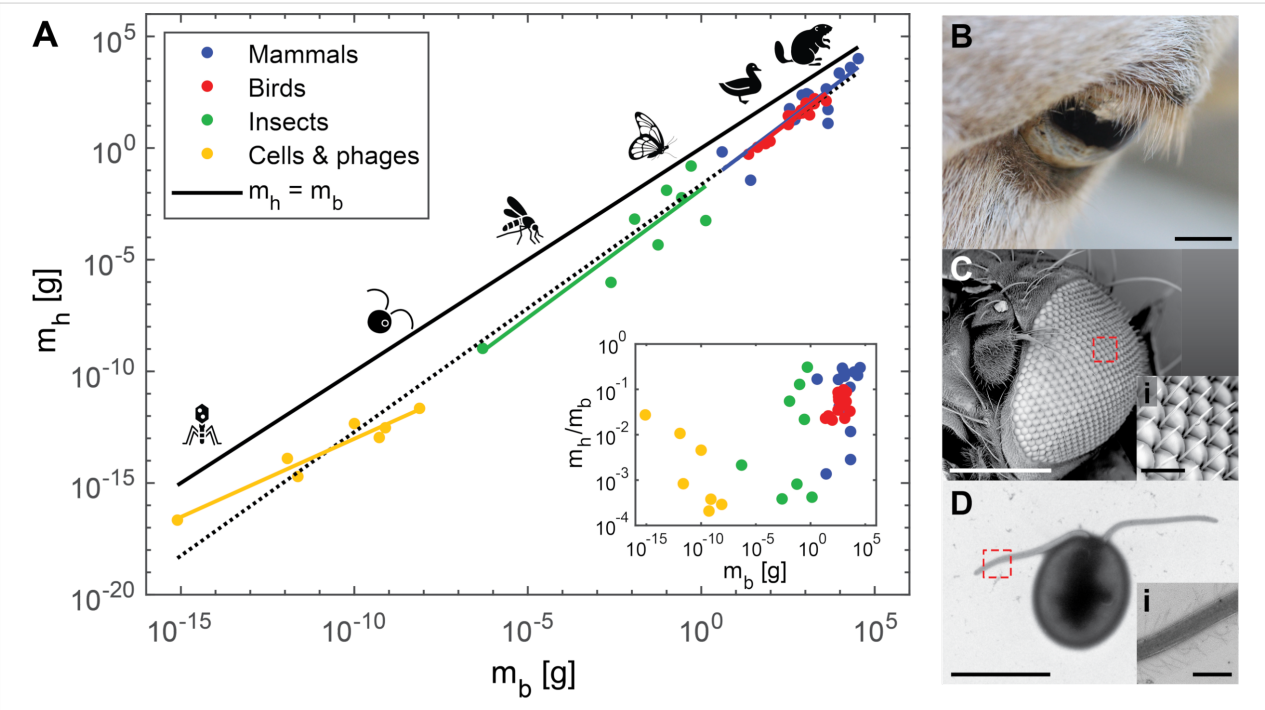

Figure 1: Scaling of hair across body size. (A) Scaling of hair mass m_h versus body mass m_b. The dots represent data with different colors referring to mammals (blue) [5], birds (red) [9,10], insects (green) [5], and cells and phages (yellow) [11-23]. The dashed black line represents the best power-law fit for all of the data: $m_h \sim m_b^{1.10}$ with R^2 = 0.98 and 95% confidence interval (CI): (1.07, 1.15). The solid black line represents equal masses: $m_h = m_b$. The solid lines with different colors represent the best power-law fits for the different groups: mammals (blue) $m_h \sim m_b^{1.17}$ with R^2 = 0.74 and CI: (0.74, 1.61), birds (red) $m_h \sim m_b^{1.20}$ with R^2 = 0.94 and CI: (1.06, 1.34), insects (green) $m_h \sim m_b^{1.15}$ with R^2 = 0.81 and CI: (0.60, 1.70), and cells and phages (yellow) $m_h \sim m_b^{0.70}$ with R^2 = 0.93 and CI: (0.48, 0.92). The inset shows a plot of the ratio of hair mass to body mass m_h/m_b as a function of body mass m_b. The ratio appears to increase with body mass following a Spearman rank test (ρ = 0.55, p = 3.35 × 10^{-5}). The silhouettes mentioned below are from Noun Project. They are distributed under the terms of the Creative Commons CC BY 3.0 License, https://creativecommons.org/licenses/by/3.0, and attributed to the following creators: Andre Buand (phage), ProSymbols (mosquito), Creative Stall (butterfly), Laymilk (duck), and Pham Thanh Loc (beaver). (B) The eye of a sheep. Scale bar represents 10 mm. (C) The eye of a fruit fly and (i) close-up of its ommatidia. Scale bars represent 200 µm and (i) 20 µm, respectively. (D) Green microalgae and (i) close-up of its flagellum with mastigonemes. Scale bars represent 10 µm and (i) 1 µm, respectively.

Figure 1A, the ratio of hair mass to body mass m_h/m_b is higher for larger organisms. A Spearman's rank test supports this observation, with ρ = 0.55, which corresponds to an increasing trend between m_h/m_b and m_b. Therefore, it seems that larger organisms dedicate more energy and resources to growing and maintaining hair. This finding motivates the following questions: (1) What are the purposes of hair? (2) How do these purposes vary with organism size?

For countless animal species, hairs are strategically placed throughout the body, varying in size and structure. Figure 1B–D show examples of various hairs found in mammals, insects, and micro-algae, respectively. Depending on their location and configuration, hairs serve a multitude of functions that can contribute to an organism's homeostasis. The diversity of their function is exemplified by hair's resistance to heat transfer in humans [4,24], and the role of hair in sensing mates by male mosquitoes [25]. Additionally, plants may exhibit hair-like fibrillar structures, such as the nanometer-thick mastigonemes on the flagella of microalgae [26] and the high-aspect-ratio, hair-like trichomes on plant surfaces [27]. Overall, to promote homeostasis in plants, animals, bacteria, and bacteriophages, fibrillar structures contribute to the following functions: protection (e.g., thermal insulation and defense), locomotion and feeding, and sensing. This review will present how biological hairs, or fibrillar structures, contribute to those functions across 20 orders of magnitude in organism mass and six orders of magnitude in hair thickness, from the nanometer-thick fibers on bacteriophages to the millimeter-thick hair and fur on mammals.

Review

Protection

Plants and animals often encounter potential danger in their surroundings. For example, extreme weather, such as precipitation and low temperatures, predators, and disease vectors. Because of their protruding, fibrillar structures serve as one of the first lines of defense against such dangers. They can protect against heat loss by providing insulation (Figure 2A), prevent the penetration of water through hierarchical superhydrophobicity (Figure 2B), or provide protection from predators or disease vectors through mechanical interactions (Figure 2C).

Thermoregulation

Regarding thermal regulation, mammals have evolved certain traits that differentiate them from other animals. In addition to regulating their temperatures by exploiting metabolic processes, mammals tend to be covered in dense coats of fur or hair. A key attribute of these fibrillar structures that promotes insulation is their air-filled center core [28].

Animal pelts and furs are still being utilized by humans as jackets and blankets in order to provide thermal insulation. The fur trade still rears 100 million animals annually, and millions of wild animals are caught in the U.S. every year for their fur [29]. While their continued use is ethically debatable, furs have presumably persisted because of their thermal insulation properties. In mammals, the thickness and packing density of hair arrays was found to coincide with the geometrical parameters that minimize convective heat loss, with the hair diameter d scaling as $d \sim m_b^{1/12}$ [5,24].

In aquatic mammals, hair morphology, including shape and packing density, differ from terrestrial mammals in order to maintain a trapped air layer within the arrays of hair when submerged in water [30]. Hairs of aquatic animals have been found to be flatter, shorter, and packed in higher densities. Additionally, mammals that also rely on blubber for insulation, such as sea lions and walruses, were found to have lower hair-

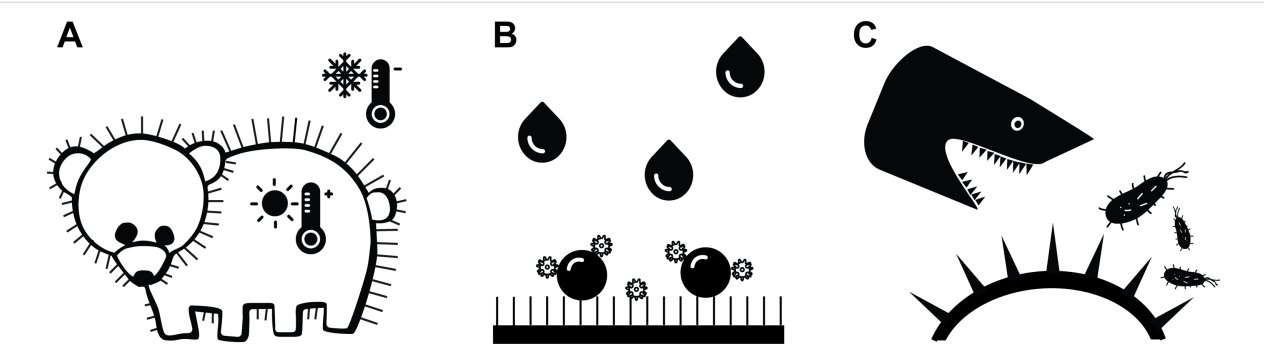

Figure 2: Protection through hairs. Schematics showing (A) an array of hairs providing thermal insulation, (B) a superhydrophobic hairy surface with self-cleaning properties, and (C) hairs defending from unwanted interactions with other organisms. The silhouettes mentioned below are from Noun Project. They are distributed under the terms of the Creative Commons CC BY 3.0 License, https://creativecommons.org/licenses/by/3.0, and attributed to the following creators: madness stock (hot and cold thermometers), Petra Prgomet (bear), Manish (falling water drops), Parallel Digital Studio (pollen grains), and twist.glyph (bacteria).

packing densities [30]. In extreme cases of reliance on blubber (e.g., in bowhead whales) instead of hair for insulation, arrays of hairs are limited to specialized regions where sensory information can be measured, for example, around the chin, lips, and blowhole [31].

While dense arrays of hair can trap a thermally insulating layer of air to protect the animal from cold temperatures, sparse arrays of hair can act like fins, which enhance heat exchange with the surroundings and help to cope with hot temperatures. When hair densities are low, such as in elephants, sparse hair arrays can help to shed heat [32]. The hair density of elephants is around 0.03–0.07 hairs per square centimeter, which is more than three orders of magnitude sparser than the typical hair density on human head (200−300 hairs per square centimeter) [32].

Hairs on humans have also been reported to protect the skin from UVA and UVB radiation from the sun [33]. UV radiation from the sun can not only heat up human skin but is also linked to skin cancers. Therefore, in mammals and birds, hairs provide protection from thermal effects, depending on their density, and from cancer-causing radiation. This demonstrates the multifunctionality of hairs, even within one species, such as humans.

When comparing fur and feathers, it has been found that feathers can outperform fur in protecting against solar radiation. In arid environments in Australia, the feathers of emus (*Dromaius novaehollandiae*) prevent nearly all solar radiation from reaching the bird's body, while the fur of red kangaroos (*Macropus rufus*) prevents 75–85% of the solar radiation from reaching the mammal's body [34]. It is thought that the deep coat of feathers protects from solar radiation, so the emus are able to reside in the open without needing to search for shade to cool down. In the ground hornbill (*Bucorvus leadbeateri*), lash-like feathers on the upper rim of their eyelids were found to provide shading from the sun to protect their corneas from intense sunlight [35].

At the scale of insects, setae may also contribute to thermoregulation. Bumblebees, which inhabit globally northern regions, possess dense arrays of setae on their thorax, while other species of bees inhabiting the tropics and hot deserts have very sparse arrays of setae [36]. Such a stark difference is associated with the colder temperatures that bumblebees have to contend with. However, there are trade-offs in possessing dense arrays of fibrillar structures, that is, they contribute to increased aerodynamic drag. Wasps, which are predators that need to outpace their prey during flight, do not possess such insulating arrays of setae [36].

Finally, when an organism is extremely small, such as single-celled organisms and bacteriophages, thermoregulation is limited. Theoretically, the largest temperature difference that a cell with a diameter of 10 μm and calorimetric heat generation of 100 pW can experience is only $\approx 10^{-5}$ °C [37]. Additionally, even if a cell of the same size was capable of maintaining a 10-μm-thick air layer (with thermal conductivity of 3×10^{-3} $W \cdot m^{-1} \cdot K^{-1}$) along its surface, following steady-state one-dimensional heat conduction, it could still only experience a temperature difference of $\approx 10^{-4}$ °C. Therefore, thermal insulation would have a negligible effect on thermoregulation at this scale. Instead, cells may be able to regulate their metabolic rates in response to changes in environmental temperatures [38].

Wettability

Superhydrophobic surfaces have the unique capability of preventing water from spreading; thus, they exhibit low wettability. In order to achieve superhydrophobicity, surfaces should have structural hierarchy and be composed of materials with low surface energy. The classic example of such a surface in nature is the lotus leaf [39], which possesses wax-covered microscopic pillars. The superhydrophobic surface is self-cleaning since water droplets bead up on the surface, and, when they roll off, they pick up any dirt or other particles and remove them from the leaf's surface. This phenomenon was termed the "Lotus effect" and has been translated to the development of a self-cleaning paint called Lotusan®.

Superhydrophic, fibrillar surfaces are also present in animals, such as insects, spiders, and geckos. Similar to plants, these structures help to maintain a clean body surface by enabling the rolling-off of water, which collects unwanted contaminants, or by providing low adhesion. Such structures are typically found on body parts where contamination is common, such as adhesive pads [40], or where cleanliness is crucial for survival, such as insect wings [41].

Hairs provide more ways to prevent or clean contamination. For a dedicated review on the topic, please see [5]. However, we will mention some of the cleaning functions of hairs here. Hairs around the eyes of mammals (eyelashes) and on the eyes of insects (interommatidial setae) have been found to minimize the deposition of particle-laden contaminants through aerodynamic interactions [42,43]. Hairs on honey bees have been found to facilitate both the collection and removal of pollen grains through the geometries of the hair arrays on their eyes and grooming appendages [44]. Mammalian fur effectively sheds contaminants because the hair deflects when exposed to a fluid flow. This deflection generates a shear flow that removes contaminants [45].

In addition to superhydrophobicity, in certain water plants, such as *Salvinia* spp., specialized structures have been observed to combine superhydrophobicity and superhydrophilicity [46]. In these plants, the fiber-like structures have hydrophilic tips, while the rest of the structure is hydrophobic. The combination of these different wetting properties enables the plants to maintain a stable layer of air while underwater. The hydrophilic tips pin the water surface so that it does not penetrate the fiber array and, thus, trap an air layer directly on the plant's surface.

While the combination of hydrophilic tips with superhydrophobic structures enables stable air film retention underwater, some animals exploit superhydrophobic surfaces for various functions on or under the water surface. For example, water striders (*Gerridae* spp.) possess superhydrophobic structures on their limbs, which help them locomote on the water surface [47]. Similarly, groups of ants form rafts to float on water and escape flooded regions [48]. This function relies on the wetting properties of their cuticle and its substructures. When underwater, spiders, such as the diving bell spider (*Argyroneta aquatica*), and insects, such as aquatic bugs and beetles, use hydrophobic hairs to trap air and form an air bubble that encompasses their body [49,50]. Insects, such as the green dock beetle (*Gastrophysa viridula*), trap air between the adhesive fibers on their footpads when walking underwater to generate adhesion [51].

Mechanical protection

While hairs provide protection via their thermal and chemical properties, they also offer protection based on their mechanical properties. Hairs are typically made of stiff materials, such as keratin and chitin, that have Young's moduli of the order of gigapascals, comparable to typical values for wood. Therefore, they can be quite robust to mechanical stimuli from external sources.

Mammals possess guard hairs, that are interspersed with the rest of their body hairs or furs. These hairs are distinctly thicker than the rest and have been reported to help provide protection to the rest of the mammal's coat from abrasion [52]. Guard hairs are also involved in mechano- and thermosensation [53,54]. In addition to guard hairs, some mammals have developed spines or quills to provide protection from predators [52]. These are typically thicker but still made of the protein complex keratin.

Plants also make use of fibrillar structures to provide defense against predators. These structures are known as trichomes and vary in morphology and density. While trichomes may also secrete chemicals to warn predators, they can impale insects and their larvae when they have a hooked morphology or even sting herbivores [55]. It has been observed that plants with higher densities of trichomes suffer less from insect herbivory. Also, there is a reduced incidence of internal egg laying by insects with ovipositors [55].

Locomotion and feeding

While hairs can help to protect organisms and to promote homeostasis, strategically placed arrays of hairs are crucial for locomotion through various mediums, such as granular soil, air, and water. By possessing hairs on appendages, organisms across wide length scales are capable of enhancing their locomotory performance. Examples are reversible adhesion in geckos (Figure 3A), anchoring in burrowing earthworms (Figure 3B), flying in bristled-wing insects, such as thrips, (Figure 3C), and swimming in unicellular microorganisms, such as microalgae (Figure 3D).

Climbing

Adhesive hairs have been observed on the foot and toe pads of insects, spiders, and geckos [56]. These hairs range in diameter from hundreds of nanometers in geckos, to micrometers in

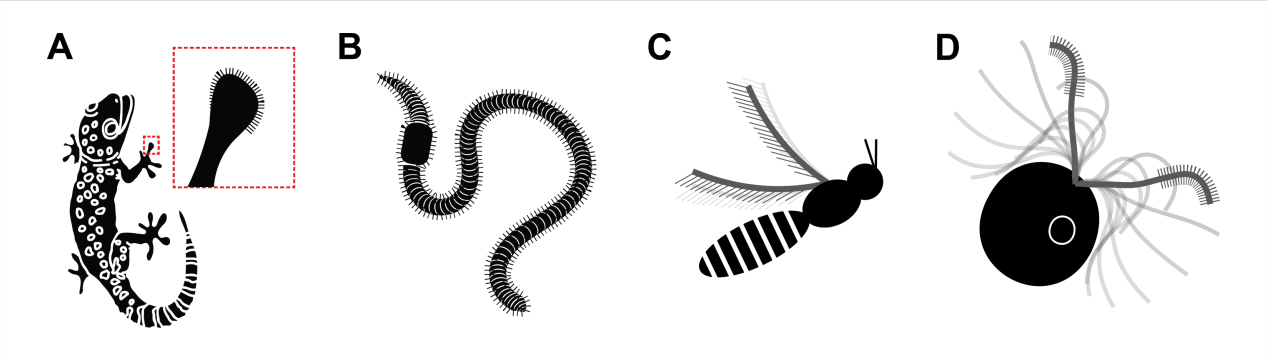

Figure 3: Locomotion enhanced by hairs. Schematics showing (A) an array of hairs (or setae and spatulae) on the toe pad of a climbing gecko, (B) hairs (or setae) on the body of a burrowing earthworm for anchoring when pushing through soil, (C) hairs (or bristles) on the wing of a thrip, instead of a thin membrane as in other flying insects, and (D) hairs (or mastigonemes) on the flagella of swimming microalgae. The silhouettes from (A, B) are from Noun Project. They are distributed under the terms of the Creative Commons CC BY 3.0 License, https://creativecommons.org/licenses/by/3.0, and attributed to the following creators: Hey Rabbit (gecko) and DracoVisions (earthworm).

spiders, to tens of micrometers in insects. The hairs are capable of generating adhesive forces through either capillary interactions, when an adhesive fluid is present [57], or intermolecular interactions, when no adhesive fluid is present [58]. In addition to adhesive forces that enable inverted climbing, the hairs can also generate friction forces whenever the animals climb on vertical surfaces [59].

For geckos, these adhesive hairs are referred to as setae, which branch into spatulae at the tips [60]. The branching ensures a high density of hairs to generate high adhesive forces [61]. With advances in fabrication techniques at the micrometer scale, gecko-inspired adhesive hairs have been developed, which are capable of generating adhesion without the use of glues or fluids [62,63].

For insects, the adhesive hairs are around one order of magnitude thicker than those of geckos, and they rely on fluid secreted by the hairs to generate adhesive forces. The hairs on insect footpads can vary in morphology, and these variations have been linked to their functions [57,59]. Green dock beetles (*G. viridula*) have been observed to possess three distinct types of adhesive hairs: discoidal, spatula-shaped, and sharp-tipped. The males possess adhesive hairs with discoidal tips, which are capable of generating large adhesive forces [57]. They are hypothesized to be used by males to attach securely to females when mating [59]. Both males and females possess adhesive hairs with spatula-shaped and sharp tips. The spatula-shaped tips enable reversibility of adhesion, while the sharp-tipped hairs are used for generating friction [59].

For microorganisms, while gravity is less of a concern, adhesive hairs are no less useful than for insects and larger animals. Microalgae, such as *Chlamydomonas reinhardtii* (10 μm in size), possess ≈100 nm long thin hairs on their flagella [11], which help them to attach to surfaces to glide or to attach with other cells to mate. Bacteria, such as *Pseudomonas aeruginosa* (2 μm in size), use thin filaments (up to several micrometers long), known as pilus (type IV), to attach to surfaces and, in effect, "tow" themselves around on the surface [64]. Bacteriophages (≈100 nm in size) rely on their tail filaments to attach to their hosts [21,22].

Burrowing

The use of hairs to generate frictional forces is not unique to animals that climb. Hair-like setae on the skin of earthworms aid in burrowing by increasing friction and providing anisotropic anchoring [65-67]. When burrowing, the earthworm mainly uses cavity expansion to create a burrow. It expands some segments of its body to anchor itself, while elongating other segments to push through the soil [68]. This kind of motion is called peristaltic motion since the coordination of expansion and elongation of segments resembles a wave traveling through the worm's body. It is similar to the motions exhibited by intestines during digestion [69]. The body expansion (increased cross-sectional size) and elongation are controlled by the worm's circular muscles. When the worm stiffens its circular muscles, the corresponding body segments expand and the setae are erected, helping the worm to anchor tighter to the surrounding soil. Meanwhile, when the circular muscles relax, the setae deflect and interact less with the soil. This anisotropic anchoring has been realized in a bio-inspired burrowing soft robot [70].

Flying

Flying organisms span about eight orders of magnitude in mass, ranging from the smallest known parasitoid wasp (*Dicopomorpha echmepterygis*, 2.5×10^{-8} kg) to the great bustard (*Otis tarda*, 21 kg). The fluid regimes experienced by these organisms vary greatly with scale, from a highly viscous, laminar environment at the smallest sizes to an inertial, turbulent environment at the largest sizes. Thus, the locomotory appendages of these organisms vary widely with size and the fluid regime they experience.

Structurally and developmentally, feathers are analogous to hair. Bird feathers, like hair, are complex structures made primarily of keratin. Despite approximately 200 million years of independent evolution, feathers and hair follicles share numerous structural similarities, including the presence of a dermal papilla and a dermal sheath [71]. However, unlike hair, feathers also have a dermal pulp, which is essential in growth and regeneration during feather cycling [72]. Much like the mammalian hair cycle [4], feathers are conveniently repaired during grooming and replaced seasonally during molt.

Feathers are highly structured and exhibit self-similarity. They are comprised of a central rachis, which gives rise to barbs. These barbs then branch into barbules, which, in turn, branch into smaller hook-like projections called barbicels. These barbicels cause the barbs to interlock, resulting in a continuous feather surface with relatively low air transmissivity [73]. Many birds have feathers that exhibit lobate cilia and hooked rami, which hook and loop together to prevent gaps between feathers [74].

Beyond forming the aerodynamic surfaces necessary for flight, feathers often exhibit species-specific adaptations. For example, owls have serrations on their leading-edge primary feathers, which are known to reduce noise during flight by mitigating flow instabilities [75,76]. Conversely, many birds use their feathers to produce sound through a variety of mecha-

nisms, including aeroelastic flutter and mechanical rubbing [77,78].

Around one third of birds, notably crepuscular and nocturnal species, such as nighthawks, have facial bristles that resemble mammalian whiskers [79]. These bristles are hypothesized to act as tactile sensors and may aid in prey handling, collision avoidance, foraging, or navigation, as well as provide eye protection [80,81].

Bats are the only mammals capable of powered flight. Their wing membrane is covered with short hairs, which act as tactile airflow sensors [82,83]. The hairs grow sparsely on the membrane of the wing and in fringes on the wing's leading edge. The neurons associated with these hairs can discriminate airflow directionality, and exhibit the highest firing rate when airflow is reversed, which is associated with slow flight and stall [84]. Indeed, when these hairs are removed, bats alter their flight performance by increasing speed and reducing their turning radius [85].

The membranous wings of insects are covered with bristle (or "hair") sensilla that act as airflow sensors [86,87]. In Odonata wings, bristle sensilla account for approximately 60% of all wing sensors [88]. In some cases, these bristle sensilla are highly tuned for specific airflow conditions. For example, tests on the silkworm moth (*Bombyx mori*) revealed that their bristle sensilla responded to vibrating air currents but not to constant flow [89]. It is hypothesized that the height of these bristles matches the height of the boundary layer, but further aerodynamic testing is necessary [88].

The smallest insects, such as beetles, thrips, and parasitoid wasps, possess wings made entirely of bristles [90-96]. The bristles (or setae) of these wings support flapping flight by reducing inertia, enhancing aerodynamic performance, and facilitating their deployment (i.e., folding and unfolding). The wing acts as a leaky paddle, and can produce 66–96% of the aerodynamic drag force of an equivalent membranous wing [94]. Conventionally, the competition between inertial and viscous forces is captured by the Reynolds number (Re), and a large Re indicates a dominant role of inertia. At Re ≈ 4–60, the effects of viscosity are significant, and inertial forces are relatively weak [97,98]. Consequently, traditional steady-state lift-based flight, as observed in larger organisms, is not possible. Thus, miniature insects use unsteady aerodynamics through a combination of wing flapping, wing clap-and-fling, and recapture of vortices to generate lift and thrust through the manipulation of air resistance (drag) [99]. In essence, the very smallest insects move by rowing through the air, generating drag much like a paddle. The bristles are also known to improve control of the boundary layer and delay stall via the generation of leading-edge vortices.

Swimming

For microorganisms, whose body sizes typically range from 10^{-7} to 10^{-4} m and who live predominantly in water, "inertia is totally irrelevant" [100]. While Re is around 10^5 for a flying eagle or a swimming whale, it is 10^{-3} to 10^{-5} for moving microbes. A thought experiment gives a straightforward illustration to such drastic distinction [101]. Imagine that an animal flying or swimming at high speed suddenly freezes the motion of its body parts (wings, fins, or flukes), how long would it continue to travel through the medium? While displacement for an eagle or a whale can continue for some time and distance, typically, an *Escherichia coli* bacterium (3 μm long, swimming at 10 $\mu m \cdot s^{-1}$) will stop immediately, that is, within 10^{-6} s and 10^{-10} m [100].

In this viscosity-dominated regime, because there is no inertia to depend on, microorganisms must constantly deform body parts in a non-time-reversible fashion to swim. Therefore, swimming efficiency depends on the order (or pattern) in which deformations take place. Three types of patterns are the most common: (1) rotation of a corkscrew-like tail found in archaea [102,103] and bacteria [15,104], (2) travelling waves along filaments (flagella) adopted by sperm cells and some algae [15], and (3) cyclic beating pattern consisting of a power stroke of large amplitude and a recovery stroke of small amplitude (similar to the arm movement during breaststroke swimming), which is adopted by microalgae [105] and ciliates [15].

In these locomotory patterns, microbial hairs are consistently involved in drag force generation. The flagella of archaea and bacteria are themselves passive hairs and are driven by protein motors at the base. Hair-like ultrastructures, or mastigonemes, on eukaryotic flagella/cilia comprise helical glycoproteins (≈10–20 nm thick) and lack a membrane [106]. They can be either stiff or flexible. Flagella with thick and stiff hairs (tubular mastigonemes) are sometimes referred to as the "tinsel" type [12,107]. These stiff hairs help to increase the effective surface area of flagella and, thus, enhance swimming speed [15]. Moreover, the stiff hairs help to reverse the resultant swimming direction when travelling waves patterns are employed [108]. For example, the smooth flagellum of sperm [109] and the tinsel-like flagellum of golden algae *Ochromonas*[12] beat in the same pattern, featuring waves travelling away from the cell body. In *Ochromonas*, this results in a swimming direction towards the waves' travelling direction, while sperm cells swim towards the opposite direction. This modulation effect has already inspired designs of swimming microrobots [110].

The role of thin and flexible hairs (fibrous mastigonemes) is still, to some extent, enigmatic. These soft hairs may appear in a range of number densities, from ca. 1 per micrometer of length of flagellum in *Phytophthora*[107] and *Ochromonas*[12], over ca. 10 per micrometer in the green algae *C. reinhardtii*[26], to 10^2–10^3 per micrometer in *Euglena*[111]. At least for the hair density found in *C. reinhardtii*, they do not help the cell to swim faster [26]. Nevertheless, without these hairs, swimming in *C. reinhardtii* is interrupted by frequent and sudden turns [26]. A possible explanation for this is that the fibrous hairs are involved in sensory functions, which may be crucial for stable, controlled swimming [112].

Microbial hairs commonly serve multiple roles at the same time. Hence, one should avoid understanding these hairs' existence from a single, locomotory perspective. While the flagella of *E. coli* is most obviously an apparatus for swimming motility, it can also help the cell to attach to a surface and act as a sensor thereafter [113]. Intriguingly, even after attachment, having motile flagella still matters for the cell as it appears to enable sensing of substrate stiffness [114]. In addition to flagella, other hairs of E. coli include the type-I pili (frimbriae) and type-IV pili [113]. Collaboration between these hairs also helps the cell. When pproaching a solid surface, the cells become trapped as they move in circular orbits because of hydrodynamic effects [101,104]. While staying close to the surface may be beneficial as it facilitates surface attachment and, hence, the formation of bacterial biofilms, remaining in circular trajectories hinders the cell's ability to explore the surface thoroughly. Thus, possibly with the help of the other hairs, *E. coli* near the surface can transiently attach to the surface to break the circular trajectories, thus, pushing their exploration efficiency close to the theoretical optimum [115].

Developing tools with one-dimensional structures is arguably the most basic and economical (materials-wise) solution for microorganisms. In this light, the "hairs" are their available tools, where most tools happen to look alike. This is the primary reason why microbial hairs defy easy classifications. Future research linking form and function in microbial hairs may lead to a better understanding of their evolution, as well as providing inspiration for the development of functional fibrillar structures at the micrometer and nanometer scales.

Filter feeding

Locomotion is key for searching for food, and hairs may also serve crucial roles in feeding, particularly via filtering. Filter feeding uses a porous material to capture prey and nutrients in fluid flows. Dense arrays of hairs may serve as the porous material that captures the food, separating it from the surrounding flow or from other unwanted objects. The capturing can occur via sieving, where food larger than the gaps between the fibers gets trapped, or through hydrodynamic interactions that transport food to the fiber surface, where it can stick and become trapped [116].

At the largest scales, baleen whales (Mysticeti) use keratinous fibers, or baleen, in their mouths instead of teeth to filter and capture prey [117-119]. When feeding, the whales use three different strategies, depending on their species. Bowhead and right whales (Balaenidae) use ram filter feeding where they continuously swim through groups of prey with their baleen exposed, collecting prey while the filtered water exits through an opening in the posterior of their mouths. Rorqual whales (Balaenopteridae) use lunge feeding where they swallow mouthfuls of prey and water and then push the seawater out through their bristled baleen in order to isolate the prey for swallowing. Grey whales (*Eschrichtius robustus*) use suction filter feeding [119].

At the smaller scales, aquatic insects of the orders Ephemeroptera, Trichopteram, and Diptera use filter feeding to consume organic matter from their aqueous environment [120]. The fibrillar filters used by insects include setae, mouth brushes, and fans. The setae are present around the mouthparts or forelimbs and may be lined with arrays of smaller fibers, called microtrichia. The mouth brushes are dense arrays of fibers present on the lower jaw, or labrum. Fans are arrays of fibers that can be opened (splayed) and closed. The captured organic matter in the fans is consumed by sweeping the mandibles over the closed fans [120].

Choanoflagellates are unicellular organisms that use filter feeding. They drive fluid flow through a conical filter consisting of microvilli with diameters of 100–200 nm, spaced 200–700 nm apart [121,122]. While the microvilli contain actin and myosin, which together enable motility during escapes and help to transport trapped organic matter for consumption [123], they function passively when filtering organic matter. The structure driving the fluid flow through the filter remains elusive. A flagella alone does not seem to provide enough flow to explain the experimentally observed filtering rates. However, it has been proposed that a flagellar vane, which behaves like an undulating wall, could induce enough flow through the conical filter [122].

Sensing

Perceiving the environment using sensory organs in order to respond to stimuli is vital for survival in animals [124]. Hairy receptors are a type of sensing organ that exists widely across nature. They are systematically distributed throughout the surface of the bodies of organisms and play an important role in

reacting to external stimuli in order to perceive the environment, such as external touch (Figure 4A), odor (Figure 4B), temperature (Figure 4C), and humidity [125-127]. Hairy receptors can be classified into several types according to their various functions and sensing modes, such as mechanoreceptors, chemoreceptors, thermoreceptors, and hygroreceptors. While there are different types of hairy receptors, depending on their location and type of stimulus they sense, they all generate electrical signals through their sensory cells and transmit the signals to the nervous system in order to paint a picture of the outside world or determine body or appendage orientation [128].

Mechanosensation

Hairs, as mechanical receptors, are capable of perceiving and distinguishing a multitude of external stimuli such as touch, vibration, or fluid flows [129,130]. The mechanosensation of hairs relies on the sensory cells at their base. When the hair is deflected by mechanical forces, the membrane potential of the sensory cells is altered, and an electrical signal is sent to the nervous system. By receiving, analyzing, and finally reacting to the signal, the organism is able to respond to changes in the surroundings [131].

Mechanical perception via hair is important for living organisms across length scales and evolutionary backgrounds. Cats, for instance, can sense the position, shape, and texture of objects by moving their whiskers, and can even use whiskers to sense the direction and speed of air flow to help them move in the dark or catch prey [132]. A review of hairy sensation in mammals can be found here [133]. Spider appendages [134], cockroach antennae [135], and cricket cerci [136] possess hairs capable of detecting delicate vibrations, airflow, and interactions with various objects, enabling them to locate their prey, evade obstacles, or detect potential dangers [130,137]. Airflow sensors with bio-inspired, fibrillar structures based on the working principles of cricket cerci, which, when clustered in arrays, aid in detection of oscillating flows following “viscous coupling” [138], have been developed [139].

At the microscopic scale, microalgae, such as *C. reinhardtii*, may utilize the hair-like ultrastructures, or mastigonemes, on their flagella to sense fluid flow while swimming [26]. The mastigonemes have been observed to be anchored to a channel protein that shows ion conductivity, and the mastigoneme–channel protein complex may provide mechanical gating to sense deflections of the mastigonemes caused by fluid flow [112]. Additionally, for bacteria, *E. coli*, their passive flagella have been linked to sensing the material stiffness of surfaces they attach to [114].

Clusters of hairs, or hair plates, on the limbs of insects are used for proprioreception or to sense the orientation and motion of the limbs, which helps in their control of locomotion [131]. Furthermore, many insects, such as bees, can enhance their foraging speed by utilizing hairy mechanical receptors to detect physical characteristics such as food viscosity and texture [140,141]. Mechanosensing with hairs, regardless of stimulus, relies on deflections of the hairs triggering deformations to the sensory cells they are attached to.

Chemoreception

In addition to touch, hairs are able to sense their less-immediate environment by detecting the presence and alteration of chemicals [142], which differs from the way hairs sense touch and vibration. The binding of receptor proteins on sensory cells to chemicals in the air or solution initiates a sequence of biochemical reactions, resulting in the production of electrical signals,

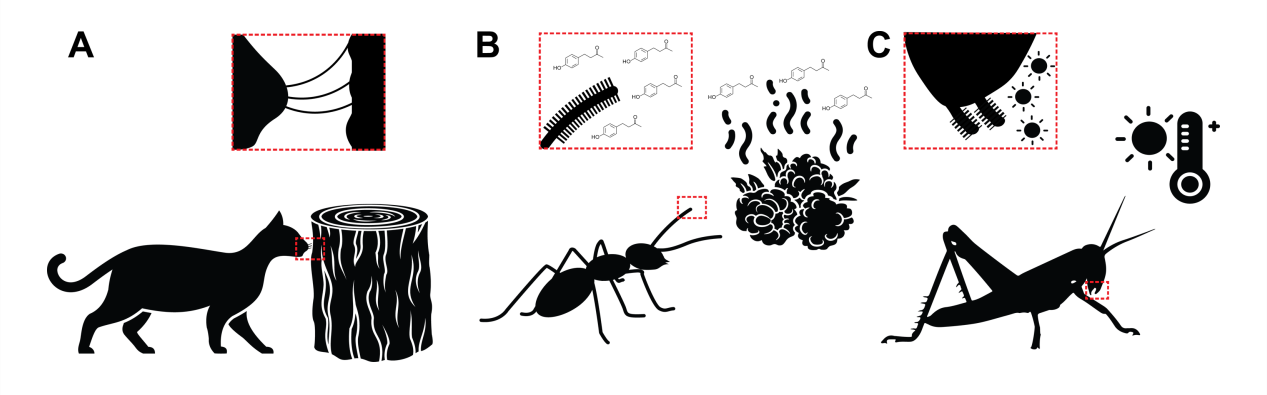

Figure 4: Sensing via hairs. Schematics showing (A) whiskers on cats sensing objects through mechanical interactions, (B) hairs on the antennae of ants detecting the odor of molecules, and (C) hairs on the labial palps of cave-dwelling crickets sensing temperature. The silhouettes mentioned below are from Noun Project. They are distributed under the terms of the Creative Commons CC BY 3.0 License, https://creativecommons.org/licenses/by/3.0, and attributed to the following creators: Hafid Firman Syarif (cat), Fardan (tree trunk), Jacob Eckert (ant), Hey Rabbit (raspberries), bsd studio (odor lines), Ed Harrison (cricket), and madness stock (hot thermometer).

which are then transmitted to the nervous system. The brain interprets these electrical signals as a specific scent or flavor after they are processed by the nervous system [143].

Arthropods, including spiders [144], ants [145], and bees [146], possess chemical receptors on their limbs and antennae that detect chemicals in their surroundings, enabling them to locate sustenance, recognize their species, and avoid danger [147]. Moth antennae possess dense arrays of hairs, which have been found to interact with surrounding airflow in order to enhance diffusion of chemicals to the antennae for detection [148]. Based on this knowledge, bio-inspired, fibrillar chemical sensors have been developed [149,150]. Furthermore, insects can utilize hairs to sense atmospheric carbon dioxide [151,152]. The human scalp follicles also possess an olfactory perception and can even stimulate hair growth upon exposure to a specific fragrance [153].

Thermosensation

Hair can also act as a temperature sensor, helping organisms to choose the right temperature environment to keep their body thermally stable. The receptors typically have a short hair that protrudes through a small hole to interface with the environment, also known as a peg-in-pit sensillum [154]. The protruding hair-like receptors help to absorb thermal radiation, since the penetration depth of infrared radiation into insect cuticle is quite shallow [155]. Additionally, the hair-like sensillum possesses electron-dense filaments that may improve absorption [154]. Leaf-cutting ants (*Atta vollenweideri*), for instance, can utilize the temperature receptors of their appendages to detect intense heat outside their nests as indicators of where to locate food [156]. Cave-dwelling crickets (*Tachycines plumiopedella*) rely on thermosensation to detect temperature gradients and locate appropriate habitats in the environment, utilizing hair receptors on their labial palps [157]. In plants such as the Venus flytrap (*Dionaea muscipula*), heat was observed to trigger closure of their trap [158]. At the base of their trigger hairs, there are sensory cells that may be triggered by either mechanical or thermal energy [158].

Hygrosensation

Studies have also shown that hairs exhibit heightened sensitivity to changes in humidity levels, enabling arthropods to discern variations in air humidity with remarkable precision. There are three potential mechanisms for hygrosensation with hairs or sensilla: (1) Changes in humidity may cause changes in the volume of the sensilla, which could mechanically trigger sensory cells. (2) For hollow sensilla, the external humidity could cause lymph fluid to evaporate, and the change in fluid volume may trigger sensory cells. (3) Changes in humidity could cause changes in temperature of the sensilla and trigger thermoresponsive sensory cells [159]. These sensilla are distributed across the body, including antennae, legs, and other appendages. Insects such as locusts [160] and beetles [161] utilize hygroreceptors on their antennae to detect humidity fluctuations in their environment. Similarly, arachnids such as the harvestman (*Heteromitobates discolor*) also possess hygroreceptive sensilla on their legs [162].

Funding

GJA acknowledges funding from Netherlands Organization for Scientific Research (NWO) Vidi Grant (project number VI.Vidi.213.122). BKvO acknowledges funding from the Wageningen Graduate School (WGS) Postdoctoral Talent Programme. DW acknowledges funding from the National Natural Science Foundation of China (No. 12204525).

Author Contributions

Guillermo J. Amador: conceptualization; data curation; formal analysis; funding acquisition; project administration; visualization; writing – original draft; writing – review & editing. Brett Klaassen van Oorschot: data curation; formal analysis; funding acquisition; writing – original draft; writing – review & editing. Caiying Liao: writing – original draft; writing – review & editing. Jianing Wu: writing – original draft; writing – review & editing. Da Wei: data curation; formal analysis; visualization; writing – original draft; writing – review & editing.

ORCID® iDs

Guillermo J. Amador - https://orcid.org/0000-0003-3594-125X
Brett Klaassen van Oorschot - https://orcid.org/0000-0003-4347-5391
Da Wei - https://orcid.org/0000-0002-6226-0639

Data Availability Statement

Data sharing is not applicable as no new data was generated or analyzed in this study.

References

1. Shoulders, M. D.; Raines, R. T. *Annu. Rev. Biochem.* **2009,** *78,* 929–958. doi:10.1146/annurev.biochem.77.032207.120833
2. Hepler, P. K.; Palevitz, B. A. *Annu. Rev. Plant Physiol.* **1974,** *25,* 309–362. doi:10.1146/annurev.pp.25.060174.001521
3. Jin, H.-J.; Kaplan, D. L. *Nature* **2003,** *424,* 1057–1061. doi:10.1038/nature01809
4. Krause, K.; Foitzik, K. *Semin. Cutaneous Med. Surg.* **2006,** *25,* 2–10. doi:10.1016/j.sder.2006.01.002
5. Amador, G. J.; Hu, D. L. *J. Exp. Biol.* **2015,** *218,* 3164–3174. doi:10.1242/jeb.103937
6. West, G. *Scale: The Universal Laws of Life, Growth, and Death in Organisms, Cities, and Companies;* Penguin: New York, NY, USA, 2018.
7. McMahon, T. A.; Bonner, J. T. B. *On Size and Life;* Scientific American Library: New York, NY, USA, 1983.

8. Labonte, D.; Clemente, C. J.; Dittrich, A.; Kuo, C.-Y.; Crosby, A. J.; Irschick, D. J.; Federle, W. *Proc. Natl. Acad. Sci. U. S. A.* **2016,** *113,* 1297–1302. doi:10.1073/pnas.1519459113
9. Seamans, T. W.; Hamershock, D. W.; Bernhardt, G. E. *Ibis* **1995,** *137,* 424–428. doi:10.1111/j.1474-919x.1995.tb08046.x
10. Hopps, E. C. *Trans. Ill. State Acad. Sci.* **2002,** *95,* 229–237.
11. Goodenough, U. W.; Adair, W. S.; Collin-Osdoby, P.; Heuser, J. E. *J. Cell Biol.* **1985,** *101,* 924–941. doi:10.1083/jcb.101.3.924
12. Bouck, G. B. *J. Cell Biol.* **1971,** *50,* 362–384. doi:10.1083/jcb.50.2.362
13. Andersen, R. A.; Graf, L.; Malakhov, Y.; Yoon, H. S. *Phycologia* **2017,** *56,* 591–604. doi:10.2216/17-15.1
14. Markey, D. R.; Bouck, G. B. *J. Ultrastruct. Res.* **1977,** *59,* 173–177. doi:10.1016/s0022-5320(77)80077-4
15. Brennen, C.; Winet, H. *Annu. Rev. Fluid Mech.* **1977,** *9,* 339–398. doi:10.1146/annurev.fl.09.010177.002011
16. Podwin, A.; Kubicki, W.; Dziuban, J. A. *Biomed. Microdevices* **2017,** *19,* 63. doi:10.1007/s10544-017-0205-0
17. Helmuth, R.; Achtman, M. *Proc. Natl. Acad. Sci. U. S. A.* **1978,** *75,* 1237–1241. doi:10.1073/pnas.75.3.1237
18. Spaulding, C. N.; Schreiber, H. L., IV; Zheng, W.; Dodson, K. W.; Hazen, J. E.; Conover, M. S.; Wang, F.; Svenmarker, P.; Luna-Rico, A.; Francetic, O.; Andersson, M.; Hultgren, S.; Egelman, E. H. *eLife* **2018,** *7,* e31662. doi:10.7554/elife.31662
19. Chen, M.; Zhao, Z.; Yang, J.; Peng, K.; Baker, M. A.; Bai, F.; Lo, C.-J. *eLife* **2017,** *6,* e22140. doi:10.7554/elife.22140
20. Koo, J.; Lamers, R. P.; Rubinstein, J. L.; Burrows, L. L.; Howell, P. L. *Structure* **2016,** *24,* 1778–1787. doi:10.1016/j.str.2016.08.007
21. Leiman, P. G.; Arisaka, F.; van Raaij, M. J.; Kostyuchenko, V. A.; Aksyuk, A. A.; Kanamaru, S.; Rossmann, M. G. *Virol. J.* **2010,** *7,* 355. doi:10.1186/1743-422x-7-355
22. Leiman, P. G.; Chipman, P. R.; Kostyuchenko, V. A.; Mesyanzhinov, V. V.; Rossmann, M. G. *Cell* **2004,** *118,* 419–429. doi:10.1016/j.cell.2004.07.022
23. Taslem Mourosi, J.; Awe, A.; Guo, W.; Batra, H.; Ganesh, H.; Wu, X.; Zhu, J. *Int. J. Mol. Sci.* **2022,** *23,* 12146. doi:10.3390/ijms232012146
24. Bejan, A. *J. Heat Transfer* **1990,** *112,* 662–667. doi:10.1115/1.2910438
25. Nijhout, H. F.; Sheffield, H. G. *Science* **1979,** *206,* 595–596. doi:10.1126/science.40308
26. Amador, G. J.; Wei, D.; Tam, D.; Aubin-Tam, M.-E. *Biophys. J.* **2020,** *118,* 2914–2925. doi:10.1016/j.bpj.2020.05.003
27. Koch, K.; Bhushan, B.; Barthlott, W. *Soft Matter* **2008,** *4,* 1943–1963. doi:10.1039/b804854a
28. Fish, F. E.; Smelstoys, J.; Baudinette, R. V.; Reynolds, P. S. *Aquat. Mamm.* **2002,** *28,* 103–112.
29. Hughes, A. C. *Curr. Biol.* **2021,** *31,* R1218–R1224. doi:10.1016/j.cub.2021.08.056
30. Liwanag, H. E.; Berta, A.; Costa, D. P.; Abney, M.; Williams, T. M. *Biol. J. Linn. Soc.* **2012,** *106,* 926–939. doi:10.1111/j.1095-8312.2012.01900.x
31. Drake, S. E.; Crish, S. D.; George, J. C.; Stimmelmayr, R.; Thewissen, J. G. M. *Anat. Rec.* **2015,** *298,* 1327–1335. doi:10.1002/ar.23163
32. Myhrvold, C. L.; Stone, H. A.; Bou-Zeid, E. *PLoS One* **2012,** *7,* e47018. doi:10.1371/journal.pone.0047018
33. de Gálvez, M. V.; Aguilera, J.; Bernabó, J.-L.; Sánchez-Roldán, C.; Herrera-Ceballos, E. *Photochem. Photobiol.* **2015,** *91,* 966–970. doi:10.1111/php.12433
34. Dawson, T. J.; Maloney, S. K. *Aust. Mammal.* **2004,** *26,* 145–151. doi:10.1071/am04145
35. Martin, G. R.; Coetzee, H. C. *Ibis* **2004,** *146,* 18–26. doi:10.1111/j.1474-919x.2004.00211.x
36. Heinrich, B. Thermoregulation. In *Encyclopedia of Insects;* Resh, V. H.; Cardé, R. T., Eds.; Academic Press: Burlington, MA, USA, 2009; pp 993–999. doi:10.1016/b978-0-12-374144-8.00262-9
37. Baffou, G.; Rigneault, H.; Marguet, D.; Jullien, L. *Nat. Methods* **2014,** *11,* 899–901. doi:10.1038/nmeth.3073
38. Song, P.; Gao, H.; Gao, Z.; Liu, J.; Zhang, R.; Kang, B.; Xu, J.-J.; Chen, H.-Y. *Chem* **2021,** *7,* 1569–1587. doi:10.1016/j.chempr.2021.02.027
39. Barthlott, W.; Neinhuis, C. *Planta* **1997,** *202,* 1–8. doi:10.1007/s004250050096
40. Hansen, W. R.; Autumn, K. *Proc. Natl. Acad. Sci. U. S. A.* **2005,** *102,* 385–389. doi:10.1073/pnas.0408304102
41. Watson, G. S.; Green, D. W.; Cribb, B. W.; Brown, C. L.; Meritt, C. R.; Tobin, M. J.; Vongsvivut, J.; Sun, M.; Liang, A.-P.; Watson, J. A. *ACS Appl. Mater. Interfaces* **2017,** *9,* 24381–24392. doi:10.1021/acsami.7b08368
42. Amador, G. J.; Mao, W.; DeMercurio, P.; Montero, C.; Clewis, J.; Alexeev, A.; Hu, D. L. *J. R. Soc., Interface* **2015,** *12,* 20141294. doi:10.1098/rsif.2014.1294
43. Amador, G. J.; Durand, F.; Mao, W.; Pusulri, S.; Takahashi, H.; Nguyen, V.-T.; Shimoyama, I.; Alexeev, A.; Hu, D. L. *Eur. Phys. J.: Spec. Top.* **2015,** *224,* 3361–3377. doi:10.1140/epjst/e2015-50094-x
44. Amador, G. J.; Matherne, M.; Waller, D.; Mathews, M.; Gorb, S. N.; Hu, D. L. *Bioinspiration Biomimetics* **2017,** *12,* 026015. doi:10.1088/1748-3190/aa5c6e
45. Krsmanovic, M.; Ghosh, R.; Dickerson, A. K. *J. R. Soc., Interface* **2023,** *20,* 20230485. doi:10.1098/rsif.2023.0485
46. Barthlott, W.; Schimmel, T.; Wiersch, S.; Koch, K.; Brede, M.; Barczewski, M.; Walheim, S.; Weis, A.; Kaltenmaier, A.; Leder, A.; Bohn, H. F. *Adv. Mater. (Weinheim, Ger.)* **2010,** *22,* 2325–2328. doi:10.1002/adma.200904411
47. Bush, J. W. M.; Hu, D. L.; Prakash, M. *Adv. Insect Physiol.* **2007,** *34,* 117–192. doi:10.1016/s0065-2806(07)34003-4
48. Mlot, N. J.; Tovey, C. A.; Hu, D. L. *Proc. Natl. Acad. Sci. U. S. A.* **2011,** *108,* 7669–7673. doi:10.1073/pnas.1016658108
49. Woermann, D. *Belg. J. Zool.* **2010,** *140,* 246–248. doi:10.26496/bjz.2010.177
50. Crisp, D. J.; Thorpe, W. H. *Discuss. Faraday Soc.* **1948,** *3,* 210–220. doi:10.1039/df9480300210
51. Hosoda, N.; Gorb, S. N. *Proc. R. Soc. B* **2012,** *279,* 4236–4242. doi:10.1098/rspb.2012.1297
52. Jones, J. K.; Wilson, D. E.; Armstrong, D. M. Mammal. *Encyclopedia Britannica;* Britannica, Inc.: Chicago, IL, USA, 2023.
53. Straile, W. E. *Nature* **1958,** *181,* 1604–1605. doi:10.1038/1811604a0
54. Baker, I. M. *R. Soc. Open Sci.* **2021,** *8,* 210740. doi:10.1098/rsos.210740
55. Levin, D. A. *Q. Rev. Biol.* **1973,** *48,* 3–15. doi:10.1086/407484
56. Federle, W. *J. Exp. Biol.* **2006,** *209,* 2611–2621. doi:10.1242/jeb.02323
57. Gernay, S.; Federle, W.; Lambert, P.; Gilet, T. *J. R. Soc., Interface* **2016,** *13,* 20160371. doi:10.1098/rsif.2016.0371
58. Autumn, K.; Sitti, M.; Liang, Y. A.; Peattie, A. M.; Hansen, W. R.; Sponberg, S.; Kenny, T. W.; Fearing, R.; Israelachvili, J. N.; Full, R. J. *Proc. Natl. Acad. Sci. U. S. A.* **2002,** *99,* 12252–12256. doi:10.1073/pnas.192252799
59. Bullock, J. M. R.; Federle, W. *J. Exp. Biol.* **2009,** *212,* 1876–1888. doi:10.1242/jeb.030551

60. Autumn, K.; Liang, Y. A.; Hsieh, S. T.; Zesch, W.; Chan, W. P.; Kenny, T. W.; Fearing, R.; Full, R. J. *Nature* **2000,** *405,* 681–685. doi:10.1038/35015073
61. Shah, G. J.; Sitti, M. Modeling and design of biomimetic adhesives inspired by gecko foot-hairs. In *2004 IEEE International Conference on Robotics and Biomimetics,* IEEE, 2004; pp 873–878. doi:10.1109/robio.2004.1521899
62. Geim, A. K.; Dubonos, S. V.; Grigorieva, I. V.; Novoselov, K. S.; Zhukov, A. A.; Shapoval, S. Y. *Nat. Mater.* **2003,** *2,* 461–463. doi:10.1038/nmat917
63. Kamperman, M.; Kroner, E.; del Campo, A.; McMeeking, R. M.; Arzt, E. *Adv. Eng. Mater.* **2010,** *12,* 335–348. doi:10.1002/adem.201000104
64. Talà, L.; Fineberg, A.; Kukura, P.; Persat, A. *Nat. Microbiol.* **2019,** *4,* 774–780. doi:10.1038/s41564-019-0378-9
65. Griffith, H.; Telford, M. *Biol. Bull. (Chicago, IL, U. S.)* **1985,** *168,* 296–311. doi:10.2307/1541242
66. Jumars, P. A.; Dorgan, K. M.; Mayer, L. M.; Boudreau, B. P.; Johnson, B. D. Material constraints on infaunal lifestyles: may the persistent and strong forces be with you. *Trace Fossils;* Elsevier: Amsterdam, Netherlands, 2007; pp 442–457. doi:10.1016/b978-044452949-7/50152-2
67. Asawalertsak, N.; Heims, F.; Kovalev, A.; Gorb, S. N.; Jørgensen, J.; Manoonpong, P. *Soft Rob.* **2023,** *10,* 545–555. doi:10.1089/soro.2022.0004
68. Edwards, C. A.; Arancon, N. Q. Earthworms, soil structure, fertility, and productivity. *Biology and Ecology of Earthworms;* Springer: New York, NY, USA, 2022; pp 303–334. doi:10.1007/978-0-387-74943-3_10
69. Edwards, C. A.; Lofty, J. R. *Biology of Earthworms;* Chapman and Hall: New York, NY, USA, 1977. doi:10.1007/978-1-4613-3382-1
70. Tirado, J.; Jørgensen, J.; Rafsanjani, A. Earthworm-inspired multimodal soft actuators. In *2023 IEEE International Conference on Soft Robotics (RoboSoft),* IEEE, 2023; pp 1–6. doi:10.1109/robosoft55895.2023.10122032
71. Yu, M.; Yue, Z.; Wu, P.; Wu, D.-Y.; Mayer, J.-A.; Medina, M.; Widelitz, R. B.; Jiang, T.-X.; Chuong, C.-M. *Int. J. Dev. Biol.* **2004,** *48,* 181–191. doi:10.1387/ijdb.15272383
72. Wu, P.; Jiang, T.-X.; Lei, M.; Chen, C.-K.; Hsieh Li, S.-M.; Widelitz, R. B.; Chuong, C.-M. *Development* **2021,** *148,* dev198671. doi:10.1242/dev.198671
73. Müller, W.; Patone, G. *J. Exp. Biol.* **1998,** *201,* 2591–2599. doi:10.1242/jeb.201.18.2591
74. Matloff, L. Y.; Chang, E.; Feo, T. J.; Jeffries, L.; Stowers, A. K.; Thomson, C.; Lentink, D. *Science* **2020,** *367,* 293–297. doi:10.1126/science.aaz3358
75. Rao, C.; Ikeda, T.; Nakata, T.; Liu, H. *Bioinspiration Biomimetics* **2017,** *12,* 046008. doi:10.1088/1748-3190/aa7013
76. Le Piane, K.; Clark, C. J. *Biol. J. Linn. Soc.* **2022,** *135,* 84–97. doi:10.1093/biolinnean/blab138
77. Niese, R. L.; Clark, C. J.; Tobalske, B. W. *Integr. Comp. Biol.* **2020,** *60,* 1160–1172. doi:10.1093/icb/icaa051
78. Clark, C. J. *Integr. Comp. Biol.* **2021,** *61,* 696–709. doi:10.1093/icb/icab008
79. Delaunay, M. G.; Brassey, C.; Larsen, C.; Lloyd, H.; Grant, R. A. *Sci. Rep.* **2022,** *12,* 21108. doi:10.1038/s41598-022-24781-7
80. Cunningham, S. J.; Alley, M. R.; Castro, I. *J. Morphol.* **2011,** *272,* 118–128. doi:10.1002/jmor.10908
81. Delaunay, M. G.; Larsen, C.; Lloyd, H.; Sullivan, M.; Grant, R. A. *J. Anat.* **2020,** *237,* 355–366. doi:10.1111/joa.13188
82. Sterbing, S. J.; Moss, C. F. *J. Mammal.* **2018,** *99,* 124–130. doi:10.1093/jmammal/gyx146
83. Rummel, A. D.; Sierra, M. M.; Quinn, B. L.; Swartz, S. M. *Anat. Rec.* **2023,** *306,* 2681–2692. doi:10.1002/ar.25176
84. Sterbing-D'Angelo, S. J.; Chadha, M.; Marshall, K. L.; Moss, C. F. *J. Neurophysiol.* **2017,** *117,* 705–712. doi:10.1152/jn.00261.2016
85. Sterbing-D'Angelo, S.; Chadha, M.; Chiu, C.; Falk, B.; Xian, W.; Barcelo, J.; Zook, J. M.; Moss, C. F. *Proc. Natl. Acad. Sci. U. S. A.* **2011,** *108,* 11291–11296. doi:10.1073/pnas.1018740108
86. Dickinson, M. H.; Hannaford, S.; Palka, J. *Brain, Behav. Evol.* **1997,** *50,* 13–24. doi:10.1159/000113318
87. Page, K. L.; Matheson, T. *J. Exp. Biol.* **2004,** *207,* 2691–2703. doi:10.1242/jeb.01096
88. Fabian, J.; Siwanowicz, I.; Uhrhan, M.; Maeda, M.; Bomphrey, R. J.; Lin, H.-T. *iScience* **2022,** *25,* 104150. doi:10.1016/j.isci.2022.104150
89. Ai, H.; Yoshida, A.; Yokohari, F. *J. Insect Physiol.* **2010,** *56,* 236–246. doi:10.1016/j.jinsphys.2009.10.007
90. Vogel, S. *Life in Moving Fluids: The Physical Biology of Flow,* 2nd ed.; Princeton University Press: Princeton, NJ, USA, 1994. doi:10.1515/9780691212975
91. Thompson, D. W.; Bonner, J. *On Growth and Form;Canto classics;* Cambridge University Press: Cambridge, UK, 1961.
92. Ellington, C. P. *J. Exp. Biol.* **1980,** *85,* 129–136. doi:10.1242/jeb.85.1.129
93. Santhanakrishnan, A.; Robinson, A. K.; Jones, S.; Low, A. A.; Gadi, S.; Hedrick, T. L.; Miller, L. A. *J. Exp. Biol.* **2014,** *217,* 3898–3909. doi:10.1242/jeb.084897
94. Kolomenskiy, D.; Farisenkov, S.; Engels, T.; Lapina, N.; Petrov, P.; Lehmann, F.-O.; Onishi, R.; Liu, H.; Polilov, A. *Exp. Fluids* **2020,** *61,* 194. doi:10.1007/s00348-020-03027-0
95. Jiang, Y.; Zhao, P.; Cai, X.; Rong, J.; Dong, Z.; Chen, H.; Wu, P.; Hu, H.; Jin, X.; Zhang, D.; Liu, H. *iScience* **2022,** *25,* 103692. doi:10.1016/j.isci.2021.103692
96. Farisenkov, S. E.; Kolomenskiy, D.; Petrov, P. N.; Engels, T.; Lapina, N. A.; Lehmann, F.-O.; Onishi, R.; Liu, H.; Polilov, A. A. *Nature* **2022,** *602,* 96–100. doi:10.1038/s41586-021-04303-7
97. Santhanakrishnan, A.; Jones, S. K.; Dickson, W. B.; Peek, M.; Kasoju, V. T.; Dickinson, M. H.; Miller, L. A. *Fluids* **2018,** *3,* 45. doi:10.3390/fluids3030045
98. Sun, M. *Rev. Mod. Phys.* **2023,** *95,* 041001. doi:10.1103/revmodphys.95.041001
99. Weis-Fogh, T. *Sci. Am.* **1975,** *233,* 80–87. doi:10.1038/scientificamerican1175-80
100. Purcell, E. M. *Am. J. Phys.* **1977,** *45,* 3–11. doi:10.1119/1.10903
101. Lauga, E.; Powers, T. R. *Rep. Prog. Phys.* **2009,** *72,* 096601. doi:10.1088/0034-4885/72/9/096601
102. Yachai, M.; Tanasupawat, S.; Itoh, T.; Benjakul, S.; Visessanguan, W.; Valyasevi, R. *Int. J. Syst. Evol. Microbiol.* **2008,** *58,* 2136–2140. doi:10.1099/ijs.0.65592-0
103. Albers, S.-V.; Jarrell, K. F. *Front. Microbiol.* **2015,** *6,* 23. doi:10.3389/fmicb.2015.00023
104. Berg, H. C.; Brown, D. A. *Nature* **1972,** *239,* 500–504. doi:10.1038/239500a0
105. Rüffer, U.; Nultsch, W. *Cell Motil.* **1985,** *5,* 251–263. doi:10.1002/cm.970050307
106. Huang, J.; Tao, H.; Chen, J.; Shen, Y.; Lei, J.; Pan, J.; Yan, C.; Yan, N. *Cell* **2024,** *187,* 1733–1744.e12. doi:10.1016/j.cell.2024.02.037

107. Tran, Q. D.; Galiana, E.; Thomen, P.; Cohen, C.; Orange, F.; Peruani, F.; Noblin, X. *eLife* **2022,** *11,* e71227. doi:10.7554/elife.71227
108. Brennen, C. *J. Mechanochem. Cell Motil.* **1975,** *3,* 207–217.
109. Woolley, D. M.; Crockett, R. F.; Groom, W. D. I.; Revell, S. G. *J. Exp. Biol.* **2009,** *212,* 2215–2223. doi:10.1242/jeb.028266
110. Tottori, S.; Nelson, B. J. *Biomicrofluidics* **2013,** *7,* 061101. doi:10.1063/1.4827915
111. Bouck, G.; Rogalski, A.; Valaitis, A. *J. Cell Biol.* **1978,** *77,* 805–826. doi:10.1083/jcb.77.3.805
112. Liu, P.; Lou, X.; Wingfield, J. L.; Lin, J.; Nicastro, D.; Lechtreck, K. *J. Cell Biol.* **2020,** *219,* e202001122. doi:10.1083/jcb.202001122
113. Kimkes, T. E. P.; Heinemann, M. *FEMS Microbiol. Rev.* **2020,** *44,* 106–122. doi:10.1093/femsre/fuz029
114. Song, F.; Brasch, M. E.; Wang, H.; Henderson, J. H.; Sauer, K.; Ren, D. *ACS Appl. Mater. Interfaces* **2017,** *9,* 22176–22184. doi:10.1021/acsami.7b04757
115. Perez Ipiña, E.; Otte, S.; Pontier-Bres, R.; Czerucka, D.; Peruani, F. *Nat. Phys.* **2019,** *15,* 610–615. doi:10.1038/s41567-019-0460-5
116. Rubenstein, D. I.; Koehl, M. A. R. *Am. Nat.* **1977,** *111,* 981–994. doi:10.1086/283227
117. Tullberg, T. *Nova Acta Regiae Soc. Sci. Ups.* **1883,** *11,* 1–36.
118. Fudge, D. S.; Szewciw, L. J.; Schwalb, A. N. *Aquat. Mamm.* **2009,** *35,* 226–252. doi:10.1578/am.35.2.2009.226
119. Goldbogen, J. A.; Cade, D. E.; Calambokidis, J.; Friedlaender, A. S.; Potvin, J.; Segre, P. S.; Werth, A. J. *Annu. Rev. Mar. Sci.* **2017,** *9,* 367–386. doi:10.1146/annurev-marine-122414-033905
120. Wallace, J. B.; Merritt, R. W. *Annu. Rev. Entomol.* **1980,** *25,* 103–132. doi:10.1146/annurev.en.25.010180.000535
121. Pettitt, M. E.; Orme, B. A. A.; Blake, J. R.; Leadbeater, B. S. C. *Eur. J. Protistol.* **2002,** *38,* 313–332. doi:10.1078/0932-4739-00854
122. Nielsen, L. T.; Asadzadeh, S. S.; Dölger, J.; Walther, J. H.; Kiørboe, T.; Andersen, A. *Proc. Natl. Acad. Sci. U. S. A.* **2017,** *114,* 9373–9378. doi:10.1073/pnas.1708873114
123. Ros-Rocher, N.; Brunet, T. *Anim. Cognit.* **2023,** *26,* 1767–1782. doi:10.1007/s10071-023-01776-z
124. Stevens, M. *Sensory Ecology, Behaviour, and Evolution;* Oxford University Press: Oxford, UK, 2013. doi:10.1093/acprof:oso/9780199601776.001.0001
125. Granovsky, Y.; Matre, D.; Sokolik, A.; Lorenz, J.; Casey, K. L. *Pain* **2005,** *115,* 238–247. doi:10.1016/j.pain.2005.02.017
126. Abraira, V. E.; Ginty, D. D. *Neuron* **2013,** *79,* 618–639. doi:10.1016/j.neuron.2013.07.051
127. An, J.; Chen, P.; Wang, Z.; Berbille, A.; Pang, H.; Jiang, Y.; Jiang, T.; Wang, Z. L. *Adv. Mater. (Weinheim, Ger.)* **2021,** *33,* 2101891. doi:10.1002/adma.202101891
128. Burgess, P. R.; Petit, D.; Warren, R. M. *J. Neurophysiol.* **1968,** *31,* 833–848. doi:10.1152/jn.1968.31.6.833
129. Wang, Q.; Fan, C.; Gui, Y.; Zhang, L.; Zhang, J.; Sun, L.; Wang, K.; Han, Z. *Adv. Mater. Technol. (Weinheim, Ger.)* **2021,** *6,* 2100352. doi:10.1002/admt.202100352
130. Humphrey, J. A. C.; Barth, F. G. *Adv. Insect Physiol.* **2007,** *34,* 1–80. doi:10.1016/s0065-2806(07)34001-0
131. Tuthill, J. C.; Wilson, R. I. *Curr. Biol.* **2016,** *26,* R1022–R1038. doi:10.1016/j.cub.2016.06.070
132. Boublil, B. L.; Diebold, C. A.; Moss, C. F. *Sensors* **2021,** *21,* 6375. doi:10.3390/s21196375
133. Lechner, S. G.; Lewin, G. R. *Physiology* **2013,** *28,* 142–150. doi:10.1152/physiol.00059.2012
134. Barth, F. G. *Curr. Opin. Neurobiol.* **2004,** *14,* 415–422. doi:10.1016/j.conb.2004.07.005
135. Zill, S. N. Mechanoreceptors: Exteroceptors and proprioceptors. *Cockroaches As Models for Neurobiology: Applications in Biomedical Research;* CRC Press, 2019; pp 247–267.
136. Stritih-Peljhan, N.; Rühr, P. T.; Buh, B.; Strauß, J. *Comp. Biochem. Physiol., Part A: Mol. Integr. Physiol.* **2019,** *233,* 89–96. doi:10.1016/j.cbpa.2019.04.003
137. Magal, C.; Dangles, O.; Caparroy, P.; Casas, J. *J. Theor. Biol.* **2006,** *241,* 459–466. doi:10.1016/j.jtbi.2005.12.009
138. Casas, J.; Steinmann, T.; Krijnen, G. *J. R. Soc., Interface* **2010,** *7,* 1487–1495. doi:10.1098/rsif.2010.0093
139. Krijnen, G.; Lammerink, T.; Wiegerink, R.; Casas, J. Cricket inspired flow-sensor arrays. In *SENSORS, 2007,* IEEE, 2007; pp 539–546. doi:10.1109/icsens.2007.4388455
140. Liao, C.; Amador, G. J.; Liu, X.; Wu, Z.; Wu, J. *Bioinspiration Biomimetics* **2023,** *18,* 016012. doi:10.1088/1748-3190/aca577
141. Deora, T.; Ahmed, M. A.; Daniel, T. L.; Brunton, B. W. *J. Exp. Biol.* **2021,** *224,* jeb239442. doi:10.1242/jeb.239442
142. Foelix, R. F. Mechano-and chemoreceptive sensilla. *Neurobiology of Arachnids;* Springer: Berlin, Heidelberg, 1985; pp 118–137. doi:10.1007/978-3-642-70348-5_7
143. Kaissling, K. *Annu. Rev. Neurosci.* **1986,** *9,* 121–145. doi:10.1146/annurev.ne.09.030186.001005
144. Barth, F. G. Chemoreception. *A Spider's World: Senses and Behavior;* Springer: Berlin, Heidelberg, 2002; pp 145–150. doi:10.1007/978-3-662-04899-3_12
145. Gellert, H. R.; Halley, D. C.; Sieb, Z. J.; Smith, J. C.; Pask, G. M. *Sci. Rep.* **2022,** *12,* 19328. doi:10.1038/s41598-022-21507-7
146. de Brito Sanchez, M. G. *Chem. Senses* **2011,** *36,* 675–692. doi:10.1093/chemse/bjr040
147. Pitts, R. J.; Zwiebel, L. J. *Malar. J.* **2006,** *5,* 26. doi:10.1186/1475-2875-5-26
148. Mohebbi, N.; Schulz, A.; Spencer, T. L.; Pos, K.; Mandel, A.; Casas, J.; Hu, D. L. *Integr. Comp. Biol.* **2022,** *62,* 81–89. doi:10.1093/icb/icac006
149. Spencer, T. L.; Lavrik, N.; Hu, D. L. Synthetic moth antennae fabricated as preconcentrator for odor collection. In *2017 ISOCS/IEEE International Symposium on Olfaction and Electronic Nose (ISOEN),* IEEE, 2017; pp 1–3. doi:10.1109/isoen.2017.7968911
150. Spencer, T. L.; Mohebbi, N.; Jin, G.; Forister, M. L.; Alexeev, A.; Hu, D. L. *J. Fluid Mech.* **2020,** *884,* A34. doi:10.1017/jfm.2019.927
151. Stange, G.; Stowe, S. *Microsc. Res. Tech.* **1999,** *47,* 416–427. doi:10.1002/(sici)1097-0029(19991215)47:6<416::aid-jemt5>3.0.co;2-x
152. Kleineidam, C.; Tautz, J. *Naturwissenschaften* **1996,** *83,* 566–568. doi:10.1007/bf01141981
153. Chéret, J.; Bertolini, M.; Ponce, L.; Lehmann, J.; Tsai, T.; Alam, M.; Hatt, H.; Paus, R. *Nat. Commun.* **2018,** *9,* 3624. doi:10.1038/s41467-018-05973-0
154. Ruchty, M.; Romani, R.; Kuebler, L. S.; Ruschioni, S.; Roces, F.; Isidoro, N.; Kleineidam, C. J. *Arthropod Struct. Dev.* **2009,** *38,* 195–205. doi:10.1016/j.asd.2008.11.001
155. Schmitz, A.; Sehrbrock, A.; Schmitz, H. *Arthropod Struct. Dev.* **2007,** *36,* 291–303. doi:10.1016/j.asd.2007.02.002
156. Ruchty, M.; Roces, F.; Kleineidam, C. J. *J. Neurophysiol.* **2010,** *104,* 1249–1256. doi:10.1152/jn.00390.2010
157. Yin, K.; Huang, S.; Luo, C. *Zoomorphology* **2023,** *142,* 169–179. doi:10.1007/s00435-023-00594-8

158. Huang, S.; Hedrich, R. *Curr. Biol.* **2023,** *33,* 3962–3968.e2. doi:10.1016/j.cub.2023.07.069
159. Tichy, H.; Loftus, R. *Naturwissenschaften* **1996,** *83,* 255–263. doi:10.1007/bf01149598
160. Altner, H.; Routil, C.; Loftus, R. *Cell Tissue Res.* **1981,** *215,* 289–308. doi:10.1007/bf00239116
161. Harbach, R. E. Antennal Sensilla and Hygroreception in the Adult Mealworm Beetle Tenebrio Molitor L.(Coleoptera: Tenebrionidae). Ph.D. Thesis, University of Illinois at Urbana-Champaign, Champaign, IL, USA, 1976.
162. Gainett, G.; Michalik, P.; Müller, C. H. G.; Giribet, G.; Talarico, G.; Willemart, R. H. *Zool. Anz.* **2017,** *270,* 81–97. doi:10.1016/j.jcz.2017.10.004

License and Terms

This is an open access article licensed under the terms of the Beilstein-Institut Open Access License Agreement (https://www.beilstein-journals.org/bjnano/terms), which is identical to the Creative Commons Attribution 4.0 International License (https://creativecommons.org/licenses/by/4.0). The reuse of material under this license requires that the author(s), source and license are credited. Third-party material in this article could be subject to other licenses (typically indicated in the credit line), and in this case, users are required to obtain permission from the license holder to reuse the material.

The definitive version of this article is the electronic one which can be found at:
https://doi.org/10.3762/bjnano.15.55

BEILSTEIN JOURNAL OF NANOTECHNOLOGY

Investigation on drag reduction on rotating blade surfaces with microtextures

Qinsong Zhu, Chen Zhang*, Fuhang Yu and Yan Xu

Full Research Paper

Open Access

Address:
College of Mechanical and Electrical Engineering, Nanjing University of Aeronautics & Astronautics, Nanjing, 210016, China

Email:
Chen Zhang* - meeczhang@nuaa.edu.cn

* Corresponding author

Keywords:
blade; drag-reducing microtexture; geometrical parameters; placement position; simulations

Beilstein J. Nanotechnol. **2024,** *15,* 833–853.
https://doi.org/10.3762/bjnano.15.70

Received: 08 April 2024
Accepted: 26 June 2024
Published: 10 July 2024

This article is part of the thematic issue "Biomimetics and bioinspired surfaces: from nature to theory and applications".

Guest Editor: T. H. Büscher

© 2024 Zhu et al.; licensee Beilstein-Institut.
License and terms: see end of document.

Abstract

To enhance the aerodynamic performance of aero engine blades, simulations and experiments regarding microtextures to reduce the flow loss on the blade surfaces were carried out. First, based on the axisymmetric characteristics of the impeller, a new simulation method was proposed to determine the aerodynamic parameters of the blade model through the comparison of flow field characteristics and simulation results. Second, the placement position and geometrical parameters (height, width, and spacing) of microtextures with lower energy loss were determined by our simulation of microtextures on the blade surface, and the drag reduction mechanism was analyzed. Triangular ribs with a height of 0.2 mm, a width of 0.3 mm, and a spacing of 0.2 mm exhibited the best drag reduction, reducing the energy loss coefficient and drag by 1.45% and 1.31% for a single blade, respectively. Finally, the blades with the optimal microtexture parameters were tested in the wind tunnel. The experimental results showed that the microtexture decreased energy loss by 3.7% for a single blade under 57° angle of attack and 136.24 m/s, which was favorable regarding the drag reduction performance of the impeller with 45 blades.

Introduction

In order to survive, organisms in nature have undergone billions of years of evolution; their body structures have been adapted to the current environment and exhibit special functions on biological surfaces [1]. For the purpose of drag reduction, valuable inspiration can be derived from rapidly moving animals, such as the “denticles” found on the surface of shark skin, which enable high-speed swimming [2], as well as the texture of bird feathers [3]. The phenomenon of drag reduction can also be observed on the surface of plants. For example, there is a superhydrophobic structure on the surface of lotus leaves [4]. A thin gas film captured by the superhydrophobic structure creates a slip interface between gas and liquid, which effectively improves the

drag reduction and antifouling performance of lotus leaves [5]. However, the structures on biological surfaces are rather complex and not directly applicable in practice. Therefore, researchers have explored the drag reduction mechanisms through replication or imitation of the microtexture found on biological surfaces; it was found that the contribution of microtextures to drag reduction primarily occurs within the boundary layer [6,7]. Lang et al. [8] constructed rectangular and sinusoidal grooves with 2 mm in width, 3 mm in depth, and 1 mm in spacing, thus mimicking the transverse grooves on the surface of dolphin skin. They observed the effect of the grooves on flow separation and boundary layer using digital particle image velocimetry. Xiao et al. [9] analyzed the drag reduction mechanism of bionic microtextures and constructed simplified V-shaped, trapezoidal, and wavy ribs by grinding. Experimental and simulation studies on aeroengine blades with such microtextures showed that the drag reduction performance of wavy ribs is better than that of the other two structures. Tian et al. [10] pointed out that, because of the complexity of microstructures on the shark skin surface, it is difficult to use a uniform method to characterize the skin surface. Triangular grooves or rectangular grooves can be used to simplify the microstructures on the shark skin surface to study the effects on hydrodynamics and aerodynamics.

Within these extremely small structures, a low-speed, stable fluid flow exists, which can mitigate turbulences and enhance the stability of fluid motion within the boundary layer, resulting in a reduction of frictional drag [11]. Based on the above principles and for large-scale manufacturing, researchers imitated and simplified the microtextures of biological surfaces to form the structures with different sectional shapes, such as triangles, trapezoids, and ellipses [12,13], as shown in Figure 1.

The drag reduction effect of biomimetic microtextures can reduce friction and turbulence pulsation on blade surfaces, thus, improving the aerodynamic performance of blades [14]. The research on drag reduction of microtextures on blade surfaces can be traced back to the 1980s. In 1982, Walsh et al. [15] from NASA Langley Laboratory conducted a pioneering microtexture study on surfaces. Their experiments focused on longitudinal grooves with various shapes, revealing that symmetrical V-shaped grooves exhibited a remarkable drag reduction effect at low flow rates. The highest drag reduction rate (DRR) attained was 8%. Chamorro [16] studied fans with a grooved surface and found that, under certain operating conditions, the drag reduction effect of local coverage on the textured blade surface surpassed that of a complete covering. Additionally, they designed microgrooves of various sizes on the suction surface to achieve the optimal drag reduction effect. Zhang et al. [17] proposed a method to determine the placement position of microtextures by using finite element analysis. The suggested microtextures were arranged on blade surfaces and exhibited drag reduction compared to smooth blades. Mischo et al. [18] improved the cooling capability of turbine blades by adding grooves to the blade tips of axial turbines. Experimental and numerical simulation results showed that the addition of grooves increased turbine efficiency by 0.2% and 0.38%, respectively. In order to reduce aerodynamic losses in turbines caused by tip leakage, Parkash et al. [19] added grooves at the blade tips and verified their effectiveness through computational fluid dynamics (CFD) simulations. After the incorporation of grooves, the turbine efficiency improved by 0.1% to 0.2%.

It is evident that arranging microstructures on blade surfaces can optimize the aerodynamic performance of the blades, thereby achieving energy savings. However, the rational arrangement of microstructures on blade surfaces also requires investigation, as the shape, size, and placement position of microstructures can all affect drag reduction performance [20,21]. Wu et al. [22] investigated the effect of different sizes of triangular grooves on the drag of NACA 0012 airfoils, finding an optimal DRR of 9.65% when the microstructure dimensions were $s = h = d = 0.1$ mm. Liang et al. [23] arranged various sizes of triangular microstructures on rotating disks and found through comparative analysis that microtextures with

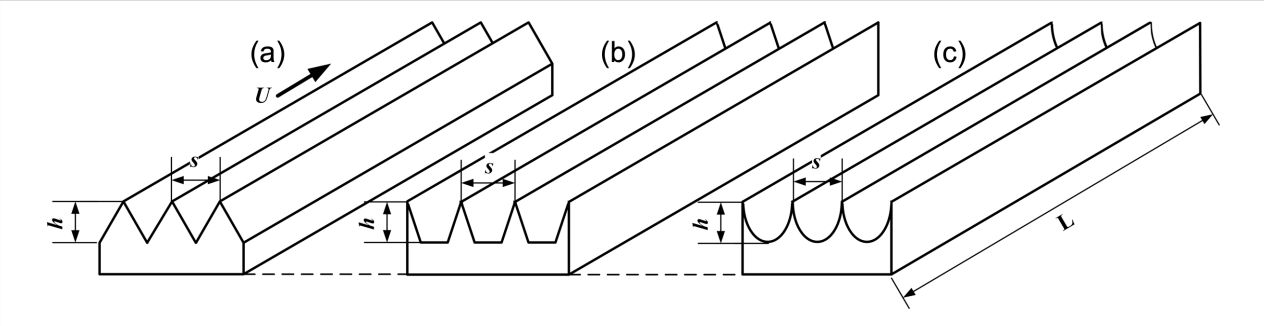

Figure 1: Microtextures with different sectional shapes: (a) triangles; (b) trapezoids, and (c) ellipses. The variables *s, h, L* and *U* represent the spacing, height, length, and the inflow velocity, respectively.

dimensions of s = 0.5 mm and h = 0.2 mm yielded a maximum DRR of 8.46%, with the DRR varying with changes in Reynolds number. Yang and Baeder [24] designed wavy structures on the trailing edge (TE) of a wind turbine blade to reduce the recirculation flow and coherent vortex shedding; the influence of wave depth, TE thickness, and chord length on the drag force were investigated by numerical simulations. The results indicated that the maximum drag was observed at a ratio of wave depth/TE thickness = 0.25. Hossain et al. [25] constructed inward and outward dimple-like structures on the upper surface of a NACA 4415 airfoil. The results from wind tunnel experiments showed that the dimples on the airfoil surface delayed flow separation; the inward dimples increased lift by 16.43% and reduced drag by 46.66%. However, while these researches have yielded encouraging achievements in the application of microtextures on blade surfaces, achieving good drag reduction performance relies heavily on the appropriate microtextures regarding size, type, and position. The determination of such microtextures is typically impractical for the following two reasons: (1) There is a lack of analysis on the flow field over smooth blades. The phenomenon of flow separation on blades occurs because of the complex curved surface in the air flow. The placement position of microstructures needs to be determined based on the locations of flow separation on blade surfaces. (2) The analysis of drag reduction performance is mostly based on numerical simulation results, with a lack of technology research regarding the processing of microtextures and of analysis of experimental results. On the one hand, the small size of microtextures may lead to significant errors in conventional machining methods, thereby increasing the difficulty of verifying microtexture drag reduction. On the other hand, the cost associated with experiments required for microtexture testing, such as wind tunnel tests, is high.

The present study employs numerical simulations, high precision milling, and wind tunnel experiments for solving the two problems discussed above. The main contributions of this article are as follows: (1) Based on the highly symmetrical characteristics of rotating machinery such as compressors, a new numerical simulation method for blade analysis was proposed to determine the flow field on the smooth blade surface and provide references for the placement of microtextures. (2) The influence of microstructure size on drag reduction of blade surfaces was analyzed to determine the optimal parameters for microstructures. The drag reduction mechanism of the microstructures was also analyzed based on simulation results. (3) A high-precision five-axis computerized numerical control (CNC) milling machine was used to process the microtextured blades. In order to obtain high-quality surfaces on the microtextured blades, three types of end milling tools were utilized to rough- and fine-mill blade and microtextures. The microtextured blades were tested in a wind tunnel to obtain drag reduction results.

Methods

This section introduces the modeling of microtextures on blade surfaces, as well as the equipment and processes in the actual processing of microtextures. Finally, the wind tunnel experiment platform used to measure the drag reduction of the microtextured blades is described.

Impeller

The research object of this paper is the impeller of an axial flow compressor, which consists of a hub and blades [26]. In order to generate high pressure, axial flow compressors typically comprise multiple stages of impellers, as shown in Figure 2a. When the compressor is working, the air flow is driven by the rotation of the impeller from the inlet to the outlet, as shown in Figure 2b. The working conditions of the impeller mainly include the rotational speed and the environmental conditions (temperature and pressure) at inlet and outlet. The impeller considered in this paper has 45 blades and is designed to operate at a rotational speed of 2880 rpm. The operating environment for the impeller is at standard temperature (25 °C) and pressure (101325 Pa).

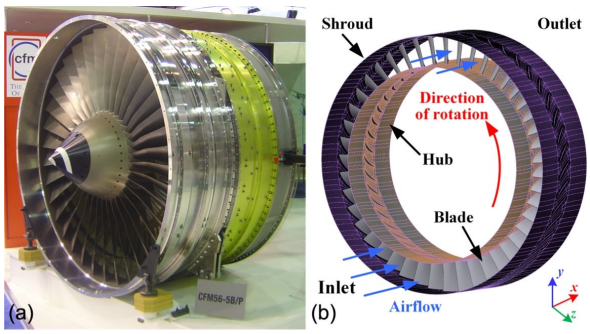

Figure 2: (a) Axial flow compressor [27] and (b) schematic of the impeller with 45 blades. Figure 2(a) was reproduced from [27] (Copyright © 2005 David Monniaux; "File:CFM56 dsc04641.jpg", Wikimedia Commons, https://commons.wikimedia.org/wiki/File:CFM56_dsc04641.jpg, distributed under the terms of the Creative Commons Attribution-Share Alike 3.0 Unported License, https://creativecommons.org/licenses/by-sa/3.0/deed.en). This content is not subject to CC BY 4.0. Figure 2b is used courtesy of ANSYS, Inc.

Modeling of microtextures on blade surface

To determine the geometry and position of the microtextures on the blade surface, a new simulation method is proposed based on the axisymmetric characteristics of rotating machinery. The complete flow domain model of the compressor was simplified into a single flow channel model, so that the flow field on the smooth blade surface could be obtained quickly and accurately. A flow diagram consisting of four steps is shown in Figure 3.

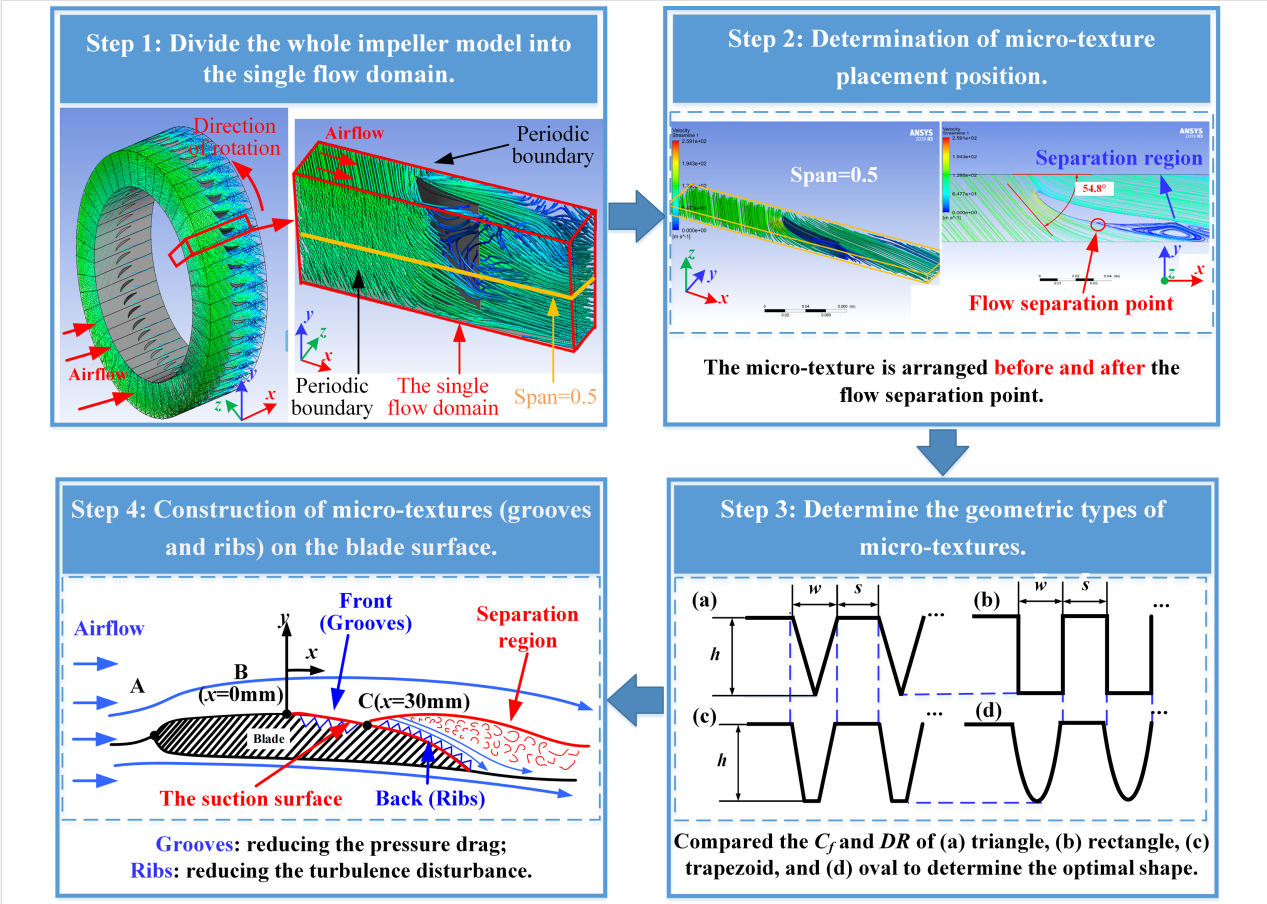

Figure 3: Flow chart of the simplified numerical simulation method. Images used courtesy of ANSYS, Inc.

Step 1

The compressor model has rotational symmetry, and each blade is uniformly installed on the compressor. Therefore, the compressor model was evenly divided according to the number of blades to obtain a calculation domain model including a single blade and a single flow channel. In the simulation setup, the walls on both sides of the channels were set as periodic boundaries, which can simulate the flow domain with symmetry and make up for the calculation error caused by the simplified model. Through the above simplification, the calculation cost can be greatly reduced while ensuring calculation accuracy.

Step 2

The microtexture placement position is determined according to the flow field of the smooth blade. Flow separation occurs during high-speed air flow over the curved blade surface. Here, a reasonable arrangement of microtexture can effectively improve the drag reduction. Therefore, CFD was employed to simulate a single channel model of the blade and the flow separation region was obtained. In order to verify the accuracy of the simulation calculation, the theoretical calculated value of the angle of attack was compared with the simulation results.

Step 3

First, the drag reduction performance of four microtextures was compared by numerical simulations to determine the geometric type with the optimal drag reduction. Then, different widths (w), spacings (s), and heights (h) of the microtextures were compared to determine the scale range with drag reduction. In the simulation setup, the initial conditions and the flow domain are consistent with the single flow domain of the blade. The coefficient of friction and the DRR from the simulation results were compared to determine the geometric types and size ranges of the microtexture with drag reduction performance.

Step 4

According to the flow field on the smooth blade surface, groove and rib microtextures were arranged before and after the flow separation point on the suction surface. The difference between grooves and ribs will described in the passage referring to step 4 in the Results and Discussion section. Also, based on the microtexture types and size range determined in step 3, the drag reduction results of grooves and ribs with different size parameters were compared to determine the combination of microtexture parameters with the best drag reduction performance. This

parameter combination was employed for machining microtextures on the blade surface, and the microtextured blade was placed in the wind tunnel for experiments.

Details of step 1 and step 3

Here, the details about the simulation setup method and the determination method of microtextures in step 1 and step 3 of the proposed method are described. To enhance readability, the relevant results from steps 2, 3, and 4 will be analyzed in the Results and Discussion section.

Step 1

The whole impeller with 45 blades was divided evenly, that is, each single flow domain occupies an 8° fan-shaped flow channel, as shown in Figure 4. The length of the flow channel is 300 mm, and the bottom radius and top radii are 300 and 410 mm, respectively.

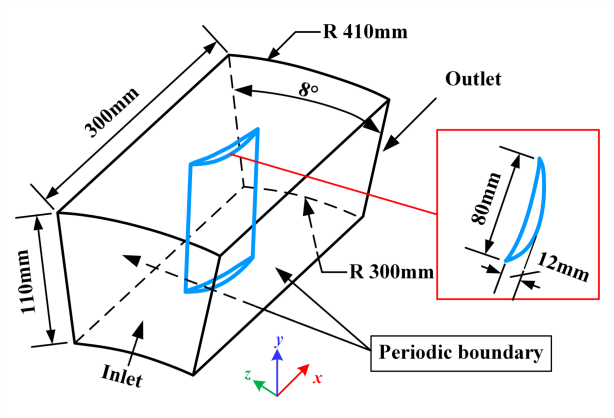

Figure 4: The size of flow domain and the single blade.

In the simulation setup, the k–epsilon (k-ε) model with enhanced wall treatment, which has better prediction results for rotation, boundary layer separation with large back pressure gradient, and backflow phenomena, was used for turbulence modeling in Ansys® CFX, Release 2020 R2 [28]. The boundary conditions were set according to the working conditions of the impeller, that is, the inlet of the impeller was set as the velocity inlet with a value of 75 m/s; the outlet was set as the pressure outlet with the value of 101325 Pa. Periodic boundary conditions were applied on both sides of the flow domain, and the upper and lower walls were no-slip walls, as shown in Figure 4. According to the above impeller parameters, we used the method of speed triangle [29] to calculate the theoretical value of the 0.5 blade height (span = 0.5). The relative airflow velocity was determined to be 130.67 m/s, with an angle of attack of 54.97°.

The height of the first layer mesh should be calculated according to the requirement of y^+ (dimensionless distance from the wall), which is determined according to each turbulence model requirements. In order to obtain good mesh quality and meet the k-ε model requirements used in this paper, y^+ needs to be between 1 and 5 [30]. In this paper, the height of the first layer mesh is 0.005 mm, and y^+ = 1.5, as shown in Figure 5.

Step 3

The method of dimensionless size was used to determine the size range of microtextures with drag reduction performance [31]. In this section, the microtexture sizes (i.e., h, w, and s) were determined according to the boundary layer theory as shown in Figure 6.

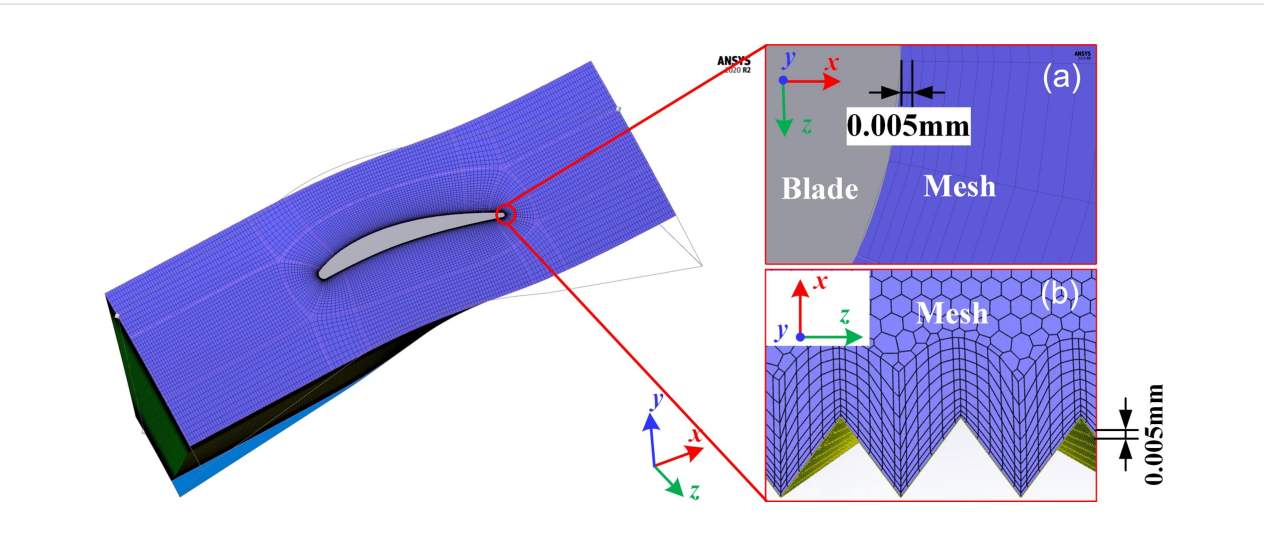

Figure 5: Meshed model of (a) a smooth blade surface and (b) a microtextured surface with 0.005 mm height of the first layer mesh according to y^+ = 1.5. Images used courtesy of ANSYS, Inc.

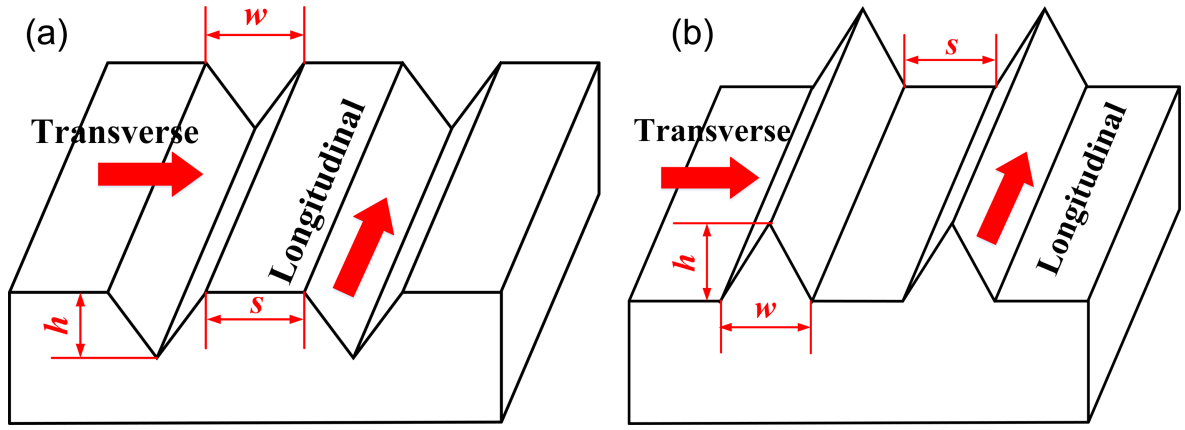

Figure 6: Characteristic parameters of (a) grooves and (b) ribs.

The dimensionless size calculation formula of microtextures with drag reduction performance are as follows [32]:

$$s^+ = \frac{su_\tau}{\nu}, \tag{1}$$

$$h^+ = \frac{hu_\tau}{\nu}, \tag{2}$$

$$w^+ = \frac{wu_\tau}{\nu}, \tag{3}$$

$$u_\tau = \left(\frac{\tau_w}{\rho}\right)^{1/2}, \tag{4}$$

$$\mu = \rho\nu, \tag{5}$$

where μ is the dynamic viscosity, ν is the kinematic viscosity, u is the average flow velocity, u_τ is the wall stress shear rate, τ_w is the wall shear stress, and ρ is the density.

$$\tau_w = 0.0225\rho u^2\left(\frac{\nu}{u\delta}\right)^{1/4}, \tag{6}$$

where δ is the thickness of the boundary layer. The flow condition around the flat plate wall can be determined by the dimensionless local Reynolds number.

$$\mathrm{Re}_x = \frac{\rho u x}{\mu}, \tag{7}$$

where x is the distance from the inlet along the fluid flow direction. For $\mathrm{Re}_x < 3 \times 10^5$, the flow in the boundary layer is laminar, and the following equation yields δ_L:

$$\delta_L = 4.96\times\left(\frac{\nu}{ux}\right) = 4.96\mathrm{Re}_x^{-1/5}. \tag{8}$$

The flow is turbulent if $\mathrm{Re}_x > 3 \times 10^6$, and the thickness of δ_T is calculated as:

$$\delta_T = 0.37\times\left(\frac{\nu}{ux}\right) = 0.37\mathrm{Re}_x^{-1/5}. \tag{9}$$

The flow in the boundary layer is transitional when Re_x is between 3×10^5 and 3×10^6. The turbulent area is selected for the arrangement of microtextures. Therefore, Equation 9 is entered into Equation 6:

$$\tau_w = 0.029\rho u^2\left(\mathrm{Re}_x\right)^{-1/5}. \tag{10}$$

Entering Equation 10 into Equation 4 gives:

$$u_\tau = 0.17u\mathrm{Re}_x^{-1/10}. \tag{11}$$

Entering Equation 11 into Equation 1, Equation 2, and Equation 3, respectively, yields:

$$s^+ = \frac{0.17su\mathrm{Re}_x^{-1/10}}{v}, \quad (12)$$

$$h^+ = \frac{0.17hu\mathrm{Re}_x^{-1/10}}{v}, \quad (13)$$

$$w^+ = \frac{0.17wu\mathrm{Re}_x^{-1/10}}{v}. \quad (14)$$

Based on Equations 12–14, the dimensionless sizes corresponding to microtextures under different Re_x can be obtained; Re_x needs to be determined according to the flow velocity and the characteristic dimensions (x) of the calculation domain. For our blades, u is 75 m/s, and the maximum value of x is 300 mm, as shown in Figure 4. Therefore, according to Equation 13 and the range of h^+ given in Table 1, the values of h of the microtextures with drag reduction performance were first determined. The range determination for w and s in Table 1 will be described in the Results and Discussion section.

Table 1: Microtexture parameters.

Parameter	Values
direction	spanwise, longitudinal
type	grooves, ribs
height (h)	$5 < h^+ < 25$ [15]
width (w)	$<3h$
spacing (s)	$<3h$
position	front, back

Experimental method

The overall process of experiments involves machining the microtextures on the blade surface and conducting experiments with the microtextured blades in a wind tunnel. The Results and Discussion section will give details about the determined microtexture types and sizes.

Experimental equipment

A list of equipment used in the experiment is shown in Table 2.

Microtexture processing of blade surfaces

A JDGR400-A13S five-axis CNC machine tool was used to process the blade and the microtextures; the processing steps are shown in Figure 7. First, the blank blade was installed in the machine tool, the size of the blank is $h \times l \times w = 140 \times 100 \times 25$ mm^3. Second, the end milling tool was used to mill the blank roughly to improve the processing efficiency. Third, the high-quality blade models were obtained by finishing the rough blade models. Finally, the microtextures were machined on the blade surfaces; this step was also divided into roughening and finishing because the end milling tool would break if the tool with a smaller radius was used to process the microtextures directly. The tool parameters used in different processing stages are given in Table 3.

Wind tunnel platform

The experiment was conducted at the intermittent wind tunnel platform at the College of Energy and Power Engineering, Nanjing University of Aeronautics and Astronautics. Pictures and a schematic diagram of the wind tunnel test platform are shown in Figure 8. Figure 8b shows that the wake measurement device consisting of a three-hole probe, a motor, and a guide rail. Ten probes were utilized to measure the wake, while the

Table 2: Overview of the equipment used in the experiment.

Equipment name	Model	Purpose	Manufacturer
five-axis CNC machine tool	JDGR400-A13S	processing of blades and microtextures	Beijing Jingdiao Technology Group Co., LTD, China.
flat end mill tool	⌀8 × 37 × ⌀8 × 81 × 3F[a]	processing of blades	Shanghai Mituo CNC Equipment Co., Ltd, China.
ball end mill	⌀0.3 × 0.6 × ⌀4 × 50 × 2F[a]	roughening of microtextures	MISUMI (China) Precision Machinery Trading Co., Ltd.
ball end mill	⌀0.2 × 0.3 × ⌀4 × 50 × 2F[a]	finishing of microtextures	MISUMI (China) Precision Machinery Trading Co., Ltd.
trinocular stereo microscope	JSZ6S	observing the processed blades	Nanjing Jinsong Optical Instrument Co., Ltd, China.
three-dimensional video microscope	KH-7700	high-precision 3D imaging	QUESTAR Corporation, Japan
intermittent wind tunnel	customized equipment	aerodynamic performance testing	Nanjing Power Tiger Electromechanical Technology Co., Ltd, China.

[a]⌀(tool diameter in mm) × (cutting edge length in mm) × ⌀(shank diameter in mm) × (overall length in mm) × (number of flutes)F.

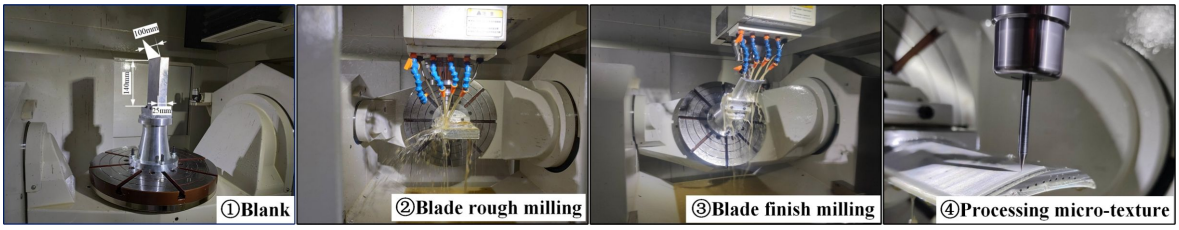

Figure 7: The manufacturing procedure of the microtextured blade.

Table 3: Tool parameters in different machining stages.

Process stage	Tools	Tool radius (mm)	Number of flutes
roughening of blades	flat end mill	4	3
finishing of blades	flat end mill	4	3
roughening of microtextures	ball end mill	0.15	2
finishing for microtextures	ball end mill	0.1	2

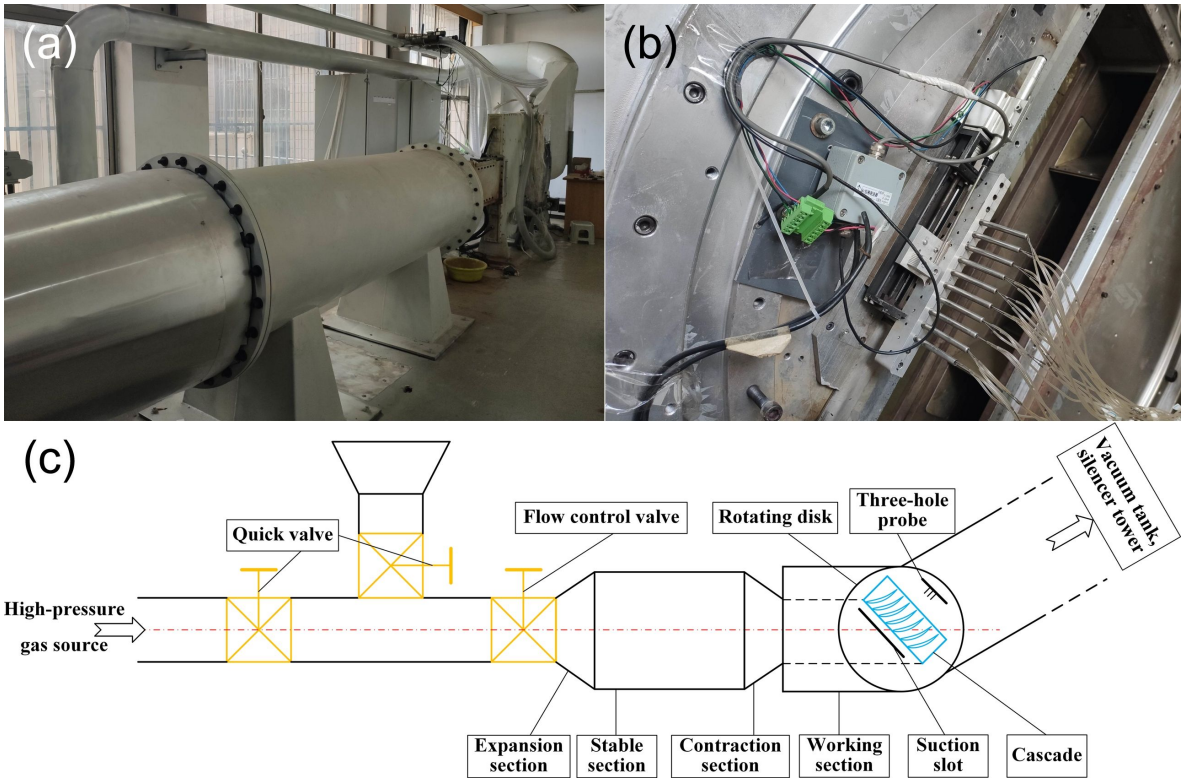

Figure 8: Experimental platform and schematic diagram. (a) Wind tunnel test platform. (b) Three-hole probe measuring device. (c) Schematic diagram of the wind tunnel test platform.

motor facilitates control and adjustment of their position. The total pressure (*TP*), static pressure (*P*) and velocity of the air flow (*V*) in the experiment were obtained by the three-hole probe measuring device. These results can be calculated according to Equations S5–S8 in Supporting Information File 1 to obtain Mach number (Ma) and energy loss coefficient (ξ). The

angle of attack can be set by controlling the motor and, thus, turning the disc (Figure 8c). In Figure 8c, the inlet of the test platform is connected with the high-pressure gas source, which is a 100 m^3 high-pressure gas tank with a maximum of 25 atm; the air extraction source is a 200 m^3 vacuum tank with a minimum of 0.1 atm.

Experimental steps

To ensure the accuracy of experiments, the velocity and angle of attack for blade heights of 0.25, 0.5, and 0.75 were selected to carry out multiple tests to verify the drag reduction effect of the microtextured blade. The specific steps of the experiment are as follows: (1) preparation of two blades in contrast, that is, one smooth blade and another blade with a microtexture on the surface; (2) test the smooth blade first; adjust the wind tunnel flow velocity and the angle of attack to 123.98 m/s and 52.8°, respectively; (3) measurement of the *TP* and *P* at the inlet and outlet, respectively, and calculation of ξ and observation of the wake loss distribution; (4) change of velocity and angle of attack to 130.67 m/s and 54.8°, respectively, and continuation according to step 3; (5) change of velocity and angle of attack to 137.54 m/s and 57.0°, respectively, and continuation according to step 3; (6) installation of the blades with microtextures and repetition of steps 3–5. The results obtained from the above steps will discussed in the "Results of the experiments" section.

Results and Discussion

Determined microtextures

The details about the results obtained in steps 2–4 of the simulation method described in the Methods section are given here. In step 2, the simulation results of a single impeller blade were analyzed to determine the flow field characteristics around the blade, such as angle of attack, velocity, and air flow state. As shown in Figure 9a, we sliced the calculation domain to analyze the simulation results and selected the green plane at 0.25 of the total length of the flow domain in streamwise direction. In the radial direction, three curved surfaces with spans of 0.25, 0.50, and 0.75 of the blade height, progressing from the bottom to the top, were chosen for analyzing the velocity distribution at the intersection between these curved surfaces and the green plane. Figure 9b indicates an increase in the peripheral speed of the blade as the radius increases. The average velocity at span = 0.5 is 131.5 m/s, with an error of only 0.6% from the theoretical value of 130.67 m/s. This result serves as evidence supporting the reliability of the simplified simulation method; hence, the velocity in the local area simulation was set at 130.67 m/s.

In Figure 10, two-dimensional flow streamlines of the curved surface at span = 0.25, 0.5, and 0.75 are analyzed. The relative velocity angle of airflow and blade changes as the blades rotate. A comparison of simulation results is shown in Table 4, the error between the simulation value and the theoretical value of the angle of attack is only 0.31%. Hence, the flow field of the smooth blade surface at span = 0.5 is further analyzed.

Table 5 presents the resistance results of the smooth blade, where the total drag (T_d) in the direction of airflow was divided into pressure drag (P_d) and friction drag (F_d). The primary impact of the microtextures is to modify the flow state of the boundary layer near the wall, reducing of F_d. For our blade, the contribution of F_d is small, accounting for only 2.39% of T_d. Thus, this paper primarily focuses on assessing the influence of microtextures on system energy loss.

From the leading edge to the trailing edge of the blade, the pressure surface exhibits a favorable pressure gradient, whereas the suction surface presents an adverse pressure gradient. This observation is complemented by Figure 11a, which illustrates that the turbulent kinetic energy (k) on the blade surface is small. The position of X = 0 mm in Figure 11a corresponds to the

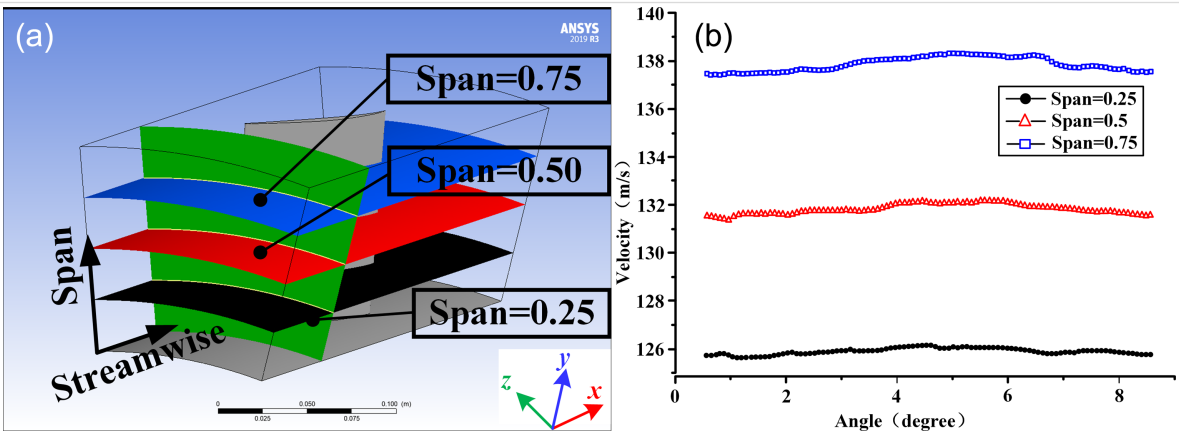

Figure 9: Single blade and simulation results. (a) Slices of the calculation domain. (b) Simulation results of flow velocity at span = 0.25, 0.5, and 0.75. Figure 9a used courtesy of ANSYS, Inc.

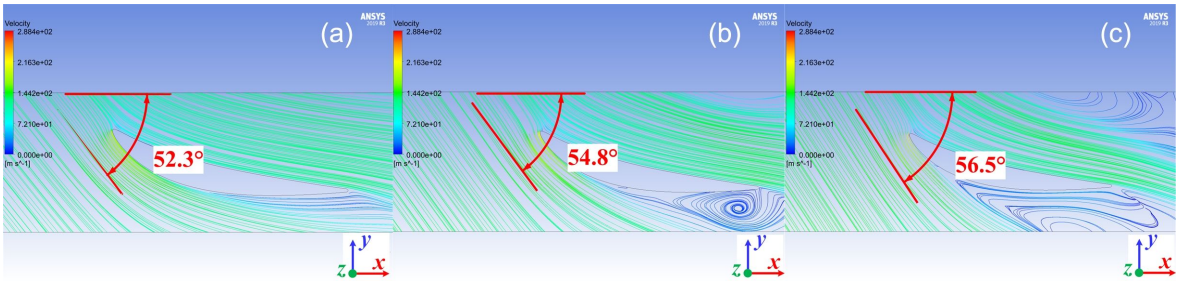

Figure 10: Simulation values of attack angle at (a) span = 0.25, (b) span = 0.50, and (c) span = 0.75. *x* is the axial direction, *y* is the radial direction, and *z* is the rotation direction of the blade. Images used courtesy of ANSYS, Inc.

Table 4: The comparison of simulated and theoretical values of the angle of attack.

Surface	Simulation values (°)	Theoretical values (°)	Error (%)
span = 0.25	52.30	52.80	0.95
span = 0.50	54.80	54.97	0.31
span = 0.75	56.50	57.00	0.88

Table 5: Aerodynamic parameters of the smooth blade.

Type	P_d (N)	F_d (N)	T_d (N)	F_d/T_d (%)
smooth	1.3288	0.0325	1.3613	2.39

highest point of the blade surface (point B in step 4 of Figure 3). Observing the distribution of *k* on the periodic boundary shows that *k* is zero in the front region of the blade ($X \leq 0$ mm). However, *k* begins to rise sharply from $X = 40$ mm, indicating that boundary layer separation at this position generates turbulence. The peak of *k* indicates that this position corresponds to the center of the turbulent vortex. According to Figure 11b, the turbulent vortices manifest on the adverse pressure surface within the system. Therefore, the microtextures were arranged on the adverse pressure surface.

Based on Figure 11, the air flow separation is initiated at $X = 30$ mm. As a result, the suction surface can be divided into two regions (front and back) at $X = 30$ mm, which serves as the critical point to discuss the drag reduction performance of the microtexture.

In step 3, the geometric types and size ranges of the microtextures were determined. Because of the high flow velocity on the blade surface, transverse microtextures would significantly increase the projected area in the flow direction, leading to a drastic increase in P_d. Therefore, longitudinal microtextures were considered here. Because the flow projection area in longitudinal microtextures is small, F_d contributes the most to T_d. F_d is related to the friction drag coefficient and the surface area, while the shape of the microtextures affects the surface area and surface flow. Therefore, microtextures of four shapes was investigated in this paper, as shown in step 3 of Figure 3.

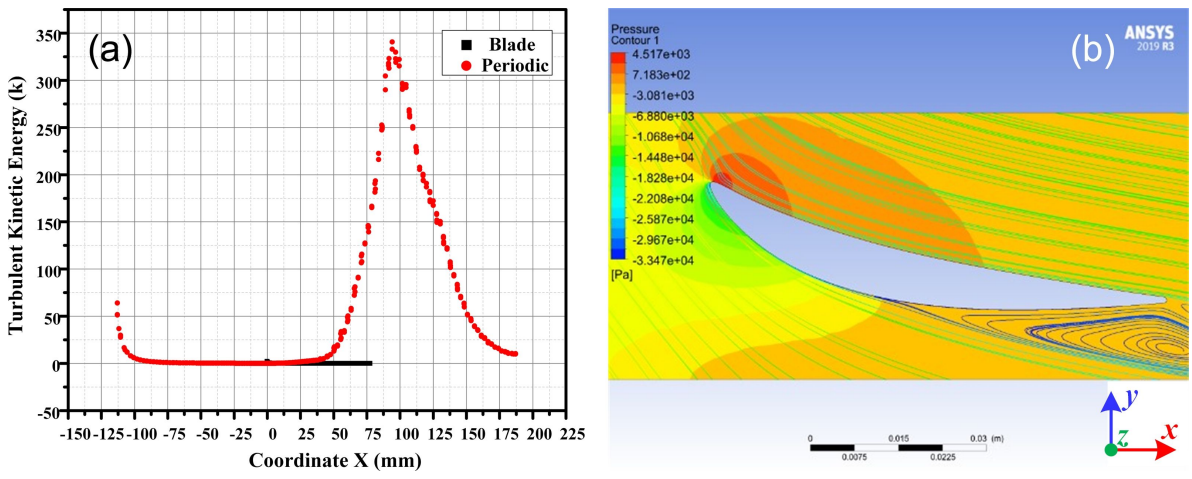

Figure 11: The distribution of (a) *k* and (b) the flow field on the blade surface. Figure 11b used courtesy of ANSYS, Inc.

The drag reduction of the above four microtextures was simulated using the same simulation settings as in step 1. The flow velocity and the angle of attack were obtained from the results at span = 0.5, which were 130.67 m/s and 54.8°, respectively. The DRR of the four microtextures is shown in Figure 12. First, by comparing the rectangle and triangle 1 with the same values of h, w, and s, it is evident that the DRR of the triangle is greater than that of the rectangle. This is because the surface area of the rectangle is larger than that of triangle 1, resulting in higher frictional drag of the rectangle. Comparing triangle 2, trapezoid, and oval microtextures, it can be seen that the DRR of triangle 2 is higher than that of the other two using the same size parameters.

Figure 13 shows the coefficient of friction (C_f) of the microtexture surface. The C_f at the bottom of the microtextures is smaller because of the low speed of the fluid, which also confirms that the C_f is affected by Re. From Figure 13, it can be observed that there is a significant variation in C_f at the corners

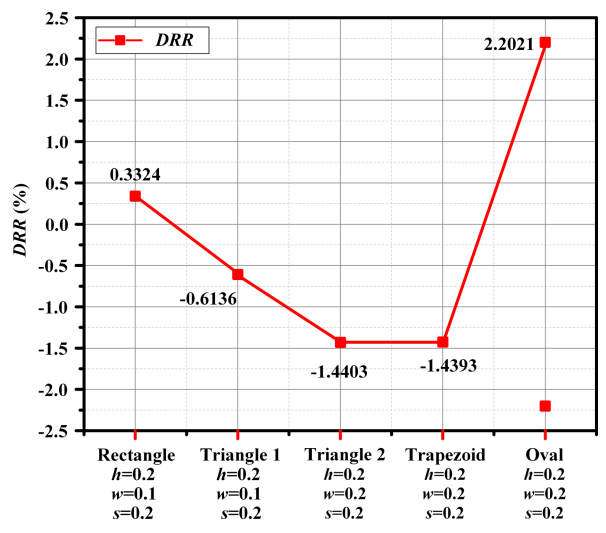

Figure 12: DRR results of four microtextures with different sizes. The formula for calculating DRR is shown in Equation S4 of Supporting Information File 1.

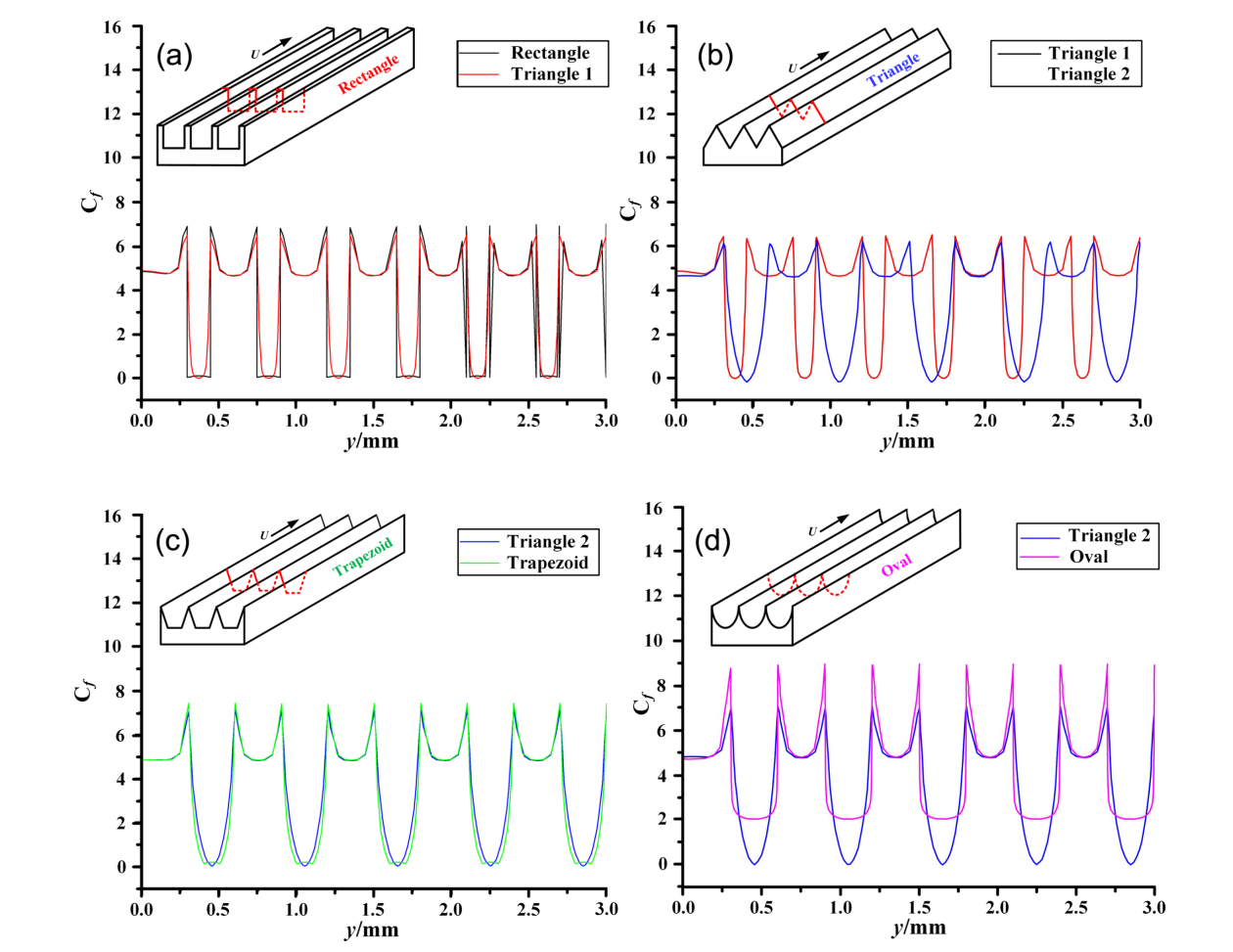

Figure 13: Comparison of coefficient of friction (C_f) on the surface of (a) rectangle and triangle 1, (b) triangle 1 and triangle 2, (c) triangle 2 and trapezoid, and (d) triangle 2 and oval. The source of C_f is shown by the red line in the upper left corner of each panel.

of the microtextures. Inside the grooves, C_f is smaller because the airflow velocity is lower. According to Figure 13c, there is little difference in the C_f distribution between the triangular and trapezoidal surfaces. The average values of C_f on microstructured surfaces are shown in Table 6; triangle 2 has the lowest average C_f. Therefore, after comprehensive analysis of Figure 12, Figure 13, and Table 6, the triangular microstructure was chosen to be machined in the blade surface.

The range of h has been discussed in the Methods section. In order to determine the ranges of w and s, different values of w and s of the triangular microtexture were chosen, and the DRRs were compared, as shown in Table 7 and Table 8.

Table 7 shows the change of DRR for different w when h and s of the triangular microtexture are fixed values. It can be clearly seen that the microtexture increases the resistance (DRR < 0) when $w/h = 3$, and the microtexture has the best drag reduction performance when $h = 0.2$ mm, $w = 0.3$ mm, and $s = 0.3$ mm. Therefore, one of the requirements for the triangular microtexture with drag reduction is to meet the condition of $w/h < 3$. Table 8 shows the influence of different s on the DRR. The maximum value of DRR is −5.5138% when $s = 0$ of the triangular microtexture, and the DRR gradually decreases with the increase of s. The triangular microtexture exhibits drag reduction under the condition of $s/h < 3$. In summary, the microtexture under the flow conditions described in this paper exhibits drag reduction only when $w/h < 3$ and $s/h < 3$.

In step 4, construction and comparison of different microtextures were carried out. To explore the effect of the microtextures on flow field and resistance, the grooves and ribs were arranged at the front and back sections of the suction surface, respectively, as shown in step 4 of Figure 3. According to the

Table 6: Average values of C_f.

Microtexture	Rectangle	Triangle 1	Triangle 2	Trapezoid	Oval
mean value of C_f	4.323	4.2000	3.8230	3.9906	5.6677

Table 7: The influence of the w of the triangular microtexture on the resistance.

Group	h (mm)	w (mm)	w/h	s (mm)	F_s (10^{-5} N)[a]	F_m (10^{-5} N)[b]	DRR (%)
W1	0.2	0.1	0.5	0.3	5.957	5.930	−0.4459
W2	0.2	0.15	0.75	0.3	6.689	6.633	−0.8353
W3	0.2	0.2	1.0	0.3	7.415	7.317	−1.3114
W4	0.2	0.3	1.5	0.3	8.853	8.673	−2.0360
W5	0.2	0.4	2.0	0.3	10.300	10.181	−1.1593
W6	0.2	0.6	3.0	0.3	13.090	13.192	0.0147

[a]F_s is the total resistance of the smooth wall from the simulation results; [b]F_m is the total resistance of the microtextured wall from the simulation results.

Table 8: The influence of the s of the triangular microtexture on the resistance.

Group	h (mm)	w (mm)	s (mm)	s/h	F_S (10^{-5} N)[a]	F_m (10^{-5} N)[b]	DRR (%)
S1	0.2	0.3	0	0	4.361	4.121	−5.5138
S2	0.2	0.3	0.10	0.50	5.866	5.683	−3.1191
S3	0.2	0.3	0.15	0.75	6.613	6.427	−2.8093
S4	0.2	0.3	0.20	1.00	7.359	7.172	−2.5400
S5	0.2	0.3	0.30	1.50	8.853	8.673	−2.0360
S6	0.2	0.3	0.40	2.00	10.346	10.167	−1.7255
S7	0.2	0.3	0.60	3.00	13.333	13.155	−1.3335

[a]F_s is the total resistance of the smooth wall from the simulation results; [b]F_m is the total resistance of the microtextured wall from the simulation results.

flow field information from the smooth blade, the velocity in the front section of the suction surface is faster. The placement of ribs here increases the projection area, resulting in the increase of P_d, which will lead to advanced transition and separation of the flow; hence, the groove structure needs to be arranged in the front section. In contrast, the back section of the suction surface already exhibits separated boundary layers and turbulent vortices, and the ribs closer to the vortex have a more significant impact on the flow of the vortex. The ribs were arranged in the back section of the blade suction surface to optimize the lifting effect on the vortex. The results of drag reduction performance of microtextured surfaces are shown in Table 9.

Table 9 shows that adding microtexture changes the force on the blade. Compared with the back section of the suction surface, the drag increase and loss coefficient changes caused by the microtextures in the front section are more pronounced. Case 1 to case 3 indicate an increase in system energy loss without drag reduction effect. Moreover, a linear relationship exists between the rate of drag change and the height of the microtexture as the height directly influences the projected area and surface area. Ribs located in the back section of the blade exhibit a drag reduction effect, which is independent of the rib height.

The surface pressure distribution at the front end of the textured blade is shown in Figure 14a. It is evident that grooves substantially influence the pressure distribution, with more significant impact observed as the height of the microtexture increases. Conversely, the pressure distribution trend of the groove surface with a height of 0.1 mm resembles that of a smooth surface. Therefore, the groove has little effect on drag and ξ.

According to Figure 14b, the grooves arranged in the front section of the blade suction surface lead to an increase in turbulent kinetic energy. This results in an earlier increase in turbulence intensity, indicating the premature separation of the boundary layer and an associated increase in energy loss. From both the perspective of resistance changes and energy loss, grooves do not effectively contribute to drag reduction performance.

In Table 9, the microtextures were arranged at the back of the blade suction surface, which explicitly affects the DRR and ξ.

Table 9: Simulation results of different types of microtexture in different regions on the blade suction surface.

Group	Region	Type	*h* (mm)	*w* (mm)	*s* (mm)	DRR (%)	ηξ (%)[a]
case 1	front	grooves	0.1	0.1	0.1	0.23	1.70
case 2	front	grooves	0.2	0.2	0.2	6.52	26.88
case 3	front	grooves	0.3	0.3	0.3	18.36	42.13
case 4	back	ribs	0.1	0.1	0.1	−1.31	−1.37
case 5	back	ribs	0.2	0.2	0.2	−1.17	−1.43
case 6	back	ribs	0.3	0.3	0.3	−1.16	−1.09

[a]The change rate of energy loss coefficient from Equation S5 in Supporting Information File 1.

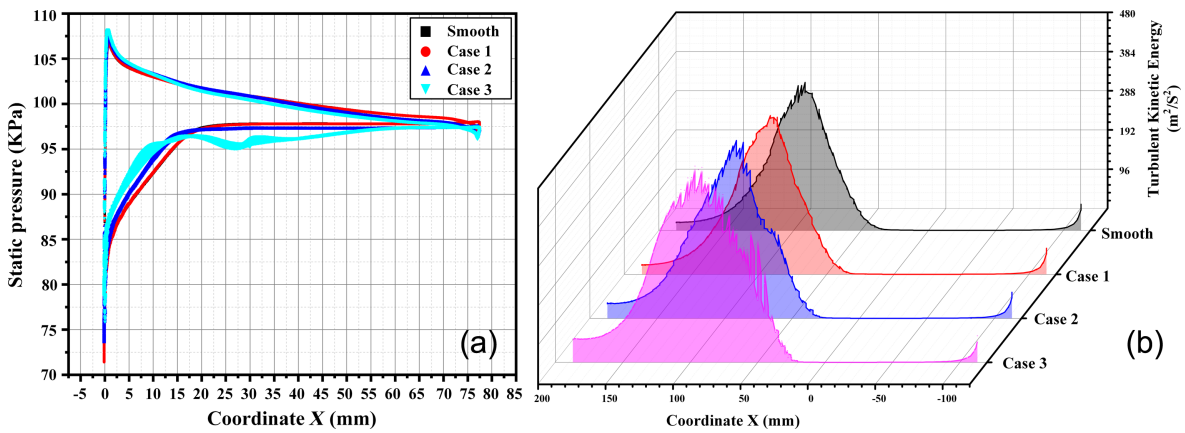

Figure 14: (a) Static pressure and (b) turbulent kinetic energy distribution of blade surfaces with different groove parameters.

In order to explore the drag reduction characteristics of ribs on the back, the rib parameters were further analyzed. The specific simulation results are shown in Table 10.

As shown in Figure 15a, the resistance increases with the height of the ribs. However, this relationship is not linear and is influenced by the coupling effect of the microtexture on P_d and F_d. The highest DRR of −1.31% is obtained when h = 0.1 mm, while the lowest energy loss coefficient is observed when h = 0.2 mm. As shown in Figure 15b, the DRR is the highest when w = 1.5h, basically the same as for w = 0.5h, and the energy loss coefficient is the highest when w = 1.5h. We therefore select cases 8–10 (w = 1.5h) to research the spacing parameter further. According to Figure 15c, the spacing exhibits the same effect on the DRR and energy loss coefficient. Moreover, the drag reduction effect is optimal when s = h.

Table 10: Simulation results of ribs with different parameters arranged at the back section of the blade surface.

Group	Region	Type	h (mm)	w (mm)	s (mm)	DRR (%)	η_ξ (%)[a]
case 4	back	ribs	0.1	0.1	0.1	−1.31	−1.37
case 5	back	ribs	0.2	0.2	0.2	−1.17	−1.43
case 6	back	ribs	0.3	0.3	0.3	−1.16	−1.09
case 7	back	ribs	0.2	0.1	0.2	−1.30	−1.13
case 8	back	ribs	0.2	0.3	0.2	−1.31	−1.45
case 9	back	ribs	0.2	0.3	0	−1.19	−1.23
case 10	back	ribs	0.2	0.3	0.1	−1.15	−1.09

[a]The change rate of energy loss coefficient from Equation S5 in Supporting Information File 1.

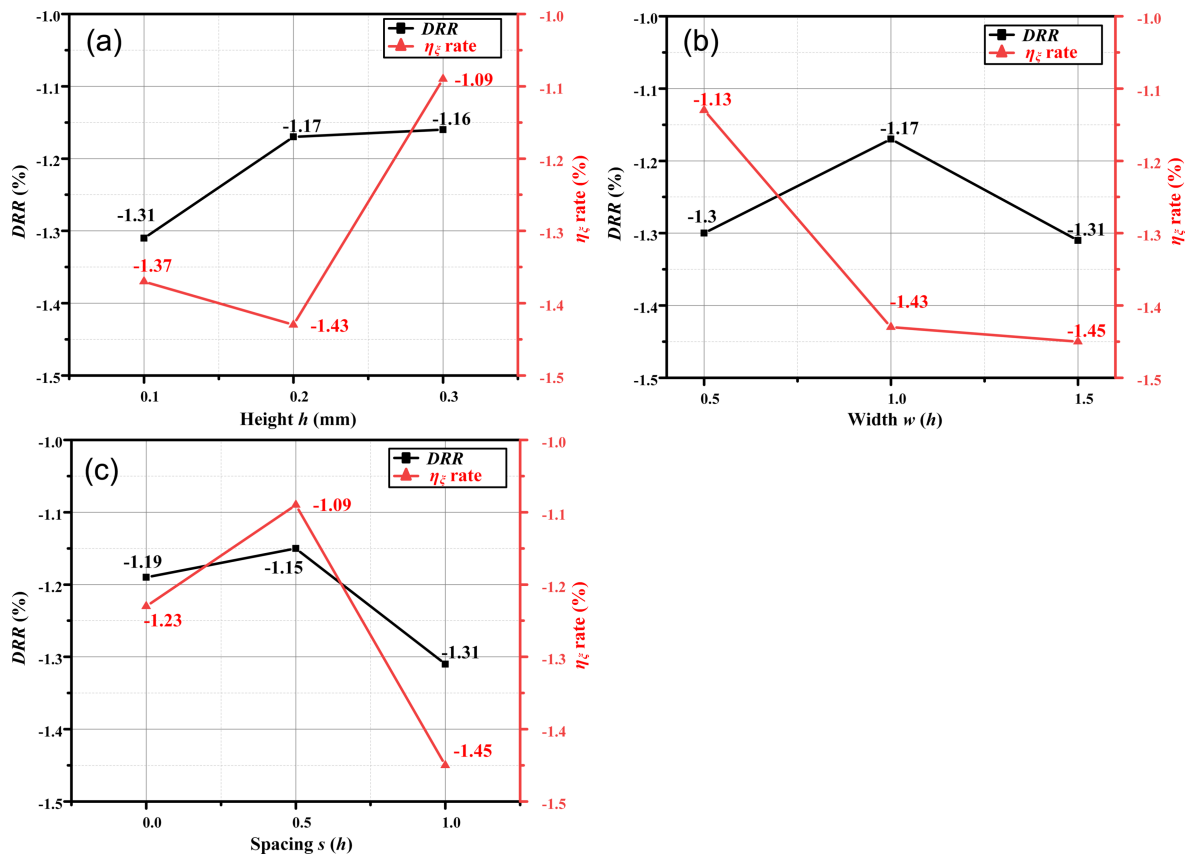

Figure 15: Influence of (a) height, (b) width, and (c) spacing of microtextures on drag reduction performance.

The DRR alone cannot fully represent the overall energy consumption for the entire impeller system. Thus, we comprehensively consider the two simulation results to guide the microtexture design. The selection criterion is based on achieving the smallest energy loss coefficient and the highest DRR. Following this standard, ribs with h = 0.2 mm, w = 0.3 mm, and s = 0.2 mm (case 8) exhibit the best performance. The maximum DRR and η_ξ = are −1.31% and −1.45%, respectively, in case 8, and the drag reduction effect is significant for the whole impeller system with 45 blades.

Drag reduction mechanism analysis

The effective method to reduce drag in the flow field is to delay boundary layer separation and inhibit turbulence generation [33]. Because turbulence generation leads to energy dissipation, increasing the energy loss. Therefore, the drag reduction of the microtextured blade surface was analyzed by considering turbulent kinetic energy, eddy viscosity ratio, and flow field. Figure 16a compares smooth blades and textured blades (case 8) regarding the turbulence in the surrounding flow field. The presence of the microtexture on the blade surface results in a decrease in turbulent kinetic energy at the back end of the blade, thereby reducing energy losses. Figure 16b compares the eddy viscosity ratio, representing the stress generated by turbulent motion. The microtexture significantly reduces the stress generated by turbulent motion. As a result, the energy loss in the entire flow channel system is substantially reduced.

The influence of the microtexture on turbulent vortices is shown in Figure 17a; the contour shows the pressure distribution in

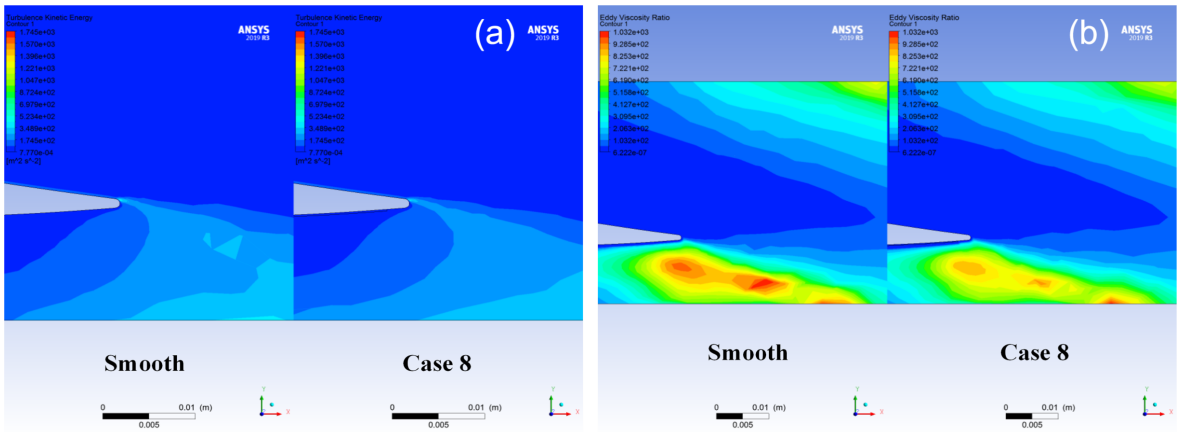

Figure 16: The effect of microtexture on (a) turbulent kinetic energy and (b) eddy viscosity ratio around blades. Images used courtesy of ANSYS, Inc.

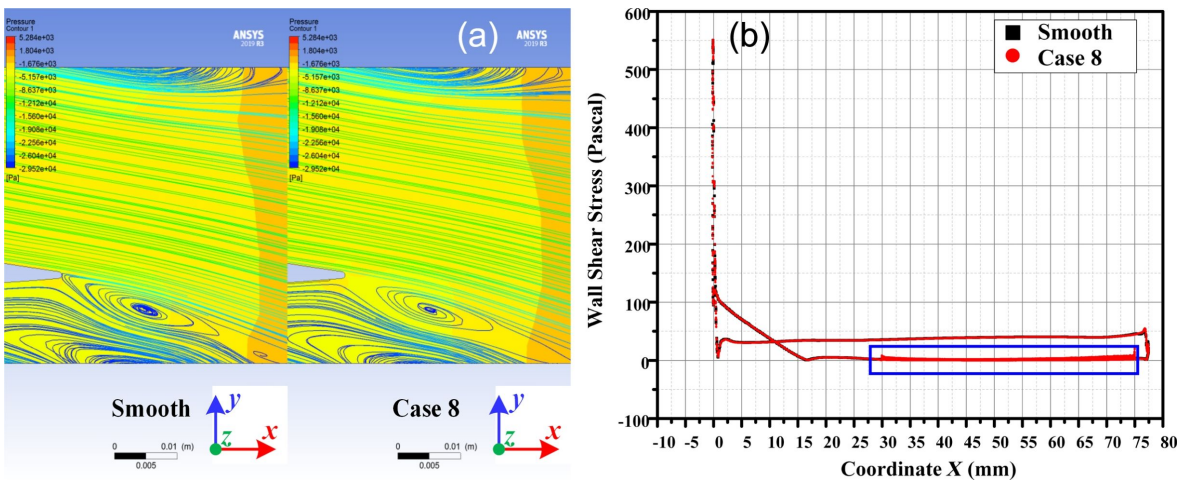

Figure 17: The effect of microtexture on (a) turbulent vortex and (b) overall shear stress distribution. Figure 17a used courtesy of ANSYS, Inc.

the flow domain. The periodic boundary was used in the two pictures as the streamline release entrance, with identical streamline. It can be seen from the streamline that the microtexture effectively inhibits turbulence generation and reduces system energy consumption. Weakening of turbulences will cause a reduction of wall shear stress, which is reflected in the reduction of friction resistance.

The shear stress distribution on the smooth blade and the microtextured blade is shown in Figure 17b; the blue mark indicates that the placement of microtextures does not change the overall shear stress distribution of the blade. Instead, it generates shear stress fluctuations within the microtextured area.

Wind tunnel experiment with the microtextured blade surface

Surface quality analysis of the microtextured blade

The processed blade, composed of 7075 series aluminum alloy, is displayed in Figure 18. The blade surface quality was assessed using a JSZ6S trinocular stereo microscope; the results showed that the processed blade has high quality and no obvious defects. In order to further analyze the processing quality, a HIROX KH-7700 three-dimensional video microscope was used to examine the microtexture and blade surface morphology, as shown in Figure 19.

The rib surface morphology and dimensional data are shown in Figure 19a. The theoretical height is 0.2 mm, the width is 0.3 mm, the spacing is 0.2 mm, and the rib–tip spacing is 0.5 mm. In contrast, the actual height measures are 0.202 mm, and the actual rib–tip spacing is 0.534 mm. The minimal machining error is due to the utilization of a ball end milling tool with a diameter of 0.2 mm, which has a processing residue at the corner of the bottom rib area (Figure 20a). Figure 19b indicates slight height fluctuations on the surface of the smooth blade, reaching a maximum deviation of 0.007 mm. This can be attributed to the point contact nature of the ball tip tool during the machining process and the spacing between tool paths. Thus, the machining coverage rate does not reach 100%, resulting in a residual height h as shown in Figure 20b. To sum up, the microtexture here meets the quality requirements.

Results of the experiments

The experimental results are given in Table 11 and Table 12.

The results in Table 11 indicate that ξ_0 rises with increasing angle of attack. The simulation reveals distinct phenomena occurring at three angles of attack; the separation phenomenon and vortex at the back section of the blade become more apparent and intense with the increase of the angle. Table 12 shows that the textured blade has a more significant effect on reducing ξ_1 as the flow angle increases. At the flow angle of 57°, $\eta_\xi = -3.7\%$ based on Equation S5 of Supporting Information File 1, which indicates that the microtexture reduces energy consumption and improves the overall aerodynamic performance of the blades.

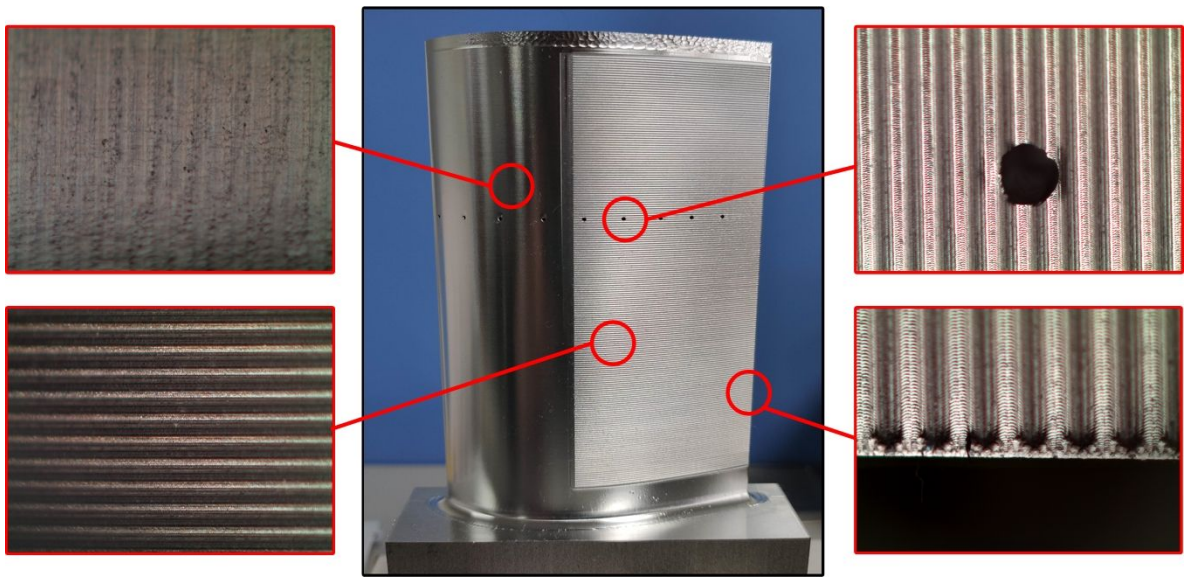

Figure 18: The processed blade with microtexture.

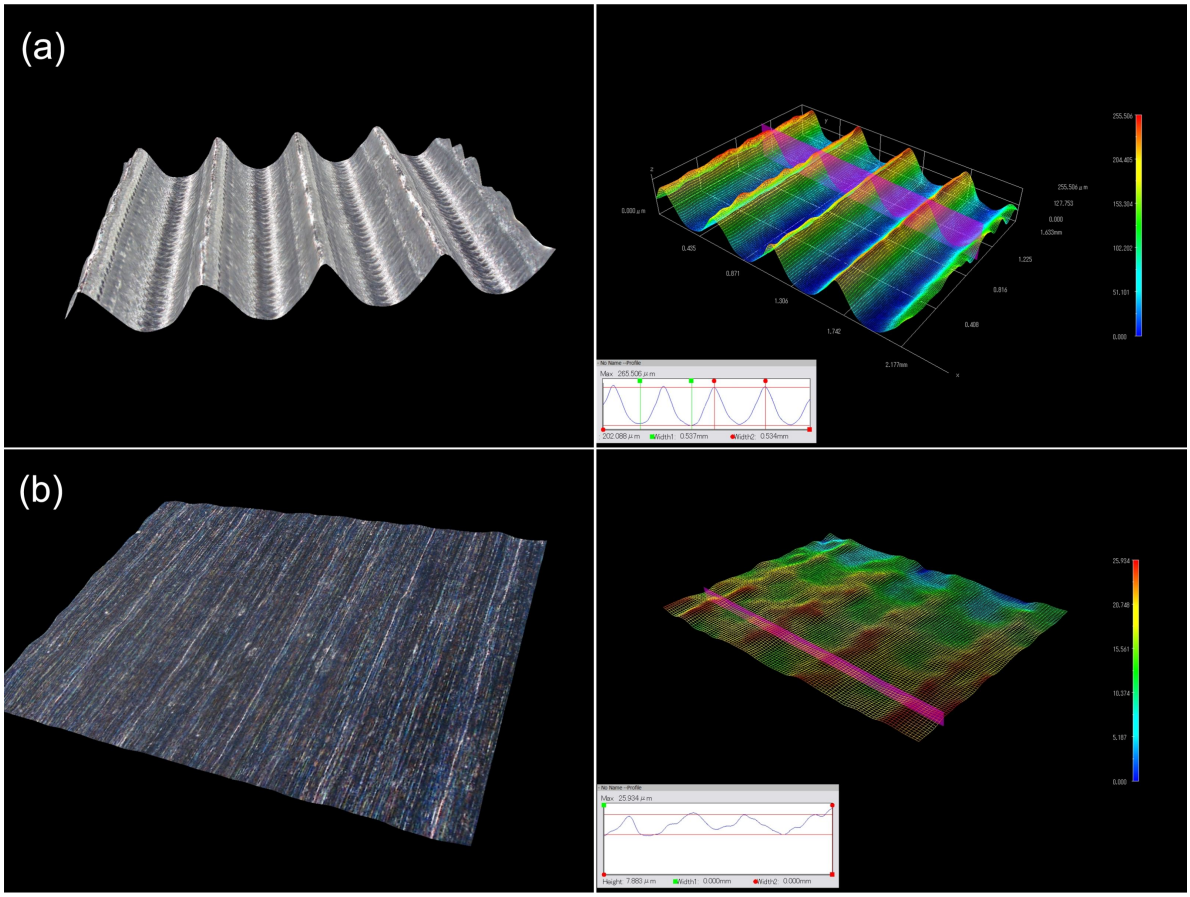

Figure 19: Microscopy observation of (a) microribs surface morphology and (b) blade surface morphology.

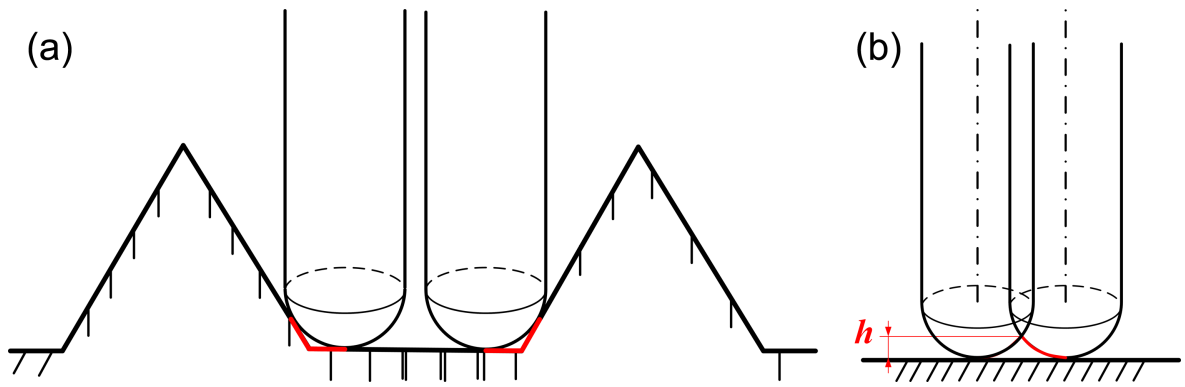

Figure 20: Machining error analysis diagram of (a) the microtexture and (b) plane processing.

Figure 21 and Figure 22 illustrate the distribution of LC_{TP} and outlet Ma at three different angles of attacks. A higher LC_{TP} and a lower Ma indicate a poorer aerodynamic performance of the blade. According to Figure 21a and Figure 22a, the blade with microtexture exhibits an increase in LC_{TP} from 0.4 to 0.5, while the Ma in the flow channel center decreases from 0.2 to 0.13. These results indicate that, at the flow angle of 52.8°, the microtexture has an adverse effect on the aerodynamic performance of the blade, resulting in increased drag. Figure 21c and Figure 22c show that the blade with microtexture yields a smaller LC_{TP} compared to the smooth blade, and the Ma is slightly higher. These results indicate a reduction in system

Table 11: Experimental results at inlet and outlet of the smooth blade.

Angle of attack (°)	TP_1 (Pa)	P_1 (Pa)	TP_2 (Pa)	P_2 (Pa)	V_1 (m/s)[a]	V_2 (m/s)[b]	ξ_0 (%)
52.8	108056	98763	105010	100920	123.66	91.56	41.61
54.8	109091	98833	104266	101071	129.50	69.00	58.98
57.0	111402	99905	104647	101292	135.91	70.21	65.45

[a]inlet velocity; [b]outlet velocity; [c]energy loss coefficient of the smooth blade.

Table 12: Experimental results at inlet and outlet of the microtextured blade.

Angle of attack (°)	TP_1 (Pa)	P_1 (Pa)	TP_2 (Pa)	P_2 (Pa)	V_1 (m/s)[a]	V_2 (m/s)[b]	ξ_1 (%)[c]
52.8	108840	99248	105190	101131	125.23	79.23	46.17
54.8	109810	99393	104571	101269	130.10	69.38	60.09
57.0	110853	99359	104828	101488	136.24	69.87	63.02

[a]inlet velocity; [b]outlet velocity; [c]energy loss coefficient of the microtextured blade.

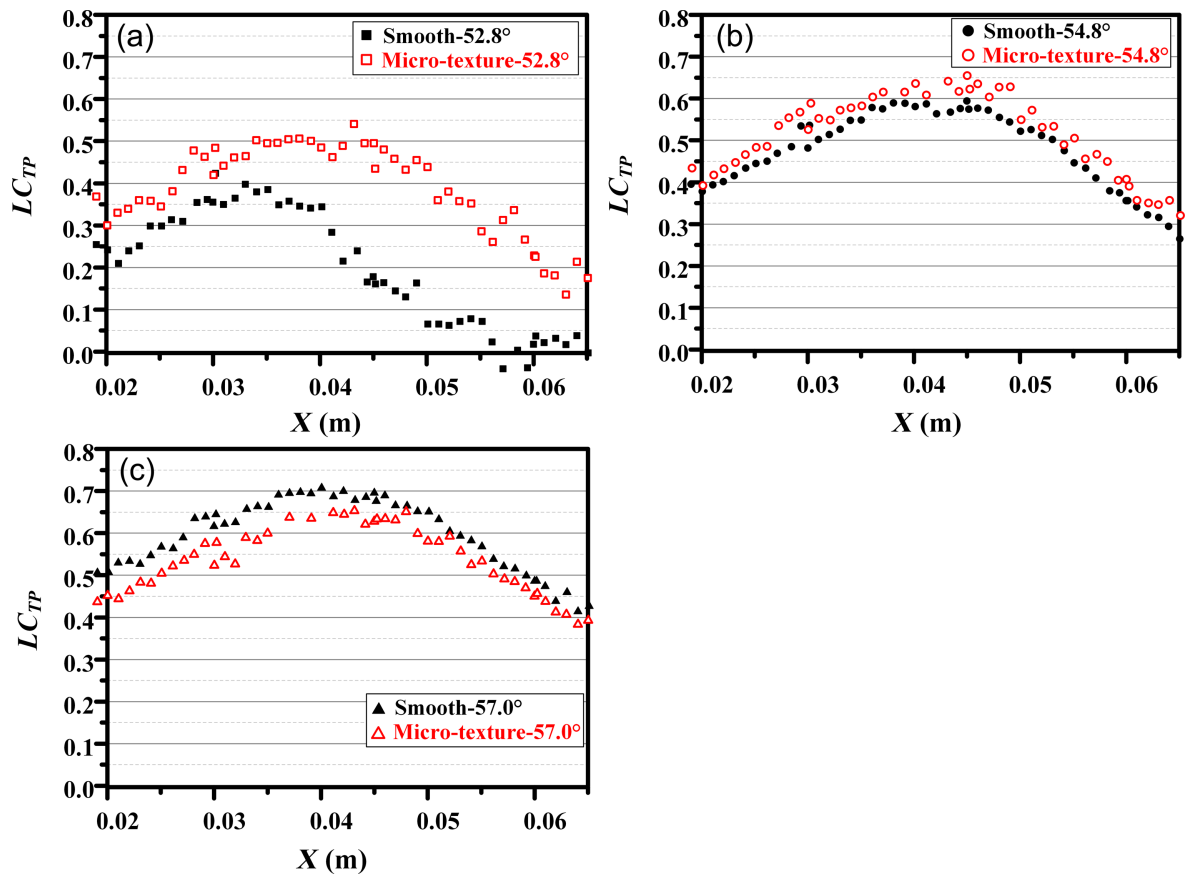

Figure 21: Distribution of LC_{TP} of the single flow channel at angles of attack of (a) 52.8°, (b) 54.8°, and (c) 57.0°.

energy loss. Overall, the microtexture arranged in the back section of the blade positively impacts aerodynamic performance and reduces system energy loss, particularly at the angle of attack of 57°.

The microtexture was arranged at the back end of the blade suction surface based on the analysis of the simulation results, and the drag reduction effect of the microtexture was verified in the wind tunnel experiment. As shown in Figure 23, the drag

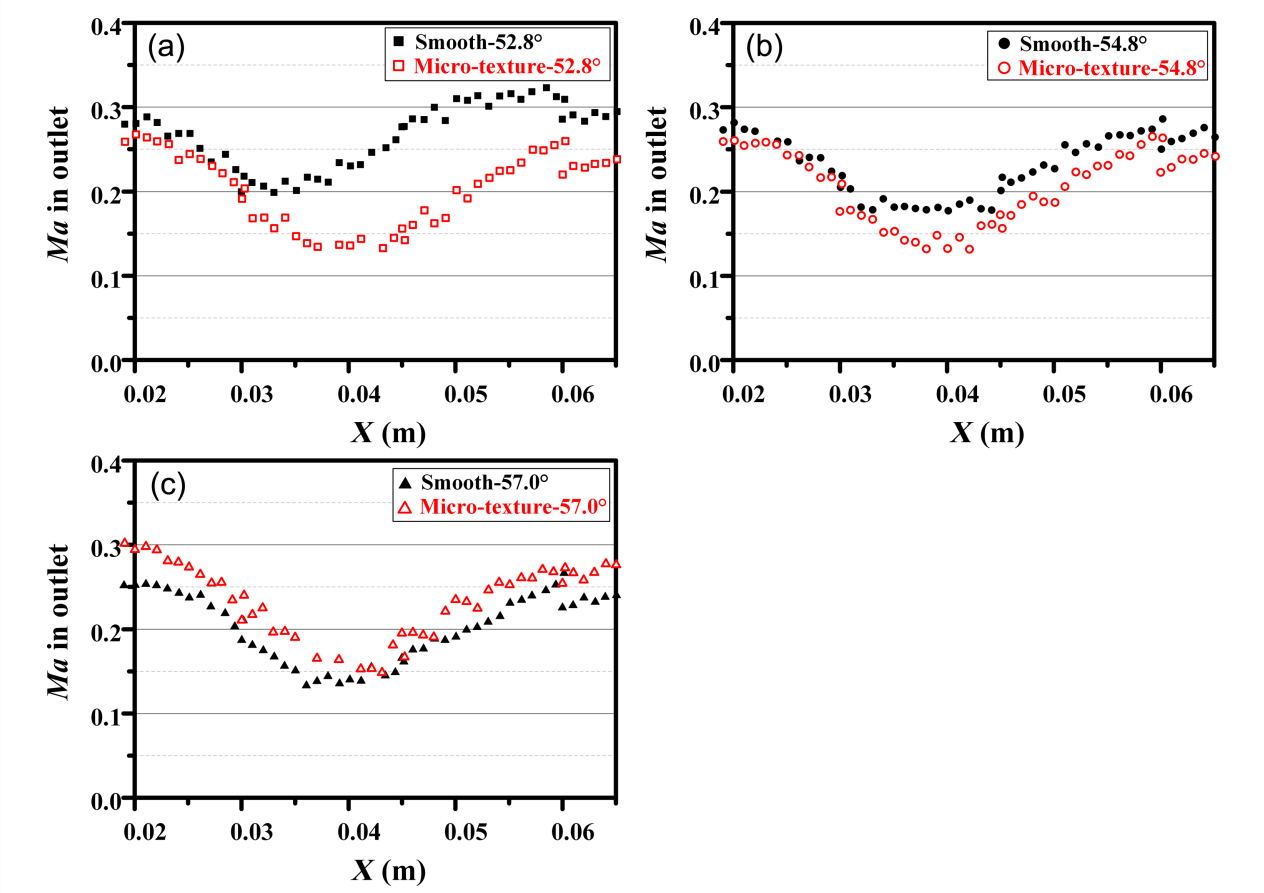

Figure 22: Distribution of Ma in the outlet of the single flow channel at angles of attack of (a) 52.8°, (b) 54.8°, and (c) 57.0°.

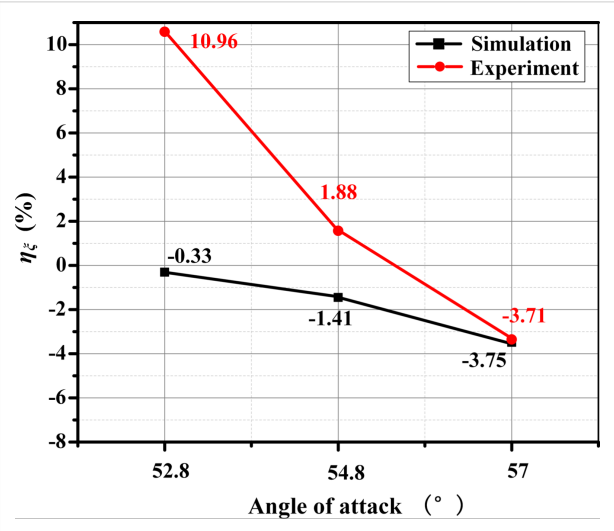

Figure 23: Comparison between the simulation value and the experimental value of η_ξ.

reduction performance of the microtexture blade is the best when the angle of attack is 57°; η_ξ in the experiment can reach −3.7%. Although the difference between the simulation results and the experimental results is large under the other two attack angles, the trend of η_ξ of the two results is the same. The larger the angle of attack, the smaller η_ξ.

Conclusion

This paper studies an axial flow compressor and presents a simplified numerical simulation method for the rotating blade surface. Furthermore, microtexture design and simulation analysis are carried out on the blade surface to explore the drag reduction performance and mechanism of microtexture. The conclusions are as follows: (1) A simplified simulation method is proposed from the whole impeller to a single impeller blade, establishing the relationship between plane and surface. Theoretical calculations and numerical simulations are employed to design and verify the optimal microtexture for drag reduction performance. The determined microtexture dimensions are a height of 0.2 mm, a width of 0.3 mm, and a spacing of 0.2 mm. (2) The drag reduction mechanism is analyzed and compared for microtextures with different geometric size factors. The presence of microtextures on the blade surface effectively impedes turbulence generation, thus, reducing the turbulent kinetic energy and wall shear stress to reduce drag. (3) The

simulation results reveal that positioning the optimally sized microstructure at the back end of the blade yields significant benefits. The DRR for a single blade reaches 1.31%, accompanied by a reduction of 1.45% in η_ξ. (4) A blade cascade experiment is conducted in the high-speed wind tunnel to analyze the energy loss coefficient and wake loss distribution. The results demonstrate a reduction in energy consumption of 3.7% at a flow velocity of 136.24 m/s and an attack angle of 57°.

Bionic microstructures have little influence on the overall strength of the objects they are attached to because of their small size. Their particular functions are of high research value in the application of object surfaces, but there are also some challenges in practical applications. The cost of microstructures in large-area manufacturing and application is large. However, the size effect is the key of microstructures exhibiting good performance. Hence, the large-area manufacturing of high-precision microstructures is worth studying. Chemicals (e.g., polydimethylsiloxane) can quickly replicate biomimetic microstructures, but the operation process is complex, and the soft surfaces are not suitable for surfaces in high-speed flows.

Supporting Information

Supporting information text contains the hydrodynamic theory covered in this paper, including the boundary layer theory, the formulas for calculating the drag reduction performance of the blade and a description of flow separation on the blade surface.

Supporting Information File 1

Boundary layer theory, drag reduction formulas, and blade surface flow.
[https://www.beilstein-journals.org/bjnano/content/supplementary/2190-4286-15-70-S1.pdf]

Author Contributions

Qinsong Zhu: methodology; visualization; writing – original draft; writing – review & editing. Chen Zhang: conceptualization; supervision; writing – review & editing. Fuhang Yu: investigation; methodology. Yan Xu: investigation; resources.

ORCID® iDs

Qinsong Zhu - https://orcid.org/0000-0001-7674-7205

Data Availability Statement

The data that supports the findings of this study is available from the corresponding author upon reasonable request.

Preprint

A non-peer-reviewed version of this article has been previously published as a preprint:
https://www.beilstein-journals.org/xiv/download/pdf/20243-pdf

References

1. Koch, K.; Bhushan, B.; Barthlott, W. *Prog. Mater. Sci.* **2009,** *54,* 137–178. doi:10.1016/j.pmatsci.2008.07.003
2. Chen, D.; Liu, X.; Cui, X.; Zhang, L.; Chen, H. *Prog. Org. Coat.* **2023,** *182,* 107613. doi:10.1016/j.porgcoat.2023.107613
3. Benschop, H. O. G.; Breugem, W.-P. *J. Turbul.* **2017,** *18,* 717–759. doi:10.1080/14685248.2017.1319951
4. Barthlott, W.; Neinhuis, C. *Planta* **1997,** *202,* 1–8. doi:10.1007/s004250050096
5. Neinhuis, C.; Barthlott, W. *Ann. Bot. (Oxford, U. K.)* **1997,** *79,* 667–677. doi:10.1006/anbo.1997.0400
6. Lauder, G. V.; Wainwright, D. K.; Domel, A. G.; Weaver, J. C.; Wen, L.; Bertoldi, K. *Phys. Rev. Fluids* **2016,** *1,* 060502. doi:10.1103/physrevfluids.1.060502
7. Gabler-Smith, M. K.; Lauder, G. V. *Front. Mar. Sci.* **2022,** *9,* 975062. doi:10.3389/fmars.2022.975062
8. Lang, A. W.; Jones, E. M.; Afroz, F. *Bioinspiration Biomimetics* **2017,** *12,* 026005. doi:10.1088/1748-3190/aa5770
9. Xiao, G.; He, Y.; Huang, Y.; He, S.; Wang, W.; Wu, Y. *Proc. Inst. Mech. Eng., Part B* **2021,** *235,* 2230–2239. doi:10.1177/0954405420949744
10. Tian, G.; Fan, D.; Feng, X.; Zhou, H. *RSC Adv.* **2021,** *11,* 3399–3428. doi:10.1039/d0ra08672j
11. Park, S.-R.; Wallace, J. M. *AIAA J.* **1994,** *32,* 31–38. doi:10.2514/3.11947
12. Xu, Y.; Song, W.; Zhao, D. *AIAA J.* **2018,** *56,* 1483–1494. doi:10.2514/1.j056122
13. Yadav, N.; Gepner, S. W.; Szumbarski, J. *Int. J. Heat Fluid Flow* **2021,** *87,* 108751. doi:10.1016/j.ijheatfluidflow.2020.108751
14. Carreño Ruiz, M.; D'Ambrosio, D. *Aerosp. Sci. Technol.* **2023,** *132,* 108047. doi:10.1016/j.ast.2022.108047
15. Walsh, M. J. Turbulent Boundary Layer Drag Reduction Using Riblets. In *20th Aerospace Sciences Meeting,* Orlando, FL, USA, Jan 11–14, 1982; American Institute of Aeronautics and Astronautics (AIAA), 1982. doi:10.2514/6.1982-169
16. Chamorro, L. P.; Arndt, R. E. A.; Sotiropoulos, F. *Renewable Energy* **2013,** *50,* 1095–1105. doi:10.1016/j.renene.2012.09.001
17. Zhang, C.; Saurav Bijay, K. *Aerosp. Sci. Technol.* **2018,** *72,* 380–396. doi:10.1016/j.ast.2017.11.007
18. Mischo, B.; Behr, T.; Abhari, R. S. *J. Turbomachinery* **2008,** *130,* 021008. doi:10.1115/1.2775485
19. Prakash, C.; Lee, C. P.; Cherry, D. G.; Doughty, R.; Wadia, A. R. *J. Turbomachinery* **2006,** *128,* 639–642. doi:10.1115/1.2220050
20. Patel, D. S.; Jain, V. K.; Shrivastava, A.; Ramkumar, J. *Int. J. Adv. Manuf. Technol.* **2019,** *100,* 1269–1286. doi:10.1007/s00170-016-9700-3
21. Koeltzsch, K.; Qi, Y.; Brodkey, R. S.; Zakin, J. L. *Exp. Fluids* **2003,** *34,* 515–530. doi:10.1007/s00348-003-0590-4
22. Wu, Z.; Li, S.; Liu, M.; Wang, S.; Yang, H.; Liang, X. *Eng. Appl. Comput. Fluid Mech.* **2019,** *13,* 1024–1035. doi:10.1080/19942060.2019.1665101
23. Liang, T.; Xu, Y.; Li, J.; Cai, G. *Alexandria Eng. J.* **2022,** *61,* 2673–2686. doi:10.1016/j.aej.2021.07.029

24. Yang, S. J.; Baeder, J. D. *Wind Eng.* **2019,** *43,* 4–25. doi:10.1177/0309524x18818646
25. Amzad Hossain, M.; Nizam Uddin, M.; Mustak, R.; Mashud, M. *Int. J. Eng. Sci.* **2015,** *4,* 13–17.
26. Mao, X.; Liu, B.; Zhang, B. *Aerosp. Sci. Technol.* **2019,** *91,* 219–230. doi:10.1016/j.ast.2019.05.011
27. File:CFM56 dsc04641.jpg. Wikimedia Commons, 2005; https://commons.wikimedia.org/wiki/File:CFM56_dsc04641.jpg (accessed June 26, 2024).
28. Li, C.; Li, X.; Li, P.; Ye, X. *Energy* **2014,** *75,* 534–548. doi:10.1016/j.energy.2014.08.015
29. Kueh, T. C.; Beh, S. L.; Ooi, Y. S.; Rilling, D. G. *J. Phys.: Conf. Ser.* **2017,** *822,* 012066. doi:10.1088/1742-6596/822/1/012066
30. Song, Z.; Zheng, X.; Wang, B.; Zhou, K.; Amankwa Adjei, R. *Aerosp. Sci. Technol.* **2023,** *136,* 108187. doi:10.1016/j.ast.2023.108187
31. Raayai-Ardakani, S.; McKinley, G. H. *Phys. Fluids* **2019,** *31,* 053601. doi:10.1063/1.5090881
32. Walsh, M. J. *AIAA J.* **1983,** *21,* 485–486. doi:10.2514/3.60126
33. Raayai-Ardakani, S.; McKinley, G. H. *Phys. Fluids* **2017,** *29,* 093605. doi:10.1063/1.4995566

License and Terms

This is an open access article licensed under the terms of the Beilstein-Institut Open Access License Agreement (https://www.beilstein-journals.org/bjnano/terms), which is identical to the Creative Commons Attribution 4.0 International License (https://creativecommons.org/licenses/by/4.0). The reuse of material under this license requires that the author(s), source and license are credited. Third-party material in this article could be subject to other licenses (typically indicated in the credit line), and in this case, users are required to obtain permission from the license holder to reuse the material.

The definitive version of this article is the electronic one which can be found at:
https://doi.org/10.3762/bjnano.15.70

BEILSTEIN JOURNAL OF NANOTECHNOLOGY

The effect of age on the attachment ability of stick insects (Phasmatodea)

Marie Grote, Stanislav N. Gorb and Thies H. Büscher*

Full Research Paper

Open Access

Address:
Functional Morphology and Biomechanics, Kiel University, Am Botanischen Garten 1-9, D-24118 Kiel, Germany

Email:
Thies H. Büscher* - tbuescher@zoologie.uni-kiel.de

* Corresponding author

Keywords:
adhesion; attachment pads; friction; locomotion; morphology; material properties; wear

Beilstein J. Nanotechnol. **2024,** *15,* 867–883.
https://doi.org/10.3762/bjnano.15.72

Received: 20 March 2024
Accepted: 04 July 2024
Published: 15 July 2024

This article is part of the thematic issue " Biomimetics and bioinspired surfaces: from nature to theory and applications".

Associate Editor: P. Leiderer

© 2024 Grote et al.; licensee Beilstein-Institut.
License and terms: see end of document.

Abstract

Many insect species have found their way into ageing research as small and easy-to-keep model organisms. A major sign of ageing is the loss of locomotory functions due to neuronal disorders or tissue wear. Soft and pliable attachment pads on the tarsi of insects adapt to the substrate texture to maximize their real contact area and, thereby, generate attachment during locomotion. In the majority of stick insects, adhesive microstructures covering those pads support attachment. Stick insects do not molt again after reaching the imaginal stage; hence, the cuticle of their pads is subject to continuous ageing. This study aims to quantify how attachment ability changes with age in the stick insect *Sungaya aeta* Hennemann, 2023 and elucidate the age effects on the material and microstructure of the attachment apparatus. Attachment performance (adhesion and friction forces) on substrates with different roughnesses was compared between two different age groups, and the change of attachment performance was monitored extending over a larger time frame. Ageing effects on the morphology of the attachment pads and the autofluorescence of the cuticle were documented using light, scanning electron, and confocal laser scanning microscopy. The results show that both adhesion and friction forces decline with age. Deflation of the pads, scarring of the cuticle, and alteration of the autofluorescence, likely indicating stiffening of the cuticle, were observed to accumulate over time. This would reduce the attachment ability of the insect, as pads lose their pliant properties and cannot properly maintain sufficient contact area with the substrate.

Introduction

Ageing inexorably affects most living organisms, does not exclude insects, and makes different organs or tissues susceptible to wear or fatigue of material [1]. Research on the time-dependent decline of body functions has often been focused on vertebrates, especially mammals, but insects have found their way into ageing research as well [2-4]. They are easy to maintain and have a short lifespan, and changes in their exoskeleton can be easily observed [5]. The process of ageing has been explored most thoroughly in *Drosophila melanogaster* (Meigen, 1830) and other dipterans, often with special regards to flight

[2,4,6-8]. Other studies on ageing in insects included economically or ecologically important species, such the silkworm moth *Bombyx mori* (L., 1758) or ants [4]. One difficulty of measuring age-dependent functional decay is finding feasible methods to investigate underlying material fatigue.

One functional system affected by age and of concern for locomotion and, hence, for the survival of individual insects is the attachment system. Two different attachment mechanisms evolved in insects, namely, hairy pads consisting of flexible setae, which adapt to the surface topography, and smooth pads possessing a soft and deformable cuticle to comply with the substrate profile [9]. Both pad types, hairy and smooth, aim to maximize contact area with the substrate as the contact area of the pad is proportional to adhesion [10-12]. For rough substrates, the pads are complemented by a pair of rigid claws used for friction interlocking with surface asperities and ensuring attachment, but claws perform poorly on smooth surfaces [13]. The ability to attach to various surfaces is helpful for climbing animals [11,14], and adapting to the quality of the substrate is especially important for motile animals, which may come into contact with different surfaces, such as plants [9,11,15]. In ageing cockroaches, attachment pad discoloration and increased stiffness are accompanied by the decreased ability to climb an incline [5,16]. Zhou et al. [17] found stiffer and darker "scars" on the pads of aged cockroaches, most likely due to accumulated damage, resulting in the pads not being as compliant as in younger cockroaches. Slifer [18] made similar observations in locusts walking on abrasive sandpaper, leading to the formation of scars in older animals. Scars and stiffened cuticle likely conflict with the functionality of soft adhesive pads as the contact formation of the cuticle is hampered by the reduced material compliance.

Phasmatodea, also known as stick and leaf insects, are a lineage of large terrestrial insects encompassing around 3500 described species thriving in different habitats [19,20]. They are exclusively herbivorous and camouflage themselves as twigs, leaves, or bark [19,21]. As phasmids are slow and most of them wingless or unable to fly, they adapted strongly to their local environment [11,19,22,23]. Phasmids have evolved considerably depending on plants since pre-angiosperm times [24]. As plants display a huge range of different surface characteristics [25-28], the diversity of microstructures on phasmatodean attachment pads is assumed to result from adaptations towards these plant surfaces [23,29]. Phasmids possess smooth adhesive pads on their tarsomeres, the euplantulae, and one larger pad at the pretarsus, the arolium [30]. Investigations of the specific functionality of both euplantulae and the arolium by Labonte and Federle [31] have shown that the arolium and euplantulae each perform different tasks. The arolium is used while climbing upside down, whereas the euplantulae generate friction and are used in upright walking. Phasmid euplantulae are covered with different surface microstructures that are likely adapted to specific surface parameters in their environments [32-34]. It has been shown that nubby euplantulae perform better on rough surfaces whereas pads without protrusions perform better on smooth surfaces [35]. Experimental studies concerning the attachment ability of phasmids investigated various functions of this system and how it changes under certain conditions, such as substrate geometry [36], the presence or absence of claws [37], different surface characteristics of substrates [33,38,39], and the combined effect with pad fluids [40]. For these animals, whose lives strongly depend on plants for camouflage and nutrition, attachment to the plant surface is crucial for survival [11,14,21].

Their life history makes phasmids interesting study subjects for ageing research, as this lineage represents some of the largest insects known and species that have a prolonged life expectancy of up to three years after imaginal molt [41]. After this last molt, phasmids do not molt anymore and, hence, their cuticle is subject to continuous ageing. So far, representatives of Phasmatodea and their adhesive systems have not been investigated with regards to ageing. Nevertheless, the stiffness of the cuticle of these organs and the internal pressure are important for the functionality and likely susceptible to decay during ageing [42,43]. We investigated the change in attachment ability and tarsal morphology in the species *Sungaya aeta* Hennemann, 2023 (Heteropterygidae). Members of Heteropterygidae can reach impressive life expectancies [41,44], with anecdotal reports extending over five years. The change in attachment performance was quantified through attachment force measurements. Because of the different properties of arolium and euplantulae [31,33], the attachment forces of whole animals were compared in two directions. The pull-off force was measured perpendicular to the substrate, and the traction force parallel to the substrate, to assess the ability of the insect to attach itself in the respective direction and evaluate potential differences arising from performance decay of either of the two components of the overall attachment system.

The aim of this study was to answer the following research questions: (1) Does the attachment ability of older animals differ from that of younger animals? (2) Do pull-off and traction forces on the same substrates change during age? (3) Does the morphology of the tarsus and the attachment pads differ between younger and older animals?

Materials and Methods

1 Animals and experimental conditions

Two groups of 15 adult females per group of *Sungaya aeta* Hennemann, 2023 (Phasmatodea: Heteropterygidae, Figure 1)

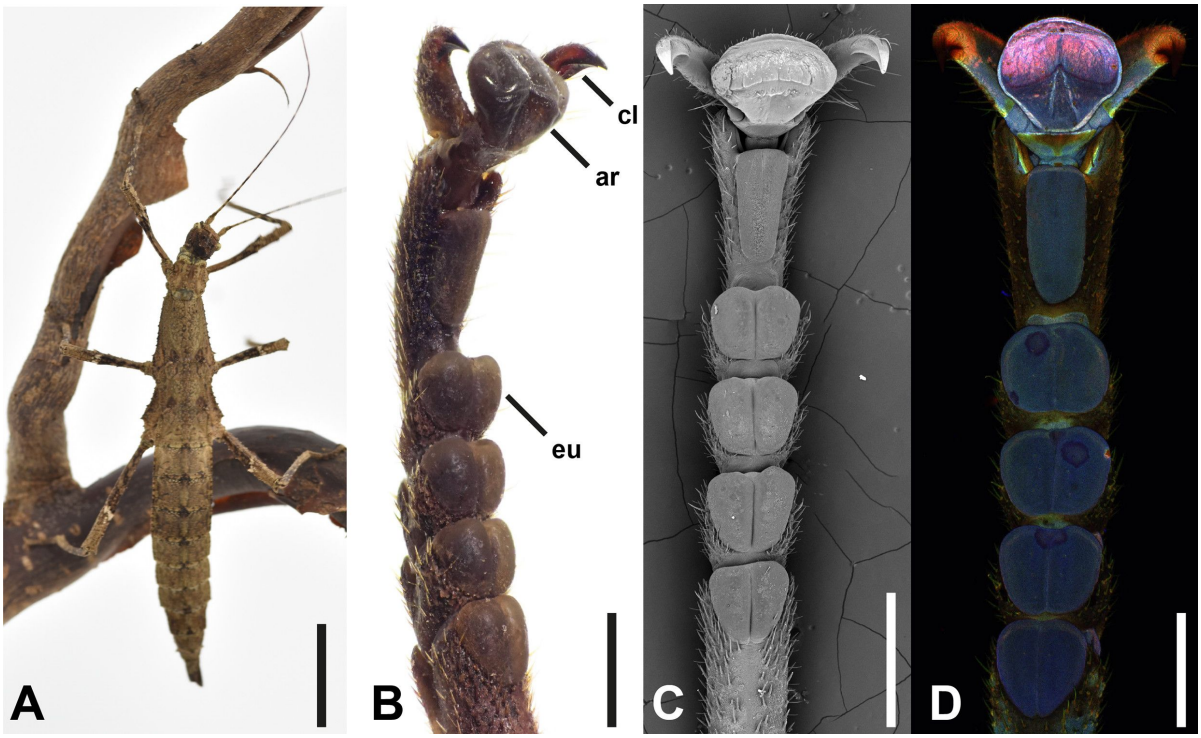

Figure 1: Focal species. (A) Adult female of *Sungaya aeta*. (B–D) Overviews of the tarsal morphology obtained with different techniques: (B) stereomicroscope, (C) scanning electron microscope, and (D) confocal laser scanning microscope. ar, arolium; cl, claw; eu, euplantula. Scale bars: (A) 2 cm, (B–D) 1 mm.

were selected from laboratory stock (Department for Functional Morphology and Biomechanics, Kiel University), kept under ambient conditions, and fed with fresh blackberry leaves ad libitum. This species was previously referred to as *Sungaya inexpectata* Zompro, 1996, until the original population of this widespread culture stock from Bataan Province, Ilanin Forest, Philippines was described as a new species [45]. The groups were selected by age, that is, "younger" females molted into the adult stage about 1 month before experiments started and "older" females ca. 3.5–4.0 months after molt respectively. The age difference between groups was approximately ten weeks. Animals were only considered for experiments with all legs and tarsi completely intact. Prior to the measurements, animals were weighed using a precision scale (Mettler Toledo AG204 DeltaRange, Mettler-Toledo International Inc., USA). Measurements were conducted during daytime, at a temperature of 24.6 ± 1.9 °C and an ambient humidity of 51.0% ± 6.9%. Deceased animals were frozen at −70 °C for subsequent investigation of the tarsal morphology.

2 Attachment on a smooth incline

The adhesive abilities on a smooth incline were determined using a custom-made tilting platform following the methodology of Berthé et al. [46] with a glass plate as substrate for attachment. Each animal was placed onto the horizontal glass plate, and the plate was then slowly tilted with an average angular velocity of ca. 3.5° per second until the insect started to slide down or fell off (Figure 2A). The positions and orientations of the animals were standardized, that is, always in the center of the plate with the head facing in the same direction. Values were recorded in intervals of 5°, and the mean of the three measurements was considered for further analysis.

3 Force measurements

Attachment force measurements were conducted using a BIOPAC MP100 data acquisition system with a TCI-102 interface (BIOPAC Systems, Inc., USA) and a 100g force transducer (Fort100, World Precision Instruments, Sarasota, FL) using the setup described in Winand and coworkers [37]. We measured pull-off (perpendicular to the substrate) and traction (parallel to the substrate) forces on substrates with three different roughnesses. The substrates were fixed onto a scissor lab jack or a precision slide (Cleveland Lineartechnik GmbH, Löfflingen, Germany). We used glass and epoxy resin [47] replicas of substrates with 1 µm and 12 µm roughness according to Büscher and Gorb [33] to test for differences in the attachment performance on different degrees of surface roughness during ageing. This range of substrate roughness was selected to test for different aspects of the functionality of the attachment pads without major influences of the claws [33,37].

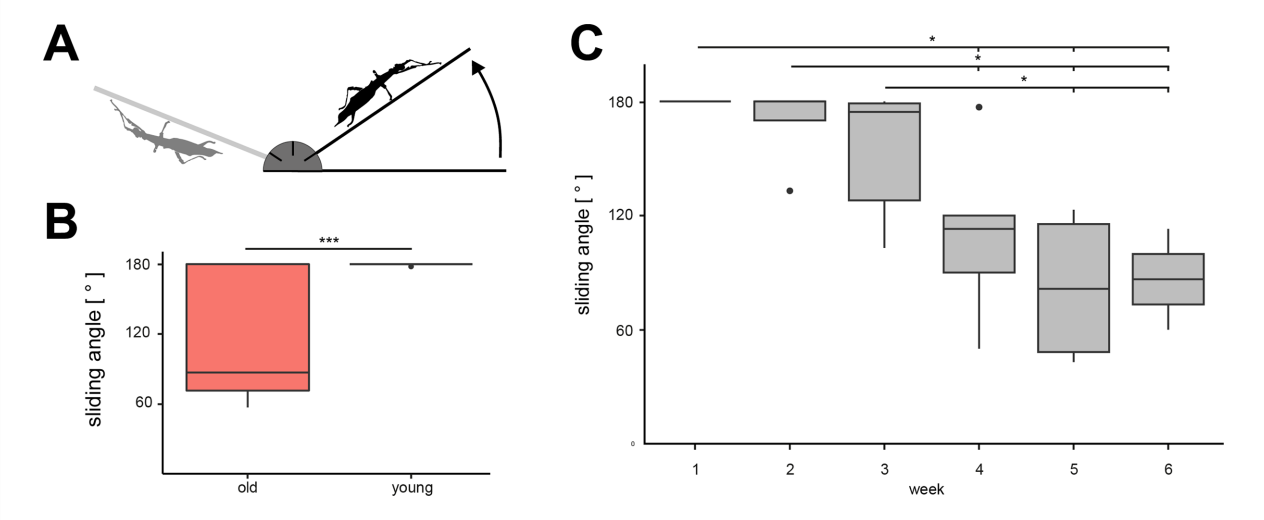

Figure 2: Attachment tests using a tilting platform. (A) Schematic of the experimental setup. (B) Comparison of sliding angles, presented by age (old/young). *** = $p < 0.001$, Wilcoxon rank sum test. (C) Weekly measured sliding angles on glass of the insects while ageing over the course of six weeks. * = $p < 0.05$, One Way Repeated Measures ANOVA/Dunn's post-hoc test with Holm correction. Boxes cover the interquartile range (IQR) from 25th to 75th percentile, the black line indicates the median. Whiskers extend to 1.5·IQR.

On smooth surfaces (0 µm), smooth pads generate proper contact with the surface. Microrough surfaces interfere with the contact formation of smooth pads; however, the dimension of the nubs on the euplantulae yield different responses to the roughness because fine roughness (1 µm) matches the size of the tips and course roughness (12 µm) matches the size of the entire nubs [33]. The combination of these three levels of roughness was used to investigate potential effects in the three mentioned perspectives of the attachment pads. For details on the fabrication process, the roughness parameters, and the contact angles of the substrates, see [12]. Per trial, the respective force was measured three times per animal and substrate. The order of the substrates was randomized for each direction (pull-off and traction forces) and animal. The insect was anaesthetized with carbon dioxide for 10–15 s before being connected to the force transducer by a string of fishing line (0.18 mm) at the mesothorax at the estimated center of mass [33,48]. The animals were allowed to recover for some minutes until they were responding to being lifted off the substrate with leg movements.

Time–force curves were recorded using AcqKnowledge (3.7.0, BIOPAC Systems, Inc., USA) while moving the substrate and platform manually with steady speed in the required direction. The maximum traction or pull-off force was recorded (see [33]). The means of the three measurements per trial were used for data analysis to reduce intra-individual variance. As one old female deceased within the experimental time, the sample size was 15 for both groups regarding pull-off forces and for the young group regarding traction forces; the sample size was 14 for traction force measurements in the old group. A list of all measurements of attachment forces and body weights is included in Supporting Information File 1.

4 Attachment over time

To further investigate the relation between progressing age and pull-off/traction force performance, six of the younger animals were used for further experiments. The abovementioned attachment measurements (see sections 2 and 3) were repeated once a week for six consecutive weeks. The measurements started ca. 1.5 months post adult molt. The order of substrates and the direction to be measured first were randomized per animal and week.

5 Light microscopy

The tarsi of all animals were documented postmortem using a stereo microscope (Nikon SMZ745T, Nikon Corporation, Tokyo, Japan). Pictures were taken using a Sony DSC-RX0 (Sony Group Corporation, Tokyo, Japan) equipped with a C-mount adapter using a RX0 Mod Kit (Back-Bone Gear Inc., Ontario, Canada). Frozen animals were allowed to thaw, and tarsi were removed for examination. Stacks of images were taken from different focus planes and combined subsequently. Images were processed using Adobe Photoshop v24.7 and Adobe Lightroom Classic 12.0 (Adobe Inc., San Jose, USA). After focus stacking and cropping, clarity and contrast were adjusted.

6 Widefield fluorescence microscopy (WFM)

Autofluorescence signals of insect cuticle can be used to investigate the material composition of the arthropod exoskeleton [49]. To scan for differences in the fluorescence, a selection of

tarsi across all age groups was examined using WFM. Freshly molted adult and subadult individuals were acquired from laboratory stock and used for imaging as well. Three individuals were chosen for each age group.

Tarsi were cut off at the tarso-tibial joint and transferred into 1.5 mL solution of phosphate-buffered saline (PBS) and Triton TM-X100 (Sigma-Aldrich, St. Louis, USA) for 30 min to reduce surface tension and enable proper glycerin coating. Afterwards, samples were rinsed three times in glycerin and then fully submerged in glycerin and covered with a high-precision cover slip (Carl Zeiss Microscopy GmbH, Jena, Germany).

Images were taken using a Zeiss Axioplan microscope and an AxioCam MRc camera with the AxioVision software (v. 4.8.2) (Carl Zeiss AG, Oberkochen, Germany). The tarsi were examined at 5× magnification. Sets of excitation and emission filters were used according to [50].

7 Confocal laser scanning microscopy (CLSM)

A confocal laser scanning microscope (Zeiss LSM 700, Carl Zeiss Microscopy GmbH, Jena, Germany) with stable solid-state lasers (wavelengths 405, 488, 555, and 639 nm) and the corresponding band- and longpass emission filters (BP420–480, LP490, LP560, and LP640 nm) was used to obtain detailed information about the autofluorescence of the cuticle [50]. The samples were prepared the same way as for WFM imaging (see section 6). One tarsus per respective age group was examined (subadult, freshly molted adult, young, and old). The ZEN2008 software (Carl Zeiss AG, Oberkochen, Germany) was used to generate maximum intensity projections.

8 Scanning Electron Microscopy (SEM)

For inspection of the tarsal morphology of different age groups, samples were chosen after CLSM to compare regions of interest, such as altered autofluorescence or damage. Selected tarsi were transferred from glycerin into 50% ethanol via a gradual series of glycerin (descending) and ethanol (ascending) mixtures. Afterwards, samples were dehydrated in an ascending ethanol series and dried using a Leica EM CPD300 (Leica, Wetzlar, Germany) critical point drier. The tarsi were mounted on SEM stubs and sputter-coated with 10 nm gold–palladium in a Leica Bal-TEC SCD500 (Leica Camera AG, Wetzlar, Germany) coater. A Hitachi TM3000 (Hitachi Ltd. Corporation, Tokyo, Japan) scanning electron microscope was used to document the tarsal morphology at 15 kV acceleration voltage.

9 Data analysis

Data analysis was performed in the R environment [51] using R Studio [52]. Data was tested for normal distribution and homoscedasticity using Shapiro–Wilk test and Levene's test, respectively, the latter from the "car" package [53]. Performance by direction and substrate for time series over six weeks was compared with One Way Repeated Measures Analyses of Variance (ANOVA) and Tukey's post-hoc test or Friedman's Repeated Measures ANOVA and Dunn's post-hoc test with Holm correction ("FSA" package, [54]), depending on the results of the preassumption tests. For pull-off and traction forces of old and young animals, Kruskal–Wallis One Way ANOVA and Dunn's test with Holm correction were used instead. Wilcoxon rank sum test was used for the comparison of sliding angles between old and young adult animals, according to the results of the Shapiro–Wilk test.

Results

Attachment on a smooth incline

On the tilting platform, young adult animals started sliding or detached from the substrate at 179.87° ± 0.52° (mean ± SD), whereas older animals lost grip at 118.87° ± 54.98° (Figure 2B). Instances where angles of 180° were reached did not cause the animals to slide. Despite the amount of variation among sliding angles on glass in older animals (range: old = 123.33°, young = 1.67°), the sliding angles of young adult animals were significantly higher than those of old adult animals (Wilcoxon rank sum test, $U = 40.500$, $p < 0.001$).

The attachment ability of the younger adult animals ($N = 6$) that were tested over the range of six consecutive weeks faded gradually (Figure 2C). The maximum angle at which the animals started sliding off the incline declined significantly (One Way Repeated Measures ANOVA, $F = 12.299$, d.f. = 5, $p < 0.001$). In the first three weeks, the mean sliding angle decreased slowly (week 1: 180.0° ± 0.0°; week 2: 168.6° ± 20.4°; week 3: 154.2° ± 36.0°). The mean sliding angles in these three weeks did not differ significantly from each other (Dunn's test with Holm correction, all $p > 0.050$). The mean sliding angle dropped to 110.0° ± 46.4° in week 4, which was significantly lower compared to the first two weeks (Dunn's test with Holm correction, all $p < 0.05$), but not different from week 3 (Dunn's test with Holm correction, $p = 0.092$). The sliding angles further decreased in week 5 (82.3° ± 41.69°) and week 6 (86.5° ± 37.5°), resulting in significantly lower sliding angles compared to the weeks 1–3 (Dunn's test with Holm correction, all $p < 0.050$). From week 5 to week 6, sliding angles remained similar (Dunn's test with Holm correction, $p = 0.752$). Variance increased over time.

Attachment forces

Attachment performance of young and old animals

In the pull-off direction (Figure 3A), both age and substrate had some effect on the measured forces (Kruskal–Wallis ANOVA

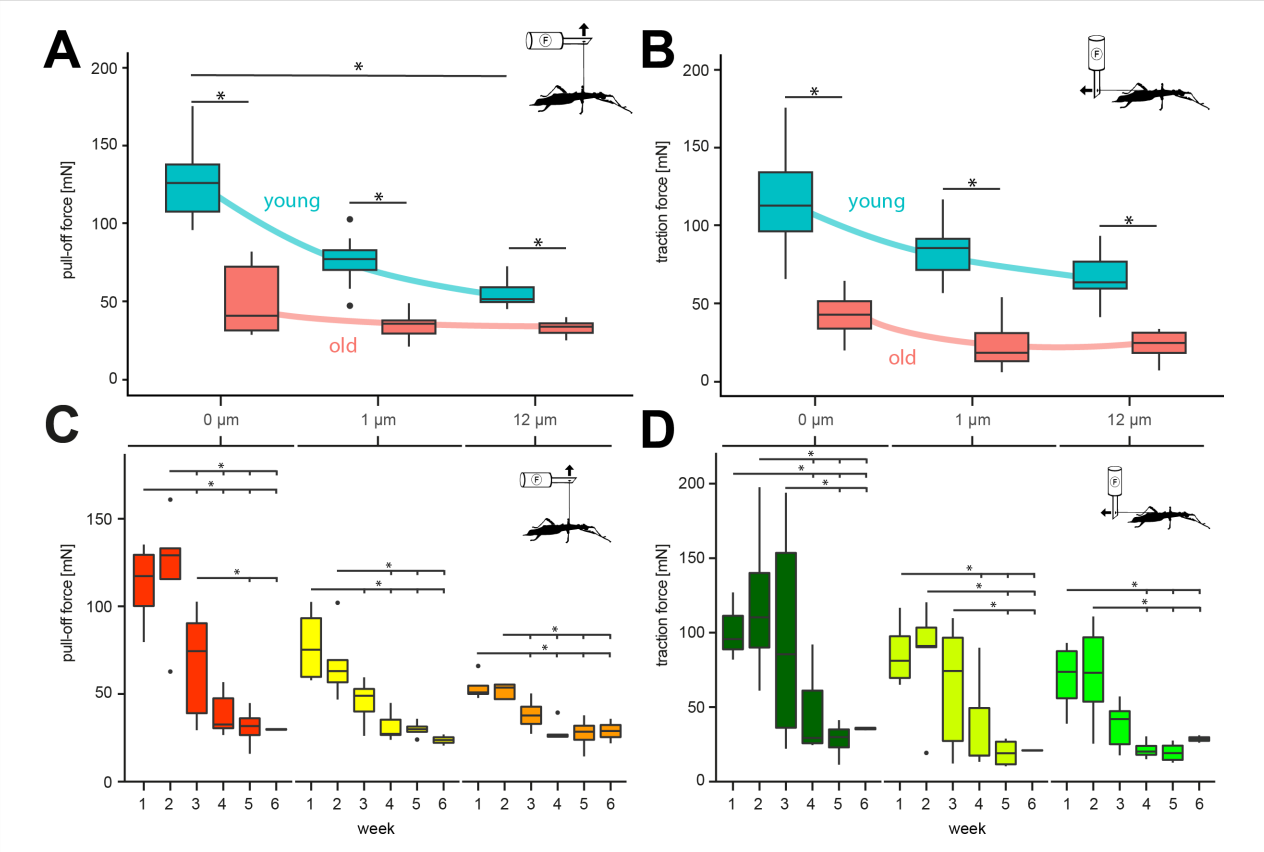

Figure 3: Attachment force measurements. (A, B) Comparisons of attachment forces of old and young adult females on substrates with different roughness. (A) Pull-off forces and (B) traction forces. * = $p < 0.05$, Kruskal–Wallis ANOVA on ranks/Dunn's post-hoc test with Holm correction. (C, D) Change of attachment forces of adult females on substrates with different roughness over the course of six weeks. Colors in C and D represent the same substrate as indicated on the top of the graph. (C) Pull-off forces. (D) Traction forces. * = $p < 0.05$, Kruskal–Wallis ANOVA on ranks/Dunn's post-hoc test with Holm correction. Boxes cover the interquartile range (IQR) from 25th to 75th percentile, the black line indicates the median. Whiskers extend to 1.5·IQR.

on ranks, H = 66.677, d.f. = 5, N_{young} = 15, N_{old} = 15, $p \leq 0.001$). In young adult animals, pull-off forces differed significantly between the three substrates (Dunn's test with Holm correction, all $p < 0.010$) and were highest on glass (124.38 ± 22.55 mN), less high on 1 µm (75.48 ± 13.51 mN), and lowest on 12 µm rough substrates (54.85 ± 8.72 mN). No significant effect was found between substrates in older animals (Dunn's test with Holm correction, all $p > 0.050$). The pull-off forces for old animals were also highest on glass (50.37 ± 21.46 mN), less high on 1 µm (34.09 ± 8.48 mN), and lowest on 12 µm rough substrates (32.46 ± 4.59 mN). Younger animals performed significantly better on all substrates compared to older animals on the same substrate (Dunn's test with Holm correction, all $p < 0.050$).

Traction forces (Figure 3B) showed relationships qualitatively similar in different animals to pull-off forces. In younger adult animals, traction forces were significantly influenced by the substrate roughness (Kruskal–Wallis ANOVA on ranks, H = 72.314, d.f. = 5, N_{young} = 15, N_{old} = 14, $p \leq 0.001$). Similar to the pull-off forces, the highest values were obtained on glass (122.31 ± 36.48 mN), lower forces on 1 µm (82.38 ± 15.25 mN), and lowest on 12 µm rough substrates (66.78 ± 14.8 mN). The traction forces on the three substrates differed significantly from each other in young adult animals (Dunn's test with Holm correction, all $p < 0.050$). Traction forces of older animals were influenced by the substrate as well (Kruskal–Wallis ANOVA on ranks, H = 72.314, d.f. = 5, N_{young} = 15, N_{old} = 14, $p \leq 0.001$). The forces were significantly higher on glass (43.13 ± 14.2 mN) compared to 1 µm (21.48 ± 14.26 mN) and 12 µm rough substrates (22.93 ± 8.74 mN) (Dunn's test with Holm correction, all $p < 0.050$). No significant difference was found between 1 and 12 µm rough substrates (Dunn's test with Holm correction, all $p > 0.050$). Differences between age groups on the same substrate were all significant (Dunn's test with Holm correction, all $p < 0.050$).

Signs of ageing were apparent during the attachment force measurements. Older animals were observed to establish less rigorous contact of their tarsi with the substrates at some occa-

sions. During traction force measurements, sometimes tarsi were not aligned with the direction of the pulling movement and were sliding more easily compared to other tarsi. However, these problems with contact formation were not persistent throughout the experiments and occurred only from time to time.

Attachment forces over time

Variances of pull-off forces were higher on glass and 1 µm roughness during the first weeks and decreased towards the fifth and sixth week, whereas results on 12 µm roughness showed the least variance across the time span. All three substrates revealed significant differences over time (RM ANOVAs, all $p \leq 0.001$). The pull-off force on glass (RM ANOVA, $F = 22.437$, d.f. = 5, $p \leq 0.001$) gradually decreased from 112.34 ± 24.83 mN in week 1 to 29.790 ± 0.56 mN in week 6. The changes of pull-off force on glass between week 1 and weeks 3–6 (Tukey's tests, all $p < 0.005$), between week 2 and weeks 4–6 (Tukey's tests, all $p < 0.001$), and between week 3 and weeks 5–6 (Tukey's tests, all $p < 0.030$) were found to be significant. On 1 µm roughness (RM ANOVA, $F = 14.346$, d.f. = 5, $p \leq 0.001$), the forces were lower than on glass in week 1 (77.72 ± 22.11 mN) and declined to 23.72 ± 4.49 mN in week 6. The changes of pull-off force on 1 µm between week 1 and weeks 3–6 (Tukey's tests, all $p < 0.003$) as well as between week 2 and weeks 4–6 (Tukey's tests, all $p < 0.003$) differed significantly. On 12 µm (RM ANOVA, $F = 15.618$, d.f. = 5, $p \leq 0.001$), the pull-off forces in week 1 were lowest compared to the other substrates (53.88 ± 8.21 mN) but still decreased towards week 6 (28.86 ± 9.83 mN). The changes from week 1 to weeks 4–6 (Tukey's tests, all $p < 0.018$) as well as from week 2 to weeks 4–6 (Tukey's tests, all $p < 0.039$) were significant as well. The pull-off forces of the remaining combinations did not differ significantly from each other (Tukey's tests, all $p > 0.15$).

The mean traction forces declined on all surfaces over time following the same trends as the pull-of forces (Figure 3D). The traction changed significantly over time as well (RM ANOVAs, $F_{glass} = 16.484$, $F_{1\ \mu m} = 12.540$, $F_{12\ \mu m} = 8.784$, all d.f. = 5, all $p \leq 0.001$). Forces declined from 126.90 ± 54.18 mN (glass), 85.99 ± 23.27 mN (1 µm), and 69.84 ± 24.59 mN (12 µm) to 35.60 ± 1.52 mN (glass), 20.95 ± 0.42 mN (1 µm), and 28.58 ± 3.47 mN (12 µm). For glass, the changes between week 1 and weeks 4–6 (Tukey's tests, all $p < 0.003$), between week 2 and weeks 4–6 (Tukey's tests, all $p < 0.007$), and between week 3 and weeks 5–6 (Tukey's tests, all $p < 0.003$) were significant. On 1 µm roughness, forces changed significantly from week 1 to weeks 4–6 (Tukey's tests, all $p < 0.011$), from week 2 to weeks 5–6 (Tukey's tests, all $p < 0.002$), and from week 3 to weeks 5–6 (Tukey's tests, all $p < 0.008$). On the 12 µm substrate, only changes from week 1 to weeks 4–6 (Tukey's tests, all $p < 0.360$) and from week 2 to weeks 4–6 (Tukey's tests, all $p < 0.044$) were significant. The traction forces of the remaining combinations did not differ significantly from each other (Tukey's tests, all $p > 0.06$).

Morphological changes

Macroscopic changes of attachment devices

All tarsi of *S. aeta* possess five euplantulae on their five tarsomeres and one arolium situated between two claws on the pretarsus (Figure 1). Ageing was mainly visible from the shape of the attachment pads themselves (Figure 4). Observations via stereomicroscopy showed that in younger animals all attachment pads are fully inflated and appear tightly filled with the fluid (Figure 4A). The condition of the attachment pads varied in older animals. Euplantulae and arolia were frequently observed to be sunken in or shriveled and discolored (Figure 4B–D). Additionally, the same pads showed variance in deflation across different specimens or legs of the same animal. Also, the attachment pads differed in the degree of deflation, depending on the tarsal segment they are located on. The degree of deflation of the pads was always higher in the distal ones. The distalmost arolium was most strongly affected by deflation in most of the cases (Figure 4B–D), whereas the degree of deflation in euplantulae differed depending on how distal the particular euplantula was situated on the tarsus (Figure 4C,D). Overall, the extent of deflation varied across the specimens and tarsi of the same animal. However, the deflation was generally strongest for older animals.

Claws were uniform in color, but claw wear was observed to vary across specimens (Figure 4E–H). In general, claw conditions ranged from fully intact (Figure 4E) to completely missing (Figure 4H). Most frequently the claw tips were broken (Figure 4F,G). The wear was strongest in older animals, but observed through all age groups.

Material changes

Changes of the cuticle of the attachment pads were investigated via WFM and CLSM. Both methods were used to visualize the autofluorescence of the pad cuticle, which is informative about the cuticle composition, for example, the degree of sclerotization [50,55]. Both methods indicate the degree of sclerotization through the autofluorescence of the materials excited with light of different wavelengths. The detected autofluorescence signals are visualized in different colors according to the excitation wavelength [50]. Blue indicates less sclerotized cuticle, green indicates rather sclerotized cuticle, and red colors indicate strongly sclerotized cuticle [50,55]. The general appearance of the autofluorescence and its distribution was uniform for all tarsi examined and corresponds to the signals known for stick

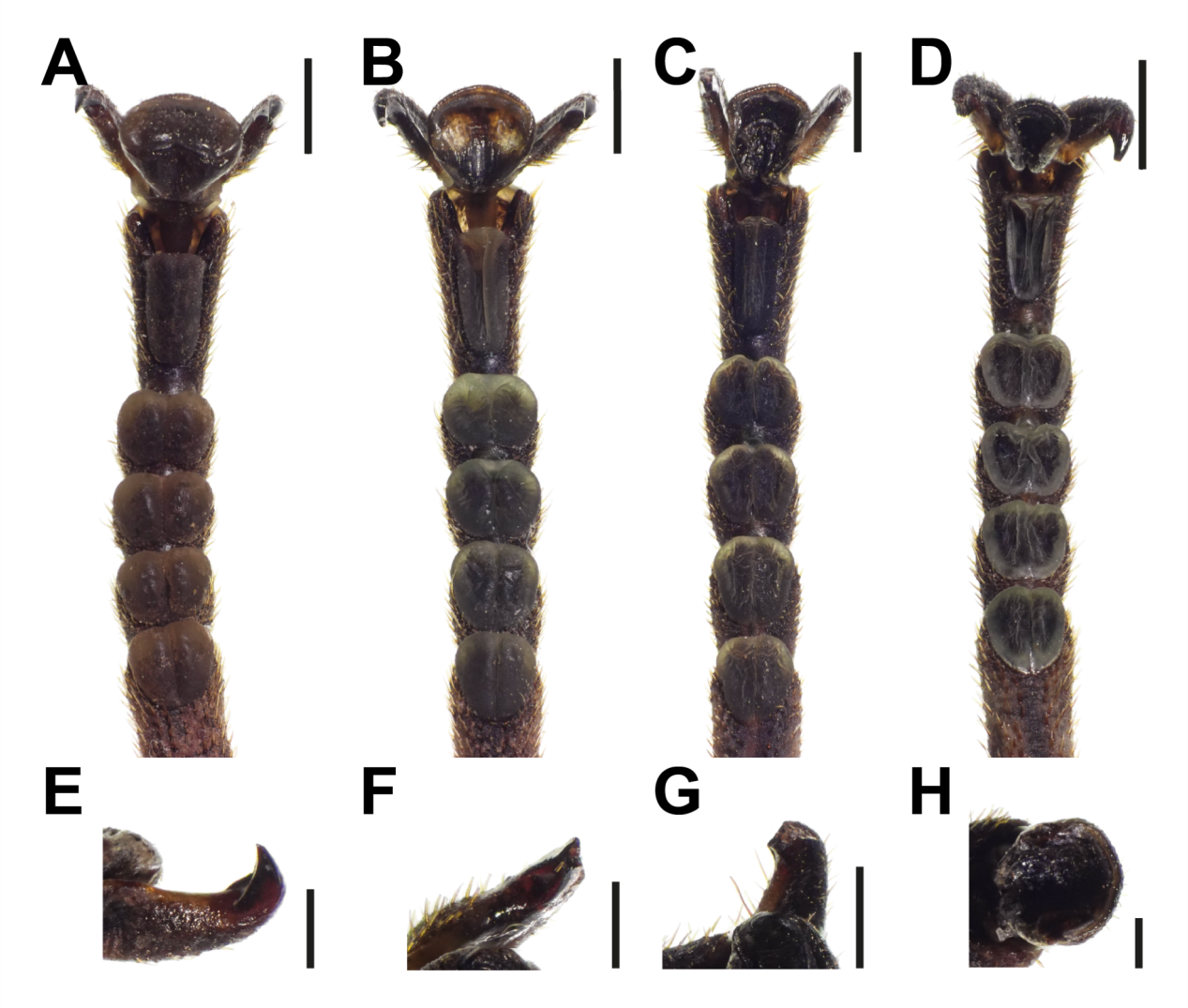

Figure 4: Morphological changes of tarsi during ageing. (A–D) Full tarsi, ventral views. (A) Young adult female with fully inflated arolium and euplantulae. (B–D) Old adult females; different degrees of deflation of arolia and eupantulae are visible. (E–H) Different degrees of claw wear in old adult females, ventral views. (E) No damage visible. (F) Claw tip broken off. (G) Larger fraction of claw broken off. (H) Claws missing. Scale bars: (A–D) 1 mm, (E–H) 300 µm.

insect tarsi [56]. Differences in color between the pads and the cuticle of the tarsus were clearly visible. The adhesive pads were generally fluorescing blue in both measurements (Figure 5 and Figure 6). Using WFM, the cuticle of the tarsomeres appeared in a yellow-orange color (Figure 5) and showed red and green signals in CLSM (Figure 6), indicating their stronger degree of sclerotization. A double row of dots with red autofluorescence located on the pads along the central groove was visible using WMF (e.g., Figure 5C); it can be assigned to the position of mechanoreceptors (see Figure 7D,H below and also [37]). No differences in the autofluorescence pattern were seen among front, middle, and hind legs.

The blue color of the cuticle of attachment pads appeared more vibrant using WFM in the subadult individuals (Figure 6A–D) and young adult animals (Figure 6E–H) than in the older animals (Figure 6I–K). Because of individual settings for each scan of the CLSM, the colors of the maximum intensity projects are not directly comparable among the images. However, the relative distribution of signals can be informative for the comparison of signs of ageing in combination with shape changes of the attachment pads. The deflation of the euplantulae and arolia of older animals is also visible in WFM (Figure 5I,L) and CLSM (Figure 6C–E). The deflation leads to strongly wrinkled pad surfaces. The tarsi of young adult animals sometimes revealed smaller patches with derived autofluorescence signals on the attachment pads (Figure 5E). Instead of the vibrant blue signal of the surrounding cuticle, some areas appear orange to brown in WMF (Figure 5F) images, or green to red in CLSM (Figure 6B) images, typical for stronger sclero-

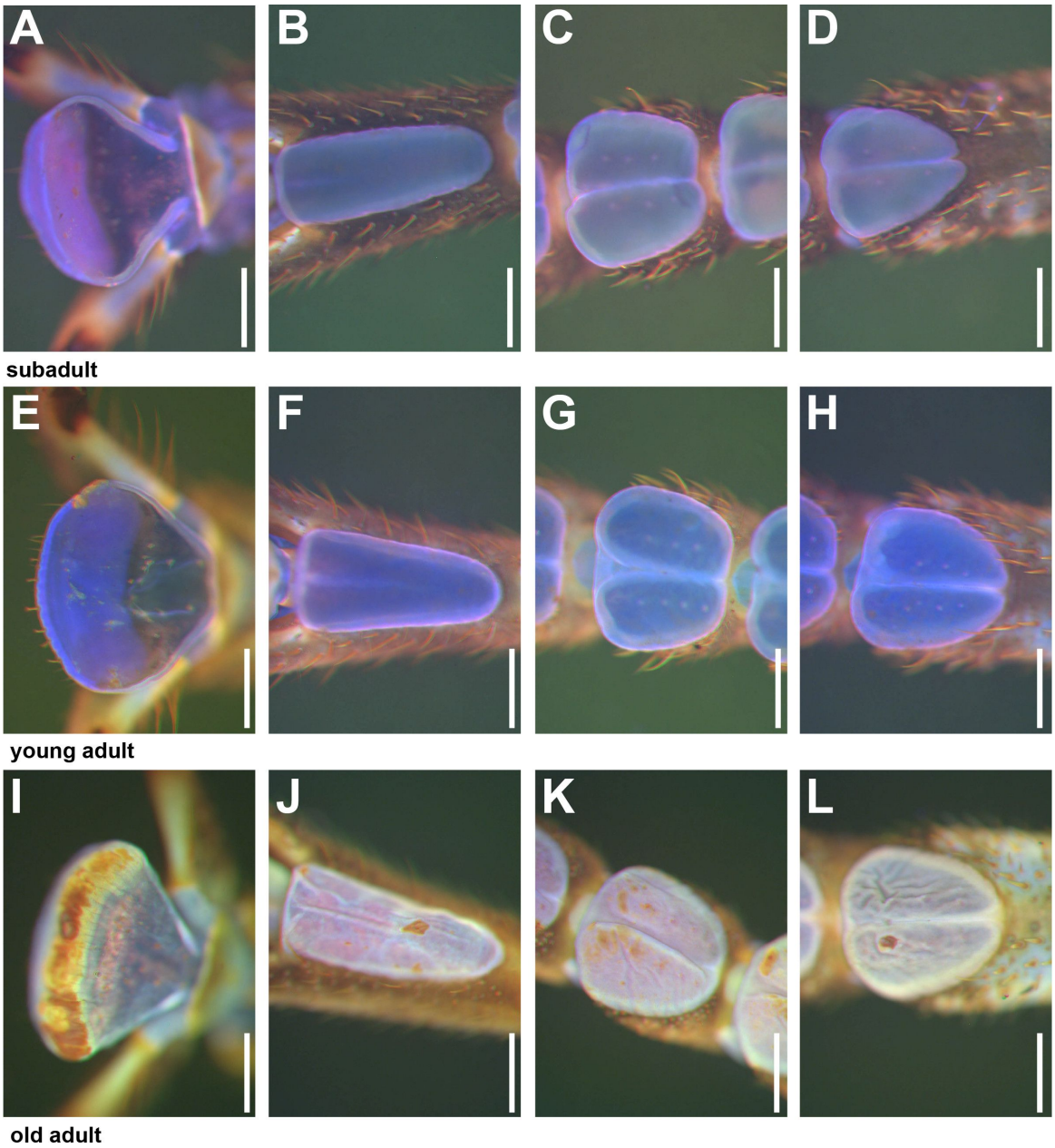

Figure 5: Ventral views of attachment pads obtained from WFM. (A–D) Subadult female. (E–H) Young adult female. (I–L) Old adult female. Images within one row are from different areas of the same sample. Vibrant blue color indicates soft cuticle, dark yellow-red color indicates stiffened cuticle. (A, E, I) Arolia. (B, F, J) Fifth euplantula. (C, G, K) Third euplantula. (D, H, L) First euplantula. Attachment pads show increasing stiffened areas with age and relatively less strong autofluorescence signals of the soft cuticle. Scale bars: 200 µm.

tized cuticle. The size and proportion of such patches was higher on the pads of older animals (Figure 5 I), and large parts of the euplantular area frequently showed an overall reddish hue throughout the pad surface (Figure 5I–L).

Microscopic ageing signs

Several further microscopic signs of ageing were visible using SEM (Figure 7). Wrinkles due to deflation of the pads often caused furrows on the surface of arolia (Figure 7A). While the original condition (Figure 7D) of the euplantula exhibits a bilobed inflated pad without major markings, except for the central grove and the nubby attachment microstructure, different wear marks were observed on the euplantulae of older animals. The wear patterns included scarred scratches (Figure 7E), scarred tissue from larger wounds (Figure 7F), and deformations of the pad surface that potentially arose from

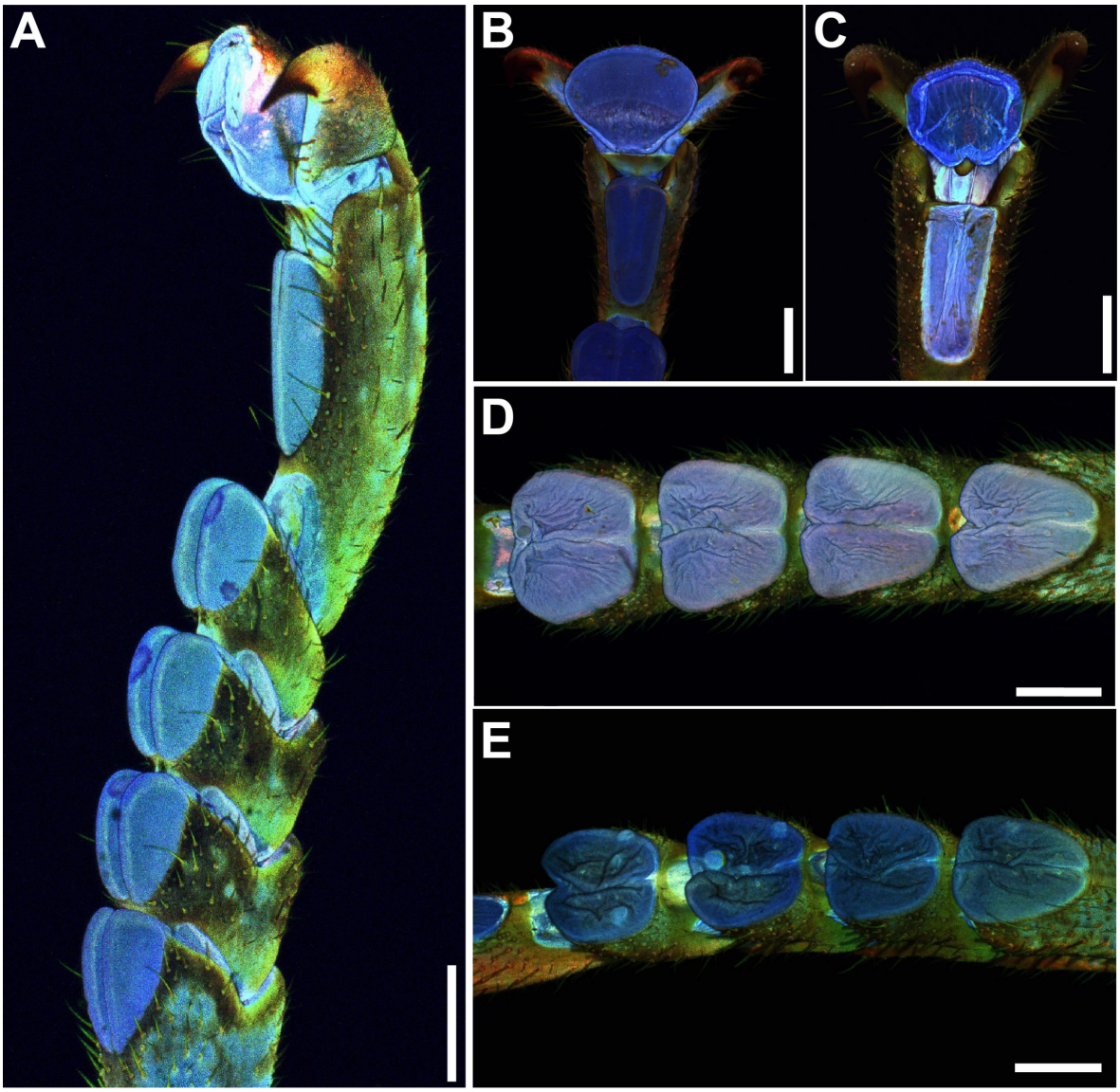

Figure 6: Maximum intensity projections of tarsi in different age groups obtained by CLSM. (A) Tarsus of subadult female, lateral view. (B) Young adult pretarsus, ventral view. (C) Old adult pretarsus, ventral view. (D) Young adult euplantulae, ventral view. (E) Old adult euplantulae, ventral view. Colors indicate relative material autofluorescence. Blue signals indicate resilin-containing weakly sclerotized cuticle, and green and red signals indicate stronger sclerotized cuticle. Scale bars: 1mm.

inhomogeneous changes of the material properties of the cuticle (Figure 7G). Other wear marks were found on the claws (Figure 7C) and on the mechanoreceptors of euplantulae (Figure 7I). While the contact sensilla on the euplantulae are usually found in pairs within groves without micro-ornamentation and are well recognizable (Figure 7H), the setae of the mechanoreceptors were often worn off in older animals (Figure 7I).

Certain changes of the attachment pad cuticle that were not visible using some methods were verified with other microscopy techniques (Figure 8). Larger deformations of the attachment pads, visible by stereomicroscopy (Figure 8A), often appeared dark and brownish in WFM (Figure 8C), which could also be due to contamination. SEM revealed most of such cases as not being caused by contaminations. They rather arose from a strong alteration of the cuticle (Figure 8E), also including changes of the surface topography of the terminal layer of the attachment pad cuticle. Profound hardening of the cuticle could yield an appearance similar to a pad coverage by other substances resulting in dark patches in WFM (Figure 8B,H,K). Such patches usually showed no covering films visible in stere-

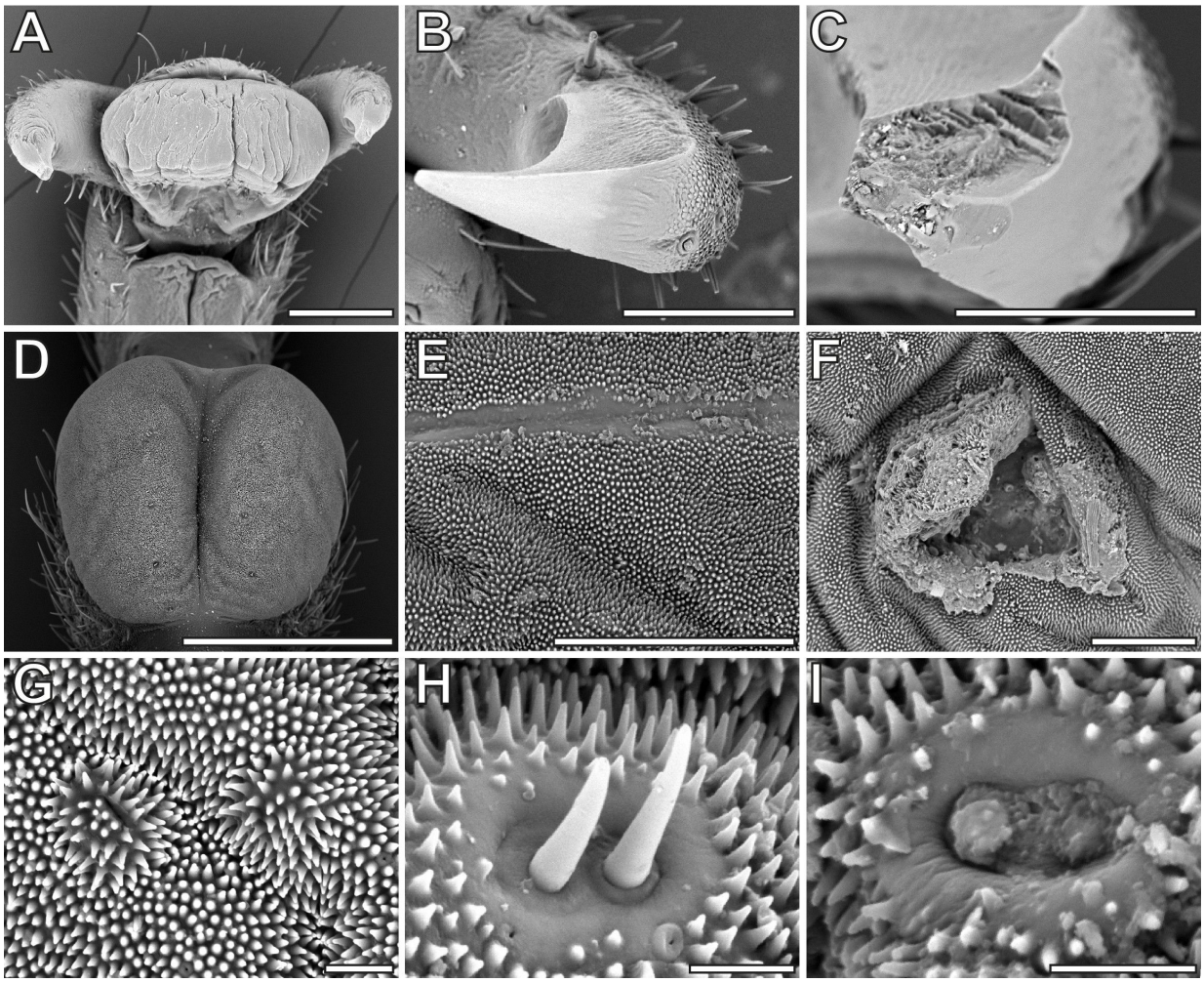

Figure 7: SEM micrographs of ageing effects on the tarsi. (A) Pretarsus of old female, ventral view. (B) Intact claw, young adult female. (C) Broken claw, old female. (D) Intact inflated euplantula, young adult female. (E) Scratches on euplantula, old female. (F) Larger scar on euplantula, old female. (G) Inhomogeneously deformed cuticle of the euplantula, old female. (H) Intact mechanoreceptors, young adult female. (I) Worn mechanoreceptors with detached setae, old female. Scale bars: (A, D) 500 mm, (B, C, E, F) 100 µm, (G–I) 10 µm.

omicroscopy (Figure 8A,G) and SEM (Figure 8D,I,J). Scars on the attachment pads (Figure 8L) also appeared red to brown in WFM (Figure 8M).

Discussion

Decay of attachment performance

Older animals showed a decline in adhesive performance similar to cockroaches as previously shown by Ridgel and coworkers [16]. The decline of attachment performance was also measurable here in repetitive tests over a longer time span. Animals lost adhesive abilities on all substrates over the course of six weeks, and their attachment performance converged to the level of the older animals in the first series of experiments. Variation of the attachment performance increased with age, which could be seen in the direct comparison of sliding angles and in the measurements over time. Ageing is a gradual process; hence, the decline of attachment abilities can be expected to be gradual as well and to show intraspecific variation [17]. A difference in activity of the animals was also noticeable during the experiments. The young individuals were more active, whereas the old animals took longer to recover from anesthesia (not quantified). Ridgel and Ritzmann [5] also detected a decrease of around 50% in walking speed of aged cockroaches. This matches the proposed loss of muscle fibers with age, leading to muscle atrophy [16].

Roughness dependence of attachment performance decay

The performance of insect attachment pads recorded on a smooth surface is usually higher than on microrough surfaces

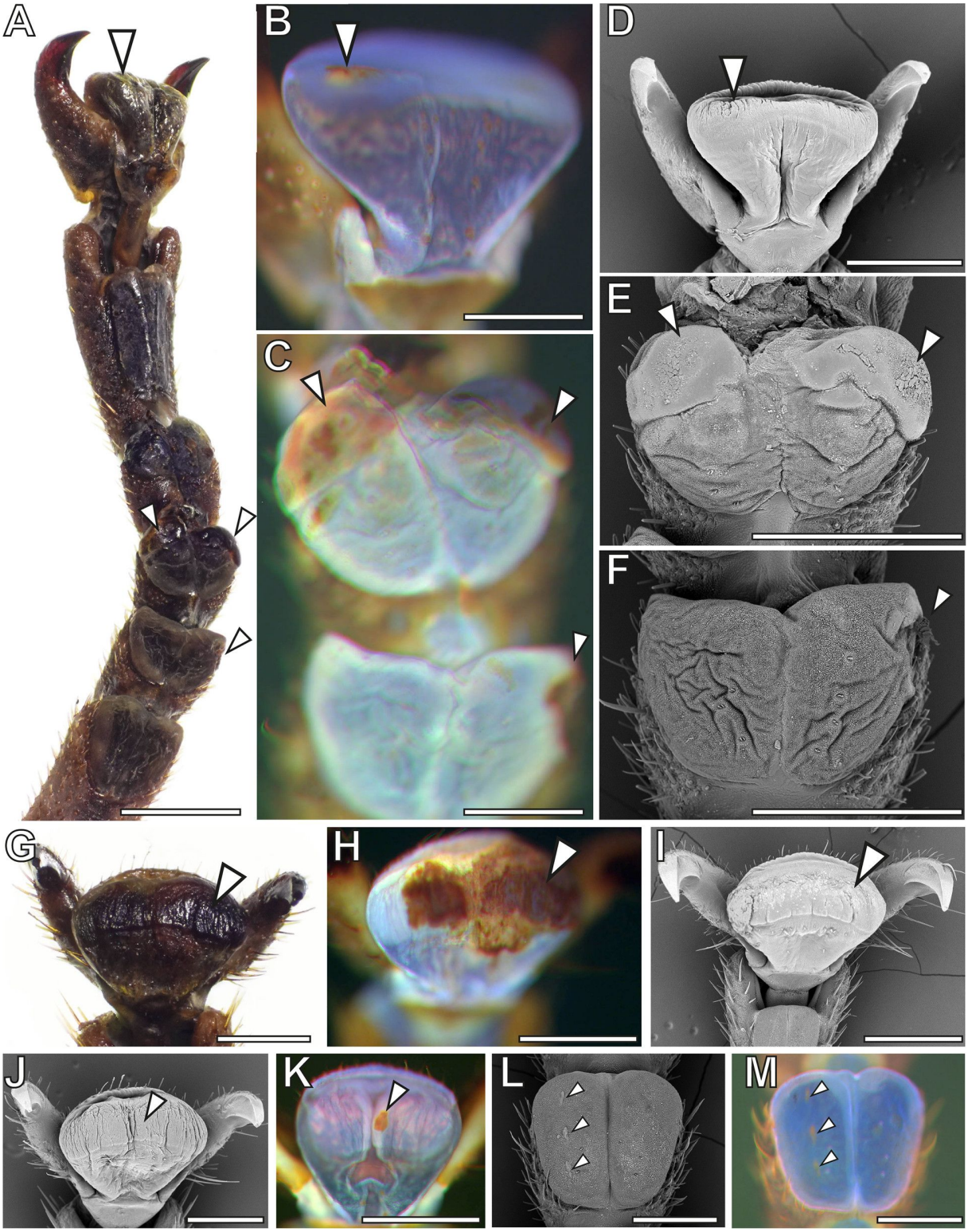

Figure 8: Combination of visualizations of the same attachment organs with different microscopy techniques. A–F, G–I, J–K, and L–M correspond to the same respective tarsi of old adult females. Arrowheads mark areas of concern. (A, G) Stereomicroscopy images showing the appearance of the attachment pads. (B, C, H, K, M) WMF images showing native bluish regions and those stiffened due to the ageing. (D–F, I, J, K) SEM images showing the topography of the surface. Scale bars: (A) 1 mm, (B–M) 500 µm.

[14], and asperity sizes around 0.3–1.0 µm have been confirmed to be a critical roughness at which adhesion is the lowest [33,57-60]. On substrates with higher roughness, claws are used for mechanical interlocking. However, this effect requires the substrate asperities to be at least the size of the claw tip diameter [61]. Claw involvement was excluded herein as surface roughnesses were chosen accordingly. Winand et al. [37] showed that a roughness of 12 µm is at the lower end of the effective claw usage for *S. aeta*. This allowed us to compare the age-related performance differences of the attachment pads.

Büscher und Gorb [33] compared the adhesive performance of two species of stick insects including *S. aeta*. The results therein for the same species were similar to the measurements of young adult animals herein and revealed generally higher pull-off and traction forces on a smooth surface, whereas the forces on microrough surfaces were lower [33]. The protuberances on the euplantulae of the stick insect *Carausius morosus* Brunner von Wattenwyl, 1907 (Lonchodidae) have a tip diameter of about 0.5 µm [31] and a ratio of length to width comparable to the nubs of *S. aeta* [37]. Apparently, the ratio of the nubs, compared to the surface asperities, makes better contact on a 1 µm rough surface, if compared to a 12 µm rough surface in younger adult individuals. This effect vanished for older adult animals, as attachment forces became more similar on all three substrates. No change of nub morphology was observed in older animals (Figure 7G,I), but a change of stiffness of the nubs could potentially affect their functionality as well. Nevertheless, pad compliance and deflation likely have a stronger effect in this experiment as discussed below. Other studies reported lowest forces on 1 µm and higher forces on 12 µm roughness for adhesion and traction in other arthropods [59,60]. This effect was presumably due to differences in micromorphology of their adhesive systems. Despite the gradual decay of attachment ability, no safety factors (attachment force per weight force) below 1 were observed, even in older animals; according to Pillai et al. [62], this would have been an indicator for the failure of the adhesive system to statically hold the insect's weight on the ceiling. Apart from insects, roughness plays a role in adhesion of non-arthropods as well. Roughnesses of 100–300 nm had the largest attachment-reducing effect for both single setae and whole geckos in experiments with the species *Gekko gecko* (Linnaeus, 1758) [63]. Similar to insects, attachment performance in geckos can vary between species on different roughnesses, depending on the morphology of their adhesive systems [64-67]. Similar to the results shown here, geckos face similar challenges to sustain attachment during ageing [64], that is, damage, contaminations, and changes of material properties of the integument of the attachment pads. Geckos, however, continuously shed their skin throughout their life, in contrast to insects; this was shown to enable regeneration of the adhesive properties of the attachment system to some extent [62].

Claw wear

Claws did not play a role in our attachment experiments, but they were morphologically investigated as part of the tarsus as well. No link between age and claw wear could be established as claw wear usually happens abruptly at single instances and accumulates over time [68]. Damage on the claws consequently rather indicates whether a particular individual claw experienced sufficient stress to be damaged than informs about the age, besides the fact that the longer life time potentially leads to the higher probability of such events. Claws are therefore unsuitable to determine the age of *S. aeta*. Some arthropod claws, such as those in ticks [69], have been shown to contain small amounts of resilin, an elastomeric protein providing flexibility in cuticle composites [70]. Voigt and Gorb [69] also suspect resilin to occur in other arthropod claws as well, but melanization impedes investigation using fluorescence microscopy. Resilin-containing structures within the claws could potentially work as damping mechanisms to reduce wear and risk of damage [69]. Claws are presumed to be more resistant to wear than the soft and pliable adhesive pads [68,71]. Most claw breakages were observed at the tips; the tips have to withstand the greatest stresses, which mostly occur in single events, rather than in normal wear [68]. Further studies could explore the role of fatigue of claw material and its effect on the mechanical properties.

Pad compliance

There are several possible ways in which attachment abilities could be affected by ageing. Compliance of the attachment pad to the substrate plays a significant role for the performance. The compliance of the attachment pad surface can be negatively affected by changes of the material properties of the cuticle and through structural damage of the surface, leading to obstacles for contact formation at the interface between the pad and substrate [11]. Ridgel et al. [16] noticed dry and dark pads in aged cockroaches, but they could not explain why the pads changed appearance and properties. Zhou et al. [17] assumed sclerotized scars to negatively impact pad compliance as such injuries accumulate with age. This effect was also found in different species of tree geckos [62]. A decrease in clinging ability in geckos was recorded with time passed since the last shedding. In contrast to insects, the geckos were able to recover their adhesive ability by molting, which repaired the damage inflicted by day-to-day use and substrate contact. We observed areas on the attachment pads of old adult *S. aeta,* using WFM and CLSM, that showed changes of the pad cuticle (Figure 5 and Figure 8). Some of these areas, appearing darkened using WFM (e.g., Figure 5K) or reddish using CLSM (Figure 6B), are

indicative for changes of the material properties of the cuticle. The autofluorescence correlates with the degree of sclerotization [50,70], and stronger cross-linking usually results in stiffer cuticle. As stiffer cuticle is less compliant, and the lower resulting actual contact area leads to lower attachment performance [72-74]. Most flexible cuticle consists at least partially of resilin [50,75,76], which needs water as a plasticizer to retain its extraordinary mechanical properties [70]. As the water evaporates, resilin becomes brittle and less resilient. Pad cuticle was also found to be more prone to evaporation than the leg cuticle [9], which could amplify the resilin degeneration due to sclerotization. Many of the regions of derived autofluorescence on the arolia and euplantulae did not show structural changes in SEM (Figure 8G–K) and likely represent areas of stiffened pad cuticle. Other ageing marks with derived autofluorescence revealed signs of persistent damage to the pad cuticle (Figure 7 and Figure 8). Such dark spots, observed using both fluorescence techniques, are likely scars resulting from repaired damage of the pad cuticle [17]. Abrasion of attachment pad cuticle can be repaired in insects. If the damage is superficial, epicuticle can be restored by depletion of waxes [18,77], but stronger damage results in sclerotization of the wound due to phenolase activity involved in the wound closure [78]. Such sclerotized scars do not only reduce the stiffness of the repaired area; they also cause structural obstacles that interfere with contact formation and reduce attachment performance [17].

Pad deflation

Besides material properties of the cuticle and microscopic surface features, further effects on attachment performance are likely results of the geometry of the attachment pads [43]. In their study, Ridgel and Ritzmann [5] proposed two ways in which age might affect attachment. They assumed either vascular insufficiency or degeneration of the tracheal system to be responsible for cockroach tarsus degeneration. Stiffer and dryer pads might be results of such ageing processes. Tracheal degeneration could lead to leg tissue dying because of a lack of oxygen and, therefore, might also influence the adhesive pads and their performance. The suspected vascular insufficiency ties into the hemolymph pressure. In the insect circulatory system, the low pressure is kept up by the heart and muscular activity [5,79]. The legs function as a terminal end in the circulatory system and often have accessory hearts to enable hemolymph flow [79]. If age has an effect on a stick insect's cardiac system, any impairment could additionally decrease the initially low hemolymph pressure. The observed stronger effect of ageing on the more distal regions of the tarsus in *S. aeta* could support the hypothesized influence of lack of the hemolymph support; more distal regions are likely stronger affected by this effect because of their peripheral connection to the circulatory system [79]. A decrease in spontaneous activity has also been reported from senescent insects [16,80]. Less activity would also mean less circulatory support by muscular activity, intensifying the circulatory problems. A relatively large fraction of the tarsus is filled with hemolymph [30], including the volume of the attachment pads [56,81].

In contrast to other insects, such as hymenopterans [82-84], the expansion of the arolium in stick insects is not supported by internal sclerites; instead, it results from the internal pressure within the pad similar to other polyneopteran insects [30,85].

Dening et al. [43] showed that the inflation degree of attachment devices in different animals and artificial attachment devices can play a role in the adhesion control. High pressure within the pad reduced the contact area with the substrate because of the curvature of the pad, and reduced inflation led to larger contact area and increased adhesive performance [43]. As the inflation is achieved by an increased hemolymph pressure in the pads of *S. aeta*, a decline in hemolymph supply to the pads would reduce inflation. The strong extent of deflation visible in these pads might lead to a decrease in adhesive properties due to the formation of folds in the pad surface, resulting in reduced actual contact area, in contrast to the findings of Dening et al. [43]. Tracheal degeneration could further harm the tarsal organs as a lack of oxygen could lead to damage in tissues. Loss of tissues, for example, exocrine cells within the arolium [81], could potentially also influence fluid production within the arolium. These exocrine cells produce adhesive secretions that play different roles in adhesive systems [11,40,85]. In stick insects, such fluids consist of a watery and a lipid phase [86] and, besides interfacial effects, contribute to the shape and curvature of the terminal layer of the attachment pad [43]. Another factor influencing effective stiffness of the cuticle is caused by depletion of these adhesive fluids. Several steps in quick succession were found to dry out the pad cuticle, making it less flexible and providing reduced attachment [40]. Jiao et al. [73] also reported desiccation and depletion of pad fluid to reduce adhesion in excised tarsi.

Pad deflation could also have negative influence on sensory feedback. The mechanoreceptors on the pads of stick insects, which provide feedback about substrate contact [37], usually occur solely on attachment pads with nubby microstructures and only rarely on smooth eupantulae [34]. The setae of mechanoreceptors are usually mounted in a flexible membrane, which also contains resilin [87]. The combination of a changed pad shape and less flexible membranes surrounding the mechanoreceptors' setae might impair the function and, therefore, reduce the information the animal is able to receive. In their paper concerning ageing cockroaches, Ridgel et al. [16] propose this lack of

sensory information to negatively impact the ability of old cockroaches to walk up an incline. It seems plausible to assume that the walking speed might also be affected by poor sensory feedback.

Conclusion

An effect of age on the attachment abilities of stick insects was found. Attachment and friction forces declined with age on both rough and smooth surfaces. Microscopy investigations revealed deflation of the attachment pads and signs of cuticle hardening, both decreasing pad flexibility and the ability of contact formation to the substrate. The changes observed in the pads of old individuals probably arise from desiccation of the pads and the cuticle, possibly caused by an impaired circulatory system and oxygen deficiency in the tarsus. The effects, such as material desiccation (pads, resilin patches, and membranes), presence of scars on the pad surface, oxygen and hemolymph deprivation, likely reinforce each other. Further experiments could explore more ageing-related effects to gain insights into the processes of attachment ability decay in insects and, thus, potentially improve sustainability of artificial biologically inspired engineering gripping systems. Such studies could include the role of hemolymph pressure for attachment control and the influence of hemolymph within the attachment pads on cuticle hydration and on the production of adhesive fluid.

Supporting Information

Supporting Information includes the raw data for all experiments, that is, pull-off forces, traction forces, and attachment angles for all animals, as well as their respective weights.

Supporting Information File 1

Raw experimental data.
[https://www.beilstein-journals.org/bjnano/content/supplementary/2190-4286-15-72-S1.xlsx]

Acknowledgements

We thank Esther Appel and Dr. Alexander Kovalev (Department of Functional Morphology and Biomechanics, Kiel University, Germany) for their technical assistance. Clara Igelmann (Kiel), Alexander Köhnsen (Wageningen University and Research, Netherlands) and Prof. Dr. Frank Edlich (Institute of Physiological Chemistry, Leipzig University, Germany) are thanked for their valuable discussions on the project.

Funding

This work was supported the German Research Foundation (DFG) (grant GO 995/34-1).

Competing Interests

The authors declare no competing or financial interests.

Author Contributions

Marie Grote: formal analysis; investigation; visualization; writing – original draft. Stanislav N. Gorb: conceptualization; funding acquisition; methodology; project administration; resources; writing – review & editing. Thies H. Büscher: conceptualization; data curation; formal analysis; methodology; project administration; resources; supervision; validation; visualization; writing – original draft.

ORCID® iDs

Stanislav N. Gorb - https://orcid.org/0000-0001-9712-7953
Thies H. Büscher - https://orcid.org/0000-0003-0639-4699

Data Availability Statement

All data that supports the findings of this study is available in the published article and/or the supporting information to this article.

References

1. López-Otín, C.; Blasco, M. A.; Partridge, L.; Serrano, M.; Kroemer, G. *Cell* **2013,** *153,* 1194–1217. doi:10.1016/j.cell.2013.05.039
2. Bonduriansky, R.; Creak, C. *Aust. J. Zool.* **2022,** *69,* 158–165. doi:10.1071/zo21052
3. Collatz, K.-G. *Arch. Gerontol. Geriatr.* **1997,** *25,* 83–90. doi:10.1016/s0167-4943(96)00773-x
4. Lee, H.-Y.; Lee, S.-H.; Min, K.-J. *Entomol. Res.* **2015,** *45,* 1–8. doi:10.1111/1748-5967.12088
5. Ridgel, A. L.; Ritzmann, R. E. *Ageing Res. Rev.* **2005,** *4,* 23–39. doi:10.1016/j.arr.2004.08.002
6. Carey, J. R.; Liedo, P. *Am. Entomol.* **1999,** *45,* 49–55. doi:10.1093/ae/45.1.49
7. Guo, S.; Wang, X.; Kang, L. *Front. Cell Dev. Biol.* **2020,** *8,* 576571. doi:10.3389/fcell.2020.576571
8. Privalova, V.; Szlachcic, E.; Sobczyk, Ł.; Szabla, N.; Czarnoleski, M. *Biology (Basel, Switz.)* **2021,** *10,* 327. doi:10.3390/biology10040327
9. Gorb, S. N. *Attachment Devices of Insect Cuticle;* Springer: Netherlands, 2001.
10. Labonte, D.; Struecker, M.-Y.; Birn-Jeffery, A. V.; Federle, W. *Proc. R. Soc. B* **2019,** *286,* 20191327. doi:10.1098/rspb.2019.1327
11. Büscher, T. H.; Gorb, S. N. *Beilstein J. Nanotechnol.* **2021,** *12,* 725–743. doi:10.3762/bjnano.12.57
12. Büscher, T. H.; Gorb, S. N. Convergent Evolution of Animal Adhesive Pads. In *Convergent Evolution;* Bels, V. L.; Russell, A. P., Eds.; Springer International Publishing: Cham, Switzerland, 2023; pp 257–287. doi:10.1007/978-3-031-11441-0_10
13. Song, Y.; Dai, Z.; Wang, Z.; Ji, A.; Gorb, S. N. *Sci. Rep.* **2016,** *6,* 26219. doi:10.1038/srep26219
14. Drechsler, P. Mechanics of adhesion and friction in stick insects and tree frogs. Ph.D. Thesis, Julius-Maximilians-Universität, München, Germany, 2008.
15. Bußhardt, P.; Kunze, D.; Gorb, S. N. *Sci. Rep.* **2014,** *4,* 6998. doi:10.1038/srep06998
16. Ridgel, A. L.; Ritzmann, R. E.; Schaefer, P. L. *J. Exp. Biol.* **2003,** *206,* 4453–4465. doi:10.1242/jeb.00714

17. Zhou, Y.; Robinson, A.; Viney, C.; Federle, W. *J. Exp. Biol.* **2015,** *218,* 2775–2781. doi:10.1242/jeb.124362
18. Slifer, E. H. *Ann. Entomol. Soc. Am.* **1950,** *43,* 173–188. doi:10.1093/aesa/43.2.173
19. Bradler, S.; Buckley, T. R. Biodiversity of Phasmatodea. In *Insect Biodiversity;* Foottit, R. G.; Adler, P. H., Eds.; John Wiley & Sons, Ltd, 2018; pp 281–313. doi:10.1002/9781118945582.ch11
20. Phasmida Species File. https://phasmida.speciesfile.org/ (accessed July 4, 2024).
21. Bedford, G. O. *Annu. Rev. Entomol.* **1978,** *23,* 125–149. doi:10.1146/annurev.en.23.010178.001013
22. Bank, S.; Buckley, T. R.; Büscher, T. H.; Bresseel, J.; Constant, J.; de Haan, M.; Dittmar, D.; Dräger, H.; Kahar, R. S.; Kang, A.; Kneubühler, B.; Langton-Myers, S. S.; Bradler, S. *Syst. Entomol.* **2021,** *46,* 487–507. doi:10.1111/syen.12472
23. Büscher, T. H.; Buckley, T. R.; Grohmann, C.; Gorb, S. N.; Bradler, S. *Front. Ecol. Evol.* **2018,** *6,* 69. doi:10.3389/fevo.2018.00069
24. Wang, M.; Béthoux, O.; Bradler, S.; Jacques, F. M. B.; Cui, Y.; Ren, D. *PLoS One* **2014,** *9,* e91290. doi:10.1371/journal.pone.0091290
25. Bullock, J. M. R.; Drechsler, P.; Federle, W. *J. Exp. Biol.* **2008,** *211,* 3333–3343. doi:10.1242/jeb.020941
26. Gorb, S. N. *Integr. Comp. Biol.* **2002,** *42,* 1127–1139. doi:10.1093/icb/42.6.1127
27. Gorb, E. V.; Gorb, S. N. *J. Exp. Bot.* **2017,** *68,* 5323–5337. doi:10.1093/jxb/erx271
28. Prüm, B.; Bohn, H. F.; Seidel, R.; Rubach, S.; Speck, T. *Acta Biomater.* **2013,** *9,* 6360–6368. doi:10.1016/j.actbio.2013.01.030
29. Büscher, T. H.; Kryuchkov, M.; Katanaev, V. L.; Gorb, S. N. *J. R. Soc., Interface* **2018,** *15,* 20180281. doi:10.1098/rsif.2018.0281
30. Beutel, R. G.; Gorb, S. N. *J. Zool. Syst. Evol. Res.* **2001,** *39,* 177–207. doi:10.1046/j.1439-0469.2001.00155.x
31. Labonte, D.; Federle, W. *PLoS One* **2013,** *8,* e81943. doi:10.1371/journal.pone.0081943
32. Büscher, T. H.; Gorb, S. N. *ZooKeys* **2017,** *645,* 1–11. doi:10.3897/zookeys.645.10783
33. Büscher, T. H.; Gorb, S. N. *J. Exp. Biol.* **2019,** *222,* jeb.209833. doi:10.1242/jeb.209833
34. Büscher, T. H.; Grohmann, C.; Bradler, S.; Gorb, S. N. *Zoologica* **2019,** *164,* 1–94.
35. Bußhardt, P.; Wolf, H.; Gorb, S. N. *Zoology (Munich, Ger.)* **2012,** *115,* 135–141. doi:10.1016/j.zool.2011.11.002
36. Büscher, T. H.; Becker, M.; Gorb, S. N. *J. Exp. Biol.* **2020,** *223,* jeb.226514. doi:10.1242/jeb.226514
37. Winand, J.; Gorb, S. N.; Büscher, T. H. *J. Comp. Physiol., A* **2023,** *209,* 313–323. doi:10.1007/s00359-022-01570-1
38. Burack, J.; Gorb, S. N.; Büscher, T. H. *Insects* **2022,** *13,* 952. doi:10.3390/insects13100952
39. Thomas, J.; Gorb, S. N.; Büscher, T. H. *J. Exp. Biol.* **2023,** *226,* jeb.244295. doi:10.1242/jeb.244295
40. Drechsler, P.; Federle, W. *J. Comp. Physiol., A* **2006,** *192,* 1213–1222. doi:10.1007/s00359-006-0150-5
41. Brock, P. D.; Büscher, T. H. *Stick and Leaf-Insects of the world;* NAP Editions: Verrières-le-Buisson, France, 2022.
42. Bennemann, M. Biomimicry of the adhesive organs of stick insects (*Carausius morosus*). Ph.D. Thesis, Rheinisch-Westfälische Technische Hochschule, Aachen, Germany, 2015.
43. Dening, K.; Heepe, L.; Afferrante, L.; Carbone, G.; Gorb, S. N. *Appl. Phys. A: Mater. Sci. Process.* **2014,** *116,* 567–573. doi:10.1007/s00339-014-8504-2
44. Loder, P. M. J. *Tissue Cell* **1992,** *24,* 301–314. doi:10.1016/0040-8166(92)90103-e
45. Hennemann, F. *Faunitaxys* **2023,** *11,* 1–135. https://hal.science/hal-04270055
46. Berthé, R. A.; Westhoff, G.; Bleckmann, H.; Gorb, S. N. *J. Comp. Physiol., A* **2009,** *195,* 311–318. doi:10.1007/s00359-008-0408-1
47. Spurr, A. R. *J. Ultrastruct. Res.* **1969,** *26,* 31–43. doi:10.1016/s0022-5320(69)90033-1
48. Theunissen, L. M.; Bekemeier, H. H.; Dürr, V. *J. Exp. Biol.* **2015,** *218,* 340–352. doi:10.1242/jeb.114173
49. Gorb, S. N.; Wildermuth, H.; Kohl, S.; Büsse, S. *Zoomorphology* **2022,** *141,* 297–306. doi:10.1007/s00435-022-00561-9
50. Michels, J.; Gorb, S. N. J. *J. Microsc. (Oxford, U. K.)* **2012,** *245,* 1–16. doi:10.1111/j.1365-2818.2011.03523.x
51. *R: A language and environment for statistical computing,* v 4.2.1.; R Foundation for Statistical Computing, 2022, https://www.R-project.org/.
52. Download RStudio | The Popular Open-Source IDE from Posit. https://posit.co/products/open-source/rstudio/ (accessed July 4, 2024).
53. R Companion 3E. https://www.john-fox.ca/Companion/index.html (accessed July 4, 2024).
54. GitHub - fishR-Core-Team/FSA. FSA (Fisheries Stock Assessment) package provides R functions to conduct typical introductory fisheries analyses. https://github.com/fishR-Core-Team/FSA (accessed July 4, 2024).
55. Appel, E.; Heepe, L.; Lin, C.-P.; Gorb, S. N. *J. Anat.* **2015,** *227,* 561–582. doi:10.1111/joa.12362
56. Thomas, J.; Gorb, S. N.; Büscher, T. H. *Beilstein J. Nanotechnol.* **2024,** *15,* 612–630. doi:10.3762/bjnano.15.52
57. Bullock, J. M. R.; Federle, W. *Insect Sci.* **2011,** *18,* 298–304. doi:10.1111/j.1744-7917.2010.01369.x
58. Fuller, K. N. G.; Tabor, D. *Proc. R. Soc. London, Ser. A* **1975,** *345,* 327–342. doi:10.1098/rspa.1975.0138
59. Voigt, D.; Schuppert, J. M.; Dattinger, S.; Gorb, S. N. *J. Insect Physiol.* **2008,** *54,* 765–776. doi:10.1016/j.jinsphys.2008.02.006
60. Wolff, J. O.; Gorb, S. N. *J. Exp. Biol.* **2012,** *215,* 179–184. doi:10.1242/jeb.061507
61. Dai, Z.; Gorb, S. N.; Schwarz, U. *J. Exp. Biol.* **2002,** *205,* 2479–2488. doi:10.1242/jeb.205.16.2479
62. Pillai, R. R.; Riedel, J.; Schwarzkopf, L. *J. Exp. Biol.* **2023,** *226,* jeb245286. doi:10.1242/jeb.245286
63. Huber, G.; Gorb, S. N.; Hosoda, N.; Spolenak, R.; Arzt, E. *Acta Biomater.* **2007,** *3,* 607–610. doi:10.1016/j.actbio.2007.01.007
64. Pillai, R.; Nordberg, E.; Riedel, J.; Schwarzkopf, L. *Ecol. Evol.* **2020,** *10,* 2597–2607. doi:10.1002/ece3.6090
65. Cole, N. C.; Jones, C. G.; Harris, S. *Biol. Conserv.* **2005,** *125,* 467–474. doi:10.1016/j.biocon.2005.04.017
66. Vanhooydonck, B.; Andronescu, A.; Herrel, A.; Irschick, D. J. *Biol. J. Linn. Soc.* **2005,** *85,* 385–393. doi:10.1111/j.1095-8312.2005.00495.x
67. Naylor, E. R.; Higham, T. E. *Integr. Comp. Biol.* **2019,** *59,* 168–181. doi:10.1093/icb/icz027
68. Pattrick, J. G.; Labonte, D.; Federle, W. *J. Exp. Biol.* **2018,** *221,* jeb188391. doi:10.1242/jeb.188391
69. Voigt, D.; Gorb, S. *J. Exp. Biol.* **2017,** *220,* 1984–1996. doi:10.1242/jeb.152942
70. Michels, J.; Appel, E.; Gorb, S. N. *Beilstein J. Nanotechnol.* **2016,** *7,* 1241–1259. doi:10.3762/bjnano.7.115
71. Labonte, D.; Federle, W. *Philos. Trans. R. Soc., B* **2015,** *370,* 20140027. doi:10.1098/rstb.2014.0027

72. Gorb, S.; Jiao, Y.; Scherge, M. *J. Comp. Physiol., A* **2000,** *186,* 821–831. doi:10.1007/s003590000135
73. Jiao, Y.; Gorb, S.; Scherge, M. *J. Exp. Biol.* **2000,** *203,* 1887–1895. doi:10.1242/jeb.203.12.1887
74. Perez Goodwyn, P.; Peressadko, A.; Schwarz, H.; Kastner, V.; Gorb, S. *J. Comp. Physiol., A* **2006,** *192,* 1233–1243. doi:10.1007/s00359-006-0156-z
75. Dirks, J.-H.; Li, M.; Kabla, A.; Federle, W. *Acta Biomater.* **2012,** *8,* 2730–2736. doi:10.1016/j.actbio.2012.04.008
76. Neff, D.; Frazier, S. F.; Quimby, L.; Wang, R.-T.; Zill, S. *Arthropod Struct. Dev.* **2000,** *29,* 75–83. doi:10.1016/s1467-8039(00)00014-1
77. Wigglesworth, V. B. *J. Exp. Biol.* **1945,** *21,* 97–114. doi:10.1242/jeb.21.3-4.97
78. Lai-Fook, J. *J. Insect Physiol.* **1966,** *12,* 195–226. doi:10.1016/0022-1910(66)90136-3
79. Brusca, R. C.; Brusca, G. J. *Invertebrates,* 2nd ed.; Sinauer Associates: Sunderland, USA, 2003.
80. Piper, M. D. W.; Partridge, L. *Biochim. Biophys. Acta, Mol. Basis Dis.* **2018,** *1864,* 2707–2717. doi:10.1016/j.bbadis.2017.09.016
81. Betz, O.; Frenzel, M.; Steiner, M.; Vogt, M.; Kleemeier, M.; Hartwig, A.; Sampalla, B.; Rupp, F.; Boley, M.; Schmitt, C. *Biol. Open* **2017,** *6,* 589–601. doi:10.1242/bio.024620
82. Federle, W.; Brainerd, E. L.; McMahon, T. A.; Hölldobler, B. *Proc. Natl. Acad. Sci. U. S. A.* **2001,** *98,* 6215–6220. doi:10.1073/pnas.111139298
83. Frantsevich, L.; Gorb, S. *Zoology (Munich, Ger.)* **2002,** *105,* 225–237. doi:10.1078/0944-2006-00067
84. Gladun, D.; Gorb, S. N.; Frantsevich, L. I. Alternative Tasks of the Insect Arolium with Special Reference to Hymenoptera. In *Functional Surfaces in Biology: Adhesion Related Phenomena;* Gorb, S. N., Ed.; Springer Netherlands: Dordrecht, Netherlands, 2009; Vol. 2, pp 67–103. doi:10.1007/978-1-4020-6695-5_4
85. Thomas, J.; Gorb, S. N.; Büscher, T. H. *Biomimetics* **2023,** *8,* 439. doi:10.3390/biomimetics8050439
86. Dirks, J.-H.; Clemente, C. J.; Federle, W. *J. R. Soc., Interface* **2010,** *7,* 587–593. doi:10.1098/rsif.2009.0308
87. Keil, T. A. *Microsc. Res. Tech.* **1997,** *39,* 506–531. doi:10.1002/(sici)1097-0029(19971215)39:6<506::aid-jemt5>3.0.co;2-b

License and Terms

This is an open access article licensed under the terms of the Beilstein-Institut Open Access License Agreement (https://www.beilstein-journals.org/bjnano/terms), which is identical to the Creative Commons Attribution 4.0 International License (https://creativecommons.org/licenses/by/4.0). The reuse of material under this license requires that the author(s), source and license are credited. Third-party material in this article could be subject to other licenses (typically indicated in the credit line), and in this case, users are required to obtain permission from the license holder to reuse the material.

The definitive version of this article is the electronic one which can be found at:
https://doi.org/10.3762/bjnano.15.72

BEILSTEIN JOURNAL OF NANOTECHNOLOGY

Beyond biomimicry – next generation applications of bioinspired adhesives from microfluidics to composites

Dan Sameoto

Perspective

Open Access

Address:
Department of Mechanical Engineering, University of Alberta, Edmonton AB, T6G 1H9, Canada

Email:
Dan Sameoto - sameoto@ualberta.ca

Keywords:
adhesion; biomimicry; composites; gecko; robotics, soft lithography

Beilstein J. Nanotechnol. **2024,** *15,* 965–976.
https://doi.org/10.3762/bjnano.15.79

Received: 16 April 2024
Accepted: 11 July 2024
Published: 05 August 2024

This article is part of the thematic issue "Biomimetics and bioinspired surfaces: from nature to theory and applications".

Guest Editor: R. Guillermo

© 2024 Sameoto; licensee Beilstein-Institut.
License and terms: see end of document.

Abstract

In this perspective article, Professor Dan Sameoto outlines his opinion on future opportunities in the field of biomimetic adhesives. Despite over twenty years of excellent academic work by groups all around the world in this subfield, the economic value and impact of these materials is somewhat underwhelming. The question for the field is whether it should have a scientific and engineering focus to create every greater performance and understanding of the materials and hope that "if we build it, they will come". Perhaps we should expand our concept on what could be the desirable end applications for such materials and focus efforts on finding better end applications in which these materials can truly shine; a few of those applications like microfluidics and composites are highlighted in this article. It is time for a next generation of research to look beyond biomimicry and look towards re-engineering applications to make use of these materials' unique properties in economically viable ways.

Perspective

As of the time of this writing, it has been 24 years since the seminal work by Kellar Autumn and his colleagues demonstrated how a single gecko foot hair could generate adhesion [1]. Autumn's discovery that van der Waals forces were the primary mechanism behind the extraordinary climbing capabilities of geckos launched over 20 years of intense scientific and engineering efforts to understand and industrially mimic this technology [2-4]. Coincidentally, in 2000, the same year that Autumn's paper was published, the Nobel Prize for physics was awarded to Zhores Alferov and Herbert Kroemer, and Kroemer's Nobel lecture that year included the statement that "the principal applications of any sufficiently new and innovative technology always have been – and will continue to be – applications created by that technology" [5]. I often come back to that statement by Dr. Kroemer and try to ask myself: Has what we have achieved with biomimetic adhesives met that criteria? The honest answer at the moment is no, but perhaps it is still possible; even Velcro® took approximately 20 years from invention to wide commercial acceptance. The difficulty with biomimetic adhesives is that they are competing in a

crowded market of existing technological solutions. Existing pressure-sensitive adhesives [6] are available in a wide range of tackiness, use cases, and temperatures; also, they are relatively inexpensive as they are usually designed for one-off uses. Hook and loop fasteners [7] and magnets are much better in terms of reliability and adhesion force than current biomimetic materials but need mating surfaces that are compatible. Traditional fasteners like screws, bolts, and nuts are available for assemblies that do not need to be disconnected frequently but are extremely strong compared to all other reversible bonds. So, when biomimetic adhesives are applied as tape, reversible adhesives, or fasteners, they are competing in a crowded marketplace in which they do not have clearly superior performance to overcome incumbent advantage. Therefore, we must think outside the box in terms of new applications for biomimetic adhesives for truly substantial industrial impacts to be made. These new application areas are my primary research focus today; it makes the efforts of all those who have participated in the academic and industrial development of the field more valuable. How can these biomimetic materials possibly serve a niche not currently fit by any existing technology or enable applications otherwise not possible with existing adhesives?

In this perspective article, I will cover three unique subtopics that our group has advanced that can be substantially improved through the use of biomimetic adhesives. These subtopics are microfluidics, soft robotics, and reconfigurable composites. Microfluidics involves the manipulation and flow of fluids on a very small scale, typically with nanoliters or less of fluid and with feature sizes ranging from a few hundred microns down to sub-micrometer size [8,9]. It has been an active area of academic research for well over 30 years. Microfluidics technology has eventually enabled a variety of new innovations, including COVID-19 rapid tests [10], microfluidic displays [11], and low-cost diagnostics [12]. Soft robotics is a newer academic topic that has gained much popularity since approximately 2010 [13] and involves using very deformable materials like elastomers to build robotic sensors, actuators, and even simple logic circuits [14] that use nearly exclusively or primarily soft materials. Soft robotics can be, in theory, very compliant and, thus, compatible with collaborative robotics, wearable components, and relatively safe human–robot interactions, which potentially provides a unique capability compared to traditional rigid robotics. However, there is a trade-off in soft robotics between the compliance of the material and the degree of controllability or even its ability to self-support under gravitational loads; thus, there is a major interest in stiffness-tunable materials for soft robotic systems [15]. This stiffness tuning in many cases relies on the temporary bonding of composite layers or materials to change effective stiffness. While soft robotics have shown a need for stiffness-tunable materials, the ability for composites in and of themselves to be reversibly bonded potentially opens up a far greater industrial impact and applications in adaptable, smart materials. Even improved sustainability could be achieved if laminates and composites could be reformed and reused. The secret to improve use cases of reversible adhesives and to improve applications in the above three subfields is to use biomimetic materials to manufacture composites which, in turn, have the capacity to change their stiffness, shape, or other mechanical properties of interest to fit the needs of soft robotics, microfluidic systems, or others.

All of such applications necessitate that the biomimetic adhesives are robust, relatively inexpensive, and highly effective at adhering to different surfaces. Several corporations, including Setex [16], Gottlieb Binder [17], and a few others, have largely addressed these requirements for artificial biomimetic adhesives in the last decade, but the price per area is still far higher than that of competing adhesive solutions. At the time of writing, Setex has sold their industrial adhesive work to Shin-Etsu in Japan, and the Setex adhesive sheets are sold out on their website at a price of approximately \$0.5/in^2. A similar area of Velcro is closer to \$0.1 (when including both halves), and strong industrial tapes like duct tape are closer to \$0.02/in^2, but can be as little as a fraction of a cent per square inch for packing tape sold in bulk. The price of materials from Gottlieb Binder is harder to find (requiring direct inquiries via their website), but, as they were constructed from silicone rubbers, the base materials costs can already be fairly high. If adhesives are made from Sylgard 184 (a very common structural material for biomimetic adhesives in academic literature and our previous publications), the list price is close to \$400 CDN/kg at the time of writing (≈\$300 USD). For an adhesive sample with an average thickness of 0.1 mm, this would represent approximately \$0.19 of material alone and, therefore, the lowest possible cost. Alternative structural materials like styrene-ethylene-butylene-styrene (SEBS) can be purchased in bulk for as low as \$5/kg and also can be microstructured in seconds via thermo-compressive molding, whereas Sylgard 184 requires at least a minute to cure even at highly elevated temperatures [18]. Both speed of molding/demolding cycles and raw materials costs are critical to the base cost of adhesive structures, so thermoplastics have both factors in their favor, even if the structural materials are inferior for specific use scenarios. I myself had an early focus on enhancing the manufacturability and adhesion performance of these adhesives [19] as have others since then [20] because commercial viability needs production rates and cost per part on par with hook and loop fasteners at a minimum. My work with biomimetic adhesives was begun in 2008 at Simon Fraser University with an intended end application in space robotics [21,22] (Figure 1), where the adhesives needed to adhere to surfaces under vacuum conditions with minimal preload and main-

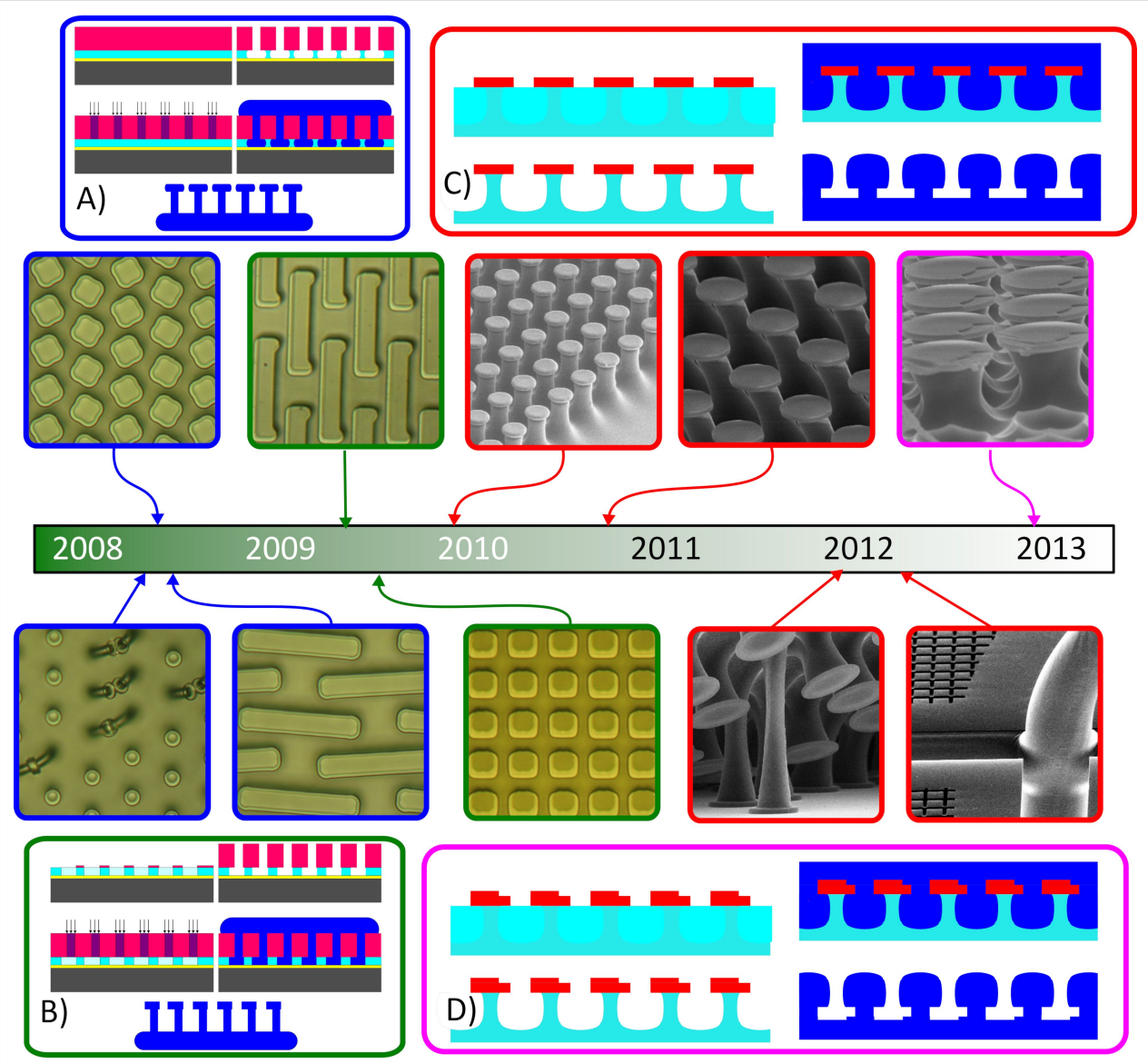

Figure 1: Chronological development of different gecko adhesive manufacturing processes that were developed by the author and then adapted by future students. Process (A) and (B) used silicone rubbers as the structural material for adhesives, and were capable of isotropic (A) or directional (B) adhesive performance depending on the symmetry of the cap. A more durable and useful system used deep-UV exposure of acrylic to form master molds, followed by a negative mold in silicone rubber (C, D). Isotropic designs were initially produced with polyurethane, and then structural materials were swapped to thermoplastic elastomers, with directional adhesion created by deliberate defects in the caps (D). Electrically conductive composite versions and geckofluidics were created in early 2012, and the focus was then switched to specific applications integrating biomimetic adhesives rather than adhesive development.

tain strong adhesion in all directions. Initially, I focused on a variety of micro-tread structures with the expectation that improving the maximum aspect ratio before fiber collapse would be the best way to enhance adhesive performance, but very shortly after I made changes to the manufacturing process to achieve the mushroom-shaped cap reported by others to produce far higher adhesive strength [23,24]. These unusually designed biomimetic adhesives were discarded in favor of the more well-known and well-characterized mushroom-shaped fiber structures, and many groups developed similar shapes around the same time [2]. I will not cover the exact mechanisms by which these mushroom shapes have proven effective, as several review articles have already been published on this topic [2,4]. However, for high normal strength and peel strength where directionality or easy off–on performance is not needed, this particular version of the biomimetic fibers tends to perform best.

Our unique contributions to these general types of mushroom-shaped adhesives included the introduction of multiheight caps

[25] or asymmetric caps [26], which produce different directional adhesion without significantly altering the manufacturing process of the caps themselves (Figure 1), and multimaterial adhesives for different adhesion mechanisms in a single sheet. A deliberate defect to yield anisotropic adhesion was described in 2013 by my student Walid bin Khaled [25]. It has been thoroughly characterized in various papers, including his work and that of visiting student Yue Wang, who collaborated with me between 2015 and 2016 [27]. Yue Wang also developed the adhesion circle test system, which has been instrumental in characterizing how these fibers with the deliberate defect function, demonstrating that the same geometry with different structural materials can exhibit vastly different adhesion properties [28]. Generally, structural materials for biomimetic adhesives such as silicone rubbers, which behave more linear-elastically, show a dramatic difference in adhesion force with defects, whereas materials that are more viscoelastic, such as thermoplastic elastomers or polyurethanes, are less sensitive to small defects intentionally introduced into the cap structure [28]. The choice of material depends on the application requirements; silicone rubber may be preferable for applications needing high directionality and easy activation/deactivation, while materials like polyurethane or thermoplastic elastomers are better suited for tolerating slight surface roughness and are far more cost-effective.

The significant influence of mechanical properties on identical fiber designs has also been extensively studied by our group and others, including work on shape memory polymers (SMPs) for biomimetic pillars [29]. These uniformly mushroom-shaped SMP fibers could function as either a Velcro-like material or a biomimetic adhesive, depending on the modulus of the shape memory polymer [29]. Using MM3520, a shape memory polymer with a transition temperature of approximately 35 °C, and toggling between cool and warm states, the mechanical modulus could change by over two orders of magnitude. This allowed the material to function either as a soft rubber or as a rigid thermoplastic. Integrated with microheaters within a soft robotic gripper, the system demonstrated that fabrics could be grasped in its rigid state, while smooth surfaces like glass could be easily adhered to in its soft state (Figure 2). Thus, it served as a dual-mechanism dry adhesive, although it could not operate

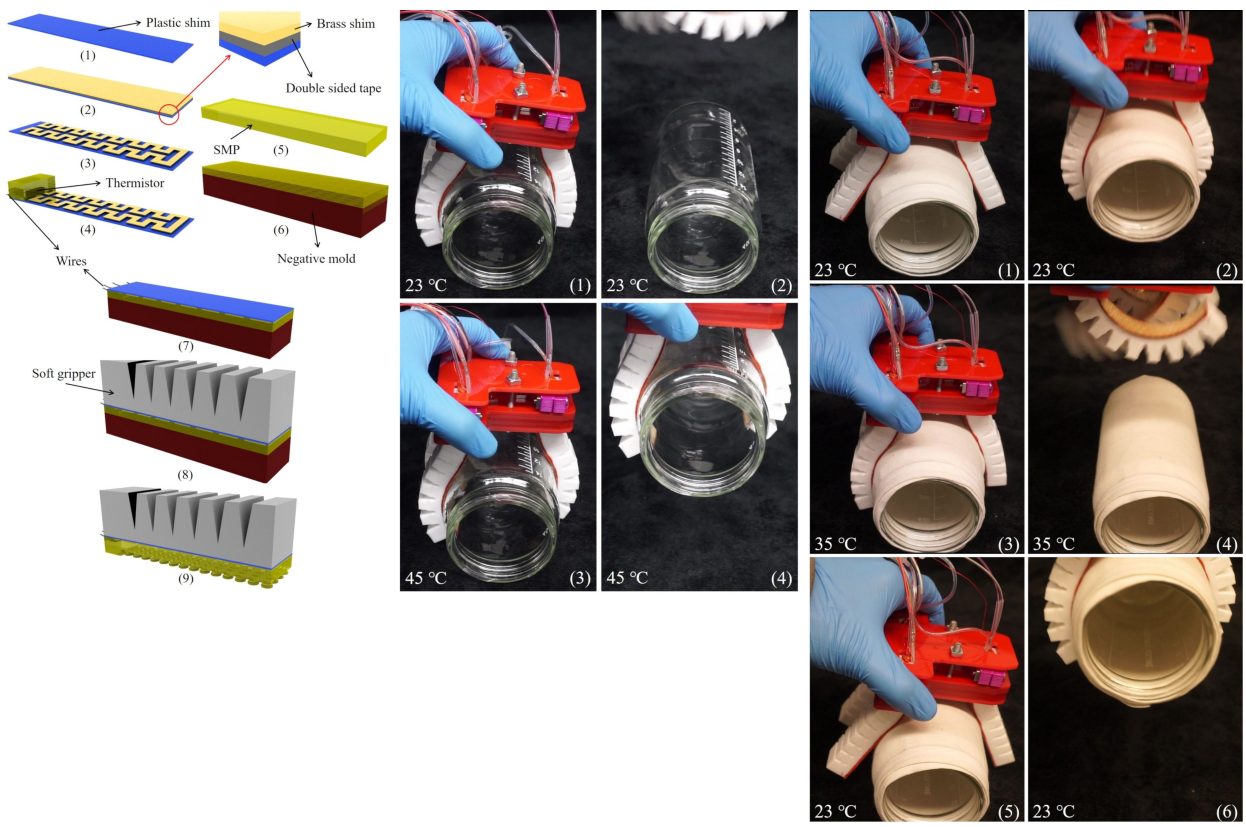

Figure 2: Compilation showing the assembly and integration of shape memory polymer dry adhesives with embedded heaters and soft robotic actuators. When in the soft state ($T > 35$ °C), the adhesive can grasp smooth surfaces but cannot support fabrics; when in the rigid state, it can pick up fabrics but not adhere to smooth glass. Compilation figure from [29] (T. Zhang et al., "Integration of Thermoresponsive Velcro-like Adhesive for Soft Robotic Grasping of Fabrics or Smooth Surfaces"; Proceedings of 2019 2nd IEEE International Conference on Soft Robotics (RoboSoft), published by IEEE. All rights reserved. Copyright © 2019 by IEEE. Reprinted with permission from IEEE. This content is not subject to CC BY 4.0.

with both mechanisms simultaneously. SMP materials are finding increasing use in newer versions of dry adhesives [30-32], and their full capabilities for switchable adhesive materials are still to be determined.

Subsequent developments during the COVID-19 pandemic showed that multiple types of thermoplastic elastomers and thermoplastics could be combined into a single dry adhesive sheet with mechanically dissimilar materials forming the same fiber mold [33] (Figure 3). This innovation enabled high shear strength on fabrics and high normal strength on smooth surfaces simultaneously without needing to alter the adhesive temperature. Such material inhomogeneity represents an underexplored aspect of biomimetic dry adhesives and warrants further investigation. It also draws inspiration from nature, as it is quite common for many animals to include multiple adhesion mechanisms. Between multimaterial 3D printing and the use of newer techniques to precisely define micro/nanofeatures [34] that are beyond the capabilities of traditional lithography, there is a good deal left to accomplish for grippers, fasteners, and other adhesive mechanisms using biologically inspired techniques from more than one animal simultaneously.

Beyond merely serving as an adhesive surface, mushroom-shaped biomimetic fibers can be functional in ways entirely absent in nature. This concept was initially applied as an adhesion mechanism for microfluidics, a distinct project I was working on in 2012, that required a reversible adhesion system offering high strength, low contamination, no damage to mating surfaces, and no need for separate glues, plasma treatments, or magnets. A simple modification of the biomimetic fibers created a continuous gasket capable of containing fluids [35] (Figure 4). In addition to generating adhesion, these fibers were sufficient to confine fluids, such as oil and water, and gases within microfluidic channels at pressures up to approximately 90 psi. This approach demonstrated an order of magnitude increase in adhesion strength compared to the reversible bonding of PDMS and achieved this without any alterations to the material itself, merely the channel geometry was made to minimize crack propagation.

Although the original geckofluidics application targeted traditional microfluidics liquids like oil and water, another student in 2017 demonstrated its utility for integrating liquid metal electronics. Mersedeh Zandvakili showed in 2017 that eutectic gallium–indium could be injected into microfluidic channels, and the gecko pillars not only provided adhesion for the channels but also directed the liquid metal flow via Laplace barriers within the channels, offering a mechanism by which we could precisely control the filling of a liquid with very high surface tension [36] (Figure 5). Additionally, small subfeatures within the microfluidic channels could allow for both air escape and the addition of acid in specific locations of the biomimetic adhesives to direct the flow of liquid metal into separate, isolated areas. Handling such extreme materials is something no animal would have evolved to manage, yet the artificial versions have proven to be very functional in contact with these liquids and have enabled for a variety of flexible electronics applications.

While the geckofluidics project was an example of a traditional application enhanced through the use of an improved bonding solution, the key to advancing the utility of biomimetic adhe-

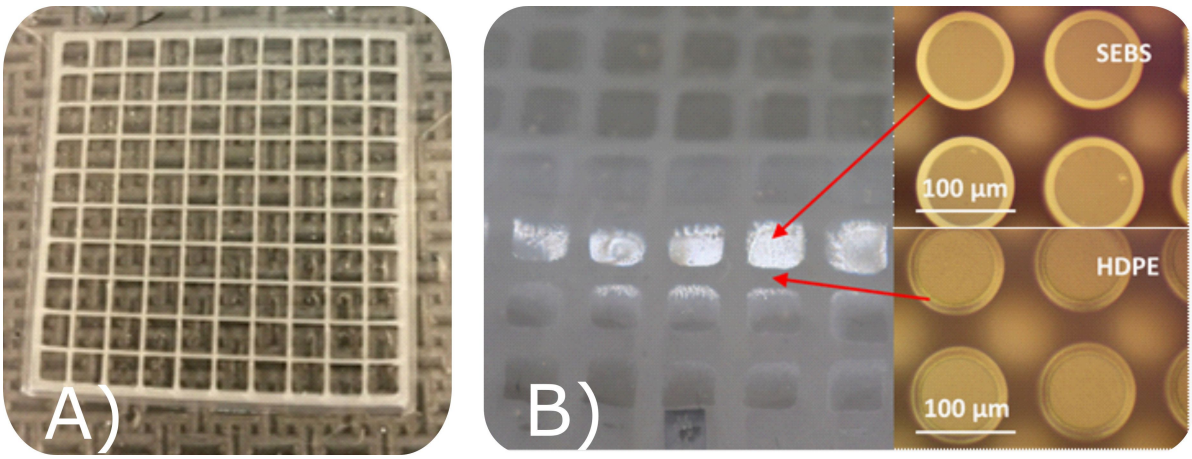

Figure 3: (A) 3D-printed grid of high-density polyethylene (HDPE) on top of a thermoplastic elastomer base. When melted together and formed into a gecko adhesive structure, a spatially heterogeneous material with fibers of the same shape (B) can simultaneously adhere to fabrics and smooth surfaces (see video in Supporting Information File 1).

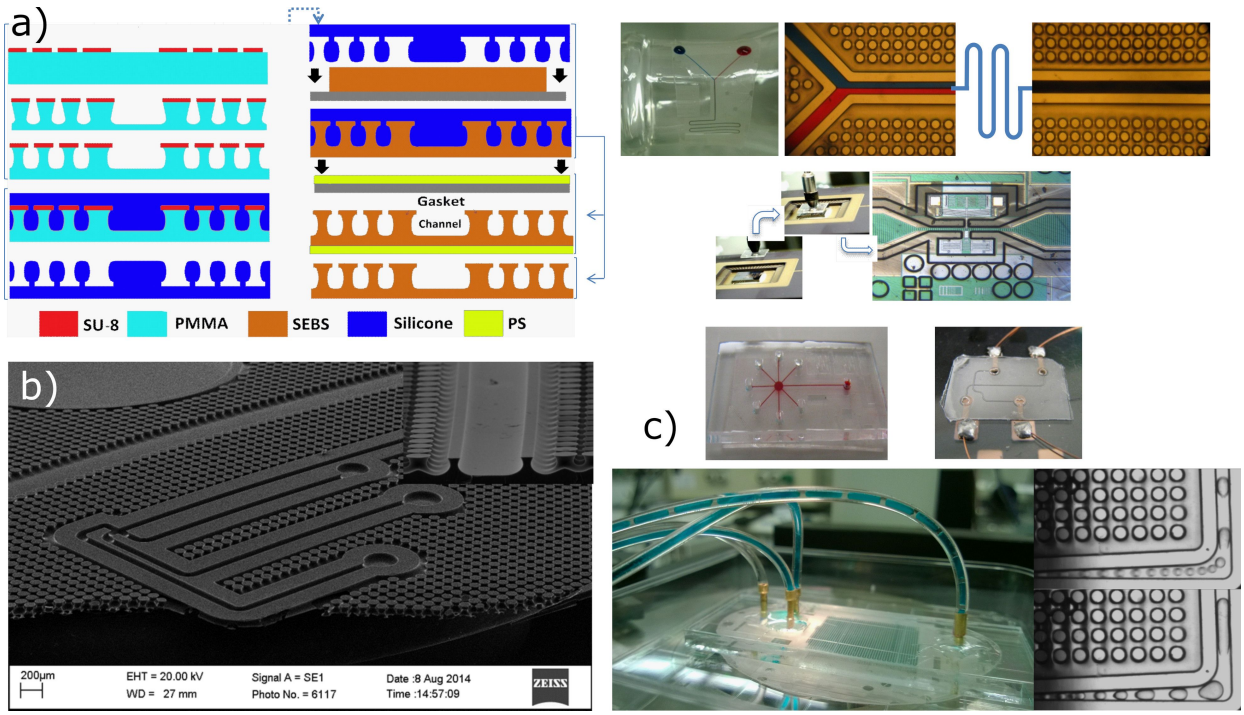

Figure 4: Geckofluidics process using similar crack-tolerant microstructures as gecko adhesives, but to define continuous gaskets for containing fluids. Figure 4 is a compilation of two figures from [35] ("Gecko gaskets for self-sealing and high-strength reversible bonding of microfluidics") by A. Wasay and D. Sameoto, distributed under the terms of the Creative Commons Attribution 3.0 Unported License, https://creativecommons.org/licenses/by/3.0. The source journal is © The Royal Society of Chemistry 2015. Panel (a) represents the fabrication process that may include gasket structures in addition to fibers and rigid backing layers to ensure that pressure within channels is distributed between more fibers surrounding the channels. Panel (b) shows a scanning electron microscopy image of a 5 × 7 mm gecko gasket design for electrophoresis. Panel (c) is a compilation image of multiple applications for the gecko gaskets, including microfluidics integrated on non-planar surfaces, bonded to microelectromechanical systems (MEMS), and their use in droplet generation with oil and water.

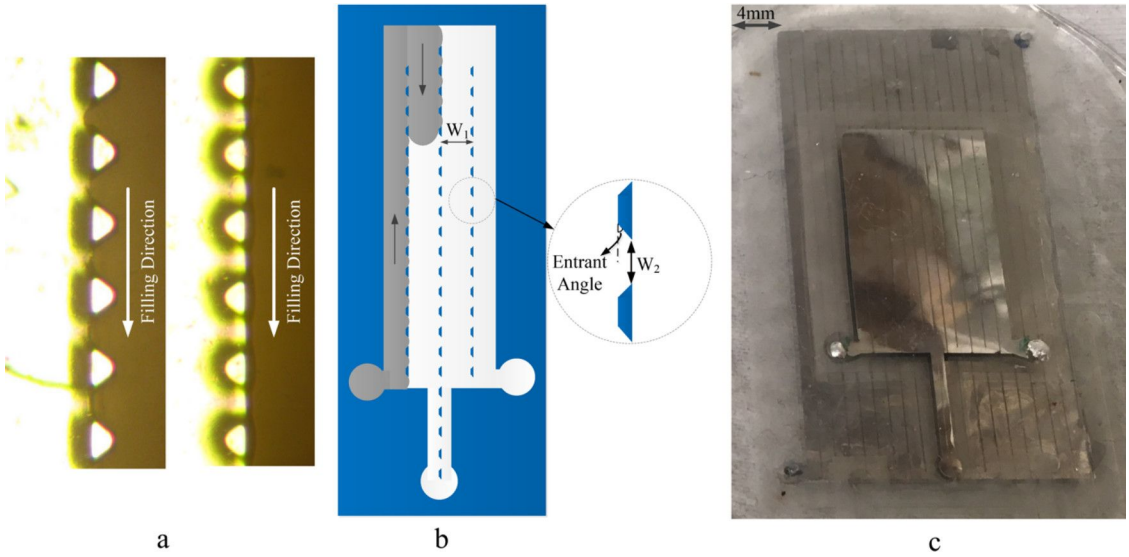

Figure 5: Laplace barriers within geckofluidic channels have directed room-temperature liquid metals (eutectic gallium–indium) with extremely high surface tension to properly fill complex microchannels (a, b) for the production of stretchable antennas (c) and electronics. Figure 5 was adapted from [36] M. Zandvakili et al., "Gecko-Gaskets for Multilayer, Complex, and Stretchable Liquid Metal Circuits and Antennas" Adv. Mater. Technol., with permission from John Wiley and Sons. © 2017 WILEY-VCH Verlag GmbH & Co. KGaA, Weinheim. This content is not subject to CC BY 4.0.

sives lies in finding a slam-dunk application that drives investment into scalable manufacturing. While microfluidics has many uses, it is still a very small market even in comparison to traditional adhesives. Since 2017, however, we have been working in an area that is very different from what biomimetic adhesives have been applied to previously, and a very promising application is the development of shape- and stiffness-tunable composites.

Anyone familiar with the movies "The Terminator" or "Big Hero 6" has seen a sci-fi version of robots that can change their shape, size, or function. Science fiction offers numerous intriguing examples where versatility, customization, improved performance, and functionality result from shape- or stiffness-tunable materials. However, there are many real-world applications for shape- and stiffness-tunable materials beyond the realms of science fiction, for example, prosthetic sockets that interface with individuals with limb differences. Enhancing comfort requires the socket to precisely match the stiffness and shape of the body. However, there are significant differences between individuals and even within an individual over the course of their life, which should be easily accommodated with adaptable materials. Another, more mundane example could be the car body of a standard vehicle. Typically, a fender bender necessitates replacement of the bumper if the latter has been damaged. However, imagine if that bumper could simply "turn off and on again", healing back to its original form. Nature offers many examples of self-healing damage over time, yet human-engineered products have rarely achieved this capability in a cost-effective manner [37]. Materials that can absorb energy and deform without being permanently damaged would be highly attractive from a sustainability perspective. A final example of practical products involves protective garments. Many elderly individuals wear hip protectors to guard against broken hips in the event of a fall [38]. However, these are often bulky, unattractive, and uncomfortable. If these materials could act as regular clothing that only transforms into body armor at the moment of a fall, their acceptance by the wider public would likely be much higher, reducing the health impact of traditional falls and injuries.

Academic literature is replete with instances of stiffness-tunable materials [15], and interest in this technology surged around 2010 with the advent of the modern soft robotics field. Traditional stiffness-switching mechanisms include phase change materials [39], jamming actuators [40], electrorheological fluids [41], and antagonistic actuators [42], but vacuum jamming has been the most popular in academic literature [43]. Vacuum jamming forces a series of particles, fibers, or sheets together to act as a semi-solid under vacuum. For instance, granular jamming can employ something as simple as coffee grounds in a rubber balloon to function as a shape-morphing actuator. Layer jamming, where different stacks of paper or thin film sheets combine under vacuum, offers more resilience and strength. However, vacuum jamming can present problems due to leaks, power consumption, noise from pumps, and the ultimate strength of the parts being limited by coefficients of friction and applied vacuum pressure.

My interest in stiffness tuning dates back to the inception of our biomimetic adhesive projects for the European Space Agency. I quickly realized that a very sticky and soft gecko-inspired foot lacked the structural rigidity to support a load, and those that were very stiff proved exceptionally challenging to achieve good contact with surfaces and achieve large adhesive strength [21]. A material that was soft when making contact and rigid when supporting a load would be ideal, and in fact this is still an area where modern efforts continue [31,44,45]. Our closest demonstration at the time to achieve this stiffness tuning involved using an internal wax support structure within the biomimetic adhesives, acting as a soft interior in its semi-molten state and being very rigid when cooled [39]. However, the downside of thermally induced stiffness was the time scale required for modulus change, taking about five to ten minutes with materials we were working with back in 2010 (Figure 6a–c).

Alternatively, we considered magnetic jamming including ball bearings and magnetorheological fluids within silicone pouches mixed with magnetite (Figure 6e,f). Unfortunately, the weak link in these jamming mechanisms was bonding the pouch to the ball bearings or internal fluid as the magnetic silicone had relatively weak attraction and was located at the furthest location from the magnetic trigger (NdFeB magnets). Without a strong bond between the silicone membrane and the internal magnetic materials, the actuator could not support substantial adhesive loads, leaving these projects unpublished and remaining an internal curiosity.

During a sabbatical in 2017, I first encountered projects related to layer jamming in the George Whitesides Lab for soft robotics applications. I quickly realized that the layer jamming concept could be perfectly suited for biomimetic adhesives, as their coefficient of friction could be significantly higher than one, and our work on geckofluidics with rigid backing materials was already indicating similar capabilities. Once in contact with a smooth surface, isotropic biomimetic adhesives do not require power to maintain adhesion and can function in various relatively extreme environments while providing adhesion pressures up to several megapascals [34], which is an order of magnitude better than vacuum-based jamming under standard atmospheric conditions.

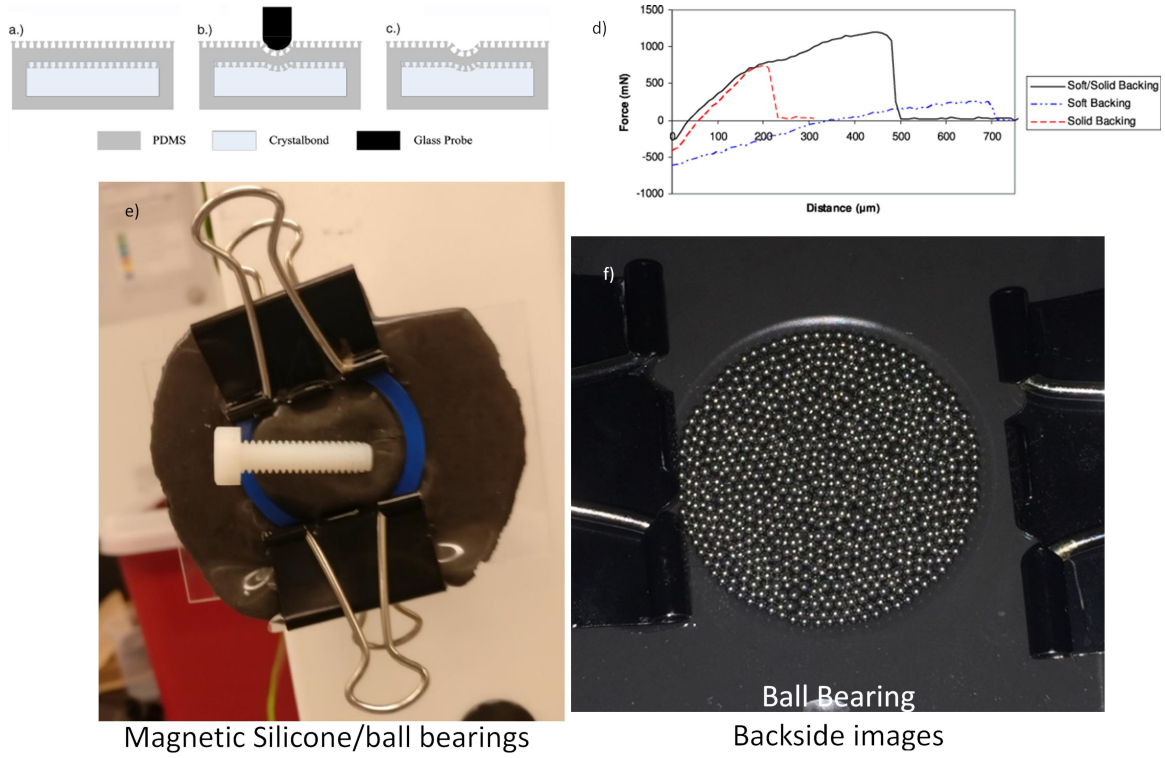

Figure 6: Non-vacuum jamming based stiffness-tunable prototypes developed for use in space applications. Figure 6a–d were republished from [39] ("Controllable biomimetic adhesion using embedded phase change material", Smart Materials and Structures, vol. 20, article no. 015014, published on 9 December 2010; https://doi.org/10.1088/0964-1726/20/1/015014); © 2010 IOP Publishing. Reproduced with permission via Copyright Clearance Center. All rights reserved. This content is not subject to CC BY 4.0. Panels (e, f) are unpublished work with image credit and permission from Samuel Lehmann 2016 – this content is not subject to CC BY 4.0.

This revelation that biomimetic adhesives could in fact be best suited as the internal surface of a composite material sparked a new and exciting research direction for soft robotics and adaptable composites. The reasons to use these materials as an internal rather than an external surface can be broadly categorized as follows:

- Uniform contact surfaces: Unlike a gecko, the adhesive materials do not need to be overdesigned for potentially touching dirty, rough, wet surfaces but can always be in contact with an ideally suited surface.
- No contaminants: When contained within a composite, these adhesives can be almost entirely free of contaminants and remain so if there is an outer sleeve to keep dust and debris out.
- High bond strength: Theoretically, a biomimetic adhesive can exhibit far higher bond strength than vacuum jamming. Literature reports adhesion strengths greater than 1 MPa with optimization [34], whereas vacuum jamming can at best support approximately 100 kPa of normal load between individual sheets when operating under normal atmospheric conditions.
- No active vacuum or power needed: Once adhered, no continuous vacuum or power is required to maintain the jamming state, an attractive property for applications that maintain their state for long durations and only need to be reformed occasionally.
- Energy damping: Depending on the structural layers for the biomimetic adhesives, there could be significant internal energy damping for energy absorption, that is, highly viscoelastic fibers and energy dissipation as heat during deformation and adhesion failures may possibly provide better crash protection or armor functionality in wearable composites.
- Triggering mechanisms: The actuation of these materials can be combined with electrostatic forces or magnets to enhance overall functionality. Pneumatic pressures acting globally (for vacuum triggering) or locally (using positive pressure in geckofluidic channels) are also feasible.

The utility of multiheight fibers, understood back in 2008 based on personal observations of spider foot hairs' adhesion mechanisms, is that a biomimetic adhesive can remain in a default

non-adhesive state under light loads but become adhesive upon applying a certain minimum pressure level. This concept inspired the first generation of gecko-jammed composites presented at the Adhesion Society annual meeting in 2020 [46]. To achieve a cost-effective system, we opted for commercial biomimetic materials from Setex, modified to incorporate anti-adhesive features that we could typically produce in our custom processes. We applied cell disruption media, consisting of 100 µm diameter glass spheres, randomly or deterministically on sheets of these dry adhesives. The glass beads were large enough that the normal state of two sheets of dry adhesives would be non-adhesive unless a preload exceeding approximately 5 kPa was applied, at which point the fibers could self-adhere and prevent relative motion between the two sheets. The results were dramatic as these biomimetic composites did not merely act as two jammed sheets but rather as a sandwich composite. This significantly increased overall stiffness because the stiff material, that is, the backing layers, is supported a considerable distance from the core axis. Figure 7 shows demonstrations of how these materials can function statically for changing stiffness or dynamically so that the materials can be deformed and then fixed into multiple states. While no substantial work continued on this for several years because of the COVID-19 pandemic, we are now pursuing different optimized geometries, structural materials, and methods to control the internal adhesion for improved reconfigurability.

Simple mathematical models and simulations can predict the overall effectiveness of these biomimetic adhesively jammed structures compared to traditional layer jamming with uniform layers of material (Figure 8). Information on the basic guidelines for sandwich composites can be found elsewhere [47]; the bending stiffness D is a function of the outer film modulus E_f, the distance between the central axis of those films (defined by the core thickness d and the film thickness t), the modulus of the core E_c, and the width of the composite b. If the "core" is made of independent fibers, it can have an effective E_c that is close to zero when in the unadhered state and will, therefore, minimally affect bending stiffness in comparison to two independent thin films of E_f.

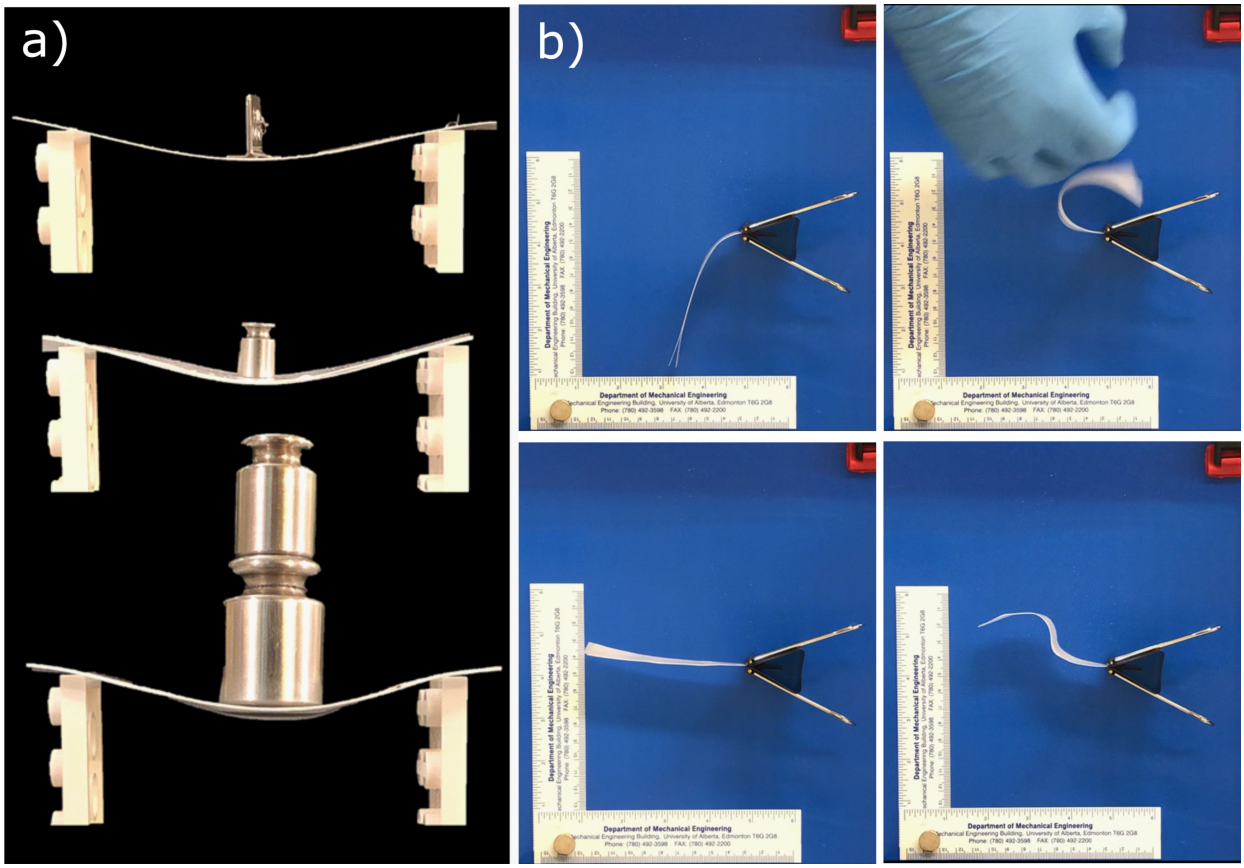

Figure 7: (a) Composite images of one and two-layer SETEX tapes prior to adhesion (top two images) and, at the bottom, a demonstration of how the bending stiffness increases with the adhered tapes. (b) Images taken as screen captures from a video demonstrating shape morphing/fixing capability of a gecko tape composite. Images are reproduced from [46] © The Adhesion Society. This content is not subject to CC BY 4.0.

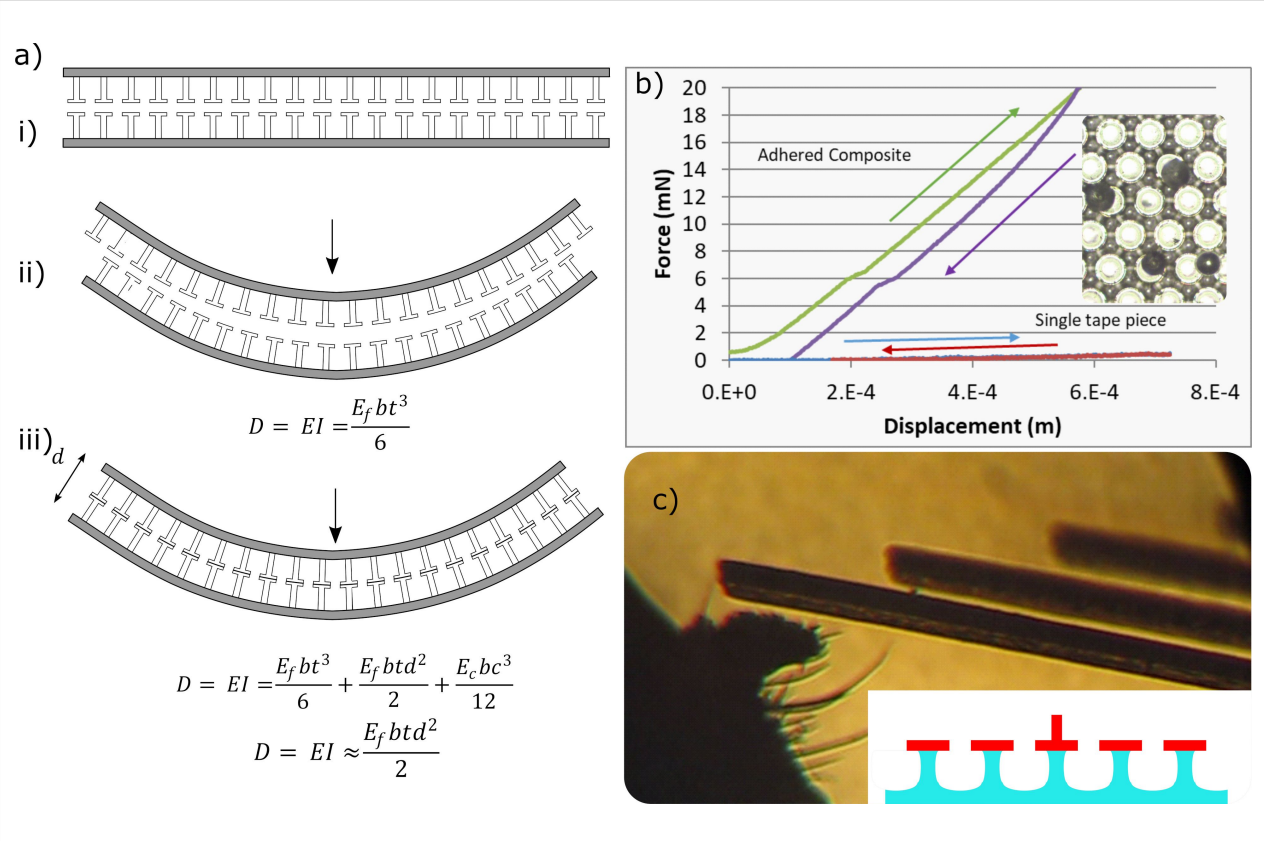

Figure 8: (a) i) Schematic of two gecko adhesives in their default non-adhesive state, ii) simplified modeling of effective bending stiffness as either two parallel non-adhesive sheets or as iii) a bonded sandwich composite structure. (b) Small scale tests show substantial bending stiffness increase as anticipated, but the large hysteresis indicates that internal delamination and plastic behavior can occur with these proof-of-principle designs. The inset shows the relative size of the anti-adhesive beads on top of the Setex surface. (c) Multiheight fibers inspired by spider legs (2008 experiments) as previously disclosed [48] may further enhance composite behaviors for on–off functionality.

For the simplified model shown in Figure 8, if $E_c \ll E_f$ and $t \ll d$, then the overall bending stiffness increase for the adhered composite compared to its unadhered state can be approximated as:

$$\frac{D_{\text{jammed}}}{D_{\text{unjammed}}} = \frac{d^2}{3t^2}$$

For a film thickness merely one tenth that of the core material, we would expect approximately a 30-times increase in bending stiffness, simply by bonding two pieces of biomimetic tape. In practice, this also works with materials like pressure-sensitive adhesive tapes. However, the assumption of negligible E_c is less appropriate, and their geometries are less suited for the purpose, resulting in lower bending stiffness increase per layer. Since the publication of this work, other similar mechanisms [49] have been demonstrated and may yet be improved by other groups working toward similar goals. Hence, the tuning of adhesion within composites could be an important area of investigation for years to come.

While this is a demonstration of bending stiffness increase, similar effects can be achieved regarding tension, much like an electrostatic clutch; in those instances, an even higher effective stiffness can be achieved in comparison to the unbonded state [50]. While work on this topic is just now restarting in our own group after disruption and delays from the COVID-19 pandemic, we hope to develop better designs suited for the purpose of on–off adhesion with bioinspired adhesives and apply them to morphing, stiffness-tunable composites for a variety of applications in the coming years.

Conclusion

Gecko-inspired adhesives have had a long run in the academic literature, but the question of their future utility is at a crossroads: Do they remain a niche curiosity restricted to high-value, low-volume applications, or could they still become a breakout technology on par with Velcro® or the zipper? I personally hope that we can eventually push manufacturing and performance of these materials to such a low cost and high performance that it would be possible to build laminates, composites, clothing, and protective equipment out of these adhesive materi-

als. We can ideally enable a type of van der Waals-based construction set for manufacturing products with strong, reversibly adhered laminates to improve adaptability, sustainability, and product performance. The future of reversible adhesives will come from looking within, and going beyond, biomimicry.

Supporting Information

A demo of integrated HDPE fibers within an SEBS biomimetic adhesive sheet showing high shear strength (and negligible adhesion) on fabrics like spandex, while also being capable of having high peel strength on smooth plastic surfaces like polystyrene. The demonstration was completed in winter 2021 and presented at the Adhesion Society Virtual conference that year. Adhesive manufacturing, 3D printing, and demonstration was carried out by Dan Sameoto.

Supporting Information File 1

Multimaterial biomimetic adhesive demonstration. [https://www.beilstein-journals.org/bjnano/content/supplementary/2190-4286-15-79-S1.mp4]

Acknowledgements

The graphical abstract is © The Adhesion Society. This content is not subject to CC BY 4.0. The author would like to thank the many students who have worked on this topic in his group including Brendan Ferguson, Walid Bin Khaled, Ben Bschaden, Abdul Wasay, Babak Soltannia, Yue Wang, Samuel Lehmann, Mersedeh Zandvakili, and Teng Zhang.

Author Contributions

Dan Sameoto: formal analysis; funding acquisition; investigation; writing – original draft; writing – review & editing.

ORCID® iDs

Dan Sameoto - https://orcid.org/0000-0003-4879-2935

Data Availability Statement

Data sharing is not applicable as no new data was generated or analyzed in this study.

References

1. Autumn, K.; Liang, Y. A.; Hsieh, S. T.; Zesch, W.; Chan, W. P.; Kenny, T. W.; Fearing, R.; Full, R. J. *Nature* **2000,** *405,* 681–685. doi:10.1038/35015073
2. Li, X.; Tao, D.; Lu, H.; Bai, P.; Liu, Z.; Ma, L.; Meng, Y.; Tian, Y. *Surf. Topogr.: Metrol. Prop.* **2019,** *7,* 023001. doi:10.1088/2051-672x/ab1447
3. Russell, A. P.; Stark, A. Y.; Higham, T. E. *Integr. Comp. Biol.* **2019,** *59,* 101–116. doi:10.1093/icb/icz032
4. Wang, W.; Liu, Y.; Xie, Z. *J. Bionic Eng.* **2021,** *18,* 1011–1044. doi:10.1007/s42235-021-00088-7
5. Kroemer, H. *Rev. Mod. Phys.* **2001,** *73,* 783–793. doi:10.1103/revmodphys.73.783
6. Creton, C. *MRS Bull.* **2003,** *28,* 434–439. doi:10.1557/mrs2003.124
7. Jeffries, L.; Lentink, D. *Appl. Mech. Rev.* **2020,** *72,* 050802. doi:10.1115/1.4048448
8. Whitesides, G. M. *Nature* **2006,** *442,* 368–373. doi:10.1038/nature05058
9. Raj M, K.; Chakraborty, S. *J. Appl. Polym. Sci.* **2020,** *137,* 48958. doi:10.1002/app.48958
10. Dong, X.; Liu, L.; Tu, Y.; Zhang, J.; Miao, G.; Zhang, L.; Ge, S.; Xia, N.; Yu, D.; Qiu, X. *TrAC, Trends Anal. Chem.* **2021,** *143,* 116377. doi:10.1016/j.trac.2021.116377
11. Li, J.; Kim, C.-J. "CJ". *Lab Chip* **2020,** *20,* 1705–1712. doi:10.1039/d0lc00144a
12. Sharma, S.; Zapatero-Rodríguez, J.; Estrela, P.; O'Kennedy, R. *Biosensors* **2015,** *5,* 577–601. doi:10.3390/bios5030577
13. Whitesides, G. M. *Angew. Chem., Int. Ed.* **2018,** *57,* 4258–4273. doi:10.1002/anie.201800907
14. Preston, D. J.; Rothemund, P.; Jiang, H. J.; Nemitz, M. P.; Rawson, J.; Suo, Z.; Whitesides, G. M. *Proc. Natl. Acad. Sci. U. S. A.* **2019,** *116,* 7750–7759. doi:10.1073/pnas.1820672116
15. Manti, M.; Cacucciolo, V.; Cianchetti, M. *IEEE Rob. Autom. Mag.* **2016,** *23,* 93–106. doi:10.1109/mra.2016.2582718
16. Setex Technologies. Setex Tapes. https://www.setextechnologies.com/tapes/ (accessed April 4, 2024).
17. Gottlieb Binder GmbH & Co. KG. Gecko Tape. https://www.binder.de/en/products/basic/gecko/ (accessed April 4, 2024).
18. Zhang, T.; Yue, X.; Sameoto, D. *Micromachines* **2018,** *9,* 406. doi:10.3390/mi9080406
19. Sameoto, D.; Ferguson, B. *J. Adhes. Sci. Technol.* **2014,** *28,* 337–353. doi:10.1080/01694243.2012.693802
20. Kim, J.-K.; Krishna-Subbaiah, N.; Wu, Y.; Ko, J.; Shiva, A.; Sitti, M. *Adv. Mater. (Weinheim, Ger.)* **2023,** *35,* 2207257. doi:10.1002/adma.202207257
21. Sameoto, D.; Li, Y.; Menon, C. *J. Bionic Eng.* **2008,** *5,* 189–196. doi:10.1016/s1672-6529(08)60024-4
22. Li, Y.; Ahmed, A.; Sameoto, D.; Menon, C. *Robotica* **2012,** *30,* 79–89. doi:10.1017/s0263574711000373
23. Kim, S.; Sitti, M. *Appl. Phys. Lett.* **2006,** *89,* 261911. doi:10.1063/1.2424442
24. del Campo, A.; Greiner, C.; Arzt, E. *Langmuir* **2007,** *23,* 10235–10243. doi:10.1021/la7010502
25. Khaled, W. B.; Sameoto, D. *Bioinspiration Biomimetics* **2013,** *8,* 044002. doi:10.1088/1748-3182/8/4/044002
26. Sameoto, D.; Sharif, H.; Díaz Téllez, J. P.; Ferguson, B.; Menon, C. *J. Adhes. Sci. Technol.* **2014,** *28,* 354–366. doi:10.1080/01694243.2012.693809
27. Wang, Y.; Tian, H.; Shao, J.; Sameoto, D.; Li, X.; Wang, L.; Hu, H.; Ding, Y.; Lu, B. *ACS Appl. Mater. Interfaces* **2016,** *8,* 10029–10037. doi:10.1021/acsami.6b01434
28. Wang, Y.; Lehmann, S.; Shao, J.; Sameoto, D. *ACS Appl. Mater. Interfaces* **2017,** *9,* 3060–3067. doi:10.1021/acsami.6b11708

29. Zhang, T.; Liang, T.; Yue, X.; Sameoto, D. Integration of Thermoresponsive Velcro-like Adhesive for Soft Robotic Grasping of Fabrics or Smooth Surfaces. 2019 2nd IEEE International Conference on Soft Robotics (RoboSoft); IEEE, 2019; pp 120–125. doi:10.1109/robosoft.2019.8722743
30. Hassani, H. T. M.; Baji, A. *ACS Appl. Bio Mater.* **2023,** *6,* 4002–4019. doi:10.1021/acsabm.3c00504
31. Son, C.; Jeong, S.; Lee, S.; Ferreira, P. M.; Kim, S. *Robotics* **2023,** *12,* 59. doi:10.3390/robotics12020059
32. Luo, H.; Li, C.; Wang, S.; Zhang, S.; Song, J. *ACS Appl. Mater. Interfaces* **2024,** *16,* 9443–9452. doi:10.1021/acsami.3c16282
33. Liang, D. S. T. Mechanically and Spatially Variable Gecko-inspired Fibers for Multi-Mechanism Adhesion. In *Adhesion Society Annual meeting,* Feb 22–25, 2021; Virtual, 2021.
34. Fischer, S. C. L.; Groß, K.; Torrents Abad, O.; Becker, M. M.; Park, E.; Hensel, R.; Arzt, E. *Adv. Mater. Interfaces* **2017,** *4,* 10.1002/admi.201700292. doi:10.1002/admi.201700292
35. Wasay, A.; Sameoto, D. *Lab Chip* **2015,** *15,* 2749–2753. doi:10.1039/c5lc00342c
36. Zandvakili, M.; Honari, M. M.; Mousavi, P.; Sameoto, D. *Adv. Mater. Technol. (Weinheim, Ger.)* **2017,** *2,* 10.1002/admt.201700144. doi:10.1002/admt.201700144
37. Wool, R. P. *Soft Matter* **2008,** *4,* 400–418. doi:10.1039/b711716g
38. Santesso, N.; Carrasco-Labra, A.; Brignardello-Petersen, R. *Cochrane Database Syst. Rev.* **2014,** CD001255. doi:10.1002/14651858.cd001255.pub5
39. Krahn, J.; Sameoto, D.; Menon, C. *Smart Mater. Struct.* **2011,** *20,* 015014. doi:10.1088/0964-1726/20/1/015014
40. Zhao, Y.; Wang, Y. *IEEE Rob. Autom. Lett.* **2023,** *8,* 3238–3245. doi:10.1109/lra.2023.3266667
41. Sun, Y.; Wu, X.; Lu, B.; Wang, M.; Ding, J.; Pu, H.; Jia, W.; Peng, Y.; Luo, J. *IEEE/ASME Trans. Mechatronics* **2024,** *29,* 324–334. doi:10.1109/tmech.2023.3275961
42. Bruder, D.; Graule, M. A.; Teeple, C. B.; Wood, R. J. *Sci. Rob.* **2023,** *8,* eadf9001. doi:10.1126/scirobotics.adf9001
43. Fitzgerald, S. G.; Delaney, G. W.; Howard, D. *Actuators* **2020,** *9,* 104. doi:10.3390/act9040104
44. Glaser, N. C.; Langowski, J. K. A. *R. Soc. Open Sci.* **2023,** *10,* 221263. doi:10.1098/rsos.221263
45. Linghu, C.; Liu, Y.; Tan, Y. Y.; Sing, J. H. M.; Tang, Y.; Zhou, A.; Wang, X.; Li, D.; Gao, H.; Hsia, K. J. *Proc. Natl. Acad. Sci. U. S. A.* **2023,** *120,* e2221049120. doi:10.1073/pnas.2221049120
46. Sameoto, D. Reversible gecko-inspired adhesion for enhanced layer jamming actuators. In *Adhesion Society Annual Meeting,* Charleston SC, Feb 23–26, 2020; 2020.
47. Daniel, I. M.; Abot, J. L. *Compos. Sci. Technol.* **2000,** *60,* 2455–2463. doi:10.1016/s0266-3538(00)00039-7
48. Menon, C.; Sameoto, D. E. Biomimetic dry adhesives and methods of production therefor. Google Patents CA2717633C, June 19, 2018.
49. Chen, K. J.; Sakovsky, M. *Smart Mater. Struct.* **2024,** *33,* 015036. doi:10.1088/1361-665x/ad142d
50. Hajj-Ahmad, A.; Han, A. K.; Lin, M. A.; Glover, G. H.; Cutkosky, M. R. *Adv. Mater. Technol. (Weinheim, Ger.)* **2023,** *8,* 10.1002/admt.202202025. doi:10.1002/admt.202202025

License and Terms

This is an open access article licensed under the terms of the Beilstein-Institut Open Access License Agreement (https://www.beilstein-journals.org/bjnano/terms), which is identical to the Creative Commons Attribution 4.0 International License (https://creativecommons.org/licenses/by/4.0). The reuse of material under this license requires that the author(s), source and license are credited. Third-party material in this article could be subject to other licenses (typically indicated in the credit line), and in this case, users are required to obtain permission from the license holder to reuse the material.

The definitive version of this article is the electronic one which can be found at:
https://doi.org/10.3762/bjnano.15.79

BEILSTEIN JOURNAL OF NANOTECHNOLOGY

Interface properties of nanostructured carbon-coated biological implants: an overview

Mattia Bartoli*[1,2], Francesca Cardano[1,3], Erik Piatti[4], Stefania Lettieri[1,4], Andrea Fin[1,3] and Alberto Tagliaferro[2,4]

Review

Open Access

Address:
[1]Center for Sustainable Future Technologies (CSFT), Istituto Italiano di Tecnologia (IIT), Via Livorno, 60, 10144, Torino, Italy, [2]Consorzio Interuniversitario Nazionale per la Scienza e Tecnologia dei Materiali (INSTM), Via G. Giusti 9, 50121, Firenze, Italy, [3]Department of Chemistry, University of Turin, Via P. Giuria 7, 10125 Torino, Italy and [4]Department of Applied Science and Technology, Politecnico di Torino, Corso Duca Degli Abruzzi, 24, 10129, Torino, Italy

Email:
Mattia Bartoli* - mattia.bartoli@iit.it

* Corresponding author

Keywords:
biocompatibility; carbon nanotubes; coatings; graphene; nanodiamonds; surfaces

Beilstein J. Nanotechnol. **2024,** *15,* 1041–1053.
https://doi.org/10.3762/bjnano.15.85

Received: 26 March 2024
Accepted: 05 August 2024
Published: 16 August 2024

This article is part of the thematic issue "Biomimetics and bioinspired surfaces: from nature to theory and applications".

Guest Editor: R. Guillermo

© 2024 Bartoli et al.; licensee Beilstein-Institut.
License and terms: see end of document.

Abstract

The interfaces between medical implants and living tissues are of great complexity because of the simultaneous occurrence of a wide variety of phenomena. The engineering of implant surfaces represents a crucial challenge in material science, but the further improvement of implant properties remains a critical task. It can be achieved through several processes. Among them, the production of specialized coatings based on carbon-based materials stands very promising. The use of carbon coatings allows one to simultaneously fine-tune tribological, mechanical, and chemical properties. Here, we review applications of nanostructured carbon coatings (nanodiamonds, carbon nanotubes, and graphene-related materials) for the improvement of the overall properties of medical implants. We are focusing on biological interactions, improved corrosion resistance, and overall mechanical properties, trying to provide a complete overview within the field.

Introduction

For centuries, the simple manipulation of natural resources has represented the only available strategy for the realization of artifacts, buildings, and innovations, until the principles laying behind the structure of materials were discovered. The discovery of the atom-based nature of matter has revolutionized the approach to natural science, leading to the development of nanoscience. Noble laureate Richard Feynman first proposed the concept of nanomaterials in his well-known lecture entitled "*There's Plenty of Room at the Bottom*", in which he discussed the possibility of the manipulation of individual

atoms and molecules [1]. Traditionally, this first lecture was recognized as the birth of nanotechnology, although the term was first used only later by Norio Taniguchi in 1974 to describe the study of materials at the nanoscale [2]. Afterwards, nanosized and nanostructured carbon species have attracted great interest thanks to their intrinsic properties and easy functionalization [3]. The utilization of nanocarbon species has been widely deployed in advanced medical applications [4] as active species or as drug delivery platforms using tailored carbon nanotubes (CNTs) [5,6], fullerenes [7,8], carbon dots (CDs) [9,10], and graphene-related materials (i.e., graphene oxide (GO) [11], reduced graphene oxide (rGO) [12], and nanographite (nG) [13]). Furthermore, the production of nanocarbon-reinforced materials is paving the way for a new era of tissue engineering thanks to their application as high-performance biocompatible scaffolds [14,15] and implantable devices [16,17]. The key features of these materials should be compatible with the complexity of biological environments represented by implant–tissue interfaces [18] through the tuning of different parameters (i.e., surface roughness and potential as well as hydrophobicity).

Cells and biomolecules can selectively adhere to or be repelled from artificial implanted surfaces, triggering several metabolic pathways of high importance [19]. Particularly, cellular adhesion and a controlled immunological response are key features of any artificial device for being effectively implanted [20]. Additionally, responsive surfaces represent the last frontier in nanomedicine, and they require the exchange of signals and information at the molecular level with the biological environment [21]. Nanostructured and nanosized materials represent a valid solution to offer all the abovementioned features thanks to their highly controllable properties. Nevertheless, the preparation of nanocarbon-containing materials is still complex because of the efforts required for achieving a homogenous dispersion in an inorganic–organic matrix [22-24].

In this short review, we are discussing nanostructured and nanosized carbon-based materials used to improve the durability and physicochemical properties of biological implants as summarized in Figure 1.

Review

Nanostructured carbon-containing materials at biological interfaces

Interfaces between artificial and biological environments play a critical role for the design and long-term performance of any artificial implant [25,26]. The interface between an implant and the biological environment is a dynamic and complex area, where several biological, physical, and chemical interactions can take place simultaneously, including immunological

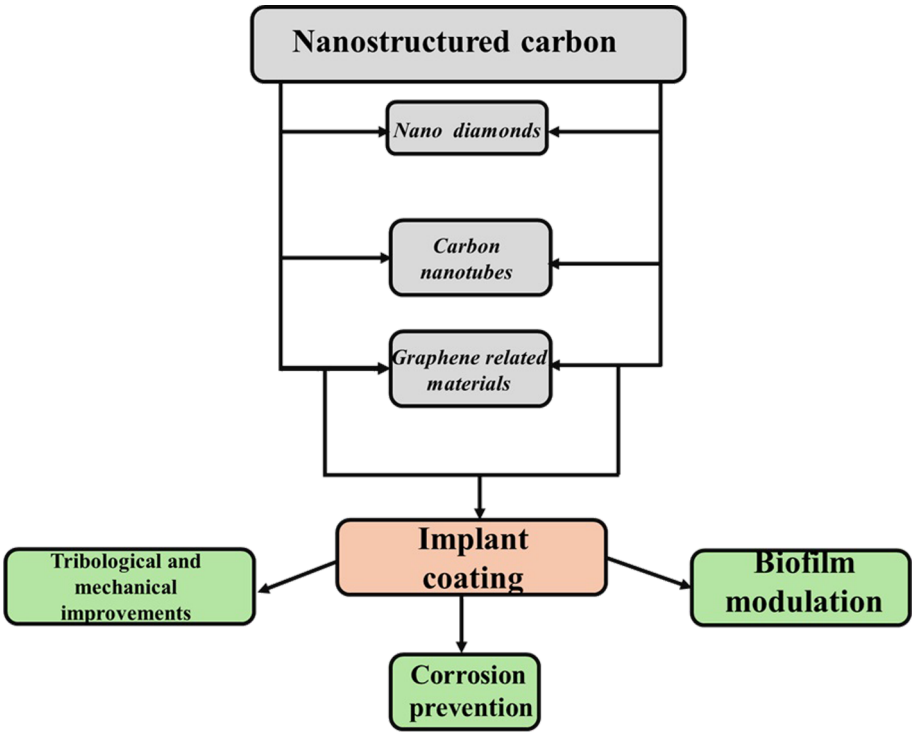

Figure 1: Relation between nanostructured carbon materials and the tuned properties in biological implants.

response [27], mechanical mismatch with the tissue [28], degradation [29], responses to stimuli [30], and proliferation of bacteria [31]. In the next section, we investigate the effect of carbon-based nanostructured interfaces on the mitigation of adverse effects occurring to biological implants, considering advantages and disadvantages as summarized in Table 1.

Nanostructured and nanosized carbon materials: an overview

The family of nanostructured carbon materials has several members with peculiar properties, namely, (i) graphene-related materials, (ii) CNTs, and (iii) nanodiamonds (NDs) as shown in Figure 2.

All nanosized carbon materials show remarkable properties regarding both thermal and electronic conduction, but they should be treated carefully to ensure reproducible production protocols. The next section briefly overviews all nanosized carbon materials since a deep understanding of each material is of capital importance for a comprehensive understanding of their applications at biological interfaces.

Graphene and graphene-related materials

In 2008, Lee and co-workers [32] stated that neat graphene was the strongest material ever tested with a tensile strength of 131 GPa and a Young's modulus close to 1 TPa. The reason for these properties of graphene is the stability of the π-bond network around the hexagonal structures of carbon rings, which prevents planar deformations [33]. The same phenomenon explains the high thermal conductivity of up to 3000 $W \cdot m^{-1} \cdot K^{-1}$ [34,35] and the outstanding electrical properties [36-38].

Compared to conventional 3D materials, the understanding of electronic transport and carrier dynamics in graphene is significantly complicated by the extreme anisotropy intrinsic to its crystal structure and its large compositional and structural variability [39]. Beyond the obvious consequences arising from the chemical composition, some of the main aspects affecting electronic transport in graphene are structural polymorphism [40] (arrangement, number, and order of layers), the electronic coupling between different layers, and the matrix in which graphene is embedded [41]. Indeed, the matrix plays a pivotal role owing to the ultimate surface-to-volume ratio and the poor electrostatic screening displayed by graphene-based composites [39]. These aspects are especially relevant in determining the in-plane electronic transport within each layer of graphene (intra-layer transport). Conversely, the electronic coupling between different layers dominates the out-of-plane electronic transport from one layer to another (inter-layer transport) and is

Table 1: Summary of advantages and disadvantages of the utilization of nanostructured carbon interfaces in biological implants.

Nanostructured material	Advantages	Disadvantages
nanodiamonds	* increased wear stress resistance	–
carbon nanotubes	* increased wear stress resistance	–
graphene and related materials	* increased wear stress resistance	–

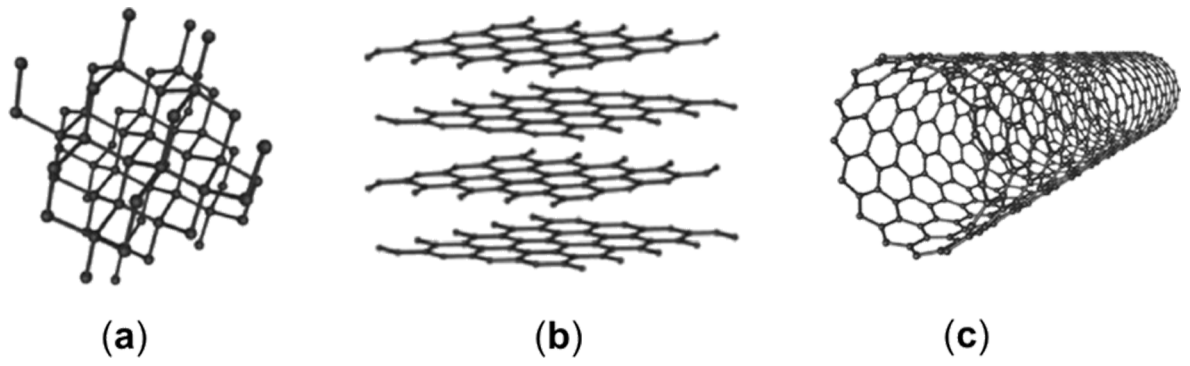

Figure 2: Summary of carbon allotropes: (a) NDs, (b) graphene-related materials, and (c) CNTs. Figure 2 was adapted from Wikimedia Commons https://commons.wikimedia.org/wiki/File:Eight_Allotropes_of_Carbon.png (created by Michael Ströck (mstroeck), distributed under the terms of the CC BY-SA 3.0 Unported License, http://creativecommons.org/licenses/by-sa/3.0).

the source of the large anisotropy typically displayed between in-plane and out-of-plane carrier mobilities [42]. Carrier injection is usually determined by energy band alignment and interface transparency, and it is limited by the number of available conduction pathways and the existence of a tunnel barrier between graphene flakes [43]. Accordingly, the transparency of the interface between different flakes determines whether the inter-flake transport is diffusive or hopping-type regardless of the intrinsic mechanisms responsible for intra-flake transport in graphene-containing materials [44].

Furthermore, the manipulation of pristine graphene is a hard task, and several derivatives (i.e., GO and rGO) have been developed to partially preserve the properties of pristine graphene while enabling better handling.

GO is an oxidized graphene derivative rich in oxygen functionalities (hydroxy, epoxy, carbonyl, and carboxylic groups) arranged according to the Lerf–Klinowski model [45]. GO is generally produced through chemical oxidation and exfoliation of graphite flakes with different protocols to tune the oxygen content [46,47]. The defective structure of GO deeply affects its electronic properties, which are considerably inferior compared with neat graphene. However, GO can be suspended in several solvents and easily functionalized to act as a chemical platform [48]. rGO stands as a compromise between the easier handling of GO and the properties of neat graphene. rGO is produced through direct reduction of GO using physical or chemical routes [49]. Thus, the carbon-to-oxygen ratio can be increased to values of around 8:1 to 246:1, significantly higher than those of GO [50]. The electrical properties show a remarkable improvement compared with GO, even if they still remain far below those of graphene. Last, GO and rGO show good interactions with polymeric matrices thanks to specific surface functionalizations [51].

Carbon nanotubes

CNTs are an allotropic state of carbon discovered in the middle of the 20th century [52-55], which became famous in 1991 [56]. CNTs can be described as single or multiple cylindrical graphite sheets rolled up in a tubular structure forming single-walled CNTs (SWCNTs) or multiwalled CNTs (MWCNTs). SWCNTs are characterized by diameters from 0.3 nm [57] to 1 nm [58], while the diameters of MWCNTs can reach 100 nm [59,60] with a very high aspect ratio. The length of CNTs varies from a few nanometers [61] to several centimeters [62], and it is strictly related to the synthesis method. Additionally, CNTs can end with fullerene-type caps that are highly reactive because of the high distortion [63].

As summarized in Table 2, individual SWCNTs or MWCNTs show incredibly good mechanical and conduction properties. Nevertheless, individual CNTs are rare, and most applications are based on CNT bundles, which are difficult to homogenously disperse in polymeric matrices, and whose properties are not comparable with those of individual CNTs [71].

Nanodiamonds

NDs are a carbon allotrope composed by sp^3-hybridized carbon atoms arranged in a tetrahedral crystalline lattice structure [72]. The structure is accountable for the high thermal conductivity due to efficient heat conduction through phonon vibrations, which can reach 550 $W \cdot m^{-1} \cdot K^{-1}$ after sintering at high pressure [73]. Nevertheless, surface defects and the granular shape of the NDs represent boundaries for phonon transport reducing the thermal energy propagation [74]. Furthermore, the thermal conductivity of NDs increases with the increment of temperature because the higher number of phonons increases the efficiency of thermal transport [75]. NDs show also exceptional mechanical strength and low chemical reactivity, making them sound candidates for thin film coatings [76]. These properties are counterbalanced by a low electrical conductivity due to quantum confinement as reported by Bolker and co-workers [77]. Authors reported that the bandgap of NDs is strongly correlated to the NDs' size, and it increases with decreasing crystallite size. However, the ND properties can be altered by heteroatomic doping and through the introduction of surface defects, including passivation and vacancies [78].

Deposition methods for the synthesis of carbon coatings

The addition of nanostructured and nanosized carbon species into materials for biological applications can be attained by several techniques such as chemical vapor deposition (CVD), physical vapor deposition (PVD), and in situ formation through laser treatments. CVD offers several advantageous features such

Table 2: Summary of properties of single SWCNTs and MWCNTs.

	Young's modulus (GPa)	Tensile strength (GPa)	Resistivity (Ω·m)	Thermal conductivity ($W \cdot m^{-1} \cdot K^{-1}$)
SWCNTs	900–1700 [64]	75 [65]	10^{-6} [66]	1750–5800 [67]
MWCNTs	690–1800 [68]	150 [65]	10^{-5} [69]	3000 [70]

as a high degree of control over the deposition process. CVD involves the deposition of a thin film of material onto a substrate through homogeneous or heterogeneous reactions [79]. Homogeneous reactions are those involving the decomposition of precursor in the gas phase forming products that condense on a target. In contrast, heterogeneous reactions are those involving the decomposition of the precursors on the solid surface of a catalyst that also acts as a support. As reported by Porro et al. [80], the variation of few parameters (i.e., precursor flux and process temperature) can be sufficient to obtain nanographite or CNTs via CVD. Furthermore, Musso et al. [81] proved that, under appropriate conditions, CNTs and carbon microfibers can be grown from different carbon precursors (i.e., camphor and cyclohexanol) on various substrates, ranging from uncoated silicon to simple glass, to yield carpets of vertically aligned CNTs. Nevertheless, a purification stage for removing the catalyst is mandatory for avoiding side effects in biological environments [82,83]. The choice of the catalyst is strictly related to the desired carbon nanomaterials. Metal catalysts with high carbon solubility primarily involve carbon segregation and precipitation throughout the metal bulk [84], while metal catalysts with low carbon solubility act from the metal surface inward [63].

PVD routes are numerous, and they are classified according to the power sources used for the process (i.e., plasma-, direct current-, radiofrequency-, and ion beam-assisted coatings) [85]. All PVD processes are based on a vacuum chamber containing the material to be deposited, known as target, and the chosen substrate onto which the deposition occurs. During electron beam evaporation, an electron beam is used to vaporize the target material, while during sputtering, a high-energy ion beam is used to bombard the target. In both cases, atoms are ejected from the target and subsequently condense onto the substrate. The thickness and some morphological properties of the deposited nanostructured film can be controlled by adjusting deposition time, substrate temperature, and deposition rate.

The response of biological surfaces to non-biological materials

The first challenge in developing biomedical implants is related to biocompatibility because the implant interfaces are the first line of contact between a foreign body and living organisms. The bulk materials used in implants are carefully chosen to minimize adverse reactions, but the immune system may still recognize them as external entities and trigger inflammatory responses due to mere surface interactions, as summarized in Figure 3.

The interaction between implants and the immune system is highly tissue-specific, with different responses observed depending on the implantation sites. Usually, the insertion of an implant is followed by the adsorption of plasma components onto the surface, forming a matrix composed by platelets and coagulation cascade components. This process triggers the inflammatory response of neutrophils, which attempt to degrade the implant through phagocytosis and the release of reactive oxygen species. Macrophages play a key role changing from pro-inflammatory to anti-inflammatory phenotypes. The final step in the immune system response involves the formation of foreign-body giant cells on the implant surface. Increased cytokine levels trigger the release of pro-fibrogenic factors and recruiting fibroblasts. Fibroblasts induce the accumulation of collagen leading to the foreign-body reaction. This phenomenon involves the formation of a fibrous capsule around the implant, which compromises its functionality (such as the flexibility of cardiovascular stents) and, thus, limits the integration of soft tissue implants.

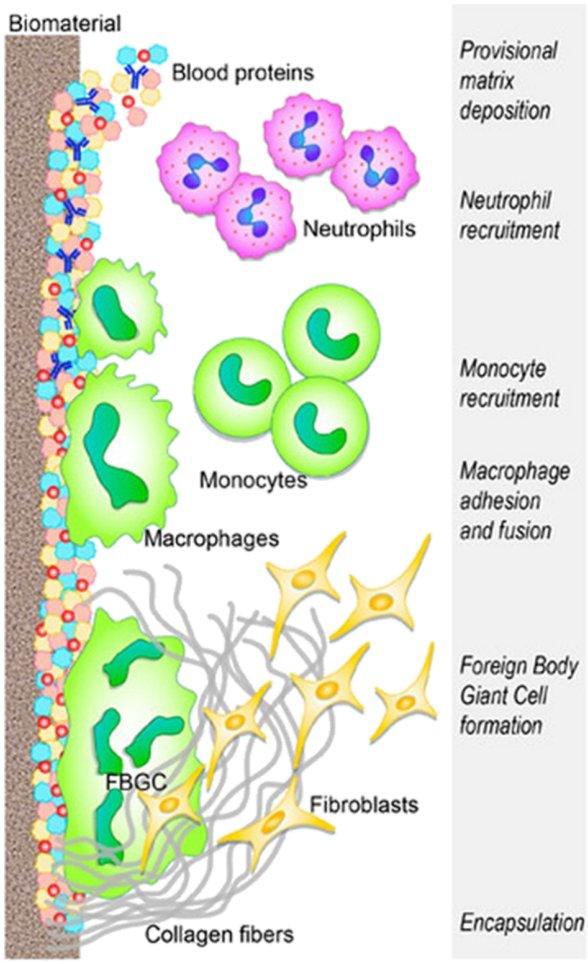

Figure 3: Summary of the immune system response to implanted biomaterials. Figure 3 was reproduced from [86] (© 2019 E. Mariani et al., published by MDPI, distributed under the terms of the Creative Commons Attribution 4.0 International License, https://creativecommons.org/licenses/by/4.0).

The effect of nanostructured carbon on surfaces on the biological response

The modulation of the implant–tissue interface is a complex field of work, which involves both chemical and biological issues. The addition of nanostructured carbonaceous layers represents a solid choice because of the intrinsic properties of carbon materials and the possibility to further tailor them with simple chemical modifications [87,88].

Thomas et al. [89] investigated ND coatings as active surface for tuning the macrophage response to estimate the long-term inflammatory effects of wear debris. The authors investigated the effect of the ND particle sizes on macrophage proliferation, platelets aggregations, and inflammatory cytokine release. NDs significantly reduced the concentration of platelet-derived growth factor compared to serum. Also, there was a complex dependence of macrophage responses on local concentration and size of the NDs, suggesting that the ND coating prevented the removal of wear debris from coated implants. The complex relation between NDs and macrophage activity can be further tuned by functionalization with short molecules as reported by Pentecost and co-workers [90], who used small amines to tune the inflammatory response. The mechanisms involved in inflammation related to NDs are not yet clear, but authors suggest that the process is started by serum protein deposition triggering the inflammatory cascade. Moreover, polymeric films containing NDs were optimum substrates for osteoblast proliferation as reported by Mansoorianfar and co-workers [91]. Booth et al. [92] dealt with foreign-body giant cell formation, disproving that significant changes in wettability and surface energy affect the in vivo effects of NDs on titanium surfaces. The authors surprisingly reported a negligible effect of ND coating on fibrous formation, suggesting that, in the specific case, NDs act only as protective layer rather than influencing the immunological response.

GO-modified surfaces exhibited better performance in tuning the immunological response, as reported by El-Kamel et al. [93], who coated AZ91E Mg alloy staples used for gastrectomy surgery. The GO coating enabled, at the same time, improved corrosion resistance, high cell proliferation, and very low inflammatory response. Similarly, Fernández-Hernán et al. [94] used graphene nanoplatelets to coat AZ31 magnesium, evaluating cytocompatibility, osteoblasts adhesion, and proliferation. The authors reported a significant improvement of cytocompatibility with the creation of a preosteoblastic monolayer on the coated surface after one week of cell culture. Chen and co-workers [95] investigated the effect of GO coating as antifibrotic on metal implants. They controlled the roughness, inducing macrophage polarization to the pro-inflammatory state without producing a great excess of pro-inflammatory factors. Furthermore, GO-coated implants showed a reduction of the expression of the fibrosis-related protein α-SMA and collagen deposition in the presence of both fibroblasts and macrophages. The reduction of fibrotic formations on the implants is of capital relevance for preventing thrombosis [96]. Hassan et al. [97] investigated graphene coatings on a stainless steel implant to minimize the negative effect of metals contained into the alloy (i.e., Cr, Mo, and Ni). The authors used PVD for producing the coating, evaluating both hemolysis and blood coagulation to assess the antithrombotic properties of the graphene coating. The coated implant showed a higher hydrophobicity with less adhered platelets and a 70% reduction of hemolysis. As mentioned, the hydrophobicity and low reactivity of carbon coatings are the key features for the lowered immunological response.

Contrary to NDs and graphene-related materials, CNT layers generally induce a strong immunological response because of their higher reactivity [98], which needs to be tuned through an appropriate functionalization tailored to the tissues where the implant will be placed [99]. Nevertheless, CNTs are able to regulate the cell proliferation better than other nanocarbon species. Patel et al. [100] coated polymer nanofibers with a 25 nm thick layer of MWCNTs modulating in vivo angiogenesis and bone regeneration. Furthermore, the authors were able to fine-tune the topology of the CNT coating, reducing inflammatory events by down-regulated pro-inflammatory cytokines and macrophages. The coated polymeric nanofibers showed the ability to up-regulate the formation of new blood vessels and osteogenic pathways, proving the key role of the CNT coating topology in the compatibility with living tissues.

The formation of biofilms and the microbial proliferation on implants surfaces

The interface between implants and tissues is a key vulnerable point for infection spreading because of the formation of bacteria biofilms [101]. Generally, gram-positive bacteria are the most common culprits for implant infections, while aerobic gram-negative ones seldomly are [102,103]. Furthermore, the biofilm formation is strongly correlated with the implantation site, and the spreading time of infection mainly depends on the virulence of bacteria according to the mechanism shown in Figure 4.

The biofilm formation consists of four stages, namely, (i) adhesion, (ii) aggregation, (iii) maturation, and (iv) dispersion. Adhesion is the first step and is ruled by the polarity of the surface as reported by Gittens and co-workers [105]. The aggregation and maturation steps involve the formation and enlargement of bacteria colonies enclosed in the extracellular biopolymeric matrix [106]. Dispersion occurs upon reaching the

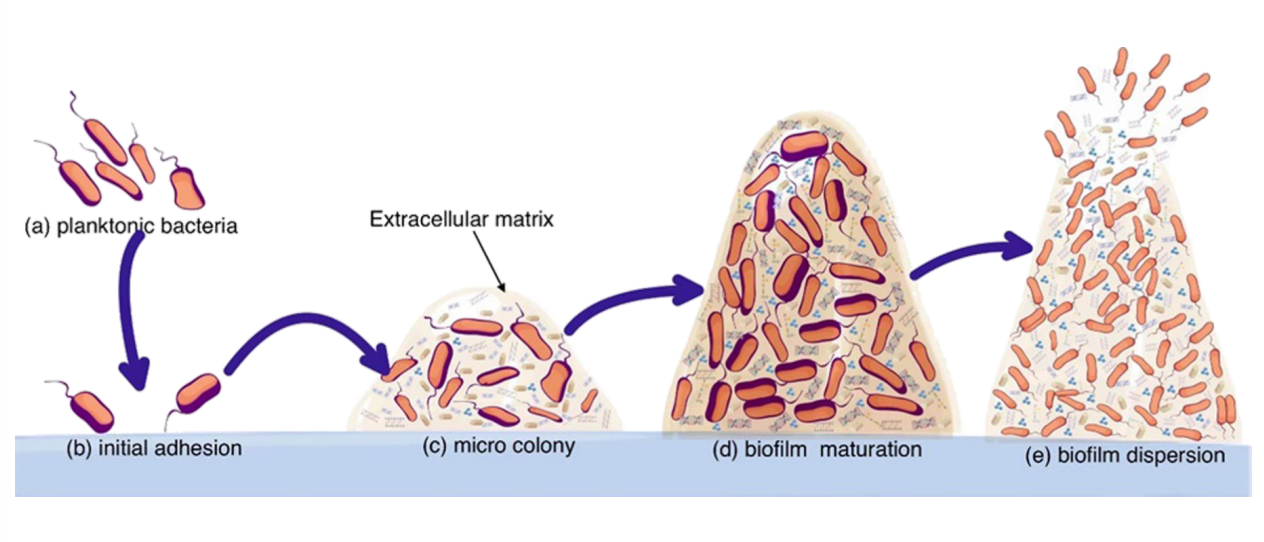

Figure 4: Biofilm formation on an implanted biomaterial due to the presence of planktonic bacteria cells. Figure 4 was reproduced and adapted from [104] (© 2022 R. Ma et al., published by Frontiers, distributed under the terms of the Creative Commons Attribution 4.0 International License, https://creativecommons.org/licenses/by/4.0).

biofilm's critical mass, allowing for the partial detachment and spread of infection through the bloodstream [31].

Carbon materials coatings for mitigation of biofilm formation

Biofilm formation represents a major concern because of the severe actions needed to restore or remove the damaged implant [107]. Prevention of biofilm proliferation can be achieved through the development of coatings changing the hydrophobicity of the implant surface using several routes [108,109], including the incorporation of nanostructured carbon species [101]. Graphene and graphene-related materials have been widely used as antimicrobial coatings for several kinds of implants to tune the surface hydrophobicity and to prevent bacteria adhesion [110,111]. Romo-Rico et al. [112] used PVD to coat a medical-grade cobalt–chromium alloy with high-grade graphene. The authors reported an appreciable antibacterial activity against *S. aureus* and *P. aeruginosa*; also, adhesion was prevented. This study proved that the balance between surface polarity and bacteria targeting is crucial for engineering coating solutions. Similarly, Al-Saadi et al. [113] used CVD for coating a nickel–copper alloy with multilayered graphene, showing the effectiveness of carbon coatings in replacing the native protective oxide layer of the alloy and in reducing the adhesion of sulfate-reducing bacteria. Furthermore, graphene coatings can also exhibit antibacterial activity through electron transfer phenomena as reported by Yang et al. [114] for graphene coatings on titania. The authors reported that the increased electrical conductivity was due to the unpaired electrons at the Schottky-like interface between graphene and titanium. The enhancement of electron transfer rate promoted a relevant bactericidal action. Furthermore, the authors proved the relationship between activity and electron transfer rate by adding an insulating layer of zirconia and observing no bactericidal effects. The authors also proved the cytocompatibility of the bactericidal coatings. GO showed similar results on titanium surfaces as reported by Yang et al. [115], reporting antibacterial activity of over 99% against both *E. coli* or *S. aureus* when a small doping with copper was applied. The synergistic effects of metal cations in GO coatings were extensively investigated [116,117]. Also, polymer blends were included instead of metal species [118,119].

ND coatings are also of particular interest for the prevention of biofilm formation [120] because of the reduced bacteria adhesion, which interferes with microbial film formation [121]. As reported by Rifai et al. [122], ND coatings can be easily applied to titanium surfaces, creating a hydrophilic surface to reduce the adhesion of *S. aureus*. Despite the lowered adhesivity, pristine NDs do not show any significant antibacterial activity. In contrast, functionalized oxidized ND layers were able to inhibit the growth of *E. coli* comparable to the effect of ampicillin [123]. Similarly, mannose ND coatings interfered with the proliferation of uropathogenic bacteria, representing a solid choice to prevent catheterization [124,125] and targeting the FimH protein complex involved in bladder infection.

CNTs also prevent the formation of biofilm as reported by Sivaraj et al. [126], who obtained zones of inhibition of up to 12 mm. Morco et al. [127] suggested that the biofilm inhibition by CNTs is mainly due to the increase of surface hydrophobicity and nanostructuring [128,129]. Kang et al. [130] sug-

gested that the main mechanism of action is cell disruption due to the mechanical effect of CNTs themselves via surface polarity changes. Rodrigues et al. [131] dwelled more deeply into CNT coatings and found a correlation between the exopolymer substances secreted and the effectiveness of CNT action.

Carbon material coatings for improved mechanical, tribological, and electrical properties

Performance and longevity of implants are closely related to their mechanical properties. A mismatch with tissues can potentially lead to stress shielding, wherein the implant bears an excessive load, consequently, causing bone resorption [132]. Coating with nanostructured carbon is a strategy to both reduce wear and improve load across the implant region. As mentioned by Zhang et al. [133], a nano- or micrometric thick layer of CNTs induced the ability of self-repairing of the damaged surfaces by filling the cracks, thus, reducing wear loss. Chen et al. [134] improved the mechanical properties of a titanium alloy though deposition of graphene flakes. The authors investigated the system through indentation showing improvements in both toughness and yield strength. The improvements are due to the graphene coating, which allowed for a better load transfer, inter-layer sliding, and crack deflection. Similarly, Askarnia et al. [135] used electrophoretic deposition for coating a magnesium alloy with GO. The authors reported an increase of both hardness and Young's modulus of 100% and 156%, reaching 60 MPa and 0.52 GPa, respectively, after coating. CNTs are generally used to reinforce the bulk of composite-based implants [136] or added to polymeric films [135]. Interestingly, they can be mixed with hydroxyapatite in order to magnify the compatibility with bone tissues [137] to reduce wear. Such layers have been widely studied as coating agents onto several metal surfaces directly in contact with bone, including steel [138], titanium [139], and magnesium [140]. As reported by Deenoi et al. [141], CNT coatings on titanium nitride at the interface with ultrahigh-density poly(ethylene) reduced the friction coefficient more than any other tested nanostructured carbon coating.

Nevertheless, surface wear remains an issue that needs to be solved in several key implants such as cardiovascular devices and joint replacements. NDs can play a crucial role because of the superior friction reduction achievable using thin ND films as reported by Blum and co-workers [142]. The authors sintered a 75 μm thick layer of NDs onto an aluminum alloy using a focused laser beam and reached a friction coefficient smaller than 0.2. Similar results can be obtained by using PVD, CVD, and sol–gel deposition of NDs on ceramics, together with excellent adhesion of the protective layer [143,144].

Chernysheva et al. [145,146] investigated the production of protective ND layers onto a xenogenic heart valve, evaluating the role of the ND surface potential. A negative surface potential influenced the mechanical characteristics, suggesting a better interaction with the surrounding tissues. Jozwik et al. [147] also reported the long durability of ND coatings in heart implants without any appreciable decrement of performance. Furthermore, ND layers can be easily integrated with other carbon-rich parts of a heart valve implant, suppressing thrombin generation from platelets as reported by Zeng and co-workers [148].

ND coatings are also able to boost the integration of implants with tissue as reported by Zalieckas and co-workers [149]. The authors coated a titanium alloy with NDs by CVD at 400 °C and observed good proliferation of osteogenic cells on a bone implant, even better than on a commonly used surface. They suggested that the osteoblast proliferation was mainly due to the surface morphology and the good match between cells and surface potentials.

Carbon-based material coatings for the prevention of corrosion

Corrosion of metallic implants is still a major concern regarding loss of integrity, thrombosis, and inflammatory processes [150]. To date, the development of highly corrosion-resistant alloys has not been satisfactorily achieved, although coating is a solid choice to prevent massive implant degradation. Carbon nanomaterial coatings can prevent adverse chemical reactions triggered by both the adsorption of proteins and the metabolism of cells [151-153]. Hassan et al. [97] extensively investigated the effect of graphene and graphitic coatings as both anticorrosion and antithrombotic elements. The authors used PVD for the deposition of a micrometer-thick coating on stainless steel, controlling morphology, roughness, and mechanical parameters. The coated surfaces showed a reduction of hemolysis of 40% and a corrosion resistance increment of 96% compared with the untreated surface. The authors suggested that the improved performance was due to the changes adsorption rate of protein and plasma compounds. Mallik et al. [154] used electrophoretically deposited graphene for coating titanium, achieving a strong reduction in corrosion with a coating thickness of 12 μm. The same technique was used by Chen et al. [155] for the deposition of GO onto magnesium alloys. The authors investigated the corrosion in 0.9 wt % NaCl solution, showing beneficial effects of GO mainly due to both being a physical barrier and having a low reactivity. Similar results can be achieved by replacing GO with a mixture of nanostructured calcium carbonate and rGO [156] or fluorohydroxyapatite and GO [157]. Guo et al. [158] also proved the ability of GO coatings to prevent the release of Ni(II) ions from a nickel–titanium alloy during corrosion.

The authors suggested that this could be due to both improved corrosion resistance and entrapping of metal ions in the porous structure of GO. Kabir et al. [159] used graphene nanoplates for the coating of zinc implants, achieving a corrosion rate of 0.09 mm/y. Similar results were shown for tantalum [160] and a titanium–aluminium alloy [161].

ND coatings can exhibit the same behavior as graphene-related materials because of their low chemical reactivity. Nezamdoust et al. [162] coated a magnesium alloy with a 20 nm layer of NDs and measured the corrosion rate in Harrison solution by means of electrochemical impedance spectroscopy. The authors observed a drastically reduction of passivation in the coated samples compared with the original specimens.

Similar results can be achieved by using CNT-containing polymeric layers [163] or CNT-based hydroxyapatite coatings [164,165]. Remarkably, neat CNTs coatings are not the best option for anticorrosion layers because of the higher reactivity compared with NDs and graphene-related materials. Nevertheless, the reactivity of CNTs in biological environments is still a topic of great discussion. As mentioned by Fadeel et al. [166], CNTs encompass a wide range of different species with peculiar chemical reactivity and resistance to oxidative stress.

Summary and Future Perspectives

The results herein discuss the complex scenario of the interaction between implants and living tissues, which is still far from being fully understood. The engineering of implant surfaces with nanosized and nanostructured carbon materials clearly represents a disruptive advancement in the field, leading to prolonged implant life, increased biocompatibility, and reduction of adverse inflammatory reactions.

The big family of low-dimensional carbon materials is a great reservoir for tuning the properties of implants and matching them with those of the tissues. The harsh biological environments, rich of highly reactive and complex species, are a significant challenge for materials science. However, coatings from CNTs, NDs, and graphene-related materials allow one to create smart multipurpose surfaces able to face these issues.

Nanostructured carbon coatings can be groundbreaking in the production of stimuli-responsive implants, such as prosthetic implants. Even if a coherently modulation of nerve signals is still far from being reached, materials such as graphene and CNTs can play a pivotal role in this ambitious long-term goal. Furthermore, the tailoring of carbon surfaces represents a valuable tool in moving from simple implants to medical platforms that are able to monitor and repair themselves, as well as to treat the surrounding tissues.

We firmly believe that the production of specialized carbon surfaces represents a new frontier in the field of durable high-performance implants.

Funding

F.C. acknowledges PNNR M4C2 Initiative 1.2: Young Researcher - Seal of Excellence" for funding.

Author Contributions

Mattia Bartoli: conceptualization; data curation; formal analysis; investigation; supervision; visualization; writing – original draft; writing – review & editing. Francesca Cardano: investigation; visualization; writing – original draft; writing – review & editing. Erik Piatti: investigation; visualization; writing – original draft; writing – review & editing. Stefania Lettieri: investigation; visualization; writing – original draft; writing – review & editing. Andrea Fin: investigation; visualization; writing – original draft; writing – review & editing. Alberto Tagliaferro: investigation; visualization; writing – original draft; writing – review & editing.

ORCID® iDs

Mattia Bartoli - https://orcid.org/0000-0002-4678-0212
Francesca Cardano - https://orcid.org/0000-0003-3237-5408
Erik Piatti - https://orcid.org/0000-0001-8733-5230
Stefania Lettieri - https://orcid.org/0000-0003-2995-3190
Andrea Fin - https://orcid.org/0000-0002-7567-4646
Alberto Tagliaferro - https://orcid.org/0000-0003-1607-5624

Data Availability Statement

The data that supports the findings of this study is available from the corresponding author upon reasonable request.

References

1. Feynman, R. P. There's Plenty of Room at the Bottom. In *APS annual meeting,* Little Brown: Boston, MA, USA, 1959; pp 1–7.
2. Taniguchi, N. On the basic concept of 'Nano-Technology'. In *Proceedings of the International Conference of Precision Engineering,* Japan Society of Precision Engineering: Tokyo, 1974.
3. Saba, N.; Jawaid, M.; Fouad, H.; Alothman, O. Y. 9 - Nanocarbon: Preparation, properties, and applications. In *Nanocarbon and its Composites;* Khan, A.; Mohammad Jawaid, M.; Inamuddin; Asiri, A. M., Eds.; Woodhead Publishing; pp 327–354. doi:10.1016/b978-0-08-102509-3.00009-2
4. Catania, F.; Marras, E.; Giorcelli, M.; Jagdale, P.; Lavagna, L.; Tagliaferro, A.; Bartoli, M. *Appl. Sci.* **2021,** *11,* 614. doi:10.3390/app11020614
5. Sharma, P.; Kumar Mehra, N.; Jain, K.; Jain, N. K. *Curr. Drug Delivery* **2016,** *13,* 796–817. doi:10.2174/1567201813666160623091814
6. Vardharajula, S.; Ali, S. Z.; Tiwari, P. M.; Eroğlu, E.; Vig, K.; Dennis, V. A.; Singh, S. R. *Int. J. Nanomed.* **2012,** 5361–5374. doi:10.2147/ijn.s35832

7. Goodarzi, S.; Da Ros, T.; Conde, J.; Sefat, F.; Mozafari, M. *Mater. Today* **2017,** *20,* 460–480. doi:10.1016/j.mattod.2017.03.017
8. Partha, R.; Conyers, J. L. *Int. J. Nanomed.* **2009,** 261–275. doi:10.2147/ijn.s5964
9. Ghosal, K.; Ghosh, A. *Mater. Sci. Eng., C* **2019,** *96,* 887–903. doi:10.1016/j.msec.2018.11.060
10. Tu, L.; Li, Q.; Qiu, S.; Li, M.; Shin, J.; Wu, P.; Singh, N.; Li, J.; Ding, Q.; Hu, C.; Xiong, X.; Sun, Y.; Kim, J. S. *J. Mater. Chem. B* **2023,** *11,* 3038–3053. doi:10.1039/d2tb02794a
11. Patil, S.; Rajkuberan, C.; Sagadevan, S. *J. Drug Delivery Sci. Technol.* **2023,** *86,* 104737. doi:10.1016/j.jddst.2023.104737
12. Bellier, N.; Baipaywad, P.; Ryu, N.; Lee, J. Y.; Park, H. *Biomater. Res.* **2022,** *26,* 65. doi:10.1186/s40824-022-00313-2
13. Khatik, N.; Sachdeva, H. *Mater. Today: Proc.* **2022,** *69,* 30–35. doi:10.1016/j.matpr.2022.08.073
14. Bellet, P.; Gasparotto, M.; Pressi, S.; Fortunato, A.; Scapin, G.; Mba, M.; Menna, E.; Filippini, F. *Nanomaterials* **2021,** *11,* 404. doi:10.3390/nano11020404
15. Edwards, S. L.; Werkmeister, J. A.; Ramshaw, J. A. *Expert Rev. Med. Devices* **2009,** *6,* 499–505. doi:10.1586/erd.09.29
16. Wujcik, E. K.; Monty, C. N. *Wiley Interdiscip. Rev.: Nanomed. Nanobiotechnol.* **2013,** *5,* 233–249. doi:10.1002/wnan.1213
17. Thompson, B. C.; Murray, E.; Wallace, G. G. *Adv. Mater. (Weinheim, Ger.)* **2015,** *27,* 7563–7582. doi:10.1002/adma.201500411
18. Lee, Y.; Geckeler, K. E. *Adv. Mater. (Weinheim, Ger.)* **2010,** *22,* 4076–4083. doi:10.1002/adma.201000746
19. Xie, X.; Zhao, W.; Lee, H. R.; Liu, C.; Ye, M.; Xie, W.; Cui, B.; Criddle, C. S.; Cui, Y. *ACS Nano* **2014,** *8,* 11958–11965. doi:10.1021/nn504898p
20. Vrana, N. E.; Palm, K.; Lavalle, P. *Future Sci. OA* **2020,** *6,* FSO607. doi:10.2144/fsoa-2020-0074
21. Dhowre, H. S.; Rajput, S.; Russell, N. A.; Zelzer, M. *Nanomedicine (London, U. K.)* **2015,** *10,* 849–871. doi:10.2217/nnm.14.222
22. Lavagna, L.; Nisticò, R.; Musso, S.; Pavese, M. *Mater. Today Chem.* **2021,** *20,* 100477. doi:10.1016/j.mtchem.2021.100477
23. Xie, X.-L.; Mai, Y.-W.; Zhou, X.-P. *Mater. Sci. Eng., R* **2005,** *49,* 89–112. doi:10.1016/j.mser.2005.04.002
24. Lavagna, L.; Bartoli, M.; Suarez-Riera, D.; Cagliero, D.; Musso, S.; Pavese, M. *ACS Appl. Nano Mater.* **2022,** *5,* 6671–6678. doi:10.1021/acsanm.2c00706
25. Alla, R. K.; Ginjupalli, K.; Upadhya, N.; Shammas, M.; Ravi, R. K.; Sekhar, R. *Trends Biomater. Artif. Organs* **2011,** *25,* 112–118.
26. Grill, W. M.; Norman, S. E.; Bellamkonda, R. V. *Annu. Rev. Biomed. Eng.* **2009,** *11,* 1–24. doi:10.1146/annurev-bioeng-061008-124927
27. Franz, S.; Rammelt, S.; Scharnweber, D.; Simon, J. C. *Biomaterials* **2011,** *32,* 6692–6709. doi:10.1016/j.biomaterials.2011.05.078
28. Gao, X.; Fraulob, M.; Haïat, G. *J. R. Soc., Interface* **2019,** *16,* 20190259. doi:10.1098/rsif.2019.0259
29. Eliaz, N., Ed. *Degradation of Implant Materials;* Springer New York: New York, NY, U.S.A., 2012. doi:10.1007/978-1-4614-3942-4
30. Morouço, P.; Azimi, B.; Milazzo, M.; Mokhtari, F.; Fernandes, C.; Reis, D.; Danti, S. *Appl. Sci.* **2020,** *10,* 9143. doi:10.3390/app10249143
31. Arciola, C. R.; Campoccia, D.; Montanaro, L. *Nat. Rev. Microbiol.* **2018,** *16,* 397–409. doi:10.1038/s41579-018-0019-y
32. Lee, C.; Wei, X.; Kysar, J. W.; Hone, J. *Science* **2008,** *321,* 385–388. doi:10.1126/science.1157996
33. Papageorgiou, D. G.; Kinloch, I. A.; Young, R. J. *Prog. Mater. Sci.* **2017,** *90,* 75–127. doi:10.1016/j.pmatsci.2017.07.004
34. Bolotin, K. I.; Sikes, K. J.; Jiang, Z.; Klima, M.; Fudenberg, G.; Hone, J.; Kim, P.; Stormer, H. L. *Solid State Commun.* **2008,** *146,* 351–355. doi:10.1016/j.ssc.2008.02.024
35. Rhee, K. Y. *Nanomaterials* **2020,** *10,* 926. doi:10.3390/nano10050926
36. Mintmire, J. W.; Dunlap, B. I.; White, C. T. *Phys. Rev. Lett.* **1992,** *68,* 631–634. doi:10.1103/physrevlett.68.631
37. Yan, J.-A.; Ruan, W. Y.; Chou, M. Y. *Phys. Rev. B* **2009,** *79,* 115443. doi:10.1103/physrevb.79.115443
38. Dresselhaus, M. S.; Jorio, A.; Saito, R. *Annu. Rev. Condens. Matter Phys.* **2010,** *1,* 89–108. doi:10.1146/annurev-conmatphys-070909-103919
39. Sangwan, V. K.; Hersam, M. C. *Annu. Rev. Phys. Chem.* **2018,** *69,* 299–325. doi:10.1146/annurev-physchem-050317-021353
40. Belenkov, M. E.; Kochengin, A. E.; Chernov, V. M.; Belenkov, E. A. *J. Phys.: Conf. Ser.* **2019,** *1399,* 022024. doi:10.1088/1742-6596/1399/2/022024
41. Piatti, E.; Prando, G.; Meinero, M.; Tresca, C.; Putti, M.; Roddaro, S.; Lamura, G.; Shiroka, T.; Carretta, P.; Profeta, G.; Daghero, D.; Gonnelli, R. S. *Commun. Phys.* **2023,** *6,* 202. doi:10.1038/s42005-023-01330-w
42. Narita, S.-i.; Terada, S.-i.; Mori, S.; Muro, K.; Akahama, Y.; Endo, S. *J. Phys. Soc. Jpn.* **1983,** *52,* 3544–3553. doi:10.1143/jpsj.52.3544
43. Wang, L.; Meric, I.; Huang, P. Y.; Gao, Q.; Gao, Y.; Tran, H.; Taniguchi, T.; Watanabe, K.; Campos, L. M.; Muller, D. A.; Guo, J.; Kim, P.; Hone, J.; Shepard, K. L.; Dean, C. R. *Science* **2013,** *342,* 614–617. doi:10.1126/science.1244358
44. Piatti, E.; Arbab, A.; Galanti, F.; Carey, T.; Anzi, L.; Spurling, D.; Roy, A.; Zhussupbekova, A.; Patel, K. A.; Kim, J. M.; Daghero, D.; Sordan, R.; Nicolosi, V.; Gonnelli, R. S.; Torrisi, F. *Nat. Electron.* **2021,** *4,* 893–905. doi:10.1038/s41928-021-00684-9
45. Szabó, T.; Berkesi, O.; Forgó, P.; Josepovits, K.; Sanakis, Y.; Petridis, D.; Dékány, I. *Chem. Mater.* **2006,** *18,* 2740–2749. doi:10.1021/cm060258+
46. Marcano, D. C.; Kosynkin, D. V.; Berlin, J. M.; Sinitskii, A.; Sun, Z.; Slesarev, A.; Alemany, L. B.; Lu, W.; Tour, J. M. *ACS Nano* **2010,** *4,* 4806–4814. doi:10.1021/nn1006368
47. Yu, W.; Sisi, L.; Haiyan, Y.; Jie, L. *RSC Adv.* **2020,** *10,* 15328–15345. doi:10.1039/d0ra01068e
48. Zhu, Y.; Murali, S.; Cai, W.; Li, X.; Suk, J. W.; Potts, J. R.; Ruoff, R. S. *Adv. Mater. (Weinheim, Ger.)* **2010,** *22,* 3906–3924. doi:10.1002/adma.201001068
49. Fathy, M.; Gomaa, A.; Taher, F. A.; El-Fass, M. M.; Kashyout, A. E.-H. B. *J. Mater. Sci.* **2016,** *51,* 5664–5675. doi:10.1007/s10853-016-9869-8
50. Lee, X. J.; Hiew, B. Y. Z.; Lai, K. C.; Lee, L. Y.; Gan, S.; Thangalazhy-Gopakumar, S.; Rigby, S. *J. Taiwan Inst. Chem. Eng.* **2019,** *98,* 163–180. doi:10.1016/j.jtice.2018.10.028
51. Huang, X.; Qi, X.; Boey, F.; Zhang, H. *Chem. Soc. Rev.* **2012,** *41,* 666–686. doi:10.1039/c1cs15078b
52. Hofer, L. J. E.; Sterling, E.; McCartney, J. T. *J. Phys. Chem.* **1955,** *59,* 1153–1155. doi:10.1021/j150533a010
53. Monthioux, M.; Kuznetsov, V. L. *Carbon* **2006,** *44,* 1621–1623. doi:10.1016/j.carbon.2006.03.019
54. Hillert, M.; Lange, N. *Z. Kristallogr., Kristallgeom., Kristallphys., Kristallchem.* **1959,** *111,* 24–34. doi:10.1524/zkri.1959.111.16.24

55. Bacon, R. *J. Appl. Phys.* **1960,** *31,* 283–290. doi:10.1063/1.1735559
56. Iijima, S. *Nature* **1991,** *354,* 56–58. doi:10.1038/354056a0
57. Zhao, X.; Liu, Y.; Inoue, S.; Suzuki, T.; Jones, R. O.; Ando, Y. *Phys. Rev. Lett.* **2004,** *92,* 125502. doi:10.1103/physrevlett.92.125502
58. Fagan, J. A.; Hároz, E. H.; Ihly, R.; Gui, H.; Blackburn, J. L.; Simpson, J. R.; Lam, S.; Hight Walker, A. R.; Doorn, S. K.; Zheng, M. *ACS Nano* **2015,** *9,* 5377–5390. doi:10.1021/acsnano.5b01123
59. Liu, W.-W.; Chai, S.-P.; Mohamed, A. R.; Hashim, U. *J. Ind. Eng. Chem. (Amsterdam, Neth.)* **2014,** *20,* 1171–1185. doi:10.1016/j.jiec.2013.08.028
60. Navas, H.; Picher, M.; Andrieux-Ledier, A.; Fossard, F.; Michel, T.; Kozawa, A.; Maruyama, T.; Anglaret, E.; Loiseau, A.; Jourdain, V. *ACS Nano* **2017,** *11,* 3081–3088. doi:10.1021/acsnano.7b00077
61. Inam, F.; Reece, M. J.; Peijs, T. *J. Compos. Mater.* **2012,** *46,* 1313–1322. doi:10.1177/0021998311418139
62. Zhang, R.; Zhang, Y.; Zhang, Q.; Xie, H.; Qian, W.; Wei, F. *ACS Nano* **2013,** *7,* 6156–6161. doi:10.1021/nn401995z
63. Manawi, Y. M.; Ihsanullah; Samara, A.; Al-Ansari, T.; Atieh, M. A. *Materials* **2018,** *11,* 822. doi:10.3390/ma11050822
64. Krishnan, A.; Dujardin, E.; Ebbesen, T. W.; Yianilos, P. N.; Treacy, M. M. J. *Phys. Rev. B* **1998,** *58,* 14013–14019. doi:10.1103/physrevb.58.14013
65. Han, J. Chapter 1 - Structures and properties of carbon nanotubes. In *Carbon nanotubes;* Meyyappan, M., Ed.; CRC Press: Boca Raton, FL, U.S.A., 2004; pp 16–45. doi:10.1201/9780203494936
66. Thess, A.; Lee, R.; Nikolaev, P.; Dai, H.; Petit, P.; Robert, J.; Xu, C.; Lee, Y. H.; Kim, S. G.; Rinzler, A. G.; Colbert, D. T.; Scuseria, G. E.; Tománek, D.; Fischer, J. E.; Smalley, R. E. *Science* **1996,** *273,* 483–487. doi:10.1126/science.273.5274.483
67. Cao, J. X.; Yan, X. H.; Xiao, Y.; Ding, J. W. *Phys. Rev. B* **2004,** *69,* 073407. doi:10.1103/physrevb.69.073407
68. Treacy, M. M. J.; Ebbesen, T. W.; Gibson, J. M. *Nature* **1996,** *381,* 678–680. doi:10.1038/381678a0
69. Mansfield, E.; Feldman, A.; Chiaramonti, A. N.; Lehman, J.; Curtin, A. E. *J. Res. Natl. Inst. Stand. Technol.* **2015,** *120,* 304–315. doi:10.6028/jres.120.019
70. Choi, T. Y.; Poulikakos, D.; Tharian, J.; Sennhauser, U. *Appl. Phys. Lett.* **2005,** *87,* 013108. doi:10.1063/1.1957118
71. Bai, Y.; Yue, H.; Zhang, R.; Qian, W.; Zhang, Z.; Wei, F. *Acc. Mater. Res.* **2021,** *2,* 998–1009. doi:10.1021/accountsmr.1c00120
72. Mochalin, V.; Shenderova, O.; Ho, D.; Gogotsi, Y. The Properties and Applications of Nanodiamonds. In *Nano-enabled medical applications;* Mochalin, V.; Shenderova, O.; Ho, D.; Gogotsi, Y., Eds.; Jenny Stanford Publishing: New York City, NY, U.S.A., 2020; pp 313–350. doi:10.1201/9780429399039-11
73. Kidalov, S. V.; Shakhov, F. M.; Vul, A. Y. *Diamond Relat. Mater.* **2008,** *17,* 844–847. doi:10.1016/j.diamond.2008.01.091
74. Paci, J. T.; Man, H. B.; Saha, B.; Ho, D.; Schatz, G. C. *J. Phys. Chem. C* **2013,** *117,* 17256–17267. doi:10.1021/jp404311a
75. Barman, S.; Srivastava, G. P. *J. Appl. Phys.* **2007,** *101,* 123507. doi:10.1063/1.2747540
76. Al Mahmud, K. A. H.; Kalam, M. A.; Masjuki, H. H.; Mobarak, H. M.; Zulkifli, N. W. M. *Crit. Rev. Solid State Mater. Sci.* **2015,** *40,* 90–118. doi:10.1080/10408436.2014.940441
77. Bolker, A.; Saguy, C.; Tordjman, M.; Kalish, R. *Phys. Rev. B* **2013,** *88,* 035442. doi:10.1103/physrevb.88.035442
78. Kumar, S.; Nehra, M.; Kedia, D.; Dilbaghi, N.; Tankeshwar, K.; Kim, K.-H. *Carbon* **2019,** *143,* 678–699. doi:10.1016/j.carbon.2018.11.060
79. Pang, J.; Bachmatiuk, A.; Ibrahim, I.; Fu, L.; Placha, D.; Martynkova, G. S.; Trzebicka, B.; Gemming, T.; Eckert, J.; Rümmeli, M. H. *J. Mater. Sci.* **2016,** *51,* 640–667. doi:10.1007/s10853-015-9440-z
80. Porro, S.; Musso, S.; Giorcelli, M.; Chiodoni, A.; Tagliaferro, A. *Phys. E (Amsterdam, Neth.)* **2007,** *37,* 16–20. doi:10.1016/j.physe.2006.07.010
81. Musso, S.; Fanchini, G.; Tagliaferro, A. *Diamond Relat. Mater.* **2005,** *14,* 784–789. doi:10.1016/j.diamond.2004.12.030
82. Porro, S.; Musso, S.; Vinante, M.; Vanzetti, L.; Anderle, M.; Trotta, F.; Tagliaferro, A. *Phys. E (Amsterdam, Neth.)* **2007,** *37,* 58–61. doi:10.1016/j.physe.2006.07.014
83. Paradise, M.; Goswami, T. *Mater. Des.* **2007,** *28,* 1477–1489. doi:10.1016/j.matdes.2006.03.008
84. Muñoz, R.; Gómez-Aleixandre, C. *Chem. Vap. Deposition* **2013,** *19,* 297–322. doi:10.1002/cvde.201300051
85. Baptista, A.; Silva, F.; Porteiro, J.; Míguez, J.; Pinto, G. *Coatings* **2018,** *8,* 402. doi:10.3390/coatings8110402
86. Mariani, E.; Lisignoli, G.; Borzì, R. M.; Pulsatelli, L. *Int. J. Mol. Sci.* **2019,** *20,* 636. doi:10.3390/ijms20030636
87. Rogala-Wielgus, D.; Zieliński, A. *Carbon Lett.* **2024,** *34,* 565–601. doi:10.1007/s42823-023-00626-9
88. Kim, C.-H.; Lee, S.-Y.; Rhee, K. Y.; Park, S.-J. *Adv. Compos. Hybrid Mater.* **2024,** *7,* 55. doi:10.1007/s42114-024-00846-1
89. Thomas, V.; Halloran, B. A.; Ambalavanan, N.; Catledge, S. A.; Vohra, Y. K. *Acta Biomater.* **2012,** *8,* 1939–1947. doi:10.1016/j.actbio.2012.01.033
90. Pentecost, A. E.; Witherel, C. E.; Gogotsi, Y.; Spiller, K. L. *Biomater. Sci.* **2017,** *5,* 2131–2143. doi:10.1039/c7bm00294g
91. Mansoorianfar, M.; Shokrgozar, M. A.; Mehrjoo, M.; Tamjid, E.; Simchi, A. *Diamond Relat. Mater.* **2013,** *40,* 107–114. doi:10.1016/j.diamond.2013.10.012
92. Booth, M. A.; Pope, L.; Sherrell, P. C.; Stacey, A.; Tran, P. A.; Fox, K. E. *Mater. Sci. Eng., C* **2021,** *130,* 112467. doi:10.1016/j.msec.2021.112467
93. El-Kamel, R. S.; Ghoneim, A. A.; Fekry, A. M. *Mater. Sci. Eng., C* **2019,** *103,* 109780. doi:10.1016/j.msec.2019.109780
94. Fernández-Hernán, J. P.; Torres, B.; López, A. J.; Martínez-Campos, E.; Rams, J. *Surf. Coat. Technol.* **2021,** *426,* 127745. doi:10.1016/j.surfcoat.2021.127745
95. Chen, C.-Y.; Tsai, P.-H.; Lin, Y.-H.; Huang, C.-Y.; Chung, J. H. Y.; Chen, G.-Y. *Mater. Today Bio* **2022,** *15,* 100326. doi:10.1016/j.mtbio.2022.100326
96. Rozmus, G.; Daubert, J. P.; Huang, D. T.; Rosero, S.; Hall, B.; Francis, C. *J. Interventional Card. Electrophysiol.* **2005,** *13,* 9–19. doi:10.1007/s10840-005-1140-1
97. Hassan, S.; Nadeem, A. Y.; Ali, M.; Ali, M. N.; Niazi, M. B. K.; Mahmood, A. *Mater. Chem. Phys.* **2022,** *290,* 126562. doi:10.1016/j.matchemphys.2022.126562
98. Dumortier, H. *Adv. Drug Delivery Rev.* **2013,** *65,* 2120–2126. doi:10.1016/j.addr.2013.09.005
99. Battigelli, A.; Ménard-Moyon, C.; Da Ros, T.; Prato, M.; Bianco, A. *Adv. Drug Delivery Rev.* **2013,** *65,* 1899–1920. doi:10.1016/j.addr.2013.07.006
100. Patel, K. D.; Kim, T.-H.; Mandakhbayar, N.; Singh, R. K.; Jang, J.-H.; Lee, J.-H.; Kim, H.-W. *Acta Biomater.* **2020,** *108,* 97–110. doi:10.1016/j.actbio.2020.03.012

101. Veerachamy, S.; Yarlagadda, T.; Manivasagam, G.; Yarlagadda, P. K. *Proc. Inst. Mech. Eng., Part H* **2014,** *228,* 1083–1099. doi:10.1177/0954411914556137
102. Geary, K. J.; Tomkiewicz, Z. M.; Harrison, H. N.; Fiore, W. M.; Geary, J. E.; Green, R. M.; DeWeese, J. A.; Ouriel, K. *J. Vasc. Surg.* **1990,** *11,* 339–347. doi:10.1016/0741-5214(90)90278-i
103. Cobo, J.; Del Pozo, J. L. *Expert Rev. Anti-Infect. Ther.* **2011,** *9,* 787–802. doi:10.1586/eri.11.95
104. Ma, R.; Hu, X.; Zhang, X.; Wang, W.; Sun, J.; Su, Z.; Zhu, C. *Front. Cell. Infect. Microbiol.* **2022,** *12,* 1003033. doi:10.3389/fcimb.2022.1003033
105. Gittens, R. A.; Scheideler, L.; Rupp, F.; Hyzy, S. L.; Geis-Gerstorfer, J.; Schwartz, Z.; Boyan, B. D. *Acta Biomater.* **2014,** *10,* 2907–2918. doi:10.1016/j.actbio.2014.03.032
106. Bürgers, R.; Gerlach, T.; Hahnel, S.; Schwarz, F.; Handel, G.; Gosau, M. *Clin. Oral Implants Res.* **2010,** *21,* 156–164. doi:10.1111/j.1600-0501.2009.01815.x
107. Costa, R. C.; Abdo, V. L.; Mendes, P. H. C.; Mota-Veloso, I.; Bertolini, M.; Mathew, M. T.; Barão, V. A. R.; Souza, J. G. S. *J. Biocorros. Tribocorros.* **2021,** *7,* 136. doi:10.1007/s40735-021-00575-8
108. Matos, A. O.; Ricomini-Filho, A. P.; Beline, T.; Ogawa, E. S.; Costa-Oliveira, B. E.; de Almeida, A. B.; Nociti Junior, F. H.; Rangel, E. C.; da Cruz, N. C.; Sukotjo, C.; Mathew, M. T.; Barão, V. A. R. *Colloids Surf., B* **2017,** *152,* 354–366. doi:10.1016/j.colsurfb.2017.01.035
109. Kulkarni Aranya, A.; Pushalkar, S.; Zhao, M.; LeGeros, R. Z.; Zhang, Y.; Saxena, D. *J. Biomed. Mater. Res., Part A* **2017,** *105,* 2218–2227. doi:10.1002/jbm.a.36081
110. Furio, A.; Landi, G.; Altavilla, C.; Sofia, D.; Iannace, S.; Sorrentino, A.; Neitzert, H. C. *Nanotechnology* **2017,** *28,* 054003. doi:10.1088/1361-6528/28/5/054003
111. Wang, S.; Zhang, Y.; Abidi, N.; Cabrales, L. *Langmuir* **2009,** *25,* 11078–11081. doi:10.1021/la901402f
112. Romo-Rico, J.; Bright, R.; Krishna, S. M.; Vasilev, K.; Golledge, J.; Jacob, M. V. *Carbon Trends* **2023,** *12,* 100282. doi:10.1016/j.cartre.2023.100282
113. Al-Saadi, S.; Raman, R. K. S.; Anisur, M. R.; Ahmed, S.; Crosswell, J.; Alnuwaiser, M.; Panter, C. *Corros. Sci.* **2021,** *182,* 109299. doi:10.1016/j.corsci.2021.109299
114. Yang, M.; Liu, H.; Qiu, C.; Iatsunskyi, I.; Coy, E.; Moya, S.; Wang, Z.; Wu, W.; Zhao, X.; Wang, G. *Carbon* **2020,** *166,* 350–360. doi:10.1016/j.carbon.2020.05.036
115. Yang, F.; Huo, D.; Zhang, J.; Lin, T.; Zhang, J.; Tan, S.; Yang, L. *J. Colloid Interface Sci.* **2023,** *638,* 1–13. doi:10.1016/j.jcis.2023.01.114
116. Song, X.; Xie, L.; Zhang, M.; Wang, W.; Li, L.; Lu, X.; Lei, P.; Liu, D.; Chen, Y.; Chen, H.; Zhao, C. *Mater. Res. Bull.* **2021,** *141,* 111345. doi:10.1016/j.materresbull.2021.111345
117. Bakhsheshi-Rad, H. R.; Ismail, A. F.; Aziz, M.; Akbari, M.; Hadisi, Z.; Khoshnava, S. M.; Pagan, E.; Chen, X. *Mater. Sci. Eng., C* **2020,** *111,* 110812. doi:10.1016/j.msec.2020.110812
118. Dhiman, N. K.; Reddy, M. S.; Agnihotri, S. *Colloids Surf., B* **2023,** *227,* 113362. doi:10.1016/j.colsurfb.2023.113362
119. Qin, W.; Ma, J.; Liang, Q.; Li, J.; Tang, B. *J. Mech. Behav. Biomed. Mater.* **2021,** *122,* 104659. doi:10.1016/j.jmbbm.2021.104659
120. Szunerits, S.; Barras, A.; Boukherroub, R. *Int. J. Environ. Res. Public Health* **2016,** *13,* 413. doi:10.3390/ijerph13040413
121. Ong, S. Y.; van Harmelen, R. J. J.; Norouzi, N.; Offens, F.; Venema, I. M.; Habibi Najafi, M. B.; Schirhagl, R. *Nanoscale* **2018,** *10,* 17117–17124. doi:10.1039/c8nr05183f
122. Rifai, A.; Tran, N.; Reineck, P.; Elbourne, A.; Mayes, E.; Sarker, A.; Dekiwadia, C.; Ivanova, E. P.; Crawford, R. J.; Ohshima, T.; Gibson, B. C.; Greentree, A. D.; Pirogova, E.; Fox, K. *ACS Appl. Mater. Interfaces* **2019,** *11,* 24588–24597. doi:10.1021/acsami.9b07064
123. Khanal, M.; Raks, V.; Issa, R.; Chernyshenko, V.; Barras, A.; Garcia Fernandez, J. M.; Mikhalovska, L. I.; Turcheniuk, V.; Zaitsev, V.; Boukherroub, R.; Siriwardena, A.; Cooper, I. R.; Cragg, P. J.; Szunerits, S. *Part. Part. Syst. Charact.* **2015,** *32,* 822–830. doi:10.1002/ppsc.201500027
124. Wellens, A.; Garofalo, C.; Nguyen, H.; Van Gerven, N.; Slättegård, R.; Hernalsteens, J.-P.; Wyns, L.; Oscarson, S.; De Greve, H.; Hultgren, S.; Bouckaert, J. *PLoS One* **2008,** *3,* e2040. doi:10.1371/journal.pone.0002040
125. Cusumano, C. K.; Pinkner, J. S.; Han, Z.; Greene, S. E.; Ford, B. A.; Crowley, J. R.; Henderson, J. P.; Janetka, J. W.; Hultgren, S. J. *Sci. Transl. Med.* **2011,** *3,* 109ra115. doi:10.1126/scitranslmed.3003021
126. Sivaraj, D.; Vijayalakshmi, K. *J. Alloys Compd.* **2019,** *777,* 1340–1346. doi:10.1016/j.jallcom.2018.10.341
127. Morco, S. R.; Williams, D. L.; Jensen, B. D.; Bowden, A. E. *J. Orthop. Res.* **2022,** *40,* 1953–1960. doi:10.1002/jor.25206
128. Tullii, G.; Donini, S.; Bossio, C.; Lodola, F.; Pasini, M.; Parisini, E.; Galeotti, F.; Antognazza, M. R. *ACS Appl. Mater. Interfaces* **2020,** *12,* 5437–5446. doi:10.1021/acsami.9b18187
129. Dong, X.; McCoy, E.; Zhang, M.; Yang, L. *J. Environ. Sci.* **2014,** *26,* 2526–2534. doi:10.1016/j.jes.2014.04.010
130. Kang, S.; Pinault, M.; Pfefferle, L. D.; Elimelech, M. *Langmuir* **2007,** *23,* 8670–8673. doi:10.1021/la701067r
131. Rodrigues, D. F.; Elimelech, M. *Environ. Sci. Technol.* **2010,** *44,* 4583–4589. doi:10.1021/es1005785
132. Allen, M.; Brett, F.; Millett, P.; Rushton, N. *J. Bone Jt. Surg., Br. Vol.* **1996,** *78-B,* 32–37. doi:10.1302/0301-620x.78b1.0780032
133. Zhang, F.-Z.; Liu, X.-B.; Yang, C.-M.; Chen, G.-D.; Meng, Y.; Zhou, H.-B.; Zhang, S.-H. *Mater. Today* **2024,** *74,* 203–234. doi:10.1016/j.mattod.2024.03.001
134. Chen, Y.; Ren, J.; Sun, Y.; Liu, W.; Lu, X.; Guan, S. *Mater. Des.* **2021,** *203,* 109585. doi:10.1016/j.matdes.2021.109585
135. Askarnia, R.; Fardi, S. R.; Sobhani, M.; Staji, H. *Ceram. Int.* **2021,** *47,* 27071–27081. doi:10.1016/j.ceramint.2021.06.120
136. Saito, N.; Usui, Y.; Aoki, K.; Narita, N.; Shimizu, M.; Ogiwara, N.; Nakamura, K.; Ishigaki, N.; Kato, H.; Taruta, S.; Endo, M. *Curr. Med. Chem.* **2008,** *15,* 523–527. doi:10.2174/092986708783503140
137. Chen, Y.; Zhang, T. H.; Gan, C. H.; Yu, G. *Carbon* **2007,** *45,* 998–1004. doi:10.1016/j.carbon.2006.12.021
138. Chakraborty, R.; Seesala, V. S.; Sen, M.; Sengupta, S.; Dhara, S.; Saha, P.; Das, K.; Das, S. *Surf. Coat. Technol.* **2017,** *325,* 496–514. doi:10.1016/j.surfcoat.2017.06.073
139. Długoń, E.; Niemiec, W.; Frączek-Szczypta, A.; Jeleń, P.; Sitarz, M.; Błażewicz, M. *Spectrochim. Acta, Part A* **2014,** *133,* 872–875. doi:10.1016/j.saa.2014.06.064
140. Khazeni, D.; Saremi, M.; Soltani, R. *Ceram. Int.* **2019,** *45,* 11174–11185. doi:10.1016/j.ceramint.2019.02.143
141. Deenoi, S.; Dechjarern, S. *Mater. Today: Proc.* **2019,** *17,* 1939–1948. doi:10.1016/j.matpr.2019.06.237

142. Blum, R.; Molian, P. *Surf. Coat. Technol.* **2009,** *204,* 1–14. doi:10.1016/j.surfcoat.2009.06.025
143. Ali, N.; Kousa, Y.; Gracio, J.; Cabral, G.; Sousa, A.; Shokufar, T.; Titus, E.; Madaleno, J. C.; Ahmed, W.; Jackson, M. J. Surface Engineering of Artificial Heart Valves to Using Modified Diamond-Like Coatings. In *Surgical Tools and Medical Devices;* Ahmed, W.; Jackson, M. J., Eds.; Springer International Publishing: Cham, Switzerland, 2016; pp 117–147. doi:10.1007/978-3-319-33489-9_6
144. Jackson, M. J.; Robinson, G. M.; Ali, N.; Kousar, Y.; Mei, S.; Gracio, J.; Taylor, H.; Ahmed, W. *J. Med. Eng. Technol.* **2006,** *30,* 323–329. doi:10.1080/03091900500441287
145. Chernysheva, M. G.; Shen, T.; Chaschin, I. S.; Badun, G. A.; Vasil'ev, V. G.; Mikheev, I. V.; Bakuleva, N. P. *Mendeleev Commun.* **2024,** *34,* 104–106. doi:10.1016/j.mencom.2024.01.031
146. Chernysheva, M. G.; Chaschin, I. S.; Badun, G. A.; Vasil'ev, V. G.; Mikheev, I. V.; Shen, T.; Sinolits, M. A.; Bakuleva, N. P. *Colloids Surf., A* **2023,** *656,* 130373. doi:10.1016/j.colsurfa.2022.130373
147. Jozwik, K.; Karczemska, A. *Diamond Relat. Mater.* **2007,** *16,* 1004–1009. doi:10.1016/j.diamond.2006.12.051
148. Zeng, H.; Yin, W.; Catausan, G.; Moldovan, N.; Carlisle, J. *Diamond Relat. Mater.* **2016,** *61,* 97–101. doi:10.1016/j.diamond.2015.11.020
149. Zalieckas, J.; Mondragon, I. R.; Pobedinskas, P.; Kristoffersen, A. S.; Mohamed-Ahmed, S.; Gjerde, C.; Høl, P. J.; Hallan, G.; Furnes, O. N.; Cimpan, M. R.; Haenen, K.; Holst, B.; Greve, M. M. *ACS Appl. Mater. Interfaces* **2022,** *14,* 44933–44946. doi:10.1021/acsami.2c10121
150. Kamachimudali, U.; Sridhar, T. M.; Raj, B. *Sadhana* **2003,** *28,* 601–637. doi:10.1007/bf02706450
151. Manam, N. S.; Harun, W. S. W.; Shri, D. N. A.; Ghani, S. A. C.; Kurniawan, T.; Ismail, M. H.; Ibrahim, M. H. I. *J. Alloys Compd.* **2017,** *701,* 698–715. doi:10.1016/j.jallcom.2017.01.196
152. Kumar, S.; Katyal, P.; Chaudhary, R. N.; Singh, V. *Mater. Today: Proc.* **2022,** *56,* 2680–2689. doi:10.1016/j.matpr.2021.09.262
153. Hansen, D. C. *Electrochem. Soc. Interface* **2008,** *17* (2), 31–34. doi:10.1149/2.f04082if
154. Mallick, M.; N, A. *Surf. Coat. Technol.* **2022,** *450,* 128946. doi:10.1016/j.surfcoat.2022.128946
155. Chen, Z.; Wang, W.; Liang, Q.; Lin, W. *Int. J. Electrochem. Sci.* **2021,** *16,* 211116. doi:10.20964/2021.11.04
156. Choudhary, L.; Banerjee, P. C.; Singh Raman, R. K.; Lobo, D. E.; Easton, C. D.; Majumder, M.; Witte, F.; Löffler, J. F. *J. Magnesium Alloys* **2024,** *12,* 394–404. doi:10.1016/j.jma.2023.12.012
157. Jafari, Z.; Pishbin, F.; Ghambari, M.; Dehghanian, C. *J. Alloys Compd.* **2024,** *976,* 172961. doi:10.1016/j.jallcom.2023.172961
158. Guo, Y.; Xu, Z.; Wang, Q.; Zu, S.; Liu, M.; Yu, Z.; Zhang, Z.; Ren, L. *Prog. Org. Coat.* **2022,** *164,* 106722. doi:10.1016/j.porgcoat.2022.106722
159. Kabir, H.; Munir, K.; Wen, C.; Li, Y. *Acta Biomater.* **2023,** *157,* 701–719. doi:10.1016/j.actbio.2022.11.060
160. Mahmoodi, M.; Hydari, M. H.; Mahmoodi, L.; Gazanfari, L.; Mirhaj, M. *Surf. Coat. Technol.* **2021,** *424,* 127642. doi:10.1016/j.surfcoat.2021.127642
161. Yigit, O.; Dikici, B.; Senocak, T. C.; Ozdemir, N. *Surf. Coat. Technol.* **2020,** *394,* 125858. doi:10.1016/j.surfcoat.2020.125858
162. Nezamdoust, S.; Seifzadeh, D.; Habibi-Yangjeh, A. *Trans. Nonferrous Met. Soc. China* **2020,** *30,* 1535–1549. doi:10.1016/s1003-6326(20)65317-1
163. Jian, Y.; Zhang, J.; Yang, C.; Qi, L.; Wang, X.; Deng, H.; Shi, X. *Colloids Surf., B* **2023,** *225,* 113227. doi:10.1016/j.colsurfb.2023.113227
164. Sivaraj, D.; Vijayalakshmi, K. *J. Anal. Appl. Pyrolysis* **2018,** *135,* 15–21. doi:10.1016/j.jaap.2018.09.027
165. Sivaraj, D.; Vijayalakshmi, K.; Ganeshkumar, A.; Rajaram, R. *Int. J. Pharm.* **2020,** *590,* 119946. doi:10.1016/j.ijpharm.2020.119946
166. Fadeel, B.; Kostarelos, K. *Nat. Nanotechnol.* **2020,** *15,* 164. doi:10.1038/s41565-020-0654-0

License and Terms

This is an open access article licensed under the terms of the Beilstein-Institut Open Access License Agreement (https://www.beilstein-journals.org/bjnano/terms), which is identical to the Creative Commons Attribution 4.0 International License (https://creativecommons.org/licenses/by/4.0). The reuse of material under this license requires that the author(s), source and license are credited. Third-party material in this article could be subject to other licenses (typically indicated in the credit line), and in this case, users are required to obtain permission from the license holder to reuse the material.

The definitive version of this article is the electronic one which can be found at:
https://doi.org/10.3762/bjnano.15.85

BEILSTEIN JOURNAL OF NANOTECHNOLOGY

Hymenoptera and biomimetic surfaces: insights and innovations

Vinicius Marques Lopez*[1], Carlo Polidori[2] and Rhainer Guillermo Ferreira[1]

Review

Open Access

Address:
[1]Lestes Lab, Federal University of Triângulo Mineiro, Uberaba, Minas Gerais, Brazil and [2]Department of Environmental Science and Policy (ESP), University of Milan, Via Celoria 26, 20133, Milan, Italy

Email:
Vinicius Marques Lopez* - ovinicius.lopez@gmail.com

* Corresponding author

Keywords:
arthropods; bio-inspired surfaces; bioengineering; cuticle; nanoscale structures

Beilstein J. Nanotechnol. **2024,** *15,* 1333–1352.
https://doi.org/10.3762/bjnano.15.107

Received: 03 July 2024
Accepted: 04 October 2024
Published: 05 November 2024

This article is part of the thematic issue "Biomimetics and bioinspired surfaces: from nature to theory and applications".

Associate Editor: K. Koch

© 2024 Lopez et al.; licensee Beilstein-Institut.
License and terms: see end of document.

Abstract

The extraordinary adaptations that Hymenoptera (sawflies, wasps, ants, and bees) exhibit on their body surfaces has long intrigued biologists. These adaptations, which enabled the immense success of these insects in a wide range of environments and habitats, include an amazing array of specialized structures facilitating attachment, penetration of substrates, production of sound, perception of volatiles, and delivery of venoms, among others. These morphological features offer valuable insights for biomimetic and bioinspired technological advancements. Here, we explore the biomimetic potential of hymenopteran body surfaces. We highlight recent advancements and outline potential strategic pathways, evaluating their current functions and applications while suggesting promising avenues for further investigations. By studying these fascinating and biologically diverse insects, researchers could develop innovative materials and devices that replicate the efficiency and functionality of insect body structures, driving progress in medical technology, robotics, environmental monitoring, and beyond.

Introduction

The body surfaces of insects are marvels of natural engineering, displaying a remarkable array of adaptations that enable them to thrive in diverse environments [1-3]. Insects have developed a variety of mechanisms to cope with the challenges posed by their habitats, from specialized structures for attachment and movement to unique features that enhance survival and reproductive success [4]. These adaptations may provide valuable insights for biomimetic and bioinspired technological advancements [1]. Hence, understanding these mechanisms not only sheds light on the evolutionary ingenuity of insects but also offers innovative solutions and technological applications.

The order Hymenoptera, which includes sawflies, wasps, ants, and bees, is one of the most diverse groups in the class Insecta, with over 153,000 described species [5] and an estimated 1 million species yet to be discovered [6]. Traditionally, this

order is divided into "Symphyta" (sawflies) and Apocrita. The primary distinction between sawflies and Apocrita lies in their body structure: Sawflies lack a "wasp waist" and exhibit a broad connection between the abdomen and thorax, similar to other insects. In contrast, Apocrita are characterized by the integration of the first abdominal tergite into the metathorax to form the propodeum. This results in a mesosoma that includes the thorax and propodeum, housing the primary locomotory structures, that is, legs, wings, and their musculature, which makes it the most complex skeletomuscular region of the insect. This structure is fundamental for generating flight power and precise wing adjustments. The remainder of the abdomen is known as the metasoma. The articulation between the mesosoma and metasoma, marked by the wasp waist (or petiole), enhances the maneuverability of the metasoma and its ovipositor or sting, allowing for efficient prey capture, defense, and oviposition (Figure 1).

Hymenoptera exhibit a remarkable variety of biological structures and functions, possessing highly specialized organs and body parts, each adapted to specific ecological roles and lifestyles. These morphological and functional innovations predominantly involve the slender waist of Apocrita wasps, the stinging mechanism observed in Aculeata, parasitoidism (a specialized form of carnivorous behavior), and secondary phytophagy (a reversion to plant-based feeding) [7]. Hymenoptera are also well known as the animal clade where complex forms of cooperative behavior (eusociality) arise most independent times, and such behavioral specialization also drove the evolution of novel morphologies related to, for instance, task specialization in the different castes [8-10]. Studying and emulating these features, scientists and engineers can develop innovative materials and devices that mirror the efficiency and functionality of Hymenopteran anatomy.

Here we describe the structural adaptations on the surfaces of the body of Hymenoptera (Figure 2) with potential biomimetic applications. By analyzing their unique morphological features and the principles behind their functionality, we aim to identify key characteristics that can inspire innovative materials and technologies.

Review

General features of body cuticle

The cuticle of Hymenoptera exhibits several fascinating properties.

Cuticle roughness

The cuticle surfaces of some species reduce friction and wear, inspiring the development of low-friction materials and coatings. By mimicking these natural textures, it is possible to create synthetic materials that exhibit similar friction-reducing properties, leading to significant advancements in mechanical efficiency and durability. For instance, low-friction coatings inspired by Hymenoptera cuticles can be applied to materials to reduce wear and tear, thereby enhancing performance, and extending the lifespan of the material.

Surface roughness can have beneficial effects on the overall aerodynamic characteristics of artificial surfaces, such as rough coatings on high-speed trains [12], dimples on golf balls [13], and shark skin denticles on aircrafts [14]. Some micromachines can also benefit from micro- and nanostructures that create roughness on surfaces and influence aerodynamics and heat transfer [15]. The sculptured and thick cuticle of some hymenopterans is also associated with increased resistance to fractures and high pressures [16] and may also potentially reduce water loss [17,18]. Alternative hypotheses yet to be tested for the function of such complex cuticle sculpturing is the air drag reduction during flight, as many hymenopterans (e.g., chrysidids, scelionids, and mutillids) have dimples on the cuticle that might have the same aerodynamic effect as those on golf balls [13]. Setose cuticle in hymenopterans also exhibits an interesting function, namely, reducing the accumulation and deposition of particles [19].

Similarly, in the medical field, these coatings can be used on surgical instruments and prosthetics to minimize friction against biological tissues, reducing discomfort and improving the functionality of medical devices. Furthermore, in the field of electronics, low-friction surfaces can prevent the wear of moving parts in devices such as hard drives and printers, ensuring longer operational life and reliability. The mechanisms behind the cuticle's friction-reducing properties also include the ability to repel dust and contaminants, which further extends the applications of these biomimetic materials. For instance, the cuticle of sawfly larvae has complex nanostructures and wax crystals that result in hydrophobicity [20]. By incorporating these properties, manufacturers may develop self-cleaning surfaces that maintain their low-friction characteristics even in harsh environments. This feature is particularly valuable in aerospace applications, where equipment is often exposed to extreme conditions.

Coloration

Cuticle coloration in Hymenoptera may be achieved through either structural coloration or pigments, the latter being essentially melanin (eumelanin and/or pheomelanin) [21-23] (but see [24,25] for other pigments). Especially structural coloration provides a wealth of inspiration for creating vivid, durable colors without the use of dyes. This natural phenomenon involves the manipulation of light by micro- and nanostructures

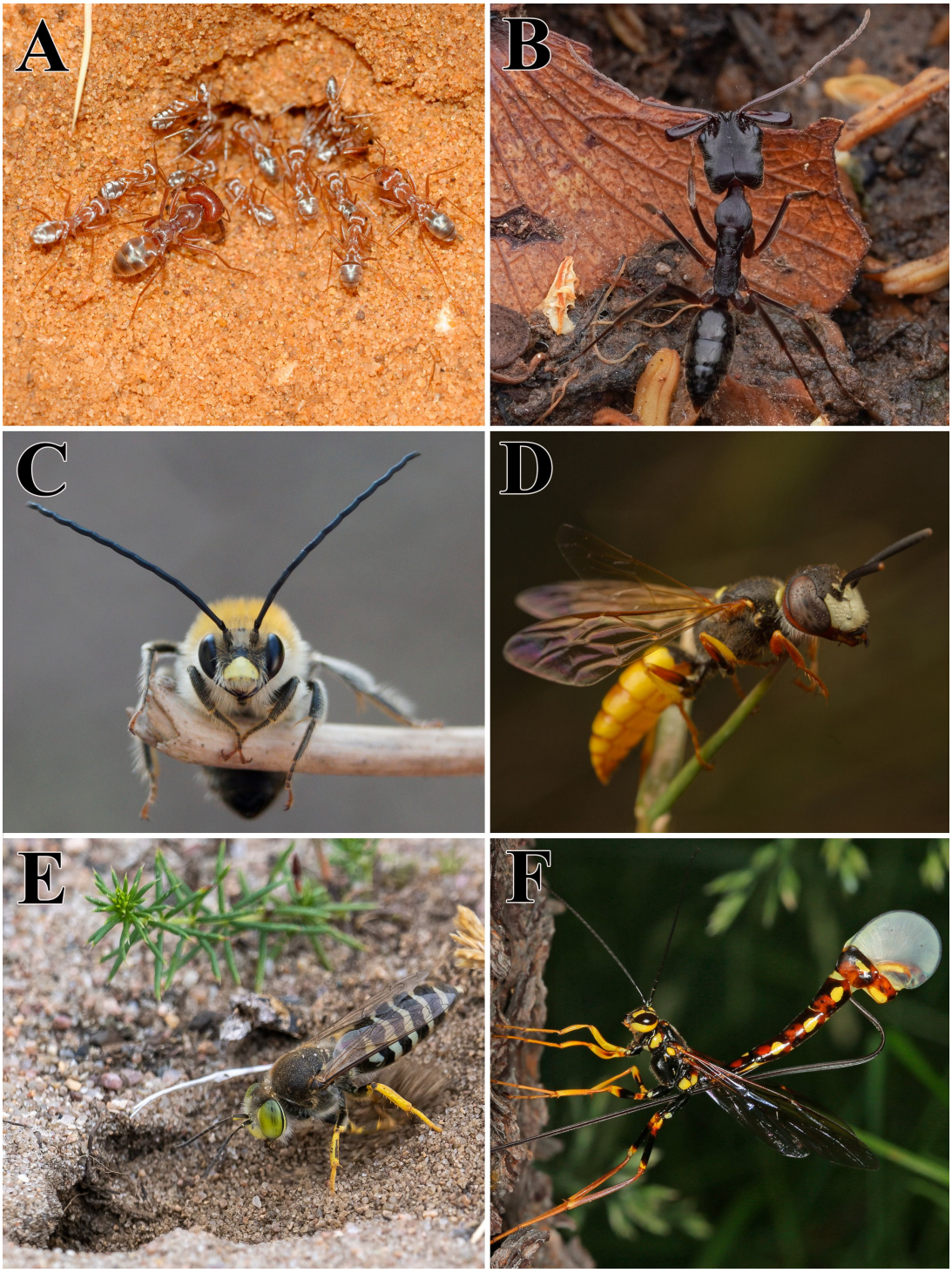

Figure 1: Diversity of hymenopteran species showcasing a range of shapes and life strategies. (A) Saharan silver ant (*Cataglyphis bombycine*) (© 2017 Manuel García-Viñó Sánchez). (B) Tap-jaw ants (*Odontomachus troglodytes*) (© 2024 Jonghyun Park). (C) Long-horned bees (*Eucera nigrescens*) (© 2020 Corinna Herr). (D) Beewolves (*Philanthus triangulum*) (© 2020 Johan Pretorius). (E) Sand wasps (*Bembix rostrata*) (© 2022 Piotr Lukasik). (F) Norton's giant ichneumonid wasp (*Megarhyssa nortoni*) (© 2015 Ed Oswalt). Figure A was taken by Manuel García-Viñó Sánchez and is used with permission. This content is not subject to CC BY 4.0. Figures B–F were reproduced from https://www.inaturalist.org/observations/204425768, https://www.inaturalist.org/observations/41894658, https://www.inaturalist.org/observations/45592397, https://www.inaturalist.org/observations/123874897 and https://www.inaturalist.org/observations/1778516 respectively (published by iNaturalist, distributed under the terms of the Creative Commons Attribution-Non Commercial 4.0 International License, https://creativecommons.org/licenses/by-nc/4.0/). This content is not subject to CC BY 4.0.

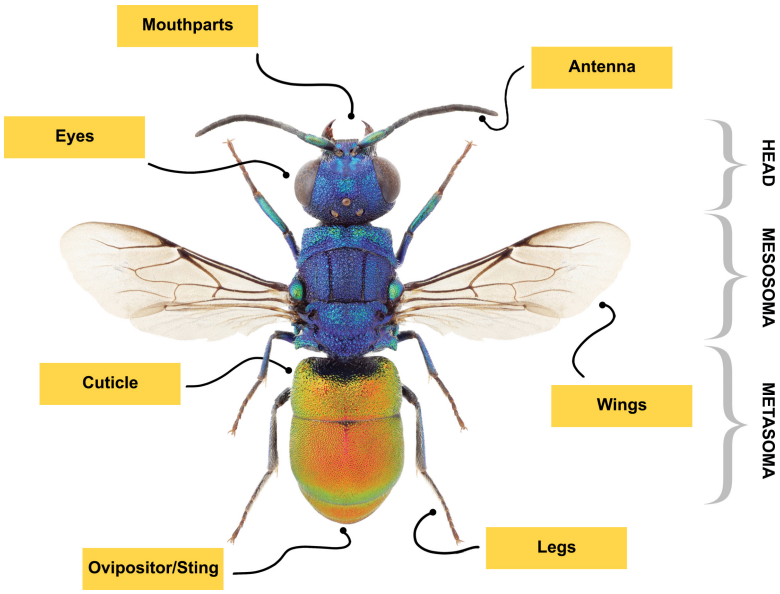

Figure 2: The body parts of Hymenoptera that can serve as sources for bioinspired and biomimetic materials and technologies. The image was adapted and reproduced from [11] (© 2015 J. Paukkunen et al., published by ZooKeys, distributed under the terms of the Creative Commons Attribution 4.0 International License, https://creativecommons.org/licenses/by/4.0).

on the cuticle (e.g., epicuticular multilayer reflectors), which can produce brilliant and iridescent colors [26-28]. The examples range from the metallic wings of some bees to the striking iridescent colors of wasps [29,30]. Blue coloration is hard to find in nature because blue pigments are rare; hence, animals tend to evolve structural coloration that reaches blue hues, like in carpenter bees [31]. Some species have ultrablack cuticles that absorb nearly all incident light (Lopez et al., this volume), a feature that can be used to create highly efficient light-absorbing materials for solar panels [32,33]. Understanding and mimicking these biological systems can lead to significant advancements in various fields, including materials science, fashion, and environmental sustainability [34].

In materials science, the principles of structural coloration can be applied to develop colorfast materials that do not fade over time [34-37]. Traditional pigments and dyes can degrade under exposure to light, heat, and chemicals, but structurally colored materials maintain their vibrancy indefinitely. This has potential applications in creating long-lasting paints, coatings, and fabrics, reducing the need for frequent replacements and repainting, thus conserving resources, and reducing waste [34]. The fashion industry can also benefit greatly from such biomimetic and bioinspired surfaces [38]. By incorporating structural coloration into textiles, designers can create clothing and accessories with striking, iridescent hues that do not rely on chemical dyes [38]. This can lead to more sustainable fashion practices, as the production of synthetic dyes often involves toxic chemicals and generates significant environmental pollution [38]. Structurally colored fabrics would offer a greener alternative, aligning with the growing demand for eco-friendly fashion.

Furthermore, structural coloration can inspire the creation of innovative security features [34]. The unique optical effects of these natural structures are difficult to replicate and counterfeit, making them ideal for use in anti-counterfeiting measures. Banknotes, identification cards, and high-value documents can incorporate structural coloration to enhance security and prevent forgery, leveraging the complexity and uniqueness of these bioinspired designs. In the field of consumer electronics, the vibrant and durable colors produced by structural coloration can be used to create more aesthetically pleasing and durable electronic devices. Smartphone cases, laptops, and other gadgets can feature iridescent colors that do not wear off or fade, enhancing both their appearance and longevity. This not only improves the user experience but also contributes to a reduction in electronic waste, as devices retain their visual appeal over a longer period. The techniques to create biomimetic materials with color producing mechanisms inspired by insects already exist [29,30] and applications of such technology have several possibilities.

Hairs

The body surface of insects is equipped with hairs (sensu lato) with different morphologies. These structures may first be categorized into two main types, that is, setae, which have a socket (which originates from an adjacent cell) and microtrichia (not

socked and thus originating from one cell) [39,40]. Such tiny structures belong to two main functional types. They are either mechanosensory and belong to the peripheral nervous system or they have no sensing role and serve to prevent wetting of, for example, wings and legs [41-44]. Other functions include the detection of airflow patterns, for example, through trichoid sensilla on the compound eyes of honeybees [45], which are important to maintain and coordinate flight. In general, the head capsule of Hymenoptera is densely covered with hairs and may be a ground-plan feature of Hymenoptera and a potential autapomorphy [46]. While the reason for such trait is still unknown, the fact that another order, the Diptera, also including mostly quick-flying insects, show the same pattern, may suggest a relationship with optimization of flight behavior. Evidence on structures and functions of some of these non-sensory hairs in ants and bees suggest intriguing applications in biomimetics.

In ant larvae, other non-sensory functions of hairs include, for example, ensuring ventilation at the body surface [47] and larval clumping, the latter function through special "hooked" hairs [48]. Adult ants of the tropical tribes Basicerotini and Stegomyrmecini, in contrast, possess brush hairs on the body that capture minute soil particles, camouflaging themselves with the soil surface [10], while adult desert ants have special long and curved hairs on the lower surface of the head and mouthparts, which improve soil digging and soil carrying [49].

In the honeybee, a special microscale hairy compliant texture on abdominal surfaces reduces friction, which is relevant considering that the abdominal sections, by undergoing many reciprocating motions, are at risk of wear or abrasion [50]. Ocular hairs in honeybees reduce airflow at the eye surface by up to 90%, deflecting incoming air and create a zone of stagnant air, potentially helping in the deployment of sensors outdoors, where they are strongly subjected to airborne dust [19].

The detailed study of hymenopteran hairs can be useful in fabricating new surfaces with friction reduction mechanisms and, consequently, longer life time. Special hairs that may be useful to create surfaces optimized for protection from overheating are those responsible for the silver appearance of the Saharan silver ant *Cataglyphis bombycine* [51] (Figure 1A). These hairs have a particular, rarely found morphology (triangular cross section with two corrugated surfaces) associated with a strong optical reflection in the visible and near-infrared (NIR) range, while maximizing heat emissivity in the mid-infrared (MIR). This allows the insects to maintain a lower thermal steady state and to cope with high temperatures (50 °C or even more) [51]. Additionally, specialized hairs with thermal functions are present in both wasps [52] and bees [53].

At last, hymenopteran hairs considerably vary in terms of length [54-56], suggesting that they may possess different physical properties, which may be variably used in biomimetic applications.

Specialized structures on the three-body tagma

Head

Mouthparts: The mouthparts of Hymenoptera, which are adapted for a variety of functions such as cutting, chewing, and sucking, provide valuable models for designing versatile tools and instruments. Within certain lineages of Hymenoptera, mandibles are known to include trace metals, mainly Zn and secondarily Mn, in the cuticle [57]; these features increase their hardness [58] (Figure 3A). Ants are by far the hymenopteran

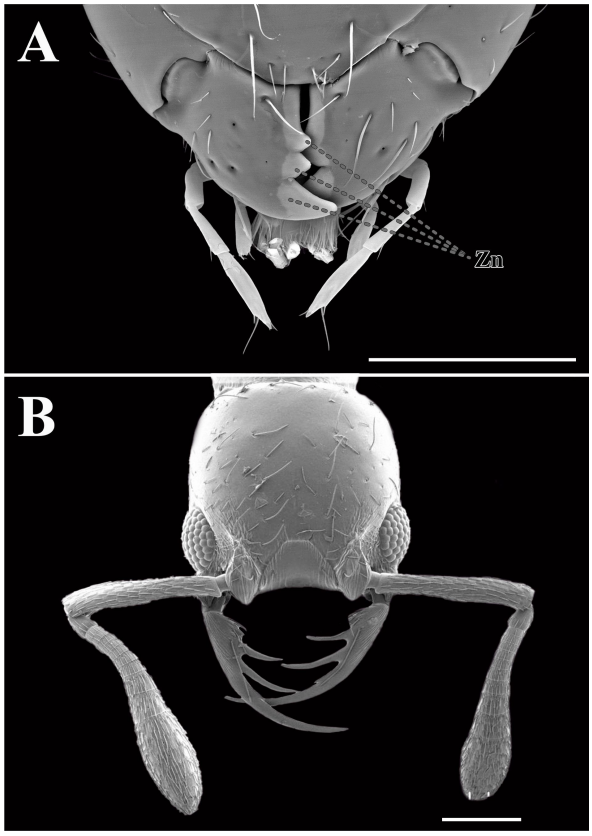

Figure 3: Scanning electron microscopy (SEM) images of ant mandibles. (A) Zinc-enriched mandibles of *Aganaspis daci*. (B) Jaw of *Thaumatomyrmex fraxini*. Zn: Zinc. Scale bars: 200 µm. Figure B was adapted from https://www.antweb.org/bigPicture.do?name=antweb1008597&shot=h&number=2 (© 2024 California Academy of Sciences, uploaded by R. Keller, specimen code ANTWEB1008597, published in AntWeb Version 8.108, accessed 13 August 2024, distributed under the terms of the Creative Commons Attribution 4.0 International License, https://creativecommons.org/licenses/by/4.0).

group where this trait was most extensively studied (21 species in total spanning five subfamilies), with the leaf-cutter genus *Atta* overrepresented in cuticular composition investigations (reviewed in [59]). Within Hymenoptera, ants are particularly fascinating because of their division into castes with distinct tasks and sizes, showcasing a hierarchical organization in their societies [60]. Among these castes, the mandibles play a critical role, with different sizes and functions correlating to specific tasks within the colony [60]. Studies found that larger leaf-cutter ants (*Atta laevigata*, Attini) have higher Zn content in their mandible cutting edges, leading to greater hardness and Young's modulus [61]. Understanding the mechanical properties and composition of leafcutter ant mandibles could offer valuable insights into biomimetic design principles, potentially inspiring the development of innovative tools and instruments with enhanced performance and adaptability for various applications [62,63]. Recently, the mandibles of leafcutter ants have inspired the design of a biomimetic stubble-cutting device, showcasing excellent performance and potential applications in agriculture [64].

Ant mandibles offer valuable inspiration for the enhancement of medical tools and devices. For instance, bioabsorbable surgical clamps modeled after the morphology and topography of the *A. laevigata* mandible, characterized by smooth internal regions and rougher external surfaces, could significantly improve grip and functionality [65]. Furthermore, the unique kinematic features of ant mandibles, such as the mobile joint axis and the tilt in the mandibular axis, provide insights for designing more efficient gripping devices [66]. Recently, a commercially available endoscopic needle holder was developed based on the morphology of *Formica rufa*, resulting in a remarkable increase in force amplification by up to 296%, with experimental measurements showing an increase of up to 433%, without altering the tool's size [66].

Mandibles can offer structural adaptations to deliver powerful and high-speed strikes, as in trap-jaw ants (e.g., *Odontomachus monticola*) [67] (Figure 1B). In these species, hollow mandibles combined with resilient fibrous helical structures enhance energy absorption and improve stress redistribution, providing additional protection against damage caused by impact loads [68]. Such adaptations not only facilitate efficient prey capture but contribute to the overall durability of the mandibles. Additionally, when threatened, these ants possess the remarkable ability to jump several centimeters propelled by the force of their mandibles [69]. Engineers and material scientists can draw inspiration from these natural designs to develop lightweight yet durable components that enhance energy absorption and mitigate damage from impact loads, thereby improving the safety and longevity of vehicles and aircraft.

The double-rowed teeth of primitive asian jumping ant (*Harpegnathos venator*), which confer enhanced tribological stability, provide a more stable coefficient of friction when pinching objects of varying sizes using different regions of the mandible [70]. This ingenious natural design could inspire the development of multifunctional robotic grippers, offering improved stability and adaptability in handling diverse objects [70]. The specialized mandibular morphology and task-specific bite mechanics observed in big-headed ants (*Pheidole*) offer insights into creating robust and efficient cutting tools that can perform specialized tasks with precision [71]. Other species awaiting study may possess even greater potential for fine object manipulation. For example, *Probolomyrmex* and *Thaumatomyrmex* (Figure 3B), which employ their specialized mandibles to capture Polyxenid millipedes and then strip them of their detachable and hazardous bristles [72,73]. Therefore, these biological inspirations can lead to the creation of advanced devices with improved performance and multifunctionality, pushing the boundaries of current engineering.

Honeybees must visit approximately 3000 flowers to produce a single gram of honey [74]. To accomplish this, they use their hairy tongues to dip into viscous nectar at high frequencies. Their mouthparts consist of a pair of galeae, labial palps, and a hairy glossa with a flabellum at the tip [75,76] (for a more detailed view of the mouthparts, see [77]). The different mouthparts combined with the characteristics of viscous food can inform the design of efficient viscous micropumps [78]. For instance, the galea ridges on the mouthparts of an Italian honeybee (*Apis mellifera ligustica*) facilitate nectar-dipping by minimizing drag, enabling the bees to feed more efficiently [75]. The unique morphology and dynamic movement of the bee's hairy tongue optimizes nectar feeding while conserving energy, providing insights into design methodologies for fluid transport devices using hairy beds [79]. Even with a damaged tongue, bees can feed normally, indicating the presence of compensatory mechanisms [74,78]. For instance, increasing the dipping frequency and utilizing the hairs can offset nectar loss caused by a damaged tongue, which can be valuable in engineering applications [78,80]. Additionally, the interaction between bee mandibles and propolis highlights the potential for developing anti-adhesive surfaces [81]. Bioinspired surfaces based on honeybee mandibles have been shown to reduce propolis adhesion by over 40% compared to control surfaces, demonstrating significant potential for application in various industries [82].

Eyes: Similar to insects and other arthropods, hymenopterans possess compound eyes, consisting of numerous small visual units called ommatidia. Each ommatidium acts as an individual photoreceptive unit, collectively providing a panoramic view

that offers several visual advantages, such large field of view, high temporal resolution, rapid capture and tracking of fast-moving objects [83,84]. This renders compound eyes particularly suitable for electronic surveillance applications, where broad observation coverage is essential for detecting multiple objects simultaneously [85,86]. They also hold potential for endoscopic examination [87] and robot navigation [88]. Recently, an innovative microfluidic-assisted 3D printing technique has facilitated the creation of a compound eye inspired by eyes of worker bees [89]. This innovative perspective can pave the way for various applications, ranging from advancements in endoscopic imaging to improvements in machine vision, ultimately enhancing the visual efficiency of robots and sensors in autonomous vehicles [89-91].

Antenna: Hymenopteran antennae are equipped with specialized structures for detecting chemical, mechanical, and hygrothermal/CO_2 cues in the environment, overall known with the term sensilla (Figure 4). Hymenoptera sensilla encompass different morphologies and sizes, which also vary in number both among species and between sexes [54,55]. Such great variability is often the result of co-evolution of these traits with ecological requirements [56,92-94]. Furthermore, they are essentially in both intra- and interspecific communications [95-97]. These antennal sensors have inspired the development of devices for the detection of volatile compounds, which have applications in environmental monitoring, food safety, and medical diagnostics [98]. The mobility of the antennae of long-horned bees (e.g., *Eucera longicornis*) are used by males to court females by gently grasping and pressing their antennae (Figure 1C). The antennae of long-horned bees and other hymenopterans may give some insight into microfilaments to grab small and delicate objects [99].

Female European beewolves (*Philanthus triangulum*) (Figure 1D) and other crabronids have developed a remarkable symbiotic relationship with bacteria of the genus *Streptomyces*, which they cultivate in specialized antennal glands [100,101]. This association is unique in that the bacteria are grown in large reservoirs within the antennae, where they receive nutrients from the gland cells. When the beewolf constructs its subterranean brood cells, it secretes these bacteria into the cells, where they produce antibiotic substances that protect the developing larvae from fungal infections. The antennal glands are highly specialized, featuring complex morphology including a monolayered epithelium and numerous gland units that facilitate the cultivation and secretion of the symbiotic bacteria. This intricate system ensures the survival of the offspring by creating a microenvironment hostile to pathogens, showcasing a fascinating example of insect–microbe symbiosis.

The ability of these wasps to maintain and apply symbiotic bacteria through their antennal glands can inspire the development of bioactive medical devices. These devices can release antimicrobial agents or probiotics to prevent infections and promote healing. For example, catheters and implants can mimic the wasp structures to reduce the risk of infection and enhance the body's natural healing processes.

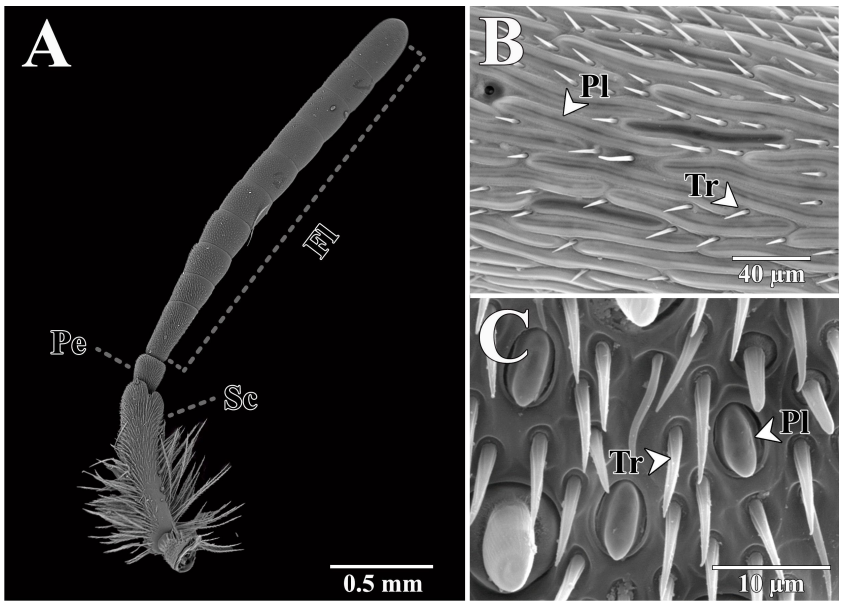

Figure 4: (A) SEM image of a hymenopteran antenna (*Anthidium oblongatum*). (B) SEM images of male antennal sensilla of *Ibalia leucospoides*. (C) SEM images of female antennal sensilla of Cerceris rubida. Pe: pedicel; Sc: scape; Fl: flagellum; Pl: placoid sensilla; Tr: trichoid sensilla.

Mesosoma

Wings: In order to fulfill their essential functions, insect wings must effectively transmit force from the muscles at their base to the surrounding air, generate lift, and uphold structural integrity without deformation [102]. Hence, wings need to be lightweight, flexible, and resilient, rendering them captivating subjects for biomimetic materials research [102,103]. For instance, an examination of the nanomechanical properties of membranous wings in Chinese bees (*Apis cerana cerana*) reveals a synergistic interplay between veins and membranes, facilitating efficient load transmission and resulting in exceptional mechanical performance and structural stiffness [104]. Research on biological membranes, inspired by the superior structures of insect wings, holds potential for advancements in various sectors, including medical, construction, aviation, and automotive industries [104-108].

Research on hymenopteran wings remains limited, with many groups still requiring fundamental studies on their properties. Exploring other Hymenoptera species could yield valuable insights. For instance, the females of scoliid wasps, solitary parasitoids of scarab beetle larvae, dig into the ground to locate these larvae. This could inspire the development of wings for exploration and rescue drones, modeled after the scoliid wasps' wings, offering high maneuverability, durability, and efficiency in flight and underground across varied terrains. Similarly, Vespidae with elongated bodies possess pointed wings for enhanced maneuverability, while stouter species have rounded wings for potentially higher flight speeds [109]. This variation could inform the design of modular drones capable of altering wing shapes to optimize either maneuverability or flight speed as needed. Additionally, the design of these devices could be enhanced by a unique feature observed in ensign wasps (*Afrevania* and *Trissevania*, Evaniidae) [110]. These wasps exhibit a sophisticated ability to fold their forewings along two intersecting fold lines, creating a four-plane wing folding mechanism [110]. By incorporating a similar four-plane wing folding mechanism, drones could achieve enhanced compactness and versatility, allowing for easy transport and storage, as well as efficient adaptation to various environments and mission requirements.

Microwasps exhibit remarkable adaptations in their wing structure, offering unique insights for biomimetic applications. Many families of microwasps are tiny, with adults measuring less than 2 mm, and their wings exhibit a distinctive morphology (Figure 5). For instance, in many microwasps (e.g., fairyflies (Mymaridae)), wings are predominantly composed of long bristles, with diameters ranging from 300 nm to 2.5 μm [111]. Although the functional basis of this morphology is not fully understood, these bristle-based wings may enable microwasps to sustain prolonged flight without the energetic costs typically associated with muscle activity [112-114]. Similar results are observed in the tiny beetle *Paratuposa placentis* (body length 395 μm), where the reduced wing mass and specific wing movement patterns contribute to enhanced flight performance [115]. In the context of biomimetic applications, understanding and replicating these adaptations can lead to significant advancements of micro-aerial vehicles [103]. By mimicking the lightweight, bristle-based wing structures of microwasps, engineers can develop microdevices that require less power to operate, thus extending their flight times and improving energy efficiency [116,117]. However, microwasps with other wing morphologies can also offer valuable insights and applications for the development of micro-aerial vehicles [118,119].

The wing-to-wing coupling mechanism in Hymenoptera functions as a multifaceted joint, linking the forewing's rolled membrane to the hindwing's hook structures, enabling synchronized movement and improved aerodynamic performance [121,122]. This mechanism is composed of a rolled membrane positioned at the trailing edge of the forewing, accompanied by small hooks (or hamuli) arranged in a line along the leading edge of the hind wing, all attached to a vein at the leading edge of the hind wing where the hooks are embedded [123]. These hooks are movable and exhibit an elastic base to ensure the high mobility of wings [124]. The coordinated movement of wings facilitated by this mechanism enables synchronized action and improved aerodynamic performance, while also allowing for decoupling during periods of rest, thereby avoiding aerodynamic interference and ensuring optimal flight dynamics. Computational models also indicate that the wing-to-wing coupling mechanism in Hymenoptera results in increased lift and drag, with the drag experiencing a higher rate of increase [122].

Despite their seemingly delicate nature and occupancy of a mere ≈0.2% of the total wing area, these hooks play a crucial role in continuously transferring forces between the wings, withstanding forces up to 180 times the insect's body weight and 40 times the aerodynamic forces encountered during flight [123]. This robust design of the coupling mechanism is essential for maintaining functionality, particularly in scenarios involving frequent collisions, where it must endure forces surpassing typical flight stresses [123]. Additionally, the microstructural properties of the wings contribute to their hydrophobicity and anti-fouling capabilities, which can be applied to the development of self-cleaning surfaces and materials resistant to biofouling in marine environments.

Legs

Adhesive pads: The adhesive organ in Hymenoptera consists of a flexible cuticle pad (i.e., arolium) situated between the

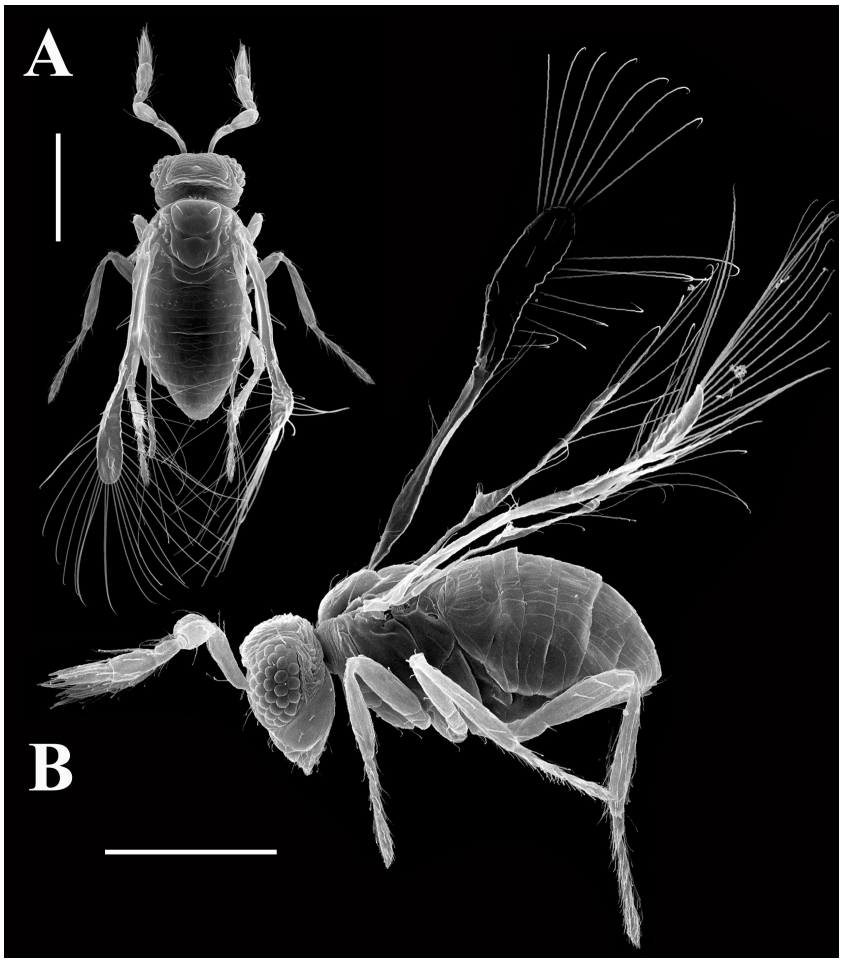

Figure 5: SEM image of wing bristles in a microwasp *Megaphragma polilovi*. (A) Dorsal view and (B) lateral view. Scale bars: 100 µm. Both figures are from [120] and were reprinted by permission from Springer Nature from the book "At the Size Limit - Effects of Miniaturization in Insects" (chapter "Structure of the Principal Groups of Microinsects. VI. Trichogrammatid Wasps (Hymenoptera: Trichogrammatidae)" by A. A. Polilov), Copyright 2016 Springer International Publishing Switzerland. This content is not subject to CC BY 4.0.

pretarsal claws, capable of unfolding and retracting with each step [125] (Figure 6A). The arolium may be structured in lines perpendicular to the longitudinal axis of the pretarsus [126]. When extended (actively or passively) [127], the arolium comes into contact with the surface, thereby enhancing its adhesive contact area. Hymenopteran species serve as valuable sources of inspiration for artificial adhesive surfaces because of their rapid stepping frequencies [127]. For instance, weaver ants (*Oecophylla smaragdin*a) can swiftly adjust and control their contact areas in less than a millisecond, a capability that helps prevent unexpected detachment and enables efficient locomotion with a smaller contact area [128]. In honeybees, these pads function in response to specific drag activities, even without neuromuscular reflexes [129]. This passive mechanism is attributed to the structural characteristics of the soft pads, which work in concert with hierarchical structures supported by numerous branched internal fibers [129]. Moreover, the pads in Hymenoptera exhibit self-cleaning capabilities [130]. The precise control of adhesive strength and contact area can inspire the development of new bioinspired surfaces that significantly reduce switching times between attachment and detachment.

In other instances, the presence of curved spines or hair on the tarsomeres enhances locomotion on irregular surfaces by penetrating the microdevices of the substrate, providing thousands of interlocking points that contribute to overall friction [131]. For example, weaver ants, renowned for their ability to cling to vertical surfaces and construct large leaf nests, utilize dense arrays of tarsal friction hairs on their tarsomeres to boost adhesion on heavily sculpted surfaces [132,133]. Similarly, females of *Anastatus bifasciatus* (Eupelmidae) employ these structures to achieve a firm grip on the uneven surfaces of host eggs [134]. These examples highlight the potential for biomimetic applica-

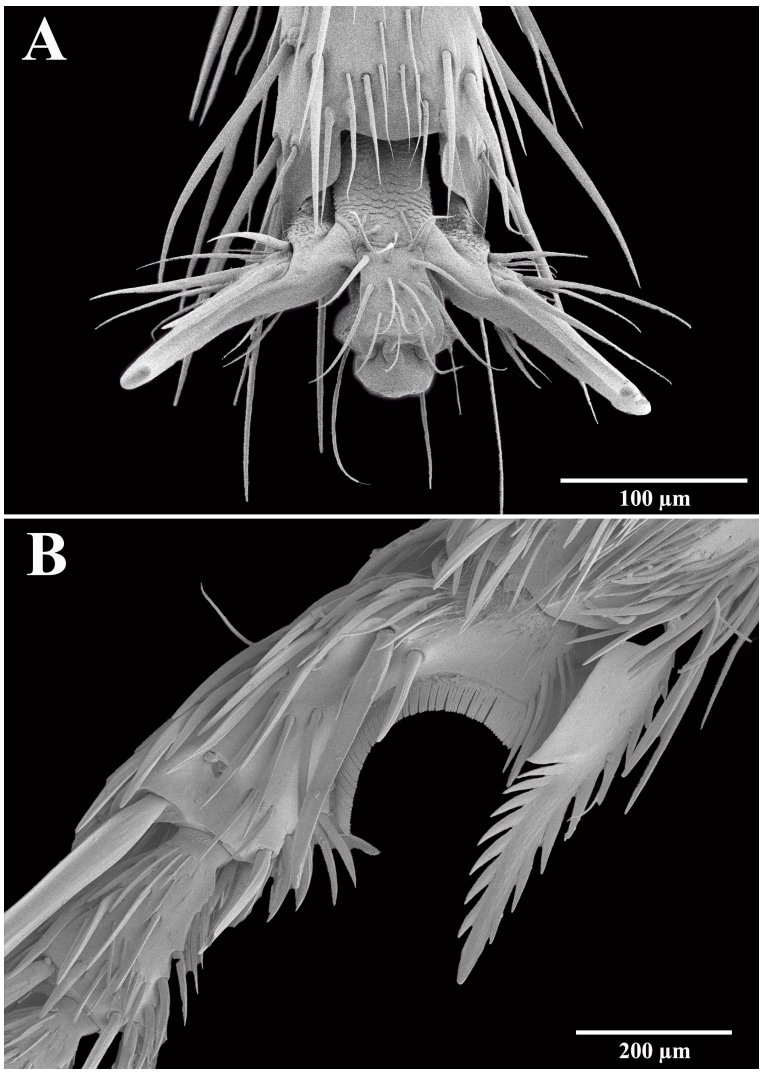

Figure 6: Structures on the leg of Hymenoptera. (A) Adhesive pads in ants (*Messor wasmanni*) and (B) antenna cleaner (strigil) of velvet ants (*Traumatomutilla bifurca*). Both figures were taken by Stanislav N. Gorb and were used with permission. This content is not subject to CC BY 4.0.

tions of such structures in developing advanced adhesive technologies and improving robotic mobility on uneven terrain and in microgravity environments [135].

Corbicula: Several bee species (e.g., honey bees, bumble bees, and orchid bees) exhibit a pollen basket on the hindlegs called corbicula [136]. Bees pack pollen grains along with vegetal resins and nectar in their corbiculae and take flight with this material without losing the attachment force even under great air drag and movement-derived forces [136]. Corbiculate bees are one of the most effective pollinator groups worldwide. Up to now, there are no studies on the potential replication of such strategy in biomimetics; however, one might suggest that the successful evolutionary history of the corbicula may be a source of inspiration for technology. Potentially, the corbicula, as other structures mentioned here, may inspire the creation of materials and innovations to carry viscous substances across large distances.

Micro-grooming tools: The maintenance of clean and functional body surfaces is crucial for insects. The typical mode of grooming occurring in Hymenoptera consists in scraping (one-directional movement of one structure against another), rubbing (two-directional movement of one or both structures in contact) or nibbling (an antenna or leg is taken into the inner mouthparts, essentially mandibles or legs) [137]. About 30 distinct types of grooming movements are actually recognized for the order [138].

The micro-grooming tools of Hymenoptera, used for cleaning and maintaining their bodies, provide models for the development of micromanipulation and cleaning devices in nanotech-

nology and microsurgery. This is especially true for the specialized two-part cleaning structure on their front legs used to clean their antennae efficiently [139]. This antenna cleaner (strigil) (Figure 6B) consists of an apical and modified protibial spur (calcar, composed of a trunk and a velum) and a modified basitarsus including a fine comb made up of setae and a notched inner surface. This structure was observed to be morphologically highly variable even within hymenopteran families [140], which may suggest that different habitat features (e.g., forests vs open grasslands or sandy soils vs clay soils) may require highly adapted cleaning structures. Simulating the cleaning strokes of the tarsal notch and tibial spur on contaminated antennae in *Camponotus rufifemur* ants demonstrated that both components effectively removed particles [141]. The cleaning occurs through both macroscopic contact and microscopic interactions between the cleaning hairs, antennal sensilla, and contaminating particles. Microscopic combs and brushes act as filters for particles of different sizes, with larger particles being scraped off by the bristles and comb, while smaller particles are picked up by the brush's flexible setae.

In the honeybee, hairs on the legs serve not only as an adhesive structure for pollen, but also for pollen removal. This is necessary since otherwise pollen widely distributed on the body would make sensing and controlled flight difficult. In particular, hair spacing and geometry on the forelegs affects the ability of pollen removal from the eyes (which are also equipped with adequately spaced hairs to promote their cleaning) [142]. All these findings highlight the sophisticated design of Hymenopteran cleaning structures, which can inspire synthetic cleaning technologies at the micro- and nanoscales, potentially improving the fabrication of delicate devices by reducing contamination-induced defects.

Digging: Many species of bees, wasps, and ants nest in the ground, showing a remarkable digging ability [143] (Figure 1E). Digging can be very efficient even in very hard soils [144], with some species excavating tunnels up to 1 m or more below the surface [145]. This activity is possible through the use of legs and mouthparts with morphologies highly adapted to this task, including, for example, robust spurs (legs) and large mandibles [146-148]. Hence, these structures and their movements while digging may be used as bionic prototypes for the design of low-resistance soil-engaging components, similar to the approach previously utilized with other insects as design models (e.g., mole crickets) [149].

Also interestingly, different Hymenoptera species have strong preferences for different types of soil [150]. Some bee and wasp species nest in highly sandy soils, while other species nest in very hard and silt- or clay-rich soil. Different soils, in turn, require different strategies of efficient digging, which can inspire different artificial instruments specialized in each soil type. This was already done using other insects as models, such as antlions, which dig in largely sandy soils and whose excavating behavior and related morphological structures inspired a biomimetic subsoiler tip that can reduce draught force in such type of soil [151,152].

Metasoma

Sting and ovipositor – drills, probes and needles: Parasitoidism is a specialized form of carnivory wherein the parasitoid completes its entire life cycle by feeding exclusively on a single host individual. This strategic adaptation is prevalent among Hymenoptera, with an estimated 70% of known hymenopteran species embracing this lifestyle [153]. As a result of evolutionary processes, hymenopterans have been bestowed with a highly specialized organ used for laying eggs, the ovipositor. The hymenopteran ovipositor consists of two pairs of valvifers located at the base, which house the muscles controlling the ovipositor mechanism, along with three pairs of valvulae capable of sliding along each other [154] (Figure 7A,B). The size of this structure can vary significantly, ranging from micrometers to the longest ovipositors documented in Arthropoda with lengths of over 100 mm [155,156], facilitating oviposition in diverse substrates such as wood, soil, or within other organisms [157] (Figure 1F, Figure 7B).

The ovipositor of certain parasitic wasps, such as those in sawflies wasp and ichneumon wasps has inspired the development of a prototype of a drill rasp designed for excavating femoral cavities, tailored for snugly inserting cementless hip prosthesis stems [158]. Apart from their highly specialized form, also the elemental structure of this organ evolved to increase drilling ability while limiting abrasion and wear. Indeed, trace metals such as Zn, Mn, and Cu were variably found within the cuticle matrix of Hymenoptera ovipositors and stings [159,160]. The mechanics of the ovipositor, characterized by its flexibility, strength, and the ability to penetrate tough materials with minimal force, offer a model for designing minimally invasive surgical instruments and precision technology [158]. Still in the medical field, the ovipositor's unique properties may lead to the development of highly specialized probes and needles for diagnostic and therapeutic purposes [161,162]. These bioinspired tools can navigate through soft tissues with minimal damage, mimicking the ovipositor's ability to penetrate substrates smoothly and efficiently [158,161-163]. Hence, drawing inspiration from ovipositors, these innovations may enhance medical procedures by amplifying precision, minimizing recovery periods, and augmenting patient outcomes, particularly in scenarios where maneuverability and accuracy are paramount.

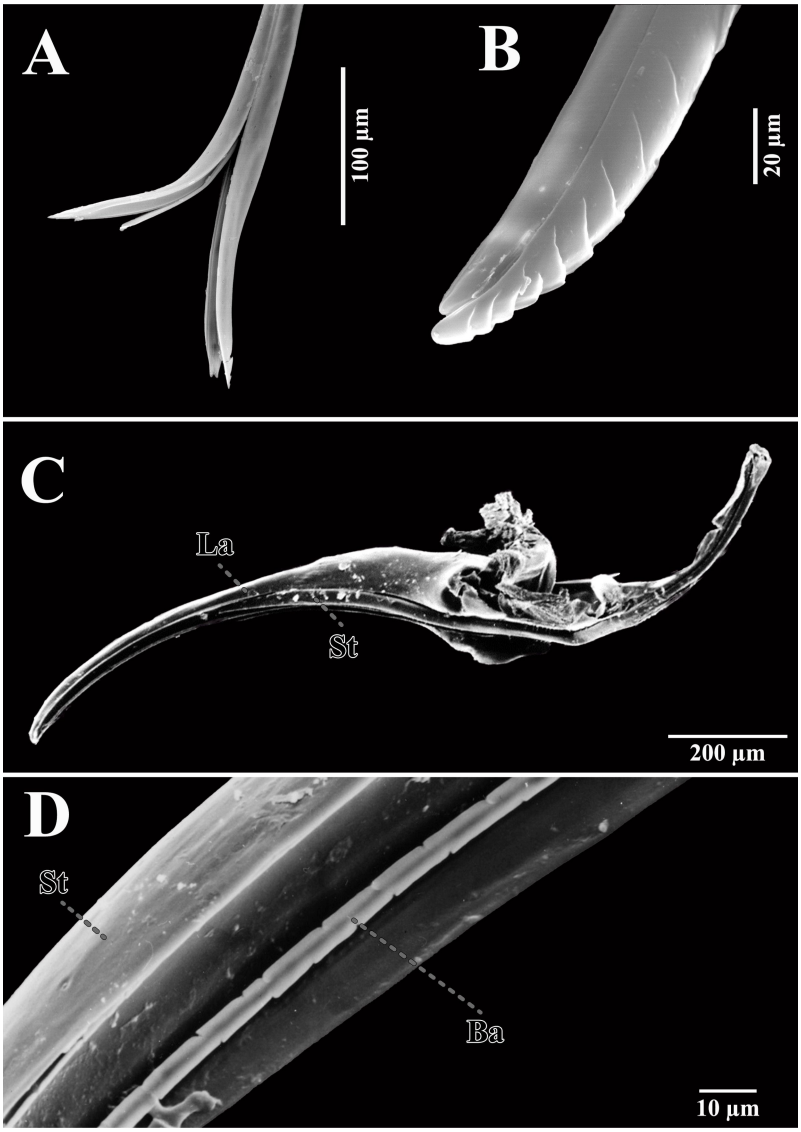

Figure 7: Perforating structures on the metasoma of Hymenoptera. (A, B) Ovipositor of *Neralsia* sp. and *Andricus coriarius*. (C, D) Sting of *Oxybelus haemorrhoidalis*. La: lancet; St: stylet; Ba: lateral barbed structure.

In addition to medical applications, the ovipositor's design principles have broader implications for engineering and technology. The ovipositor's ability to penetrate tough materials with minimal force inspires the development of tools and machinery that require high precision and efficiency [164]. For instance, researchers at the Surrey Space Centre have drawn inspiration from the wood wasp to create a drilling system that is simple, robust, lightweight, and efficient for use on extra-terrestrial subsurface exploration [165-168]. The ovipositor's structural and functional characteristics can inform the design of robotic systems. Robots equipped with ovipositor-inspired appendages can perform delicate tasks that require both strength and precision, such as handling fragile objects or performing intricate assembly operations [168]. Therefore, drilling and cutting tools modeled after the ovipositor can achieve greater accuracy and reduce wear and tear, leading to longer lasting and more effective equipment. This innovation can be applied in various industries, from construction to manufacturing, enhancing productivity, and reducing operational costs.

In environmental science, the study of ovipositor mechanics can contribute to the development of sustainable technologies for soil sampling and ecological monitoring. Devices modeled after the ovipositor can penetrate the ground to collect soil samples without causing significant disturbance to the ecosystem. This capability is important for monitoring soil health, studying

underground biodiversity, and assessing environmental impacts, providing researchers with valuable data while preserving natural habitats.

Delivery systems: Strength and efficiency of the ovipositor also offer insights into creating advanced drug delivery systems [169]. These systems can deliver medications directly to targeted areas within the body, improving the efficacy of treatments while minimizing side effects [170,171]. By emulating the ovipositor's ability to penetrate and deliver substances precisely, researchers have developed microneedles [163]. This approach is especially beneficial for administering vaccines and treatments for chronic conditions, providing a less invasive and more patient-friendly alternative to traditional methods.

The Aculeata sting represents a remarkable evolutionary transformation of the ovipositor. It has lost its original function of egg-laying to serve as a potent venom delivery system (Figure 7C,D). The venom delivery systems of Hymenoptera are precise and efficient, inspiring the design of microinjection systems and targeted drug delivery methods that minimize collateral damage to surrounding tissues [170]. Drawing inspiration from the precision and efficiency of Hymenopteran venom delivery systems, advanced microinjection devices can be crafted for laboratory applications, boasting painless insertion and extraction, minimal dermal injuries, mechanical durability, and suitable biocompatibility [172]. Furthermore, the capacity to induce mechanical tissue damage may vary across species, with those species employing the sting for offensive or defensive purposes potentially possessing cuticular microstructures proficient at inflicting significant harm [173].

Stridulatory organ: Stridulation in Hymenoptera, the process by which these insects produce sound by rubbing certain body parts together [174], primarily involves the interaction between two tergites of the metasoma [174] (Figure 8). This natural mechanism, involving specialized structures such as ridges and scrapers, can generate a wide range of frequencies with precision and efficiency, providing valuable insights for the advancement of sophisticated acoustic and vibration technologies. In nature, this acoustic strategy is likely employed for alarm signaling, sexual behavior, and as a versatile communication channel among eusocial insects (i.e., ants) [175-178]. By studying and mimicking these biological systems, it is possible to create innovative solutions in various fields, including communication, medical devices, and materials science.

Certain hymenopterans are capable of emitting stridulatory sounds at high frequencies, including ultrasound (≥20 kHz) [179,180]. The design of medical devices could greatly benefit from innovations inspired by these stridulation mechanisms. Ultrasound technology has demonstrated significant potential in

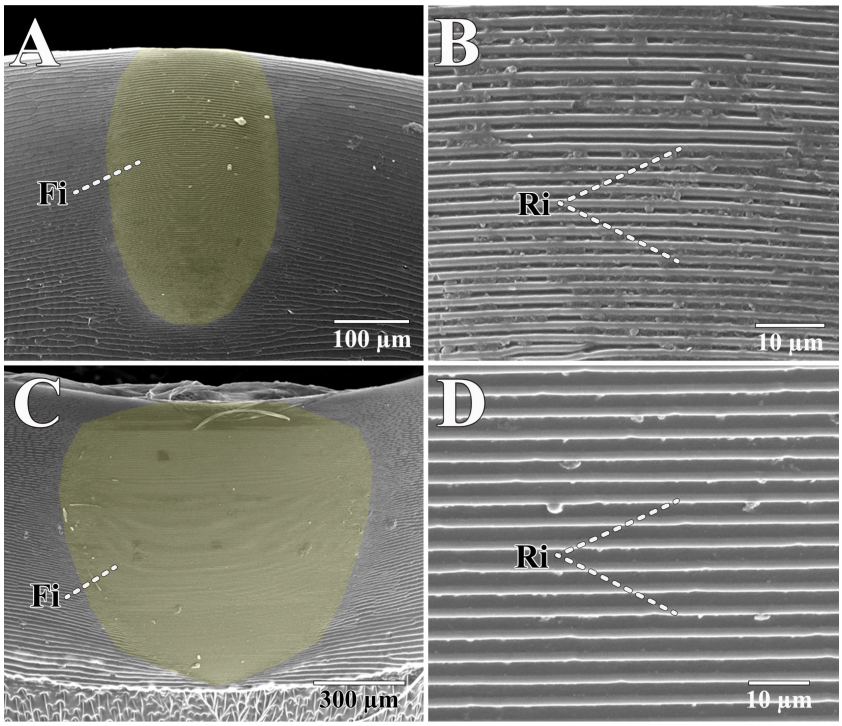

Figure 8: Scanning Electron Microscopy image showing the stridulatory organ in male velvet ants. (A, B). *Myrmilla capitata*; (C, D). *Nemka viduata.* Fi: file; Ri: ridges. Sound is produced by rubbing files and ridges against each other.

diagnostic imaging and ultrasound-responsive drug delivery [181,182]. Ultrasound technology is particularly promising for cancer treatment and disease modulation, as it facilitates the delivery of therapeutic agents such as genetic material, proteins, and chemotherapeutics [182,183]. Incorporating principles from the finely tuned frequency production observed in Hymenoptera could significantly enhance this technology, resulting in more precise and effective ultrasound equipment, thus improving patient outcomes in both diagnostics and treatment. Furthermore, studying the use of acoustic signals in hymenopterans may offer valuable inspiration for future research, as these context-dependent signals can modulate the production or inhibition of chemical signals in other individuals [178].

Moreover, the precise control over vibration frequencies observed in stridulation can inspire advancements in industrial applications where vibration control is essential. This includes machinery that operates more quietly and efficiently, reducing noise pollution and wear on components. Additionally, the principles of stridulation could be applied to develop sensors and actuators that are more sensitive and responsive, improving the performance of various mechanical and electronic systems.

Metasomal shape: The morphology of the metasoma in Hymenoptera offers significant potential for biomimetic applications, particularly within aerospace engineering. For instance, the segmented and flexible structure of a bee's metasoma facilitates efficient and dynamic flight maneuvers [184]. Bees optimize their aerodynamic performance and maneuverability through biomorphic adjustments to their shape [185]. This adaptable structure can inspire the development of aerospace vehicles with enhanced axial scalability and bending properties [185]. Incorporating a morphing structure inspired by the Hymenoptera metasoma could lead to the creation of supermaneuverable flight systems, contributing to advanced designs for aircraft and unmanned aerial vehicles, and reducing aerodynamic drag [185].

Furthermore, the metasoma of bees can dissipate residual flight energy during landing [186], and the shape of the metasoma can influence maneuverability and flight speed in wasps. Integrating these biological principles could result in vehicles capable of agile and precise movements and increased stability in turbulent conditions. Despite these promising possibilities, the shape and surface characteristics of the hymenopteran metasoma remain underexplored, and families with unique metasomal forms still lack basic research. For instance, cuckoo wasps (Chrysididae) possess a concave metasomal venter, enabling them to roll into a ball when threatened [187]. Hatchet wasps (Evaniidae) exhibit short and flag-shaped metasoma that moves up and down as they walk, resembling a flag or hatchet. In pelecinid wasps (Pelecinidae), the elongated metasoma allows them to locate and deposit eggs in subterranean hosts [188]. This unique metasomal morphology provides various adaptive advantages and can inspire innovations in designs.

Prey-carrying and prey-catching mechanisms: Some groups of predatory wasps hunt prey and subsequently transport it in flight to the nests, using either mandibles, legs or even the sting to keep the prey. Most predatory wasps use front and mid legs to carry the prey, while a few wasp species hold their prey only with the hind legs [189]. The efficient prey-loading mechanisms of some of these Hymenopteran species, that can even carry lift loads greater than the theoretical maximum as expected by their body mass and wing morphology [190], can inspire the design of robotic systems for material handling and transport, enhancing the efficiency of automated loading and unloading processes in various industries. By holding the prey on the sting, some species of *Oxybelus* (Crabronidae) have effectively freed all three pairs of legs for other purposes [189]. This peculiar way to carry the prey impaled on the aculeus is made possible through the special curvature and surface sculpture of sting elements (notably, barbs on the distal part of the lateral surface of the first valvula) [191,192], as well as by modifying the wings lift coefficient between the anterior and posterior wings movement [193].

Other features

Interlocking structures

Hymenoptera exhibit interlocking structures in their bodies that provide stability and flexibility. These structures can inform the design of modular and reconfigurable systems in robotics and materials science, especially for drones that must carry attachable items. Phoretic copulation is probably the main inspiration source [194]. Similar interlocking mechanisms can be found between male mouthparts and female head and mesosome for phoretic copulation (e.g., some mutillids) [195], and the same happens for male–female genitalia (e.g., bethylids, thynnids) [196]. Another example is the labrum–maxillae interlocking mechanism exclusive of ants [197].

Acarinaria

Mites can be found in various locations on the bodies of hymenopterans [198]. However, some species of bees and wasps have evolved specialized structures known as acarinaria, which facilitate the safe transport of mites [198-200]. The acarinarium can be located in one or more areas on the insect's body surface such as the propodeum, mesosoma, just below the apex of the first metasomal tergum, and in some cases, within the genital chamber of species such as *Ancistrocerus antilope* (Vespidae) [200]. These structures could be integrated into drones, plant leaves, or stems, providing secure havens for

biocontrol agents. This approach would naturally manage pest populations, reducing the need for chemical pesticides and promoting sustainable farming practices [201-203].

Conclusion

The diverse and highly specialized features of Hymenoptera offer a treasure trove of inspiration for biomimetic applications. By studying these insects, researchers can develop innovative materials and devices that mimic their efficiency and functionality, leading to advancements in medical technology, robotics, environmental monitoring, and beyond. The ongoing exploration of Hymenopteran biology and mechanics continues to unlock new possibilities for technological innovation, underscoring the profound impact of nature-inspired designs.

Acknowledgements

We thank Francesco Bonasoro (University of Milan, Italy) and Alberto Jorge (CSIC, Spain) for their support in producing the SEM images, which appear in this article, and José Luis Nieves-Aldrey (MNCN-CSIC, Spain), José Tormos (University of Salamanca), and Concepción Ornosa (Complutense University of Madrid, Spain) for the long-term collaborations in studying the morphological adaptations of Hymenoptera. Lastly, we extend our heartfelt gratitude to Alexey Polilov (Figure 5), Corinna Herr (Figure 1C), Ed Oswalt (Figure 1F), Johan Pretorius (Figure 1D), Jonghyun Park (Figure 1B), Juho Paukkunen (Graphical Abstract and Figure 2), Manuel García-Viñó Sánchez (Figure 1A), Piotr Lukasik (Figure 1E), Roberto Keller (Figure 3B) and Stanislav Gorb (Figure 6) for generously granting permission to use their photographs in this manuscript. The images of the graphical abstract were adapted and reproduced from [11] (© 2015 J. Paukkunen et al., published by ZooKeys, distributed under the terms of the Creative Commons Attribution 4.0 International License, https://creativecommons.org/licenses/by/4.0).

Funding

This study was supported by the National Council for Scientific and Technological Development - CNPq (proc.142299/2020-0) and Minas Gerais State Research Support Foundation - FAPEMIG (proc. APQ-05401-23). RGF thanks CNPq (Proc. 312847/2022-0) for a productivity grant.

Conflict of Interest

There are no conflicts to declare.

Author Contributions

Vinicius Marques Lopez: conceptualization; investigation; visualization; writing – original draft; writing – review & editing. Carlo Polidori: conceptualization; investigation; visualization; writing – original draft; writing – review & editing. Rhainer Guillermo Ferreira: conceptualization; investigation; visualization; writing – original draft; writing – review & editing.

ORCID® iDs

Vinicius Marques Lopez - https://orcid.org/0000-0001-9445-6540
Carlo Polidori - https://orcid.org/0000-0003-4834-0752
Rhainer Guillermo Ferreira - https://orcid.org/0000-0001-7774-5252

Data Availability Statement

Data sharing is not applicable as no new data was generated or analyzed in this study.

References

1. Gorb, S. N. Insect-Inspired Technologies: Insects as a Source for Biomimetics. In *Insect Biotechnology;* Vilcinskas, A., Ed.; Springer Netherlands: Dordrecht, Netherlands, 2011; pp 241–264. doi:10.1007/978-90-481-9641-8_13
2. Han, Z.; Li, B.; Mu, Z.; Yang, M.; Niu, S.; Zhang, J.; Ren, L. *Nanoscale Res. Lett.* **2015,** *10,* 344. doi:10.1186/s11671-015-1052-7
3. Gorb, S. N.; Gorb, E. V. Aquatic Insects as a Source for Biomimetics. In *Aquatic Insects: Behavior and Ecology;* Del-Claro, K.; Guillermo, R., Eds.; Springer International Publishing: Cham, Switzerland, 2019; pp 401–426. doi:10.1007/978-3-030-16327-3_17
4. Chown, S. L.; Terblanche, J. S. Physiological Diversity in Insects: Ecological and Evolutionary Contexts. In *Advances in Insect Physiology;* Simpson, S. J., Ed.; Academic Press, 2006; Vol. 33, pp 50–152. doi:10.1016/s0065-2806(06)33002-0
5. Peters, R. S.; Krogmann, L.; Mayer, C.; Donath, A.; Gunkel, S.; Meusemann, K.; Kozlov, A.; Podsiadlowski, L.; Petersen, M.; Lanfear, R.; Diez, P. A.; Heraty, J.; Kjer, K. M.; Klopfstein, S.; Meier, R.; Polidori, C.; Schmitt, T.; Liu, S.; Zhou, X.; Wappler, T.; Rust, J.; Misof, B.; Niehuis, O. *Curr. Biol.* **2017,** *27,* 1013–1018. doi:10.1016/j.cub.2017.01.027
6. Aguiar, A. P.; Deans, A. R.; Engel, M. S.; Forshage, M.; Huber, J. T.; Jennings, J. T.; Johnson, N. F.; Lelej, A. S.; Longino, J. T.; Lohrmann, V.; Mikó, I.; Ohl, M.; Rasmussen, C.; Taeger, A.; Yu, D. S. K. *Zootaxa* **2013,** *3703,* 51–52. doi:10.11646/zootaxa.3703.1.12
7. Blaimer, B. B.; Santos, B. F.; Cruaud, A.; Gates, M. W.; Kula, R. R.; Mikó, I.; Rasplus, J.-Y.; Smith, D. R.; Talamas, E. J.; Brady, S. G.; Buffington, M. L. *Nat. Commun.* **2023,** *14,* 1212. doi:10.1038/s41467-023-36868-4
8. Grüter, C.; Menezes, C.; Imperatriz-Fonseca, V. L.; Ratnieks, F. L. W. *Proc. Natl. Acad. Sci. U. S. A.* **2012,** *109,* 1182–1186. doi:10.1073/pnas.1113398109
9. Corona, M.; Libbrecht, R.; Wheeler, D. E. *Curr. Opin. Insect Sci.* **2016,** *13,* 55–60. doi:10.1016/j.cois.2015.12.003
10. Hölldobler, B.; Wilson, E. O. *The Ants;* Harvard University Press, 1990.
11. Paukkunen, J.; Berg, A.; Soon, V.; Ødegaard, F.; Rosa, P. *ZooKeys* **2015,** *548,* 1–116. doi:10.3897/zookeys.548.6164
12. Wang, M. Y.; Hashmi, S. A.; Sun, Z. X.; Guo, D. L.; Vita, G.; Yang, G. W.; Hemida, H. *Acta Mech. Sin.* **2021,** *37,* 1090–1103. doi:10.1007/s10409-021-01099-7
13. Bearman, P. W.; Harvey, J. K. *Aeronaut. Q.* **1976,** *27,* 112–122. doi:10.1017/s0001925900007617

14. Domel, A. G.; Saadat, M.; Weaver, J. C.; Haj-Hariri, H.; Bertoldi, K.; Lauder, G. V. *J. R. Soc., Interface* **2018,** *15,* 20170828. doi:10.1098/rsif.2017.0828
15. Wu, Y.; Yang, L.; Xu, T.; Xu, H. *Micromachines* **2019,** *10,* 155. doi:10.3390/mi10020155
16. Mora-Castro, R.; Hernández-Jiménez, M.; Sáenz-Arce, G.; Porras-Peñaranda, J.; Hanson-Snortum, P.; Avendaño-Soto, E. *Sci. Rep.* **2020,** *10,* 1418. doi:10.1038/s41598-020-58301-2
17. Buxton, J. T.; Robert, K. A.; Marshall, A. T.; Dutka, T. L.; Gibb, H. *Myrmecol. News* **2021,** *31,* 31–46. doi:10.25849/myrmecol.news_031:031
18. Hellenbrand, J. P.; Penick, C. A. *Myrmecol. News* **2023,** *33,* 123–138. doi:10.25849/myrmecol.news_033:123
19. Amador, G. J.; Durand, F.; Mao, W.; Pusulri, S.; Takahashi, H.; Nguyen, V.-T.; Shimoyama, I.; Alexeev, A.; Hu, D. L. *Eur. Phys. J.: Spec. Top.* **2015,** *224,* 3361–3377. doi:10.1140/epjst/e2015-50094-x
20. Voigt, D.; Gorb, S.; Boevé, J.-L. *Zoology (Munich, Ger.)* **2011,** *114,* 265–271. doi:10.1016/j.zool.2011.05.004
21. Polidori, C.; Jorge, A.; Ornosa, C. *PeerJ* **2017,** *5,* e3300. doi:10.7717/peerj.3300
22. Jorge García, A.; Polidori, C.; Nieves-Aldrey, J. L. *Arthropod Struct. Dev.* **2016,** *45,* 311–319. doi:10.1016/j.asd.2016.05.001
23. Hines, H. M.; Witkowski, P.; Wilson, J. S.; Wakamatsu, K. *PLoS One* **2017,** *12,* e0182135. doi:10.1371/journal.pone.0182135
24. Badejo, O.; Skaldina, O.; Gilev, A.; Sorvari, J. *Oecologia* **2020,** *194,* 27–40. doi:10.1007/s00442-020-04738-1
25. Andrade, P.; Carneiro, M. *Biol. Lett.* **2021,** *17,* 20210221. doi:10.1098/rsbl.2021.0221
26. Kroiss, J.; Strohm, E.; Vandenbem, C.; Vigneron, J.-P. *Naturwissenschaften* **2009,** *96,* 983–986. doi:10.1007/s00114-009-0553-6
27. Sun, J.; Bhushan, B.; Tong, J. *RSC Adv.* **2013,** *3,* 14862–14889. doi:10.1039/c3ra41096j
28. Stavenga, D. G.; Kats, K.; Leertouwer, H. L. *J. Comp. Physiol., A* **2023,** *209,* 877–883. doi:10.1007/s00359-022-01592-9
29. Matin, T. R.; Leong, M. K.; Majlis, B. Y.; Gebeshuber, I. C. *AIP Conf. Proc.* **2010,** *1284,* 5–14. doi:10.1063/1.3515563
30. Hou, Z.; Cai, D.; Dong, R. *IEEE Access* **2024,** *12,* 57163–57171. doi:10.1109/access.2024.3389505
31. Stavenga, D. G. *Naturwissenschaften* **2023,** *110,* 22. doi:10.1007/s00114-023-01854-9
32. Liu, X.; Tian, Y.; Chen, F.; Ahlgren, R.; Zheng, Y.; Su, M.; Xiao, G.; Zheng, Y. *Sol. Energy Mater. Sol. Cells* **2022,** *234,* 111436. doi:10.1016/j.solmat.2021.111436
33. Li, C. Q.; Chen, H. T.; Mo, R. W.; Wang, J. N. *Sustainable Mater. Technol.* **2023,** *35,* e00574. doi:10.1016/j.susmat.2023.e00574
34. Chen, F.; Huang, Y.; Li, R.; Zhang, S.; Wang, B.; Zhang, W.; Wu, X.; Jiang, Q.; Wang, F.; Zhang, R. *Chem. Commun.* **2021,** *57,* 13448–13464. doi:10.1039/d1cc04386b
35. Kawamura, A.; Kohri, M.; Morimoto, G.; Nannichi, Y.; Taniguchi, T.; Kishikawa, K. *Sci. Rep.* **2016,** *6,* 33984. doi:10.1038/srep33984
36. Zyla, G.; Kovalev, A.; Grafen, M.; Gurevich, E. L.; Esen, C.; Ostendorf, A.; Gorb, S. *Sci. Rep.* **2017,** *7,* 17622. doi:10.1038/s41598-017-17914-w
37. Zyla, G.; Kovalev, A.; Heisterkamp, S.; Esen, C.; Gurevich, E. L.; Gorb, S.; Ostendorf, A. *Opt. Mater. Express* **2019,** *9,* 2630–2639. doi:10.1364/ome.9.002630
38. Huang, M.; Lu, S.-G.; Ren, Y.; Liang, J.; Lin, X.; Wang, X. *J. Text. Inst.* **2020,** *111,* 756–764. doi:10.1080/00405000.2019.1663623
39. Richards, A. G.; Richards, P. A. *Int. J. Insect Morphol. Embryol.* **1979,** *8,* 143–157. doi:10.1016/0020-7322(79)90013-8
40. Gorb, S. N. *J. Morphol.* **1997,** *234,* 1–10. doi:10.1002/(sici)1097-4687(199710)234:1<1::aid-jmor1>3.0.co;2-i
41. Duggan, A.; Garcıa-Añoveros, J.; Corey, D. P. *Curr. Biol.* **2000,** *10,* R384–R387. doi:10.1016/s0960-9822(00)00478-4
42. Keil, T. A. *Microsc. Res. Tech.* **1997,** *39,* 506–531. doi:10.1002/(sici)1097-0029(19971215)39:6<506::aid-jemt5>3.0.co;2-b
43. Darmanin, T.; Guittard, F. *Mater. Today* **2015,** *18,* 273–285. doi:10.1016/j.mattod.2015.01.001
44. Hu, H.-M. S.; Watson, G. S.; Cribb, B. W.; Watson, J. A. *J. Exp. Biol.* **2011,** *214,* 915–920. doi:10.1242/jeb.051128
45. Taylor, G. K.; Krapp, H. G. Sensory Systems and Flight Stability: What do Insects Measure and Why?. In *Advances in Insect Physiology;* Casas, J.; Simpson, S. J., Eds.; Insect Mechanics and Control, Vol. 34; Academic Press, 2007; pp 231–316. doi:10.1016/s0065-2806(07)34005-8
46. Beutel, R. G.; Vilhelmsen, L. *Org. Diversity Evol.* **2007,** *7,* 207–230. doi:10.1016/j.ode.2006.06.003
47. Wheeler, G. C.; Wheeler, J. *Mem. Entomol. Soc. Wash.* **1976,** *7,* 1–108.
48. Wang, Y.; Zuber, R.; Laudahn, A.; Berger, J.; Moussian, B. *Arthropod Struct. Dev.* **2017,** *46,* 108–115. doi:10.1016/j.asd.2016.12.003
49. Maiol, F. *Ann. Entomol. Soc. Am.* **1934,** *27,* 467. doi:10.1093/aesa/27.3.467
50. Wang, M.; Chen, W.; Zhao, J.; Yu, L.; Yan, S. *ACS Appl. Mater. Interfaces* **2021,** *13,* 24524–24531. doi:10.1021/acsami.1c05500
51. Shi, N. N.; Tsai, C.-C.; Camino, F.; Bernard, G. D.; Yu, N.; Wehner, R. *Science* **2015,** *349,* 298–301. doi:10.1126/science.aab3564
52. Wilson, J. S.; Sidwell, J. S.; Forister, M. L.; Williams, K. A.; Pitts, J. P. *Biol. Lett.* **2020,** *16,* 20200242. doi:10.1098/rsbl.2020.0242
53. Barrett, M.; O'Donnell, S. *PLoS One* **2023,** *18,* e0271250. doi:10.1371/journal.pone.0271250
54. Polidori, C.; Nieves-Aldrey, J. L. *PLoS One* **2014,** *9,* e101843. doi:10.1371/journal.pone.0101843
55. Jorge, A.; Polidori, C.; Nieves-Aldrey, J. L. *Zool. Anz.* **2019,** *283,* 213–230. doi:10.1016/j.jcz.2019.10.001
56. Polidori, C.; Jorge, A.; Ornosa, C. *Arthropod Struct. Dev.* **2020,** *57,* 100950. doi:10.1016/j.asd.2020.100950
57. Polidori, C.; Jorge, A.; Keller, A.; Ornosa, C.; Tormos, J.; Asís, J. D.; Nieves-Aldrey, J. L. *Org. Diversity Evol.* **2020,** *20,* 511–526. doi:10.1007/s13127-020-00448-x
58. Schofield, R. M. S.; Nesson, M. H.; Richardson, K. A. *Naturwissenschaften* **2002,** *89,* 579–583. doi:10.1007/s00114-002-0381-4
59. Nalini, E.; Polidori, C. *Eur. Zool. J.* **2024,** *91,* 601–611. doi:10.1080/24750263.2024.2355308
60. Wilson, E. O. *Behav. Ecol. Sociobiol.* **1980,** *7,* 157–165. doi:10.1007/bf00299521
61. Birkenfeld, V.; Gorb, S. N.; Krings, W. *Interface Focus* **2024,** *14,* 20230048. doi:10.1098/rsfs.2023.0048
62. Püffel, F.; Pouget, A.; Liu, X.; Zuber, M.; van de Kamp, T.; Roces, F.; Labonte, D. *J. R. Soc., Interface* **2021,** *18,* 20210424. doi:10.1098/rsif.2021.0424

63. Püffel, F.; Walthaus, O. K.; Kang, V.; Labonte, D. *Philos. Trans. R. Soc., B* **2023,** *378,* 20220547. doi:10.1098/rstb.2022.0547
64. Qi, H.; Ma, Z.; Xu, Z.; Wang, S.; Ma, Y.; Wu, S.; Guo, M. *Biomimetics* **2023,** *8,* 555. doi:10.3390/biomimetics8070555
65. Brito, T. O.; Elzubair, A.; Araújo, L. S.; de Souza Camargo, S. A.; Souza, J. L. P.; Almeida, L. H. *Mater. Res. (Sao Carlos, Braz.)* **2017,** *20,* 1525–1533. doi:10.1590/1980-5373-mr-2016-1137
66. Wipfler, B.; Hoepfner, O.; Viebahn, F.; Weihmann, T.; Rieg, F.; Engelmann, C. *Proc. Natl. Acad. Sci. U. S. A.* **2024,** *121,* e2201598121. doi:10.1073/pnas.2201598121
67. Wang, Z.; Zhan, Y.; Yang, Y.; Wu, J. *J. Insect Physiol.* **2022,** *141,* 104426. doi:10.1016/j.jinsphys.2022.104426
68. Zhao, S.; Zhang, D.; Yan, Y.; Yin, X. *Bioinspiration Biomimetics* **2023,** *18,* 056005. doi:10.1088/1748-3190/acece9
69. Hao, W.; Yao, G.; Zhang, X.; Zhang, D. *J. Phys.: Conf. Ser.* **2018,** *986,* 012029. doi:10.1088/1742-6596/986/1/012029
70. Zhang, W.; Wu, Z.; Wang, Z.; Wang, Z.; Li, C.; Rajabi, H.; Wu, J. *Bioinspiration Biomimetics* **2021,** *16,* 055003. doi:10.1088/1748-3190/ac124a
71. Klunk, C. L.; Argenta, M. A.; Casadei-Ferreira, A.; Economo, E. P.; Pie, M. R. *J. R. Soc., Interface* **2021,** *18,* 20210318. doi:10.1098/rsif.2021.0318
72. Brandão, C. R. F.; Diniz, J. L. M.; Tomotake, E. M. *Insectes Soc.* **1991,** *38,* 335–344. doi:10.1007/bf01241869
73. Ito, F. *Insectes Soc.* **1998,** *45,* 79–83. doi:10.1007/s000400050070
74. Tautz, J. Honeybees – a Model for Success. *The Buzz about Bees: Biology of a Superorganism;* Springer: Berlin, Heidelberg, 2008; pp 52–69. doi:10.1007/978-3-540-78729-7_5
75. Li, C.; Wu, J.; Yang, Y.; Zhu, R.; Yan, S. *J. Bionic Eng.* **2015,** *12,* 70–78. doi:10.1016/s1672-6529(14)60101-3
76. Li, C.-C.; Wu, J.-N.; Yang, Y.-Q.; Zhu, R.-G.; Yan, S.-Z. *J. Theor. Biol.* **2016,** *389,* 1–10. doi:10.1016/j.jtbi.2015.10.010
77. Kumar, R.; Kumar, N. R. *Apidologie* **2016,** *47,* 717–727. doi:10.1007/s13592-015-0423-5
78. Chen, Y.; Wu, J.; Yang, Y.; Yan, S. *J. Insect Behav.* **2020,** *33,* 71–82. doi:10.1007/s10905-020-09747-9
79. Wang, B.; Yang, J.; Zhang, J.; Ke, Z.; Zhang, H.; Yang, Y.; Wu, J. *Bioinspiration Biomimetics* **2023,** *18,* 016009. doi:10.1088/1748-3190/ac9fb3
80. Wu, J.; Chen, Y.; Li, C.; Lehnert, M. S.; Yang, Y.; Yan, S. *J. Exp. Biol.* **2019,** *222,* jeb212191. doi:10.1242/jeb.212191
81. Saccardi, L.; Brümmer, F.; Schiebl, J.; Schwarz, O.; Kovalev, A.; Gorb, S. *Beilstein J. Nanotechnol.* **2022,** *13,* 958–974. doi:10.3762/bjnano.13.84
82. Saccardi, L.; Schiebl, J.; Balluff, F.; Christ, U.; Gorb, S. N.; Kovalev, A.; Schwarz, O. *Biomimetics* **2023,** *8,* 579. doi:10.3390/biomimetics8080579
83. Land, M. F. *Annu. Rev. Entomol.* **1997,** *42,* 147–177. doi:10.1146/annurev.ento.42.1.147
84. Kirschfeld, K. *Z. Naturforsch., C: J. Biosci.* **1974,** *29,* 592–596. doi:10.1515/znc-1974-9-1023
85. Ma, Z.-C.; Hu, X.-Y.; Zhang, Y.-L.; Liu, X.-Q.; Hou, Z.-S.; Niu, L.-G.; Zhu, L.; Han, B.; Chen, Q.-D.; Sun, H.-B. *Adv. Funct. Mater.* **2019,** *29,* 1903340. doi:10.1002/adfm.201903340
86. Choi, C.; Lee, G. J.; Chang, S.; Song, Y. M.; Kim, D.-H. *ACS Nano* **2024,** *18,* 1241–1256. doi:10.1021/acsnano.3c10181
87. Cogal, O.; Leblebici, Y. *IEEE Trans. Biomed. Circuits Syst.* **2017,** *11,* 212–224. doi:10.1109/tbcas.2016.2547388
88. Davis, J. D.; Barrett, S. F.; Wright, C. H. G.; Wilcox, M. *Bioinspiration Biomimetics* **2009,** *4,* 046002. doi:10.1088/1748-3182/4/4/046002
89. Dai, B.; Zhang, L.; Zhao, C.; Bachman, H.; Becker, R.; Mai, J.; Jiao, Z.; Li, W.; Zheng, L.; Wan, X.; Huang, T. J.; Zhuang, S.; Zhang, D. *Nat. Commun.* **2021,** *12,* 6458. doi:10.1038/s41467-021-26606-z
90. Stürzl, W.; Boeddeker, N.; Dittmar, L.; Egelhaaf, M. *Bioinspiration Biomimetics* **2010,** *5,* 036002. doi:10.1088/1748-3182/5/3/036002
91. Roubieu, F. L.; Serres, J. R.; Colonnier, F.; Franceschini, N.; Viollet, S.; Ruffier, F. *Bioinspiration Biomimetics* **2014,** *9,* 036003. doi:10.1088/1748-3182/9/3/036003
92. Wittwer, B.; Hefetz, A.; Simon, T.; Murphy, L. E. K.; Elgar, M. A.; Pierce, N. E.; Kocher, S. D. *Proc. Natl. Acad. Sci. U. S. A.* **2017,** *114,* 6569–6574. doi:10.1073/pnas.1620780114
93. Ferrari, A.; Tacconi, G.; Polidori, C. *Sci. Rep.* **2024,** *14,* 8960. doi:10.1038/s41598-024-58804-2
94. Galvani, G. L.; González-Vaquero, R. A.; Guerra-Navarro, C.; Settembrini, B. P. *Apidologie* **2017,** *48,* 437–449. doi:10.1007/s13592-016-0486-y
95. Ayasse, M.; Paxton, R. J.; Tengö, J. *Annu. Rev. Entomol.* **2001,** *46,* 31–78. doi:10.1146/annurev.ento.46.1.31
96. Elgar, M. A.; Zhang, D.; Wang, Q.; Wittwer, B.; Thi Pham, H.; Johnson, T. L.; Freelance, C. B.; Coquilleau, M. *Yale J. Biol. Med.* **2018,** *91,* 457–469.
97. Gill, K. P.; van Wilgenburg, E.; Macmillan, D. L.; Elgar, M. A. *Am. Nat.* **2013,** *182,* 834–840. doi:10.1086/673712
98. Schott, M.; Wehrenfennig, C.; Gasch, T.; Vilcinskas, A. *Adv. Biochem. Eng./Biotechnol.* **2013,** *136,* 101–122. doi:10.1007/10_2013_210
99. Paek, J.; Cho, I.; Kim, J. *Sci. Rep.* **2015,** *5,* 10768. doi:10.1038/srep10768
100. Goettler, W.; Kaltenpoth, M.; Herzner, G.; Strohm, E. *Arthropod Struct. Dev.* **2007,** *36,* 1–9. doi:10.1016/j.asd.2006.08.003
101. Kaltenpoth, M.; Schmitt, T.; Polidori, C.; Koedam, D.; Strohm, E. *Physiol. Entomol.* **2010,** *35,* 196–200. doi:10.1111/j.1365-3032.2010.00729.x
102. Hedrick, T. L.; Combes, S. A.; Miller, L. A. *Can. J. Zool.* **2015,** *93,* 925–943. doi:10.1139/cjz-2013-0196
103. Schroeder, T. B. H.; Houghtaling, J.; Wilts, B. D.; Mayer, M. *Adv. Mater. (Weinheim, Ger.)* **2018,** *30,* 1705322. doi:10.1002/adma.201705322
104. Zhao, Y.; Wang, D.; Tong, J.; Sun, J.; Zhang, J. *Appl. Bionics Biomech.* **2018,** *2018,* e2014307. doi:10.1155/2018/2014307
105. Hasan, J.; Roy, A.; Chatterjee, K.; Yarlagadda, P. K. D. V. *ACS Biomater. Sci. Eng.* **2019,** *5,* 3139–3160. doi:10.1021/acsbiomaterials.9b00217
106. Ivanova, E. P.; Linklater, D. P.; Aburto-Medina, A.; Le, P.; Baulin, V. A.; Khuong Duy Nguyen, H.; Curtain, R.; Hanssen, E.; Gervinskas, G.; Hock Ng, S.; Khanh Truong, V.; Luque, P.; Ramm, G.; Wösten, H. A. B.; Crawford, R. J.; Juodkazis, S.; Maclaughlin, S. *J. Colloid Interface Sci.* **2021,** *603,* 886–897. doi:10.1016/j.jcis.2021.06.093
107. Shyy, W.; Kang, C.-k.; Chirarattananon, P.; Ravi, S.; Liu, H. *Proc. R. Soc. A* **2016,** *472,* 20150712. doi:10.1098/rspa.2015.0712
108. Sun, G.; Fang, Y.; Zhi, H.; Li, Z. *Chem. Res. Chin. Univ.* **2015,** *31,* 895–898. doi:10.1007/s40242-015-5023-4
109. Perrard, A. *Am. Nat.* **2020,** *195,* 181–191. doi:10.1086/706914

110. Mikó, I.; Copeland, R. S.; Balhoff, J. P.; Yoder, M. J.; Deans, A. R. *PLoS One* **2014,** *9,* e94056. doi:10.1371/journal.pone.0094056
111. Triapitsyn, S. V. *Ann. Zool. Fenn.* **2021,** *58,* 87–107. doi:10.5735/086.058.0109
112. Cheer, A. Y. L.; Koehl, M. A. R. *J. Theor. Biol.* **1987,** *129,* 17–39. doi:10.1016/s0022-5193(87)80201-1
113. Miller, L. A.; Peskin, C. S. *J. Exp. Biol.* **2005,** *208,* 195–212. doi:10.1242/jeb.01376
114. Jones, S. K.; Yun, Y. J. J.; Hedrick, T. L.; Griffith, B. E.; Miller, L. A. *J. Exp. Biol.* **2016,** *219,* 3759–3772. doi:10.1242/jeb.143362
115. Farisenkov, S. E.; Kolomenskiy, D.; Petrov, P. N.; Engels, T.; Lapina, N. A.; Lehmann, F.-O.; Onishi, R.; Liu, H.; Polilov, A. A. *Nature* **2022,** *602,* 96–100. doi:10.1038/s41586-021-04303-7
116. Jiang, Y.; Zhao, P.; Cai, X.; Rong, J.; Dong, Z.; Chen, H.; Wu, P.; Hu, H.; Jin, X.; Zhang, D.; Liu, H. *iScience* **2022,** *25,* 103692. doi:10.1016/j.isci.2021.103692
117. Lapina, N. A.; Farisenkov, S. E.; Petrov, P. N.; Polilov, A. A. *Entomol. Rev.* **2021,** *101,* 1126–1141. doi:10.1134/s001387382108008x
118. Ellington, C. P. *J. Exp. Biol.* **1999,** *202,* 3439–3448. doi:10.1242/jeb.202.23.3439
119. Burrows, M.; Dorosenko, M. *J. Exp. Biol.* **2017,** *220,* 3812–3825. doi:10.1242/jeb.161463
120. Polilov, A. A. Structure of the Principal Groups of Microinsects. VI. Trichogrammatid Wasps (Hymenoptera: Trichogrammatidae). In *At the Size Limit - Effects of Miniaturization in Insects;* Polilov, A. A., Ed.; Springer International Publishing: Cham, Switzerland, 2016; pp 201–232. doi:10.1007/978-3-319-39499-2_8
121. Ma, Y.; Ning, J. G.; Ren, H. L.; Zhang, P. F.; Zhao, H. Y. *J. Exp. Biol.* **2015,** *218,* 2136–2142. doi:10.1242/jeb.117325
122. Ma, Y.; Ren, H.; Rajabi, H.; Zhao, H.; Ning, J.; Gorb, S. *J. Insect Physiol.* **2019,** *118,* 103936. doi:10.1016/j.jinsphys.2019.103936
123. Eraghi, S. H.; Toofani, A.; Khaheshi, A.; Khorsandi, M.; Darvizeh, A.; Gorb, S.; Rajabi, H. *Adv. Sci.* **2021,** *8,* 2004383. doi:10.1002/advs.202004383
124. Michels, J.; Appel, E.; Gorb, S. N. *Arthropod Struct. Dev.* **2021,** *60,* 101008. doi:10.1016/j.asd.2020.101008
125. Snodgrass, R. E. *Anatomy of the Honey Bee;* Cornell University Press, 1956.
126. Gorb, S.; Beutel, R. *Naturwissenschaften* **2001,** *88,* 530–534. doi:10.1007/s00114-001-0274-y
127. Federle, W.; Labonte, D. *Philos. Trans. R. Soc., B* **2019,** *374,* 20190199. doi:10.1098/rstb.2019.0199
128. Endlein, T.; Federle, W. *Comp. Biochem. Physiol., Part A: Mol. Integr. Physiol.* **2009,** *153,* S138. doi:10.1016/j.cbpa.2009.04.252
129. Liang, L.; Zhao, J.; Niu, Q.; Yu, L.; Ma, Z.; Wu, X.; Wang, W.; Yan, S. *Mater. Today Bio* **2023,** *21,* 100704. doi:10.1016/j.mtbio.2023.100704
130. Orchard, M. J.; Kohonen, M.; Humphries, S. *J. Exp. Biol.* **2012,** *215,* 279–286. doi:10.1242/jeb.063339
131. Beutel, R. G.; Richter, A.; Keller, R. A.; Hita Garcia, F.; Matsumura, Y.; Economo, E. P.; Gorb, S. N. *J. Morphol.* **2020,** *281,* 737–753. doi:10.1002/jmor.21133
132. Endlein, T.; Federle, W. *PLoS One* **2015,** *10,* e0141269. doi:10.1371/journal.pone.0141269
133. Federle, W.; Riehle, M.; Curtis, A. S. G.; Full, R. J. *Integr. Comp. Biol.* **2002,** *42,* 1100–1106. doi:10.1093/icb/42.6.1100
134. Rebora, M.; Salerno, G.; Piersanti, S.; Saitta, V.; Gorb, E.; Gorb, S. N. *Front. Mech. Eng.* **2022,** *8*. doi:10.3389/fmech.2022.966429
135. Countryman, S. M.; Stumpe, M. C.; Crow, S. P.; Adler, F. R.; Greene, M. J.; Vonshak, M.; Gordon, D. M. *Front. Ecol. Evol.* **2015,** *3*. doi:10.3389/fevo.2015.00025
136. Engel, M. S.; Rasmussen, C. Corbiculate Bees. In *Encyclopedia of Social Insects;* Starr, C. K., Ed.; Springer International Publishing: Cham, Switzerland, 2021; pp 302–310. doi:10.1007/978-3-030-28102-1_30
137. Jander, R. *Physiol. Entomol.* **1976,** *1,* 179–194. doi:10.1111/j.1365-3032.1976.tb00960.x
138. Basibuyuk, H. H.; Quicke, D. L. J. *Zool. J. Linn. Soc.* **1999,** *125,* 349–382. doi:10.1111/j.1096-3642.1999.tb00597.x
139. Basibuyuk, H. H.; Quicke, D. L. J. *Zool. Scr.* **1995,** *24,* 157–177. doi:10.1111/j.1463-6409.1995.tb00397.x
140. Polidori, C.; Jorge, A.; Nieves-Aldrey, J. L. *Bull. Insectol.* **2022,** *75,* 97–116. http://www.bulletinofinsectology.org/pdfarticles/vol75-2022-097-116polidori.pdf
141. Hackmann, A.; Delacave, H.; Robinson, A.; Labonte, D.; Federle, W. *R. Soc. Open Sci.* **2015,** *2,* 150129. doi:10.1098/rsos.150129
142. Amador, G. J.; Matherne, M.; Waller, D.; Mathews, M.; Gorb, S. N.; Hu, D. L. *Bioinspiration Biomimetics* **2017,** *12,* 026015. doi:10.1088/1748-3190/aa5c6e
143. Evans, H. E. *Annu. Rev. Entomol.* **1966,** *11,* 123–154. doi:10.1146/annurev.en.11.010166.001011
144. Polidori, C.; Rubichi, A.; Barbieri, V.; Trombino, L.; Donegana, M. *Psyche* **2010,** *2010,* 851947. doi:10.1155/2010/851947
145. Giovanetti, M. *Neotrop. Entomol.* **2005,** *34,* 713–719. doi:10.1590/s1519-566x2005000500002
146. Coelho, J. R.; Holliday, C. W. *Ecol. Entomol.* **2008,** *33,* 403–407. doi:10.1111/j.1365-2311.2007.00981.x
147. Evans, H. E.; O'Neill, K. M. *The Sand Wasps: Natural History and Behavior;* Harvard University Press, 2007.
148. O'Neill, K. M. *Solitary Wasps: Behavior and Natural History;* Cornell University Press: Ithaca, NY, U.S.A., 2001. doi:10.7591/9781501737367
149. Xu, Z.; Qi, H.; Gao, P.; Wang, S.; Liu, X.; Ma, Y. *Biomimetics* **2024,** *9,* 358. doi:10.3390/biomimetics9060358
150. Cane, J. H. *J. Kans. Entomol. Soc.* **1991,** *64,* 406–413.
151. Wu, B.; Zhang, R.; Hou, P.; Tong, J.; Zhou, D.; Yu, H.; Zhang, Q.; Zhang, J.; Xin, Y. *Appl. Bionics Biomech.* **2021,** *2021,* 5113453. doi:10.1155/2021/5113453
152. Zhou, D.; Hou, P.; Xin, Y.; Wu, B.; Tong, J.; Yu, H.; Qi, J.; Zhang, J.; Zhang, Q. *Appl. Sci.* **2021,** *11,* 10480. doi:10.3390/app112110480
153. Eggleton, P.; Belshaw, R. *Philos. Trans. R. Soc., B* **1992,** *337,* 1–20. doi:10.1098/rstb.1992.0079
154. Oeser, R. *Mitt. Mus. Nat.kd. Berl., Zool. Reihe* **1961,** *37,* 3–119. doi:10.1002/mmnz.19610370102
155. Nénon, J.-P.; Kacem, N.; Lannic, J. L. *Can. Entomol.* **1997,** *129,* 789–799. doi:10.4039/ent129789-5
156. Huber, J.; Noyes, J. J. *Hymenopt. Res.* **2013,** *32,* 17–44. doi:10.3897/jhr.32.4663
157. Vilhelmsen, L. *Arthropod Struct. Dev.* **2003,** *32,* 277–287. doi:10.1016/s1467-8039(03)00045-8
158. Nakajima, K.; Schwarz, O. *Int. J. Des. Nat. Ecodyn.* **2014,** *9,* 177–189. doi:10.2495/dne-v9-n3-177-189
159. Polidori, C.; García, A. J.; Nieves-Aldrey, J. L. *PLoS One* **2013,** *8,* e70529. doi:10.1371/journal.pone.0070529
160. Quicke, D. L. J.; Wyeth, P.; Fawke, J. D.; Basibuyuk, H. H.; Vincent, J. F. V. *Zool. J. Linn. Soc.* **1998,** *124,* 387–396. doi:10.1111/j.1096-3642.1998.tb00583.x

161. Sprang, T.; Breedveld, P.; Dodou, D. Wasp-Inspired Needle Insertion with Low Net Push Force. In *Biomimetic and Biohybrid Systems;* Lepora, N. F.; Mura, A.; Mangan, M.; Verschure, P. F. M. J.; Desmulliez, M.; Prescott, T. J., Eds.; Springer International Publishing: Cham, Switzerland, 2016; pp 307–318. doi:10.1007/978-3-319-42417-0_28
162. Vincent, J. *Biomimetics* **2023,** *8,* 265. doi:10.3390/biomimetics8020265
163. Scali, M.; Kreeft, D.; Breedveld, P.; Dodou, D. Design and evaluation of a wasp-inspired steerable needle. In *Bioinspiration, Biomimetics, and Bioreplication 2017;* Knez, M.; Lakhtakia, A.; Martín-Palma, R. J., Eds.; SPIE, 2017; Vol. 10162, p 1016207. doi:10.1117/12.2259978
164. Cerkvenik, U.; van de Straat, B.; Gussekloo, S. W. S.; van Leeuwen, J. L. *Proc. Natl. Acad. Sci. U. S. A.* **2017,** *114,* E7822–E7831. doi:10.1073/pnas.1706162114
165. Gao, Y.; Ellery, A.; Jaddou, M.; Vincent, J.; Eckersley, S. *IEEE Trans. Aerosp. Electron. Syst.* **2007,** *43,* 875–885. doi:10.1109/taes.2007.4383580
166. Gouache, T. P.; Gao, Y.; Coste, P.; Gourinat, Y. *Planet. Space Sci.* **2011,** *59,* 1529–1541. doi:10.1016/j.pss.2011.06.019
167. Pitcher, C.; Gao, Y. *Adv. Space Res.* **2017,** *59,* 1368–1380. doi:10.1016/j.asr.2016.12.017
168. Alkalla, M.; Pang, X.; Pitcher, C.; Gao, Y. *Acta Astronaut.* **2021,** *182,* 131–143. doi:10.1016/j.actaastro.2021.02.007
169. Ma, Y.; Xiao, X.; Ren, H.; Meng, M. Q.-H. *Biomimetic Intell. Rob.* **2022,** *2,* 100064. doi:10.1016/j.birob.2022.100064
170. Fung-A-Jou, Z.; Bloemberg, J.; Breedveld, P. *Bioinspiration Biomimetics* **2023,** *18,* 041002. doi:10.1088/1748-3190/acd905
171. Makvandi, P.; Maleki, A.; Shabani, M.; Hutton, A. R. J.; Kirkby, M.; Jamaledin, R.; Fang, T.; He, J.; Lee, J.; Mazzolai, B.; Donnelly, R. F.; Tay, F. R.; Chen, G.; Mattoli, V. *Matter* **2022,** *5,* 390–429. doi:10.1016/j.matt.2021.11.021
172. Das, R.; Yadav, R. N.; Sihota, P.; Uniyal, P.; Kumar, N.; Bhushan, B. *Sci. Rep.* **2018,** *8,* 14945. doi:10.1038/s41598-018-33386-y
173. Černý, J.; Weyda, F.; Perlík, M.; Kodrík, D. *Microsc. Microanal.* **2022,** *28,* 1808–1818. doi:10.1017/s1431927622000800
174. Polidori, C.; Ruffato, G.; Borruso, L.; Settanni, C.; Pavan, G. *Bioacoustics* **2013,** *22,* 121–135. doi:10.1080/09524622.2012.736241
175. Chiu, Y.-K.; Mankin, R. W.; Lin, C.-C. *Ann. Entomol. Soc. Am.* **2011,** *104,* 1012–1020. doi:10.1603/an11027
176. Polidori, C.; Pavan, G.; Ruffato, G.; Asís, J. D.; Tormos, J. *Zool. Anz.* **2013,** *252,* 457–468. doi:10.1016/j.jcz.2013.01.003
177. Pekár, S.; García, L. F.; Bulbert, M. W. *Anim. Behav.* **2020,** *170,* 157–166. doi:10.1016/j.anbehav.2020.10.015
178. Masoni, A.; Frizzi, F.; Nieri, R.; Casacci, L. P.; Mazzoni, V.; Turillazzi, S.; Santini, G. *Sci. Rep.* **2021,** *11,* 5933. doi:10.1038/s41598-021-84925-z
179. Pavan, G.; Priano, M.; De Carli, P.; Fanfan, A.; Giovannoti, M. *Bioacoustics* **1997,** *8,* 209–221. doi:10.1080/09524622.1997.9753363
180. Torrico-Bazoberry, D.; Muñoz, M. I. *Rev. Chil. Entomol.* **2019,** *45,* 5–13.
181. Zhao, Y.-Z.; Du, L.-N.; Lu, C.-T.; Jin, Y.-G.; Ge, S.-P. *Int. J. Nanomed.* **2013,** *8,* 1621–1633. doi:10.2147/ijn.s43589
182. Ho, Y.-J.; Huang, C.-C.; Fan, C.-H.; Liu, H.-L.; Yeh, C.-K. *Cell. Mol. Life Sci.* **2021,** *78,* 6119–6141. doi:10.1007/s00018-021-03904-9
183. Pitt, W. G.; Husseini, G. A.; Staples, B. J. *Expert Opin. Drug Delivery* **2004,** *1,* 37–56. doi:10.1517/17425247.1.1.37
184. Luu, T.; Cheung, A.; Ball, D.; Srinivasan, M. V. *J. Exp. Biol.* **2011,** *214,* 2215–2225. doi:10.1242/jeb.050310
185. Zhao, J.; Yan, S.; Deng, L.; Huang, H.; Liu, Y. *J. Bionic Eng.* **2017,** *14,* 317–326. doi:10.1016/s1672-6529(16)60400-6
186. Zhao, J.; Huang, H.; Yan, S. *J. Appl. Phys.* **2017,** *121,* 094702. doi:10.1063/1.4977844
187. Caro, T.; Ruxton, G. *Trends Ecol. Evol.* **2019,** *34,* 595–604. doi:10.1016/j.tree.2019.02.015
188. Shih, C.; Feng, H.; Liu, C.; Zhao, Y.; Ren, D. *Ann. Entomol. Soc. Am.* **2010,** *103,* 875–885. doi:10.1603/an09043
189. Evans, H. E. *Evolution* **1962,** *16,* 468–483. doi:10.1111/j.1558-5646.1962.tb03237.x
190. Polidori, C.; Crottini, A.; Della Venezia, L.; Selfa, J.; Saino, N.; Rubolini, D. *Front. Zool.* **2013,** *10,* 36. doi:10.1186/1742-9994-10-36
191. Andrietti, F.; Polidori, C.; Casiraghi, M.; Bellati, A.; Passerini, E.; Martinoli, A. *Ann. Soc. Entomol. Fr.* **2013,** *49,* 205–221. doi:10.1080/00379271.2013.815041
192. Stetsun, H.; Rajabi, H.; Matushkina, N.; Gorb, S. N. *Arthropod Struct. Dev.* **2019,** *52,* 100882. doi:10.1016/j.asd.2019.100882
193. Andrietti, F.; Polidori, C. Carrying Unbalanced Weights in Hovering Flight: Effect of Prey Position on Load Maximization in Wasps. *Advances in medicine and biology;* Nova Science Publishers, 2012; Vol. 33, pp 75–98.
194. Vivallo, F. *Zool. J. Linn. Soc.* **2021,** *191,* 627–636. doi:10.1093/zoolinnean/zlaa069
195. Waldren, G. C.; Roberts, J. D.; Pitts, J. P. J. *Hymenopt. Res.* **2020,** *78,* 69–89. doi:10.3897/jhr.78.55762
196. Semple, T. L.; Vidal-García, M.; Tatarnic, N. J.; Peakall, R. *J. Evol. Biol.* **2021,** *34,* 1406–1422. doi:10.1111/jeb.13902
197. Richter, A.; Keller, R. A.; Rosumek, F. B.; Economo, E. P.; Hita Garcia, F.; Beutel, R. G. *Arthropod Struct. Dev.* **2019,** *49,* 26–49. doi:10.1016/j.asd.2019.02.002
198. Jacinavicius, F. C.; Silva, R. A.; Bassini-Silva, R.; Lopez, V. M.; Silvestre, R.; Khaustov, A. A. *Acarina* **2018,** *26,* 167–174. doi:10.21684/0132-8077-2018-26-2-167-174
199. Klimov, P. B.; Vinson, S. B.; OConnor, B. M. *Invertebr. Syst.* **2007,** *21,* 109–136. doi:10.1071/is06019
200. Pereira, M. C. S. A.; Hermes, M. G.; Bernardi, L. F. O. *J. Nat. Hist.* **2018,** *52,* 3017–3038. doi:10.1080/00222933.2019.1568602
201. de Freitas Bueno, A.; Sutil, W. P.; Maciel, R. M. A.; Roswadoski, L.; Colmenarez, Y. C.; Colombo, F. C. *Biol. Control* **2023,** *186,* 105344. doi:10.1016/j.biocontrol.2023.105344
202. Pijnakker, J.; Hürriyet, A.; Petit, C.; Vangansbeke, D.; Duarte, M. V. A.; Arijs, Y.; Moerkens, R.; Sutter, L.; Maret, D.; Wäckers, F. *Insects* **2022,** *13,* 1146. doi:10.3390/insects13121146
203. Argolo, P. S.; Revynthi, A. M.; Canon, M. A.; Berto, M. M.; Andrade, D. J.; Döker, İ.; Roda, A.; Carrillo, D. *Biol. Control* **2020,** *149,* 104330. doi:10.1016/j.biocontrol.2020.104330

License and Terms

This is an open access article licensed under the terms of the Beilstein-Institut Open Access License Agreement (https://www.beilstein-journals.org/bjnano/terms), which is identical to the Creative Commons Attribution 4.0 International License (https://creativecommons.org/licenses/by/4.0). The reuse of material under this license requires that the author(s), source and license are credited. Third-party material in this article could be subject to other licenses (typically indicated in the credit line), and in this case, users are required to obtain permission from the license holder to reuse the material.

The definitive version of this article is the electronic one which can be found at:
https://doi.org/10.3762/bjnano.15.107

BEILSTEIN JOURNAL OF NANOTECHNOLOGY

Bioinspired nanofilament coatings for scale reduction on steel

Siad Dahir Ali[‡1], Mette Heidemann Rasmussen[‡1], Jacopo Catalano[2], Christian Husum Frederiksen[3] and Tobias Weidner[*1]

Full Research Paper

Open Access

Address:
[1]Department of Chemistry, Aarhus University, 8000 Aarhus C, Denmark, [2]Department of Biological and Chemical Engineering, Aarhus University, 8000 Aarhus C, Denmark and [3]Danish Offshore Technology Centre, Danish Technical University, 2800 Kongens Lyngby, Denmark

Email:
Tobias Weidner[*] - weidner@chem.au.dk

* Corresponding author ‡ Equal contributors

Keywords:
bioinspired materials; calcium carbonate; offshore assets; stainless-steel coating; super-hydrophobicity

Beilstein J. Nanotechnol. **2025,** *16,* 25–34.
https://doi.org/10.3762/bjnano.16.3

Received: 12 June 2024
Accepted: 16 December 2024
Published: 09 January 2025

This article is part of the thematic issue "Biomimetics and bioinspired surfaces: from nature to theory and applications".

Guest Editor: R. Guillermo

© 2025 Ali et al.; licensee Beilstein-Institut.
License and terms: see end of document.

Abstract

Scaling of steel surfaces, prevalent in various industrial applications, results in significant operational inefficiencies and maintenance costs. Inspired by the natural hydrophobicity of springtail (Collembola) skin, which employs micro- and nanostructures to repel water, we investigate the application of silicone nanofilaments (SNFs) as a coating on steel surfaces to mitigate scaling. Silicone nanofilaments, previously successful on polymers, textiles, and glass, are explored for their hydrophobic properties and stability on steel. Our study demonstrates the successful coating of stainless steel with SNFs, achieving super-hydrophobicity and resilience under high shear stress and explosion/decompression tests. Scaling experiments reveal a 75.5% reduction in calcium carbonate deposition on SNF-coated steel surfaces. This reduction is attributed to altered flow dynamics near the super-hydrophobic surface, inhibiting nucleation and growth of scale. Our findings highlight the potential of bioinspired SNF coatings to enhance the performance and longevity of steel surfaces in industrial environments.

Introduction

Small animals, such as insects, springtails (Collembola), and other hexapods, have distinctly large surface-to-volume ratios. This characteristic imposes significant challenges in terms of moisture control and water interaction [1,2]. The structure and chemistry of insect skin are finely tuned to navigate these challenges, showcasing a sophisticated natural adaptation to efficiently repel water [3]. Springtails have mastered this capability using micro- and nanostructured skin surfaces, which serve as a barrier against unwanted wetting [4,5]. Collembola breathe through their skin and, since they live in humid environments, need to retain air near their skin for survival in diverse habitats [6] (Figure 1A,B).

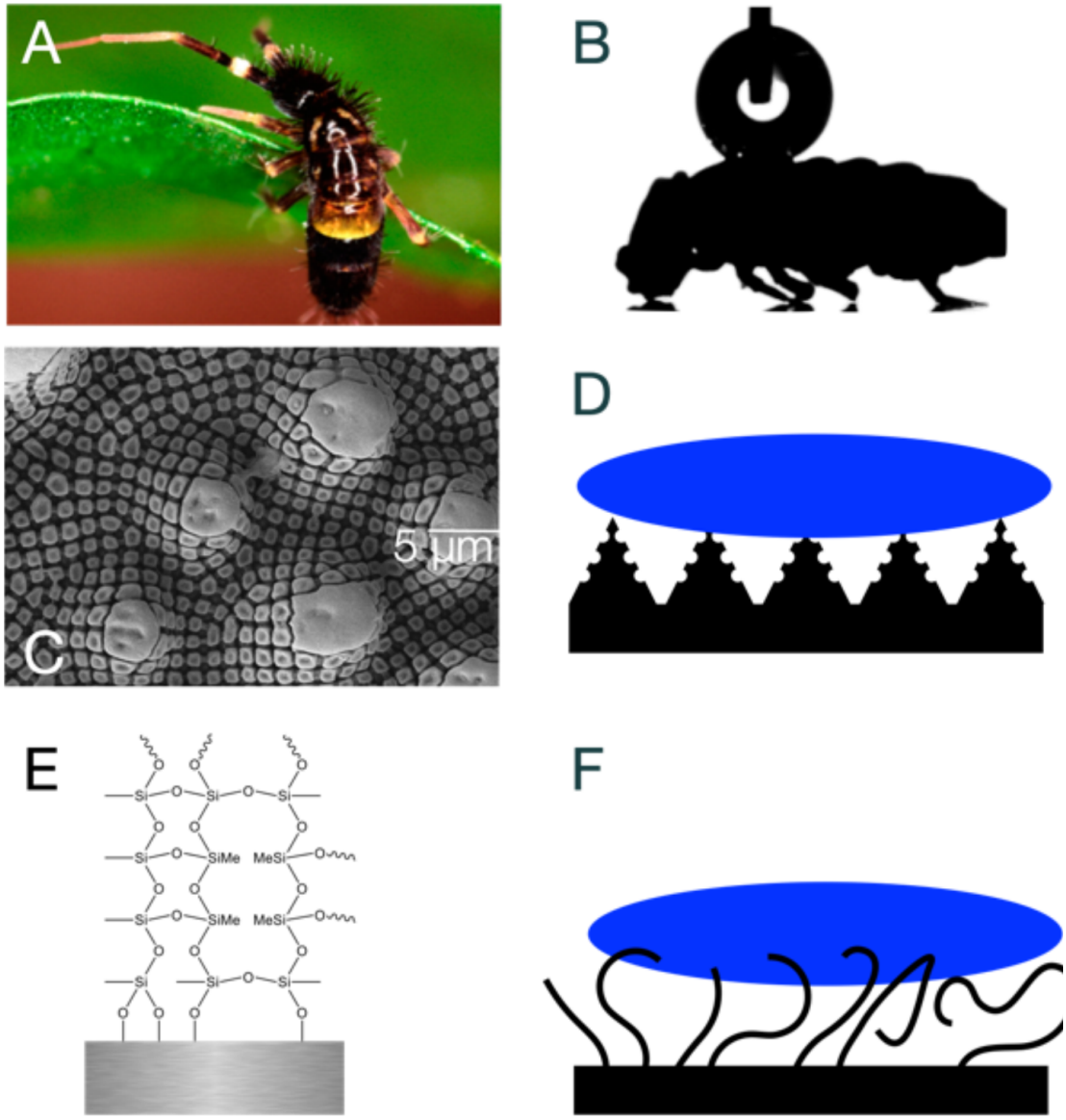

Figure 1: Bioinspired SNF coatings. (A) Springtails (Collembola) have micro- and nanostructured skin for effective water repellence. (B) High water contact angle on Collembola cuticle demonstrates natural super-hydrophobicity. (C,D) Multiscale structuring of the Collembola skin renders the surface hydrophobic [5]. (E) SNFs consist of silicone structure, which polymerize and grow on the surface. (F) SNF coating on steel mimics the multiscale springtail structuring. The coating decorates the surface with a water-repelling wire-like structure, which has been shown to be super-hydrophobic when bound to polymer, glass, and textiles. Figure 1A was adapted with permission from [5], Copyright 2020 American Chemical Society. This content is not subject to CC BY 4.0.

Drawing inspiration from Collembola, our study delves into the potential applications of mimicking the liquid-repelling properties of their skin to address a common industrial challenge: The scaling of steel surfaces. Scaling, a pervasive issue in various industries, results from unwanted water adhesion and mineral deposition, leading to corrosion, reduced efficiency, and increased maintenance costs. By understanding and replicating the nanostructured [3,7-9], liquid-repelling features of Collembola skin, we propose a novel approach to mitigate this issue. Figure 1 displays the cuticle micro- and nanostructure which leads to effective water repellency [5]. It has been shown how the multiscale structuring, from micron-sized hair-like structures all the way to nanometer-scale spikes and indentations can maintain the layer of air between the cuticle and water, which is needed for Collembola survival (Figure 1C,D).

Inspired by the intricate nanostructures found on Collembola skin, we fabricate silicone nanofilaments (SNFs) on steel sur-

faces. Here, the surface is coated by immersion of the surface in a solution of trichloromethylsilane (TCMS) in toluene in the presence of trace amounts of water (Figure 1E). This way, the surface is covered with a micrometer-thin layer of hard, stable SNFs. These filaments have been developed for coatings on polymers [10-12], textiles [12-17], aluminium and titanium [11,12], and glass [11-13,18,19], to replicate the water-repelling effects observed in nature [13,18,20,21]. Coatings with nano- or micrometer-sized protrusions that have an overhanging shape and low surface energy can effectively render a surface super-hydrophobic (Figure 1D,F). This texture creates an energy barrier, causing water droplets to rest on the protrusions while trapping air beneath them. In analogy with the texture of Collembola skin, this phenomenon, known as the Cassie state, results in the liquid being more in contact with air than with the solid surface, leading to high apparent contact angles [22]. The high contact angles also become apparent in Figure 1B, where a water droplet is resting on the Collembola surface.

Here, we explore the stability and hydrophobicity of these bioinspired nanofilaments on steel, a key material for industrial antiscaling applications that has not been investigated in this context. We test whether SNF coatings can prevent scaling of steel surfaces. In the following session, we describe a reliable procedure to coat stainless steel (Type 316) with nanofilaments, discuss stability test of the coatings, and the results of scaling experiments.

Results and Discussion

Nanofilamant performance and stability on steel

Shear stress test of SNF coatings on steel

Previous applications of SNF technology have been focused on materials with surface chemistries with polar functional groups and particularly hydroxy groups. To coat surfaces with a layer of SNFs, samples are immersed in a solution of trichloromethylsilane (TCMS) in toluene, in the presence of trace amounts of water (see Materials Section for details). After a reaction time of six hours, the surface is coated with a micrometer layer of SNFs. The surface reaction is proceeded by hydrolysis of TCMS due to water in the solvent. Subsequently, hydrolyzed TCMS molecules react with surface hydroxy moieties at the interface and thereby induce the polymerization of a polysiloxane on the material surface [18]. The polysiloxane methyl groups lower the surface energy and render the surface hydrophobic.

Clearly, the surface chemistry of steel surfaces is very different from the previously used materials such as glass [11-13,18], polymers [10-12], and textiles [11-16] as it does not offer the hydroxy moieties used previously for direct surface polymerization. It is therefore important to carefully test the stability and attachment of any SNFs growing on steel surfaces. Mechanical scratching of the coated steel surface will damage the coating visibly. Yet, most paintings and coatings will sustain damage when mechanically scratched. To evaluate shear stability under realistic operating conditions, we constructed a medium-temperature, medium-pressure, constant shear stress device (Figure 2A and Figure 2B). Our design is an adapted version of a cone-plate rheometer. Different from a classical design, we have iteratively optimized the design of the rotating truncated cone to provide a near-uniform shear stress at the static plate surface, where the SNF-coated samples are located (Figure 2C and Figure 2D). The tests of SNF coatings on steel were conducted under conditions relevant to oil production, which represents one of the most challenging applications for steel coatings. Specifically, the tests were performed in a 3 wt % toluene/water emulsion at a pressure of 70 bar and a temperature of 100 °C, with shear stresses at the plate corresponding to the flow of oil/water equivalent to 10,000 barrels per day in a 4-inch nominal steel pipe. Figure 2C shows a simulation of the fluid streamlines and shear stress on the samples matching the shear stress value in a 4-inch pipe at a flow rate of 10,000 barrels per day. The shear stress at the plate is reported in Figure 2D for different angular velocities and corresponding volumetric flow rates.

Super-hydrophobicity of SNF coatings on steel

Figure 3A shows a scanning electron microscopy (SEM) image of a stainless-steel surface coated with SNFs. The wire-type structures expected for SNF coating are clearly visible from a coated steel surface. Figure 3B and Figure 3C show the images of the measured angle of the coated and uncoated steel surfaces. The related atomic composition of the coating was analyzed by energy-dispersive X-ray spectroscopy (EDX) for both coated steel surfaces. The elemental composition in Figure 4B shows the silicon emission expected for the SNF film, which is not present on the bare steel surface. Oxygen and carbon, additional components of the SNF coating, are also detected for the SNFs. At the same time, these elements are also observed on the bare steel substrate and the elemental composition of the SNFs is difficult to disentangle.

The contact angle of the uncoated surfaces was 71°. The contact angle of the SNF-coated surfaces is more difficult to measure as the droplet will not attach itself to the surface seen for Figure 3B and Figure 5D, in agreement with what has been reported before for super-hydrophobic SNF coatings on polymers [18], glass [23], and textiles [16]. Since the water contact is well above 150° and droplets are highly mobile (please see the videos in the Supporting Information File 1–3) – the defini-

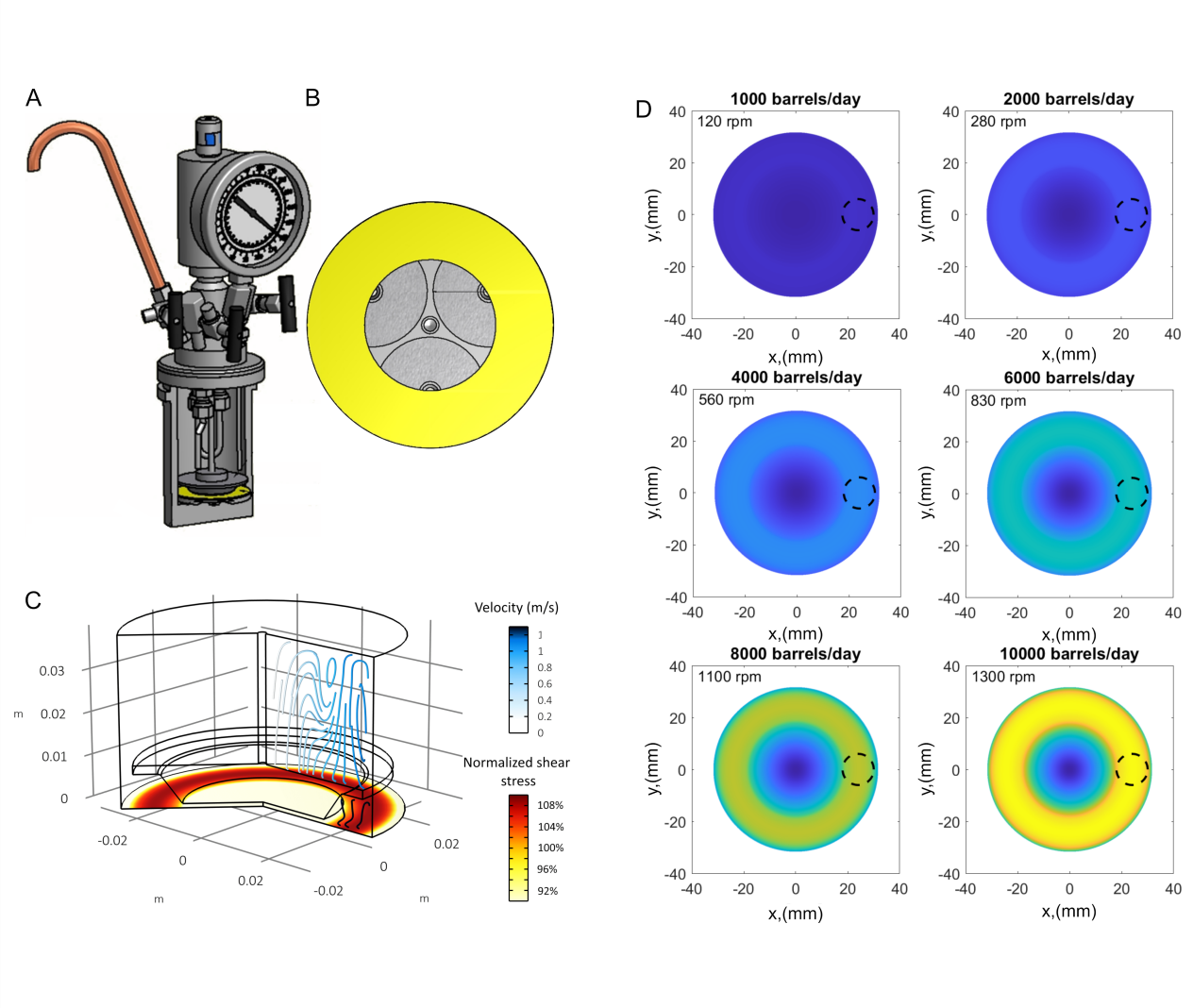

Figure 2: (A) Rendering of medium-pressure, medium-temperature, constant sheer stress device. Maximum operating temperature of 200 °C and maximum pressure of 200 bar. The liquid phase is pressurized via an inert gas (e.g., Ar or N_2). (B) Top view of the static plate where three samples are mounted; around half of the surface area for each sample is exposed at constant sheer stress. (C) Steady state simulation of the velocity profile (reported as streamlines) and normalized sheer stress at the plate (contour plot). This latter parameter is normalized with respect to the sheer stress value calculated for a flow in a 4-inch nominal pipe at a volumetric flow of 10,000 barrels per day and 100 °C. (D) Contour plots of the shear stress at the plate for different rotational speeds and respective values of volumetric flows for a 4-inch pipe. The circled area represents the region of constant-sheer stress.

tion of super-hydrophobicity – we can conclude that nanofilaments can be deposited on steel surfaces and that the grown structures render the steel surface super-hydrophobic [24].

The morphology and function of the SNF steel coatings remain intact during the shear stress test. The SEM image of the SNF coating after shear exposure in Figure 4A shows no damage of ablation of the structure. This is also supported by the EDX analysis, which shows that the composition is not changed within the error margins as the amount of oxygen and silicone remains constant in Figure 4B. The water contact angle (Figure 4C) is reduced a bit from the original value to 146 ± 3°, still at the limit to super-hydrophobicity.

To further test the coating stability, we also performed an explosion/decompression test after NACE TM0185, a standardized industry test of coating delamination. Here, the samples are pressurized in the autoclave and the pressure is quickly released after 24 hours at 100 °C and 100 bar. The pressure is reduced to 50 bar over a period of five minutes and afterwards the pressure is reduced to ambient pressure over a period of ten minutes. Any blisters or cracks in the coating indicate delamination or mechanical failure. As can be seen in in the optical images in Figure 5A and Figure 5B, no defects are visible after the explosion/decompression test, demonstrating the stability of the SNF coating on steel. This is also borne out by the SEM analysis (Figure 5C), which shows the SNF structures are fully

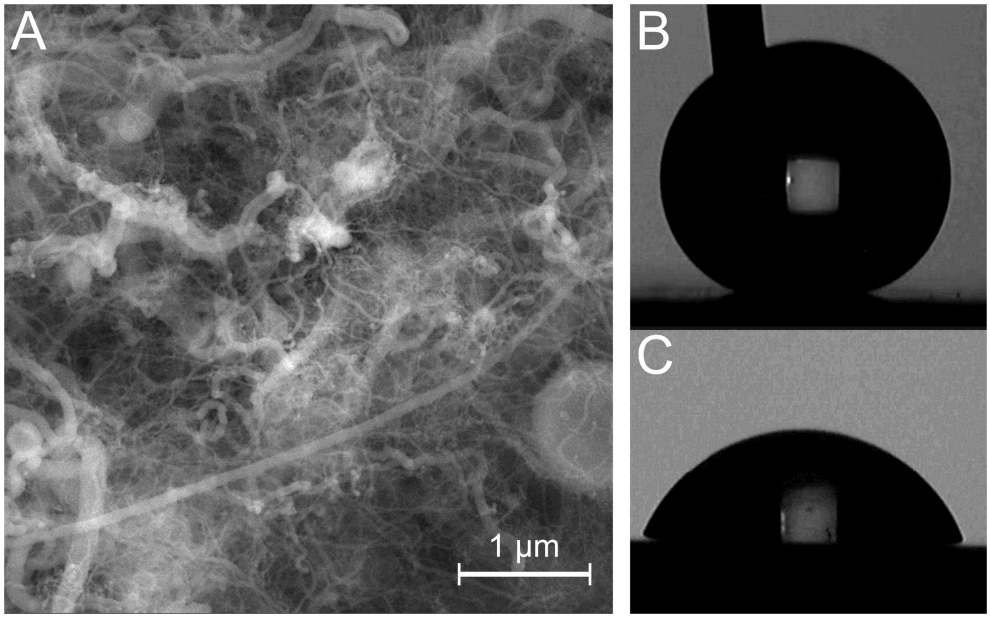

Figure 3: (A) SEM image of the coated surface. A network of SNFs with different width and diameters is visible. (B,C) Water contact angle measurements for the coated and uncoated samples.

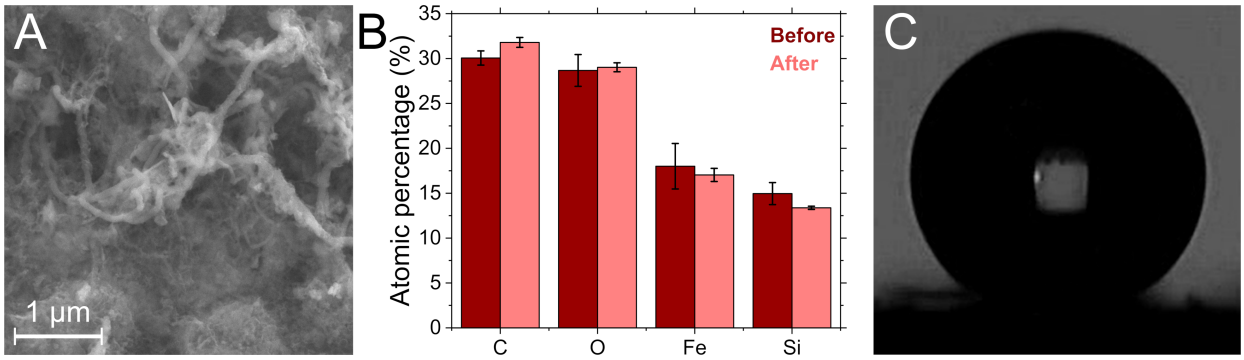

Figure 4: (A) SEM image of the SNF coating after the shear stress test. The SNF coating is still visible. (B) Composition of the SNF-coated steel before and after the shear stress test based on EDX analysis. (C) Image showing the contact angle measurement of the sample after the shear stress test. The coating is still water repelling.

intact after the test. The water contact angle also remains unchanged after the decompression/explosion test (Figure 5D).

Scale reduction on SNF-coated steel surfaces

The scaling of SNF samples was tested in a flow loop designed for the observation of calcium carbonate scaling at surfaces. Coated and uncoated steel surfaces where mounted in the sample holder within the test loop (see Methods Section for details) and exposed to a sequence of solutions. First, a solution of synthetic seawater and 3% texatherm oil was used to prime the samples. Then, a supersaturated solution of sodium carbonate and calcium chloride was added to the flow. After three hours, the samples were briefly rinsed with water in the flow loop, retrieved from the sample holder, and then dried in an oven at 80 °C. Figure 6A shows photos of coated and uncoated steel surfaces taken before and after exposure to the flow loop. While the uncoated sample shows significant scaling, small amounts of deposits are visible by the naked eye on the SNF-coated sample. This is also visible in the SEM images shown in Figure 6B. An EDX analysis of the scale clearly shows that the grown deposits mainly consist of calcium carbonate (Figure 6C). For a quantitative analysis of the extent of scaling, the samples were weighed before and after exposure to the scaling experiment.

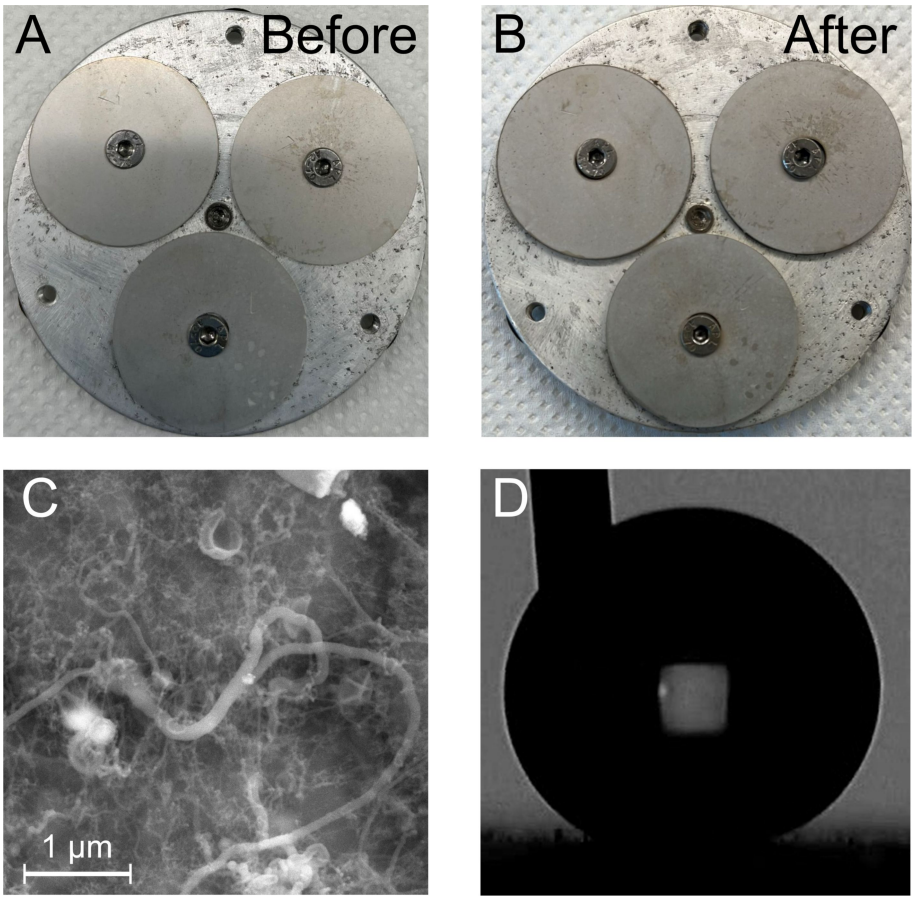

Figure 5: (A,B) Photos of the samples before and after the explosion/decompression test. The samples are still intact after the test, no delamination is visible on the samples. (C) SEM image of an SNF surface coating after the decompression/explosion test. No changes of the filament structure are discernible. (D) The water contact angle after the test shows that that coating is still functional after the test.

The results are summarized in Figure 6D. The gravimetric analysis shows that without the coating, the samples gained 16.3 ± 2.7 mg of calcium carbonate, while SNF-coated samples gained only 4.0 ± 1.5 mg. This corresponds to a scale reduction of 75.5% by the SNF coating.

Ostensibly, the non-wetting properties of the SNF films prevent attachment and growth of scale. Calcium carbonate scale formation starts with crystallization nuclei, small clusters of ions which can homogeneously form in the bulk solution or heterogeneously on material surface [25]. Once nucleation occurs, calcium carbonate crystals start to grow. The growth process involves the continuous deposition of Ca^{2+} and CO_3^{2-} ions onto the surface-bound nuclei. Over time, these crystals increase in size and adhere more strongly to the steel surface and individual crystals coalesce to form larger, continuous scale layers. While it is unclear how, in detail, an SNF coating can affect the scale growth process, we hypothesize that the flow characteristics near the surface play an important role. While at regular solid–liquid interfaces, the flow velocity is assumed to be zero when modeling viscous drag, on super-hydrophobic surfaces the shear is reduced, leading to slip of the liquid across the surfaces and a non-zero flow velocity [26]. Flow at the material interface can hinder or prevent settling, nucleation, and growth of calcium carbonate scale at the interface.

Conclusion

In conclusion, our study demonstrates the potential of biomimetic approaches to address the industrial challenge of scaling on steel surfaces. By drawing inspiration from the unique water-repelling properties of Collembola skin, we have fabricated silicone nanofilaments on steel surfaces, a novel application that has not been previously reported. The results indicate that SNF coatings can effectively render steel surfaces super-hydrophobic, as evidenced by high contact angles, high droplet mobility, and stable morphology under shear stress and explosion/decompression tests.

Furthermore, SNF-coated steel surfaces exhibited a marked reduction in calcium carbonate scaling compared to uncoated

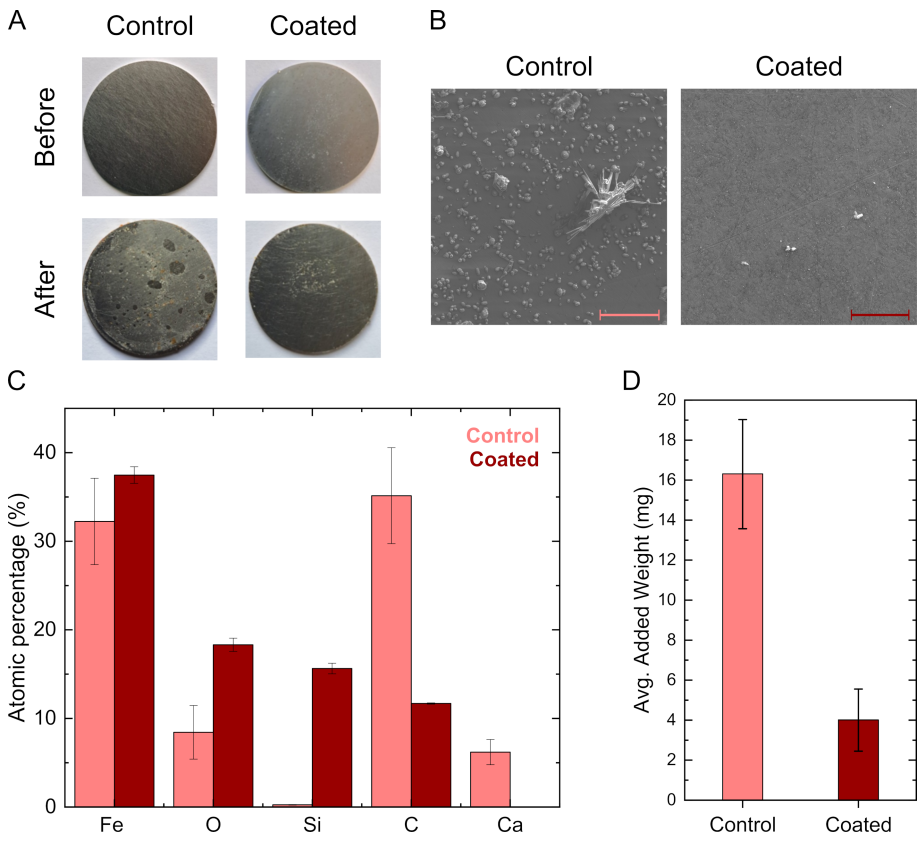

Figure 6: (A) Photos of the stainless-steel samples before and after experiments for the control and coated samples. (B) SEM images of the control and coated stainless-steel samples after the scale experiments. The scale bar depicts 200 µm. (C) Comparison of the relevant elements on the samples after the scale experiments measured with EDX. (D) Averaged added weight on the samples after the scale experiments.

surfaces. This finding demonstrates the effectiveness of SNF coatings in mitigating scale formation, which is a significant challenge in the food industry, household appliances, and oil production. The structural integrity under harsh conditions further underpins the potential for industrial antiscaling solutions.

Methods Section

Coating procedure

The coating solution was prepared with 100 mL of toluene (108-88-3, VWR) with a water content between 250–300 ppm and mixing 0.8 mL trichloromethylsilane (75-79-6, Sigma-Aldrich) into the toluene. The water content was measured with a Karl-Fischer volumetric titration setup. The solvent used for the coating is prepared by mixing oversaturated toluene (>400 ppm) with toluene from the vendor (<200 ppm). The SNF coating is based on a dip coating, where the mixture is strongly stirred with the syringe for 40 seconds. The stainless-steel samples were quickly added to the chamber whose lid was sealed with Parafilm and the reaction was left to run for three hours. The procedure was repeated two times for a total of six hours of coating. For the results presented here, the water content in toluene was between 290–300 ppm. A coating with lower and higher amounts of water in the solvent is feasible, however, a less uniform coating will be obtained. Before the coating procedure the stainless-steel samples were cleaned by sonication for five minutes in toluene, acetone, and Milli-Q water, and the samples were rinsed with the solvent following in the sequence before each sonication step. Finally, the samples were dipped into ethanol and dried. The samples were washed in toluene, acetone and Milli-Q water, toluene, and dried after the first three hours of coating. When the coating was finished after a total of six hours, the samples were washed in toluene and left in Milli-Q water for approximately 12 hours. The last washing step ensures that all produced HCl is removed from the coating which will otherwise induce corrosion of the samples.

Scanning electron microscopy and energy-dispersive X-ray spectroscopy measurements

Scanning electron microscopy images were acquired in a TESCAN CLARA (S8151) using the ANALYSIS and the UH-resolution scan mode with an accelerator voltage of

15 keV and 10 keV, a beam current of 300 pA, and a working distance of ≈10 mm and ≈7 mm in high-vacuum mode (pressure < 0.04 Pa). The SEM images were collected using an in-chamber Everhart−Thornley detector which identifies secondary electrons.

Contact angle measurements

The measurements were performed by the sessile drop method using an FTA1000 contact angle system (First Ten Angstroms, Inc.) at ambient temperature. The volume of the water droplets was 2.5–3.0 μL.

Autoclave stability and decompression/explosion tests

The autoclave (Parr series 5521) is based on a 300 mL vessel and reactor controller (4848, Parr). A home-build disc and sample holder was used. The sample holder is stationary and was placed at the bottom of the reactor chamber with the disc mounted on a spring to ensure that the distance between the disc and the samples was 1 mm. The shape of the disc is described in the text and gave a shear stress that mimics the condition offshore. The rotation of the disc was controlled by an RPM-meter, which was based on a teensy 3.6 microcontroller which scans a plate with 18 slots directly mounted on the reactor shaft. The signal was detected using library code and the RPM was subsequently calculated and shown on an LCB display.

The stability test experiments were run at 70 °C and 100 bar using pressurized argon and 700 RPM corresponding to 5000 bbl/day. The stability test has ben previously run at 300, 700, and 1300 RPM which corresponds to approx. 2000, 5000, and 10000 bbl/day, respectively. The disc and the sample holder were cleaned by rinsing in acetone, Milli-Q water, acetone, and afterwards left to air dry. The samples were placed in the sample holder and 100 mL of a mixture of 3 mL toluene and 97 mL Milli-Q water were added to the reaction chamber. The chamber was sealed and, after reaching the desired pressure and temperature, the experiment ran for three hours. The experiment was ended by releasing the pressure. The vessel was then placed in an ice water bath to lower the temperature to room temperature.

For the decompression/explosion test, the reaction chamber was cleaned by rinsing in acetone, Milli-Q water, acetone, and afterwards left to air dry. The samples were placed in the sample holder and a methane flask was attached to the reaction chamber and the pressure was set to 100 bar with a temperature of 100 °C. When the settings were reached, the experiment ran for 24 hours. The experiments commenced in two steps with the temperature kept at 100 °C. First, the pressure was reduced from 100 bar to 50 bar over a period of five minutes, and secondly the pressure was reduced from 50 bar to 1 bar over a period of ten minutes. Finally, the reaction chamber was placed in an ice water bath to lower the temperature to room temperature.

Scale experiments

All samples were weighed and photographed prior to testing. The samples were then loaded onto the sample holder, and a solution of synthetic seawater and 3% oil was flushed through the sample holder to prime the samples for three minutes. Synthetic seawater (pH 6), containing calcium carbonate, was pumped from one tank while soda ash (pH 11), containing sodium carbonate, was pumped from another tank. The solution had pH 9, leading to the formation of calcium carbonate. The flow rate was maintained at 0.88 L/min and the experiment was conducted for three hours at room temperature. After three hours, the suction line was switched to demineralized water and the samples were rinsed for three minutes to remove all loose particles.

The sample holder with loaded samples was dried in an oven at 80 °C. The samples were weighed, and photos were taken afterwards.

Supporting Information

The Supporting Information features three different contact angle videos.

Supporting Information File 1

Contact angle of the coated sample before the stability test.
[https://www.beilstein-journals.org/bjnano/content/supplementary/2190-4286-16-3-S1.wmv]

Supporting Information File 2

Contact angle of the coated sample after the stability test.
[https://www.beilstein-journals.org/bjnano/content/supplementary/2190-4286-16-3-S2.wmv]

Supporting Information File 3

Contact angle of the coated sample after the decompression/explosion test.
[https://www.beilstein-journals.org/bjnano/content/supplementary/2190-4286-16-3-S3.wmv]

Acknowledgements

M.H.R and S.D.A thank Rebekka Klemmt for help and training using the SEM. We thank Steen U. Pedersen and Kim Daasbjerg for help with contact angle experiments.

Funding

The Carlsberg Foundation (Grant no: CF20-0364) and iMAT are acknowledged for funding of the TESCAN CLARA SEM. We thank the Innovation Foundation Denmark for funding within the INNO-CCUS consortium (project grant CORROPro). The DTU Offshore Technology Center is gratefully acknowledged for funding (DTU/AU_CSP.3.D.02_CA_298).

Author Contributions

Siad Dahir Ali: conceptualization; data curation; formal analysis; methodology. Mette Heidemann Rasmussen: conceptualization; data curation; formal analysis; investigation; writing – original draft. Jacopo Catalano: investigation; methodology; resources; supervision; writing – original draft. Christian Husum Frederiksen: conceptualization; funding acquisition; methodology; project administration; supervision. Tobias Weidner: conceptualization; funding acquisition; investigation; methodology; project administration; resources; supervision; writing – original draft; writing – review & editing.

ORCID® iDs

Mette Heidemann Rasmussen - https://orcid.org/0000-0002-3814-6123
Jacopo Catalano - https://orcid.org/0000-0003-4819-5436
Tobias Weidner - https://orcid.org/0000-0002-7083-7004

Data Availability Statement

The data that supports the findings of this study is available from the corresponding author upon reasonable request.

References

1. Kærsgaard, C. W.; Holmstrup, M.; Malte, H.; Bayley, M. *J. Insect Physiol.* **2004,** *50,* 5–15. doi:10.1016/j.jinsphys.2003.09.003
2. Verhoef, H. A.; Witteveen, J. *J. Insect Physiol.* **1980,** *26,* 201–208. doi:10.1016/0022-1910(80)90081-5
3. Hensel, R.; Neinhuis, C.; Werner, C. *Chem. Soc. Rev.* **2016,** *45,* 323–341. doi:10.1039/c5cs00438a
4. Nickerl, J.; Tsurkan, M.; Hensel, R.; Neinhuis, C.; Werner, C. *J. R. Soc., Interface* **2014,** *11,* 20140619. doi:10.1098/rsif.2014.0619
5. Schmüser, L.; Zhang, W.; Marx, M. T.; Encinas, N.; Vollmer, D.; Gorb, S.; Baio, J. E.; Räder, H. J.; Weidner, T. *ACS Appl. Mater. Interfaces* **2020,** *12,* 12294–12304. doi:10.1021/acsami.9b21615
6. Nickerl, J.; Helbig, R.; Schulz, H.-J.; Werner, C.; Neinhuis, C. *Zoomorphology* **2013,** *132,* 183–195. doi:10.1007/s00435-012-0181-0
7. Kang, S. M.; Choi, J. S. *Small* **2020,** *16,* 1904612. doi:10.1002/smll.201904612
8. Yun, G.-T.; Jung, W.-B.; Oh, M. S.; Jang, G. M.; Baek, J.; Kim, N. I.; Im, S. G.; Jung, H.-T. *Sci. Adv.* **2018,** *4,* eaat4978. doi:10.1126/sciadv.aat4978
9. Shang, B.; Chen, M.; Wu, L. *ACS Appl. Mater. Interfaces* **2018,** *10,* 41824–41830. doi:10.1021/acsami.8b16485
10. Encinas, N.; Yang, C.-Y.; Geyer, F.; Kaltbeitzel, A.; Baumli, P.; Reinholz, J.; Mailänder, V.; Butt, H.-J.; Vollmer, D. *ACS Appl. Mater. Interfaces* **2020,** *12,* 21192–21200. doi:10.1021/acsami.9b22621
11. Artus, G. R. J.; Jung, S.; Zimmermann, J.; Gautschi, H.-P.; Marquardt, K.; Seeger, S. *Adv. Mater. (Weinheim, Ger.)* **2006,** *18,* 2758–2762. doi:10.1002/adma.200502030
12. Zimmermann, J.; Artus, G. R. J.; Seeger, S. *J. Adhes. Sci. Technol.* **2008,** *22,* 251–263. doi:10.1163/156856108x305165
13. Geyer, F.; D'Acunzi, M.; Sharifi-Aghili, A.; Saal, A.; Gao, N.; Kaltbeitzel, A.; Sloot, T.-F.; Berger, R.; Butt, H.-J.; Vollmer, D. *Sci. Adv.* **2020,** *6,* eaaw9727. doi:10.1126/sciadv.aaw9727
14. Deng, B.; Cai, R.; Yu, Y.; Jiang, H.; Wang, C.; Li, J.; Li, L.; Yu, M.; Li, J.; Xie, L.; Huang, Q.; Fan, C. *Adv. Mater. (Weinheim, Ger.)* **2010,** *22,* 5473–5477. doi:10.1002/adma.201002614
15. Zhang, J.; Seeger, S. *Adv. Funct. Mater.* **2011,** *21,* 4699–4704. doi:10.1002/adfm.201101090
16. D'Acunzi, M.; Sharifi-Aghili, A.; Hegner, K. I.; Vollmer, D. *iScience* **2021,** *24,* 102460. doi:10.1016/j.isci.2021.102460
17. Geyer, F.; Schönecker, C.; Butt, H.-J.; Vollmer, D. *Adv. Mater. (Weinheim, Ger.)* **2017,** *29,* 1603524. doi:10.1002/adma.201603524
18. Geyer, F.; D'Acunzi, M.; Yang, C.-Y.; Müller, M.; Baumli, P.; Kaltbeitzel, A.; Mailänder, V.; Encinas, N.; Vollmer, D.; Butt, H.-J. *Adv. Mater. (Weinheim, Ger.)* **2019,** *31,* 1801324. doi:10.1002/adma.201801324
19. Zhang, J.; Seeger, S. *ChemPhysChem* **2013,** *14,* 1646–1651. doi:10.1002/cphc.201200995
20. Gao, L.; McCarthy, T. J. *J. Am. Chem. Soc.* **2006,** *128,* 9052–9053. doi:10.1021/ja062943n
21. Zimmermann, J.; Seeger, S.; Artus, G.; Jung, S. Superhydrophobic Coating. WO2004113456A2, Dec 29, 2004.
22. Hensel, R.; Helbig, R.; Aland, S.; Voigt, A.; Neinhuis, C.; Werner, C. *NPG Asia Mater.* **2013,** *5,* e37. doi:10.1038/am.2012.66
23. Chu, Z.; Olveira, S.; Seeger, S. *ChemistrySelect* **2017,** *2,* 5463–5468. doi:10.1002/slct.201700950
24. Tian, J.; Li, C.; Xian, G. *J. Mater. Res. Technol.* **2022,** *21,* 4281–4298. doi:10.1016/j.jmrt.2022.11.034
25. Hoang, T. A. Chapter 2 - Mechanisms of Scale Formation and Inhibition. In *Water-Formed Deposits;* Amjad, Z.; Demadis, K. D., Eds.; Elsevier, 2022; pp 13–47. doi:10.1016/b978-0-12-822896-8.00031-5
26. Butt, H.-J.; Semprebon, C.; Papadopoulos, P.; Vollmer, D.; Brinkmann, M.; Ciccotti, M. *Soft Matter* **2013,** *9,* 418–428. doi:10.1039/c2sm27016a

License and Terms

This is an open access article licensed under the terms of the Beilstein-Institut Open Access License Agreement (https://www.beilstein-journals.org/bjnano/terms), which is identical to the Creative Commons Attribution 4.0 International License (https://creativecommons.org/licenses/by/4.0). The reuse of material under this license requires that the author(s), source and license are credited. Third-party material in this article could be subject to other licenses (typically indicated in the credit line), and in this case, users are required to obtain permission from the license holder to reuse the material.

The definitive version of this article is the electronic one which can be found at:
https://doi.org/10.3762/bjnano.16.3